

Dissertation
submitted to the
Combined Faculties for the Natural Sciences and for Mathematics
of the
Ruperto-Carola University of Heidelberg, Germany
for the degree of
Doctor of Natural Sciences

presented by

M.Sc. Clarissa Liesche
born in Berlin

oral examination date: 24.07.2014

**Spatio-temporal protease activity and cell death induced by
Natural Killer cells and soluble CD95L**

Dissertation referees:

Prof. Dr. Roland Eils
Prof. Dr. Carsten Watzl

Acknowledgments

I would like to thank Prof. Roland Eils for giving me the opportunity to work in his group, for all his support and motivation. I would like to thank Prof. Carsten Watzl for his helpful advices and for being referee of this thesis. I would like to thank PD Dr. Karsten Rippe for critical and helpful discussions on the project and being member of my thesis advisory committee and thesis defense committee. Moreover, I thank Prof. Michael Knop for being part of my thesis defense committee.

My big thanks goes to Dr. Joël Beaudouin, who always helped and inspired me and brought me new ideas in our discussions. In particular, I very much appreciated that you explained to me my numerous questions on physics. It is a great pleasure to work with you!

I want to thank Pau Castel Morales, Patricia Sauer and Julia Peukes for their contributions, enthusiasm, questions and ideas. It was great fun to work with you!

I thank Dr. Michael Ludwig (né Schwering) for the great collaboration, I enjoyed working with you at the TIRFM!

I gained expertise on the FCS method not at least through the kind help of Fabian Erdel and I thank Gernot Guigas and Nina Malchus for showing me the microscope for FCS measurements. At the time when IPs were carried out, I have trusted in the know-how of Kolja Schleich. I also thank you, Kolja, for sharing ideas, for inspiring work-discussions and for contributing to our group seminars even when you changed the lab.

I would also like to thank the other people attending the group seminar: Barbara DiVentura, Charley Choe, Dominik Niopek, Hannah Schmidt-Glenewinkel, Jens Keienburg, Johanna Berndt, Julia Rönsch, Lakshmi Venkatraman, Linda Klauss, Marti Bernardo, Michaela Reichenzeller, Paula Gonzales, Pierre Wehler, Sabine Aschenbrenner, Stefan Kallenberger, Stefan Legewie, Sven Meseke, Tobias Ahsendorf, ... for their comments and interest that helped to finish this project.

Many thanks to Manuela Schäfer and Corinna Sprengart, and all the other members of the eislabs: I have really enjoyed our scientific and non-scientific meetings and to work with you!

I shared the office with Simon Eck when writing this thesis. I would like to thank you for your helpful tips and this cheerful time.

I am grateful for Marti's and Paula's tips and opinions.

I thank Paula for sharing her expertise in writing T_EX and especially for the wonderful time during the iGEM. I will never forget :)

I particularly want to thank you, Sabine Aschenbrenner, for your always kind help and your good mood! I appreciated your positive, optimistic view and your opinion!

Linda and Julia R., it was lucky to meet you! Thank you for this cheerful time.

Daniela Richter, thank you for reading and commenting this thesis before submission. You were a great friend during the last years.

Ganz besonders möchte ich meiner Familie und meinen Freunden für Ihre liebevolle Unterstützung danken!

Contributions

Dr. Joël Beaudouin proposed the question on apoptosis induction by the two forms of ligand and supported me in developing mathematical models, namely the ODE-based model and the statistical model on the analysis of photobleaching data.

Dr. Michael Ludwig (né Schwering) carried out TIRF microscopy experiments.

Sabine Aschenbrenner assisted in analyzing soluble ligand mediated cell death data.

Dr. Kolja Schleich carried out immunoprecipitation and following SDS-PAGE and western blot experiments, while I designed the experiment.

Patricia Sauer was an internship student under my supervision for three months. She carried out experiments on the measurement of protease activity of the NK cell project and conducted FRAP experiments.

Julia Peukes was an internship student and afterwards also student assistant under my supervision for three months. She performed initial experiments on ligand internalization and conducted FRAP experiments.

Publications

I contributed to the work of Joel Beaudouin by conducting measurements and data analysis:

J Beaudouin, C Liesche, S Aschenbrenner, M Hörner and R Eils. *Caspase-8 cleaves its substrates from the plasma membrane upon CD95-induced apoptosis*. (2013) *Cell Death and Differ.* 20(4), 599-610.

Results on the relation of caspase-8 activity, substrate cleavage kinetics and cell death by the two different forms of ligand and the model for the analysis of TIRFM photobleaching data were presented in form of a poster (*see next page*):

-
- 18st ECDO Euroconference on Apoptosis on Concepts and Methods in Programmed Cell Death, Ghent, Belgium, 1.-4. 9. 2010, *Oligomerization and activity of soluble CD95L*, C Liesche, M Schwering, DP Herten, R Eils, J Beaudouin.
 - Scientific Retreat Research Program B, Kloster Schöntal, Germany, 16.-18. 5. 2011, poster title: *Trimer sensing: soluble CD95L weak oligomerization correlates with weak apoptotic activity.*, C Liesche, J Beaudouin, M Schwering, DP Herten, R Eils.
 - 12th International Conference on Systems Biology (ICSB), 28.8.-1. 9. 2011, poster title: *Correlation between the heterogeneity of the oligomerization of different CD95L forms and their activities.* C Liesche, M Schwering, DP Herten, S Wörz, J Beaudouin and R Eils.
 - 35th Annual Meeting of the German Society for Cell Biology, Dresden, Germany, 21.-24. 3. 2012, poster title: *Cellular sensitivity to apoptosis induced by different forms of ligand.* C Liesche, J Beaudouin, M Schwering, S Wörz, R Eils.

Results on ligand binding, internalization, receptor mobility and proposal of the impeded cross-linking model were presented in form of a poster presentation: *How CD95 ligand affinity impacts CD95 receptor cross-linking and pathway initiation.*, C Liesche, J Peukes, K Schleich, J Beaudouin, R Eils.

- International Conference on Systems Biology of Human Disease (SBHD), Heidelberg, Germany, 12-14. 6. 2013
- 21st ECDO Euroconference on Apoptosis on Concepts and Methods in Programmed Cell Death, Paris, France, 25.-28. 9. 2013

This work was carried out in the group of Prof. Roland Eils at the German Cancer Research Center, DKFZ/ Bioquant building, in the time between September 2009 and Mai 2014.

Abstract

In the CD95 signaling cascade molecular processes take place, which rely on protein multimerization for activity. In this work, I aimed at measuring the initial events in CD95-mediated apoptosis, in particular the kinetics of the molecular events ligand binding, receptor oligomerization, FADD recruitment and caspase-8 activation to understand which of those processes involve critical kinetic steps. For this, I used the model cell *HeLa*.

I have succeeded in showing and comparing the kinetics of ligand-binding, FADD recruitment and caspase-8 activation by using confocal microscopy. I have found that a critical step before caspase-8 activation is the binding of FADD to the activated receptor. Furthermore, I found that the activation of the receptor, presumably by its oligomerization, is a limiting step in CD95-mediated apoptosis. Moreover, I showed that the internalization and activation of the receptor CD95 at the plasma membrane are competing processes.

To arrive at these findings, two forms of soluble CD95L were compared, one naturally occurring form with weak activity (sCD95L) and one recombinant form with high activity (IZsCD95L). Next to biochemical methods, fluorescence-microscopy based techniques were particularly applied and I have been able to confirm that both forms are trimeric. Notably, I developed a new method to evaluate single-molecule photobleaching data suitable to infer the subunit stoichiometry of molecules at picomolar concentration.

Secondly, I aimed at understanding how natural killer cells (NK cells) mediate cell death in target cells. In addition to CD95L, NK cells use own proteases to induce the death of certain cells. In this context, I have been able to distinguish the activity of caspase-8 and granzymes in individual HeLa target cells based on the method of Beaudouin et al. 2013 and by using the NK cell line NK92. While granzyme B activity was measured in cells that died early after NK-cell contact, caspase-8 activity was measured in those which died late upon NK-cell contact. Noteworthy was the observation that granzyme B was mainly active near the plasma membrane, and in lesser amounts inside the nucleus. This was consistent with my results showing that the granzyme B inhibitor serpinB9 is localized at the plasma membrane. In contrast, granzyme A was probably not active in the cytosol, but in the nucleus of the cell.

Zusammenfassung

In der CD95 abhängigen Signalkaskade laufen molekulare Prozesse ab, die auf der Multimerisierung von Proteinen für dessen Aktivierung basieren. Ziel dieser Arbeit war es zum einen, die ersten Schritte in der CD95 Signalkaskade zu messen, insbesondere die Liganden Bindung, die Rezeptor Oligomerisierung, FADD Rekrutierung und Caspase-8 Aktivierung, um zu verstehen, welche dieser Prozesse kinetisch bestimmend sind. Dazu wurde die Modell-Zelle *HeLa* verwendet.

Es ist mir gelungen, die Kinetik der Liganden Bindung, FADD Rekrutierung sowie der Caspase-8 Aktivierung mittels Konfokal-Mikroskopie zu messen und zu vergleichen. Ich habe herausgefunden, dass ein kritischer Schritt noch vor der Caspase-8 Aktivierung die Bindung von FADD an den aktivierten Rezeptor ist. Es zeigte sich, dass auch die Aktivierung des Rezeptors, vermutlich durch Oligomerisierung desselben, ein limitierender Schritt in der CD95-vermittelten Apoptose ist. Des Weiteren konnte ich zeigen, dass die Internalisierung und die Aktivierung des Rezeptors CD95 an der Plasma-Membran konkurrierende Prozesse sind.

Um zu diesen Erkenntnissen zu gelangen, wurden zwei Formen von löslichem CD95L verglichen, eine natürlich vorkommende Form mit geringer Aktivität (sCD95L) und eine rekombinante Form mit hoher Aktivität (IZsCD95L). Es wurden neben biochemischen Methoden vor allem Techniken angewandt, die auf Fluoreszenzmikroskopie basieren, womit ich feststellen konnte, dass beide Liganden Trimere ausbilden. Insbesondere habe ich eine Methode entwickelt um Einzelmolekül-*photobleaching*-Daten auszuwerten, die generell dazu geeignet ist, den Oligomerisierungsgrad von Molekülen, welche in pikomolarer Konzentration vorliegen, zu evaluieren.

Zum anderen habe ich mir zum Ziel gesetzt, zu verstehen, wie Natürliche Killer Zellen (NK Zellen) den Zelltod in Zielzellen induzieren. Neben CD95L benutzen NK Zellen eigene Proteasen um den Tod bestimmter Zellen zu vermitteln. Es ist mir gelungen, basierend auf der Methode von Beaudouin et al. 2013 und unter Verwendung der NK Zelllinie NK92, die Aktivität von Caspase-8 und von Granzym B in einzelnen HeLa Zellen zeitgleich zu unterscheiden. Während Granzym B-abhängige Aktivität in Zellen gemessen wurde, die früh nach NK-Zell Kontakt starben, wurde Caspase-8 Aktivität in solchen gemessen, die spät nach NK-Zell Kontakt starben. Bemerkenswert war die Beobachtung, dass Granzym B vor allem nahe der Plasma-Membran, und in geringeren Mengen auch im Nukleus, aktiv war. Dies war konsistent mit Ergebnissen, die zeigten, dass der

Granzym B Inhibitor SerpinB9 an der Plasma-Membran lokalisiert ist. Im Gegensatz dazu wurde Granzym A Aktivität nicht im Zytosol, aber dennoch im Nukleus der Zelle, gemessen.

Contents

Acknowledgments	iii
Contributions	v
Abstract	vi
Zusammenfassung	ix
1 Introduction	1
1.1 Cell death	1
1.2 CD95 apoptosis signaling	3
1.3 Stoichiometries at the DISC	5
1.4 Apoptosis in the immune system	10
1.4.1 NK cell mediated target cell killing	10
1.5 The membrane and the soluble form of CD95L	14
1.5.1 CD95-CD95L interactions	15
1.5.2 Binding studies	16
1.6 CD95L non apoptotic signaling and internalization	17
1.6.1 Internalization of CD95 receptors	18
1.7 Aim of this work	19
2 Materials & Methods	21
2.1 Molecular Biology and Biochemistry	21
2.1.1 Molecular cloning for the expression of proteins and shRNA	21
2.1.2 Cell culture, production of ligand & transfection of plasmid DNA	21
2.1.3 Affinity chromatography	24
2.1.4 Chemical cross-linking of proteins	25
2.1.5 Separation of proteins by size and their detection	25
2.1.6 Immunoprecipitation of ligand bound to receptors on cells	26
2.1.7 Protein quantification	26
2.1.8 FA/GA fixation and immunostaining	26

2.2	Microscopy and F-techniques	27
2.2.1	Flow cytometry	27
2.2.2	Fluorescence (Cross) Correlation Spectroscopy	28
2.2.3	Confocal Laser Scanning Microscopy	28
2.2.4	Fluorescence Recovery After Photobleaching	32
2.2.5	Total Internal Reflection Fluorescence Microscopy (TIRFM)	36
3	Results	41
3.1	NK cell mediated cell death and protease activity	41
3.1.1	Study design: measurement of proteolytic activity in HeLa cells upon NK92 cell co-culture	41
3.1.2	Potential cleavage of <i>ELQTD</i> , <i>RIEADS</i> , <i>IGNRS</i> and <i>KVPLG</i> in target cells upon NK92 cell exposure	43
3.1.3	Localization of RIEADS- and IGNRS-probe cleavage	45
3.1.4	The amino acid sequence RIEADS is cleaved independently of CD95	48
3.1.5	ELQTD-cleavage as a read-out for CD95 pathway activation	49
3.1.6	ELQTD- and RIEADS-probe cleavage correlate with target cell death	51
3.1.7	Cell death and RIEADS-probe cleavage can occur independently of caspase activity	54
3.1.8	SerpinB9 over-expression reduces RIEADS-probe cleavage in HeLa cells	57
3.1.9	The proteinase inhibitor serpinB9 localizes to the cell membrane	59
3.1.10	RIEADS and ELQTD- cleaving proteases from NK cells are active at the cell membrane in target cells	60
3.1.11	Conclusion - Cell death by NK cells	62
3.2	The subunit stoichiometry of soluble CD95L is three	64
3.2.1	Biochemistry	64
3.2.2	Fluorescence Correlation Spectroscopy	67
3.3	Inferring subunit stoichiometries from TIRFM data	71
3.3.1	Automated extraction of intensity profiles from photobleaching data	71
3.3.2	Last identifiable Step-Analysis (<i>LiSA</i>)	72
3.4	Soluble CD95L mediated cell death and caspase-8 kinetics	79
3.4.1	The relation between caspase-8 onset time and strength to cell death is independent on the affinity and cross-linking state of ligand	79
3.5	Binding affinity of soluble CD95L	87
3.5.1	Set-up and analysis of binding experiments using confocal microscopy	87
3.5.2	Binding of mCherry-sCD95L is efficient	89
3.5.3	The adaptor protein FADD is inefficiently recruited by sCD95L	92

3.6	Internalization of soluble CD95L	98
3.6.1	CD95L might signal from early endosomes but not from late endosomes in HeLa cells	100
3.6.2	mCherry-sCD95L localizes to Rab4a- and Rab5a-positive endosomes . . .	102
3.6.3	Block of ligand internalization by methyl- β -cyclodextrin and monensin . . .	104
3.6.4	Block of internalization enhances sCD95L mediated cell death in HeLa cells	106
3.7	IZsCD95L, but not sCD95L efficiently cross-links CD95	111
3.7.1	Measurements of the unbinding kinetics - Minimal models of receptor activation	111
3.7.2	mCherry-sCD95L lowers the CD95 receptor mobility on living cells less than mCherry-IZsCD95L	116
3.7.3	Summary: why sCD95L is a weak inducer of apoptosis	122
4	Discussion	123
4.1	NK cell mediated protease activity measurements	123
4.1.1	Granzymes	123
4.1.2	Timing of RIEADS-probe and ELQTD-probe cleavage	125
4.2	TIRFM photobleaching analysis to derive the stoichiometry of labeled complexes .	126
4.2.1	Oligomerization state of sCD95L	128
4.3	sCD95L signal integration	128
4.3.1	Ligand-binding kinetics by confocal microscopy	129
4.3.2	CD95L-CD95 interaction strengths	130
4.3.3	Fluorescence recovery after photobleaching: measurements of CD95 mobility	130
4.3.4	Unbinding kinetics	132
4.3.5	FADD recruitment and caspase-8 activation	134
4.3.6	CD95L internalization competes with receptor activation kinetics in HeLa .	135
	Appendix	139
A	Unbinding measurements using confocal microscopy	139
B	Modeling binding kinetics	141
	List of Abbreviations	146
	List of Tables	147
	List of Figures	151
	Bibliography	172

1 Introduction

1.1 Cell death

Cell death is a process that plays an important role in cell homeostasis and during the development of multicellular organisms (Alberts 2008). Cell growth and cell division keep the balance with cell death and determine cell numbers and cell sizes. During the development of the organism, cell death takes place to remove supernumerary cells in a controlled way.

Cell death is also involved in shaping the tissue. A well-known example is the removal of tissue between the digits or removal of those cells that lead eventually to the four-chamber architecture of the heart (Fuchs and Steller 2011).

Moreover, it plays an important role in the immune system of mammals. The immune system protects the organism from diseases caused for example by microorganisms such as parasites and bacteria or by infection with viruses. Controlled cell death of the infected or invaded cell is beneficial because it helps to eliminate the deleterious invader.

Imbalances in cell death in humans can lead to diseases and disorders. For example, failure to kill auto-reactive immune cells can lead to autoimmune diseases such as diabetes. In type I diabetes, cells of the immune system target and destroy insulin-producing beta-cells of the pancreas. Other examples of too much cell death are the Alzheimer's disease or the Parkinson's disease. In those diseases, neuronal cells are lost by cell death (Mattson 2000). In contrast, resistance to cell death is a known property of tumorigenic and cancer cells (Hanahan and Weinberg 2011).

Forms of cell death

Different types of cell death have been described based on the different morphological features the cell adopts and later also based on molecular processes that are involved, namely apoptosis and necrosis (Kerr et al. 1972, Suzanne and Steller 2013). These death processes are triggered by different molecular and cellular events but can also share regulation dependent on the cellular context.

Apoptosis is regarded as a beneficial, well-controlled way of cell death and involves cell rounding and cell shrinkage followed by blebbing. Blebbing describes the breaking of the cell into smaller fragments, so-called apoptotic bodies without releasing intracellular content (Figure 1.1). Furthermore, apoptosis is accompanied by chromatin condensation (pyknosis), nuclear

fragmentation (karyorrhexis) and DNA fragmentation. Moreover, exposure of phosphatidyl serine to the outer leaflet of the surface cell membrane (plasma membrane) is a characteristic event that serves as a signal for phagocytic cells to take up the apoptotic cell remnant (Ravichandran 2011).

In contrast, necrosis is characterized by cellular organelle swelling and plasma membrane permeabilization (Han et al. 2011). The subsequent release of intracellular content can stimulate immune responses. Necrosis was originally regarded as a rather pathologic and accidental form of death as a consequence of heat or toxic agents for example. However, also regulated forms of necrosis and overlaps with apoptosis were observed (Zong and Thompson 2006, Han et al. 2011).

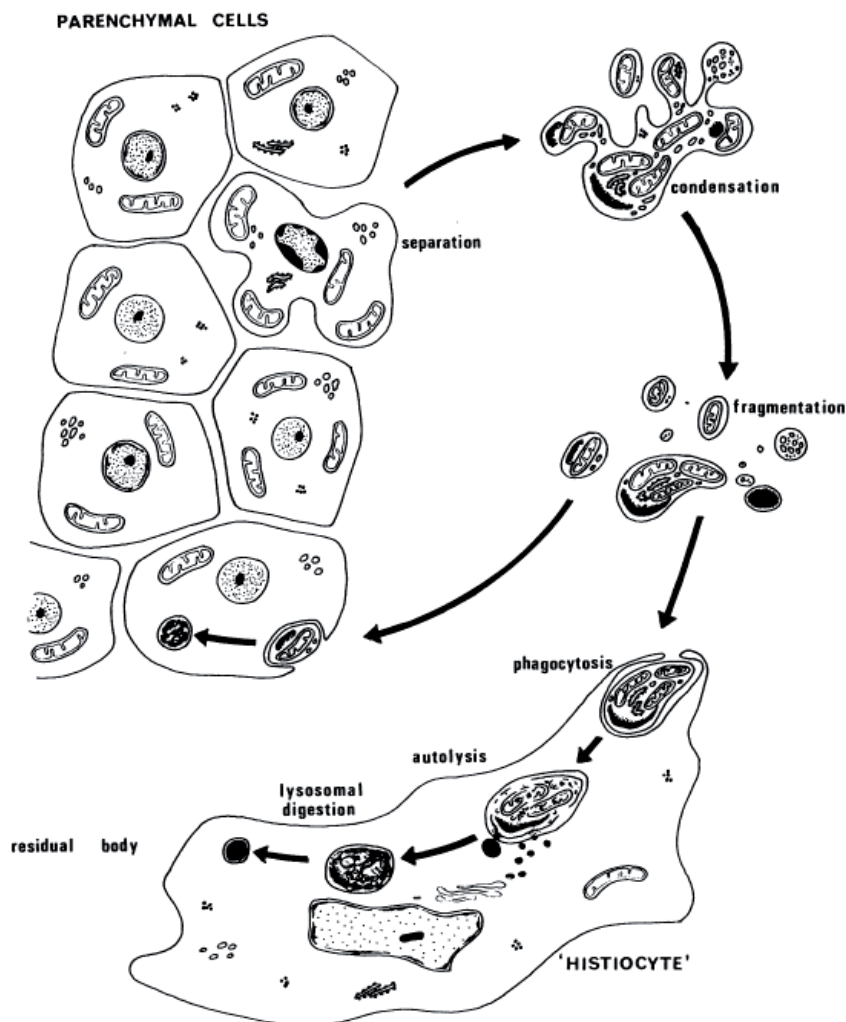


Figure 1.1: Apoptosis drawing by Kerr, Wyllie and Currie.

Their drawing was based on images acquired by electron microscopy, from Kerr et al. 1972.

1.2 CD95 apoptosis signaling

Apoptosis can be triggered by different stimuli that induce the *intrinsic* and/or *extrinsic* apoptosis pathway. Stimuli inducing the intrinsic pathway are for example UV-light that causes DNA damage. Other intrinsic apoptotic stimuli are stress of the endoplasmic reticulum and chemotherapeutic agents such as cisplatin or etoposide. Those agents damage the DNA by cross-linking or by inducing DNA breaks (Montecucco and Biamonti 2007, Tait and Green 2010).

Complementary, the extrinsic apoptotic pathway can be triggered by proteins of the TNF ligand superfamily, CD95L, TRAIL and TNF- α which specifically bind to transmembrane receptors on the extracellular side of the cell (Figure 1.2).

The receptor CD95 is expressed in our body by many cells and fulfills diverse functions (Strasser et al. 2009). However, first, CD95 (Fas/Apo-1) receptor activation was found to induce apoptosis by activation of enzymes termed caspases and was therefore coined as a death receptor (Nagata 1997, Krammer 2000).

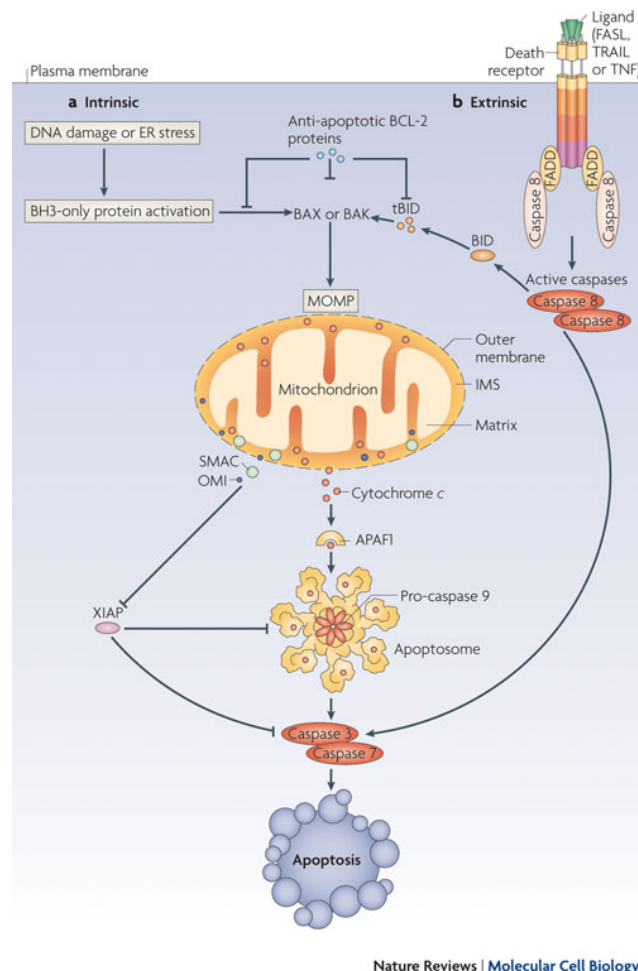


Figure 1.2: The intrinsic and extrinsic apoptosis pathways involve activation of initiator caspases (caspase-8/-9) and effector caspases (caspase-3/-7) and induction of mitochondrial outer membrane permeabilization (MOMP). Illustration from Tait and Green 2010.

Apoptosis involves caspase activity

Upon ligand binding, the receptor can recruit the adaptor protein *Fas-associated death domain-containing protein* (FADD) which in turn can bind the enzymes caspase-8/-10 and the modulators c-FLIP(L/S/R) (Figure 1.2). This protein ensemble was termed *death inducing signaling complex* (DISC, Kischkel et al. 1995).

Caspases (*cysteine-dependent aspartate-directed proteases*) were named after their mechanism to cleave proteins after the amino acid aspartic acid (Asp, D) using a cysteine in the catalytic center (Pop and Salvesen 2009). Caspase-8/-9 and -10 are so-called initiator caspases that can activate effector caspases-3/-6/-7 by proteolytic cleavage. A tetra-peptide motif is sufficient to distinguish substrate specificities between different caspases. Effector caspases cleave a defined, but large subset of proteins in different compartments of the cell leading ultimately to cell death (Mahrus et al. 2008). Substrates include the inhibitor of caspase-activated DNase (ICAD) which inhibits a protease that randomly cleaves DNA (Enari et al. 1997) and include Poly (ADP-ribose) polymerase (PARP) which is involved in DNA repair.

While effector caspases constitute dimers that become active by cleavage, initiator caspases are inactive monomeric zymogens that become active by dimerization and subsequent self-cleavage. Recruitment of caspase-8 to the DISC was proposed to *induce proximity* that allows activation of initiator caspases (Muzio et al. 1998). In this light, it is known that different initiator caspases are activated within protein assemblies in *platforms*, namely the DISC, the *apoptosome*, the *piddosome* and the *inflammasome* (Figure 1.3, Pop and Salvesen 2009).

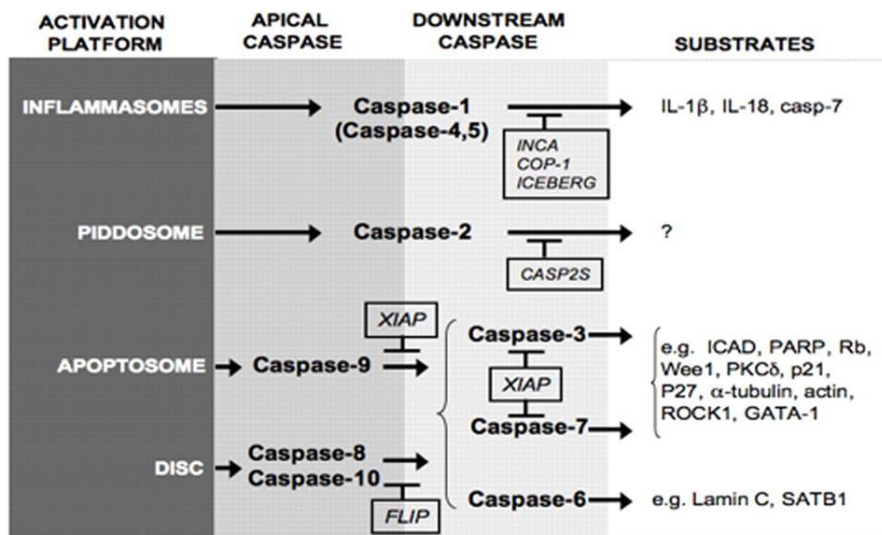


Figure 1.3: Caspase activation platforms. Apical (initiator) caspases are activated in protein complexes termed platforms (Scheme from: Pop and Salvesen 2009).

Apoptosis can occur via mitochondria

Cells in which initiator caspases efficiently cleave and activate effector caspases to induce apoptotic cell death are termed *type I* cells and include lymphoid and myeloid cells. In contrast, *type II* cells display a strong dependence on the mitochondrial (intrinsic) apoptosis pathway as activation of effector caspases by initiator caspases is inefficient (Figure 1.2) and include for example hepatocytes and pancreatic island β -cells (Scaffidi et al. 1998, Barnhart et al. 2003, Hau et al. 2012). On mitochondria, oligomerization of the proteins BAX and BAK induces mitochondrial outer membrane permeabilization (MOMP), which leads to release of cytochrome c, a protein that is involved in mitochondria in the electron transport chain and is involved in the cytosol in the formation of the apoptosome.

Furthermore, Smac/Diablo and Omi/HtrA2 can be released which inhibit proteins termed inhibitors of apoptosis (IAP). For example, XIAP binds and inhibits active caspase-3 and binds also monomeric caspase-9. Thus, inhibition of XIAP leads to increased levels of active caspase-3 and permits dimerization of caspase-9.

MOMP induction by protein multimerization of pro-apoptotic Bcl-2 family members is guarded by proteins of the same family including BCL-2, BCL-w, MCL-1, BFL-1, and BCL-X_L. These anti-apoptotic proteins keep pro-apoptotic members, for example BAX, BAK, Bim and tBid, in check (García-Sáez et al. 2009, Chipuk et al. 2006). Finally, tBid links the extrinsic pathway to the mitochondrial apoptosis pathway through its cleavage by caspase-8 (Figure 1.2).

1.3 Stoichiometries at the DISC

The receptor CD95 comprises a single transmembrane region, a cytosolic death domain and three extracellular cystein-rich domains (CRD), which are involved in self-assembly of the receptor and in the ligand-receptor interaction (Figure 1.4). Despite structural information on the CD95L-CD95 interaction is lacking, the high similarity of the proteins to the TNF/TNFR family suggests that CD95L and CD95 bind in a threefold stoichiometry (Banner et al. 1993, Nagata 1997). Three receptors would be arranged around the trimeric ligand so that one receptor binds two ligand subunits and, vice versa, one ligand subunit can bind two receptors (Figure 2.3, page 33).

Ligand-induced CD95 receptor trimerization was early proposed as a mechanism to bring receptors close and to establish proximities that are necessary for caspase-8 activation (Muzio et al. 1998). Importantly, later it has been shown that CD95 receptors self-interact at the *pre-ligand binding assembly domain* to form trimers in the non-ligated state (PLAD, Figure 1.4, Papoff et al. 1999, Siegel et al. 2000, Goldstein 2000, Edmond et al. 2012).

Concordantly, Naismith and coworkers have shown by crystallography that the TNFR1 extracellular domains dimerize (Naismith et al. 1995). Recently, dimerization was confirmed by Boschert and co-workers using chemical cross-linking (Boschert et al. 2010), though trimeric

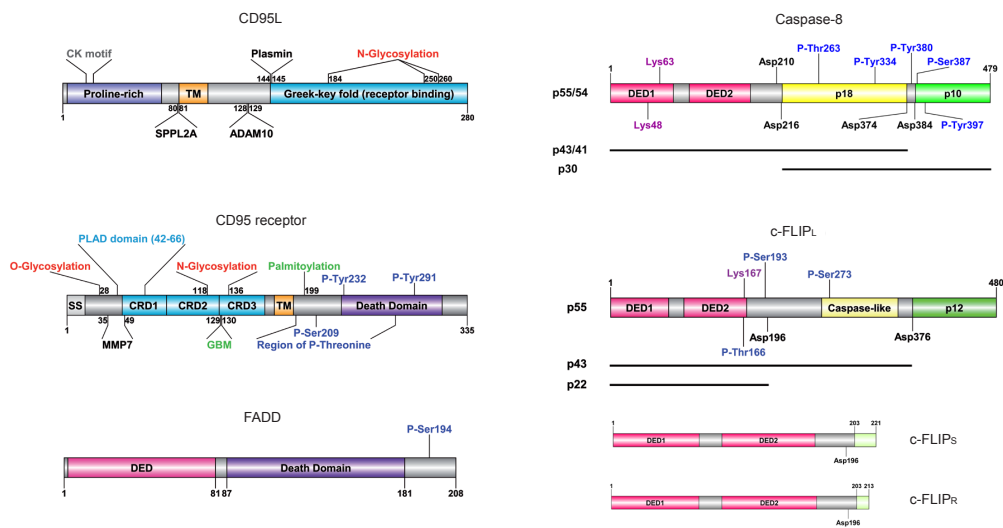


Figure 1.4: Protein informations on CD95L, CD95, FADD, Caspase-8 and FLIP. Proteins are shown from N-terminus to C-terminus, numbers indicate the amino acid position, TM = transmembrane region, CRD = cysteine rich domain, DED = death effector domain. Schemes made using the software CSS-Palm4.0, Ren et al. 2008.

TNFR receptors have been observed by biochemical cross-linking as well (Chan et al. 2000). Notably, dimerization of receptors would not interfere with ligand binding (Naismith et al. 1995) so that the formation of receptor-ligand networks was proposed (Idriss and Naismith 2000).

Interestingly, another member of the TNF receptor family, death receptor 5 (DR5), was shown to dimerize upon ligand binding. The ligand (TRAIL) - receptor (DR5) interaction was assumed to occur in a three-to-three manner. Thus, dimerization would result in large receptor networks (Valley et al. 2012).

It is well known that recruitment of signaling proteins to the receptor occurs via homotypic (homophilic) domain interactions. The adaptor protein FADD and the receptor were proposed to interact via their death domains in an antiparallel manner that would allow caspase-8 recruitment to two different receptor trimers (Figure 1.5A,D). Moreover, it has been demonstrated that FADD self-associates and is more efficiently recruited to CD95 receptors when the death effector domain (DED) of FADD is present (Boldin et al. 1995, Thomas et al. 2002, Thomas et al. 2004, Muppidi et al. 2006, Sandu et al. 2006, Carrington et al. 2006).

Initiator caspases-8/-10 contain two death effector domains (DED). It was proposed that the DED2 in caspase-8 would mediate binding to FADD (Carrington et al. 2006), however, new interpretations suggest that FADD could also bind to DED1 of caspase-8 (Dickens et al. 2012). Interestingly, it was found by two independent studies applying quantitative mass spectrometry that FADD amounts are less abundant than caspase-8 molecules and DED-domain containing molecules, respectively. Based on this, formation of chains of caspase-8 and FLIP were proposed (Schleich et al. 2012, Dickens et al. 2012).

Regarding the CD95-FADD stoichiometry at the DISC, based on structural information it was seen that the cytosolic domain of the receptor bound to FADD in a 4:4 manner (Scott et al. 2009) or in a 5:5 to 7:5 manner (Wang et al. 2010, Esposito et al. 2010, Figure 1.5A-C). Interestingly, Scott and co-workers moreover proposed a conformational change of the receptor.

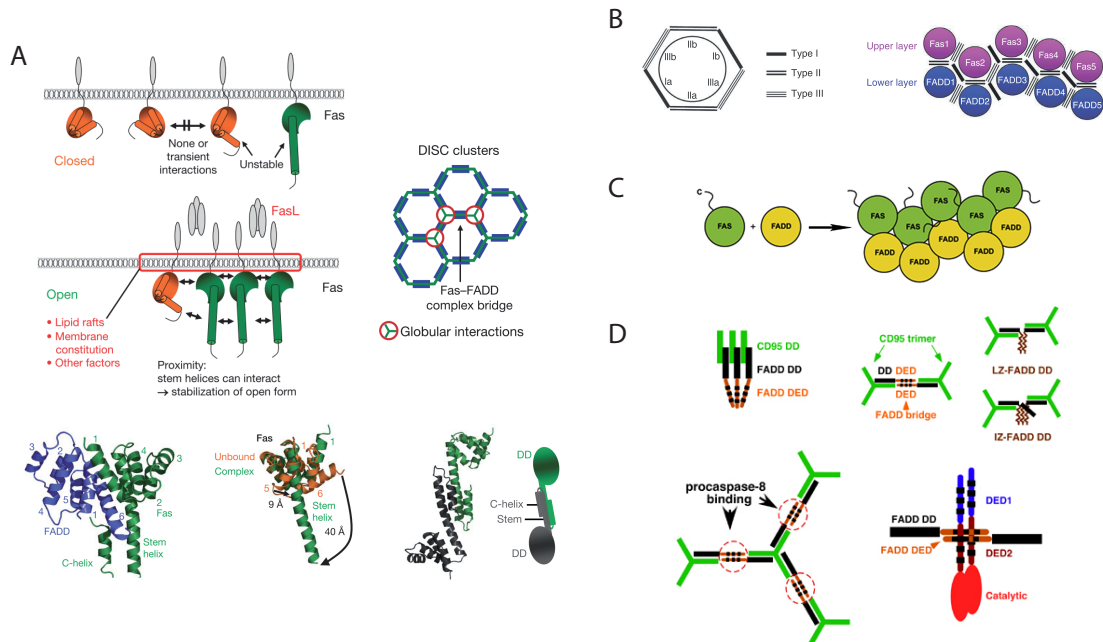


Figure 1.5: Models of FADD binding to CD95 receptor. Illustrations were taken from the indicated references. (A) Receptor opening model from Scott et al. 2009, receptor networks would be possible, red: circle represents trimeric ligand-receptor complex, two FADD molecules would bind to two receptors. (B) Model of Wang et al. 2010, 5:5 to 7:5 (Fas:FADD) stoichiometry. (C) Model of Esposito et al. 2010 similar to (B), Note that the C-terminal tails of CD95 would not contribute to clustering (D) Models of FADD binding to CD95 receptors (from: Sandu et al. 2006). Dimeric (leucine-zipper, LZ) and trimeric (isoleucine-zipper, IZ) death domains (DD) of FADD bound more efficiently to CD95 receptors than the DD of FADD without its DED or oligomerization domains. Networking of receptors on the inner leaflet of the plasma membrane would be possible. Caspase-8 would dimerize at the FADD-bridges.

Caspase-8 processing and activity

Pro-caspase-8 is an inactive, monomeric zymogen in the cytosol and exists as isoform *a* and *b* differing in size by 15 amino acids, termed p55 and p53. It contains a prodomain with two *death effector domains* (DED) and a large (p18) and a small (p10) subunit. Dimerization of caspase-8 into $(p55/53)_2$ activates the enzyme through a conformational change that enables the formation of an active site at the large and small subunits (the active site within the monomer is shown in Figure 1.6, Yu et al. 2009). Dimerization and formation of the active site thus allows proteolytic activity including auto-cleavage explained in the following. Self-processing was shown to stabilize the dimeric form of caspase-8 (for example Pop et al. 2007). Notably, in line with the induced-proximity model (Muzio et al. 1998), cleavage events have been shown to be interdimeric,

meaning that the two active sites of one dimer can cleave Asp-sites in another caspase-8 dimer (Figure 1.5, Chang et al. 2003). Caspase-8 processing involves cleavage between the p18 and the p10 subunits (Asp 374, Asp 384) resulting in the fragment $(p43/41)_2$, while non-covalent binding of p10, and thus the active site, is retained (Figure 1.4, Lavrik and Krammer 2012). Furthermore, it was demonstrated that cleavage after the second DED (Asp 210, Asp 216) can result in a fragment $(p30)_2$, which occurs simultaneously with $(p43/41)_2$ generation, though less preferred (Hoffmann et al. 2009). This is consistent with the observation that caspase-activity reporters containing the cleavage site *MTISDS* (Asp 210) and *PREQDS* (Asp 216) were less efficiently cleaved (Kallenberger et al. 2014) than reporters containing the cleavage site *PVETDS* (Asp 374) of caspase-8 and *ELQTDG* (Asp 60) of Bid (Beaudouin et al. 2013).

Moreover, the tetramers $(p43/41)_2$ and $(p30)_2$ can be further processed in a second event of cleavage into a smaller tetramer with two non-covalently binding fragments of $(p18/p10)_2$. Dimers of p55/53 only very inefficiently cleave substrates different from itself or cellular FLIP, while p43/41, p30 and p18/10 were reported to efficiently cleave other substrates such as caspase-3 and Bid (Hughes et al. 2009).

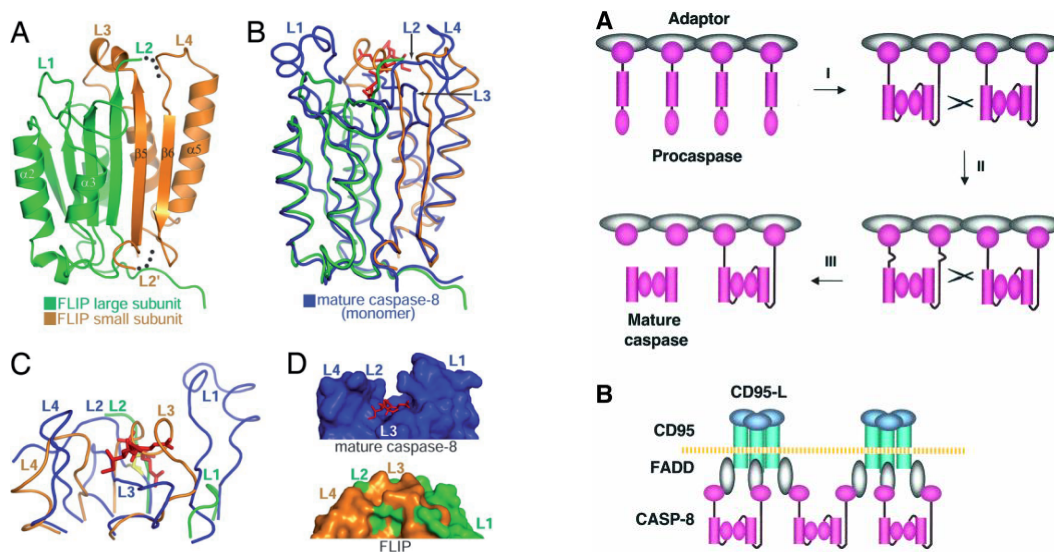


Figure 1.6: The active site of caspase-8 formed at the large and the small subunit. *Left:* (A) Monomer of FLIP_L, the large and the small subunit form a beta-sheet in the active conformation, the protein has no enzymatic activity. (B) Overlay of the amino acids of FLIP_L and caspase-8, L = loops in caspase-8 that shape the active site. (C-D) FLIP_L does not form an active site, caspase-8 shown with substrate colored in red. (Figure from: Yu et al. 2009), *Right:* Interdimer cleavage model of caspase-8 processing; I, Conformational change and dimerization renders caspase-8 proteolytically active; II, Cleavage between the large and small subunit would be followed by a conformational change favoring cleavage after the second DED. Fully cleaved caspase-8 dimers would be released into the cytosol. (B) Unpaired FADD from two trimeric receptor complexes could be bound by a caspase-8 dimer (Figure from: Chang et al. 2003)

Modulation of caspase-8 processing by c-FLIP

Apart from homodimerization, caspase-8 can also dimerize with FLIP_L but not with the short isoforms of FLIP (FLIP_{S/R}, Micheau et al. 2002). FLIP_L has a similar protein architecture to caspase-8 but does not contain an active caspase-domain (Figure 1.4, and 1.6).

Notably, Yu and co-workers showed that caspase-8 prefers cleavage of FLIP over cleavage of caspase-8 (Yu et al. 2009). Strikingly, activity from hetero-tetramers was shown to be important for non-apoptotic signaling (Micheau et al. 2002, Leverrier et al. 2011, Oberst et al. 2011). Interestingly, FLIP_L can either promote caspase-8 activation or block it depending on the dose of ligand and FLIP_L (Fricker et al. 2010). In turn, the short isoforms which lack the caspase-like domain and the p12 domain, generally block the formation of active caspase-8 (Yu et al. 2009).

Caspase-8 spatial localization of activity

Recently, we have published our observation that caspase-8 readily cleaves substrates from the plasma membrane in HeLa cells and in MDA-MB-231, HT-1080, T98G and MCF-10A cells (Beaudouin et al. 2013). We concluded this from findings that (i) a prodomain mutant of caspase-8, Asp 210/216/223 Ala, lowered probe cleavage at the endoplasmic reticulum but neither changed cell death kinetics nor caspase-probe cleavage kinetics in the cytosol and at the plasma membrane, (ii) targeting the proteins caspase-3 and Bid to the plasma membrane enhanced cell death and also caspase-3/-8 probe cleavage kinetics in comparison to expression of these proteins soluble in the cytosol or at the endoplasmic reticulum, (iii) a membrane reporter was more efficiently cleaved than a soluble cytosolic reporter and than differently trapped cytosolic reporters facing the cytosol.

We showed furthermore that the cleavage site *PVETDS* (Asp 374) present in caspase-8 and the site *LLEVDG* (Asp 376) present in FLIP_L are as efficiently cleaved as the cleavage site *ELQTD* (Asp 60) of Bid in a context where FLIP_L protein levels were low compared to caspase-8 levels.

Dr. Joël Beaudouin also tested the spatial activity of caspase-8 in HeLa cells that were stimulated with TNF- α and cyclo-heximide. Strikingly, reporter cleavage measurements showed that caspase-8 activity was more present inside the cell than at the plasma membrane, consistent with previous models of TNF activity from endosomes (Micheau and Tschopp 2003, Tchikov et al. 2011). Caspase-8 activity at the plasma membrane does not exclude the possibility of activity from the observed so-called *complex II* inside the T-cell lines J16 and JA3, *type II* cells, and HUT78, SKW6.4, Raji, BJAB *type I* cells (Lavrik et al. 2008). Thus, by interpreting our observations, the main contribution of caspase-8 (pro-apoptotic) activity would be localized at the plasma membrane in *type II* cells, possibly in the so-called *complex I*.

1.4 Apoptosis in the immune system

Hematopoietic stem cells from the bone marrow can differentiate into specialized cells of the blood and the lymph. Cells of the myeloid lineage give rise to erythrocytes, thrombocytes, granulocytes and phagocytes, while cells of the lymphoid lineage become Natural Killer cells (NK cells), T-cells and B-cells. Apoptosis can be initiated by some cells of the lymphoid lineage.

For example, to regulate cell homeostasis of clonal expanded activated T-cells, those can undergo caspase-dependent or -independent cell death (Krammer et al. 2007). A disease termed large granular lymphocyte leukemia showed, on the molecular level, resistance of Cytotoxic T-cells (CTLs) to CD95 mediated apoptosis despite high CD95 expression levels (Lamy et al. 1998).

Furthermore, dysfunctional CD95 caused by diverse somatic mutations in the gene can cause a disease termed autoimmune lymphoproliferative syndrome (ALPS, Worth et al. 2006). The ALPS disease can be accompanied by elevated levels of auto-reactive antibodies. These examples demonstrate the important role of CD95-mediated apoptosis in B-cells and CTLs (Paulsen and Janssen 2011, Strasser et al. 2009).

Moreover, NK cells and CTLs are known for their ability to defeat a virus infection or tumor progression (reviewed in Momburg et al. 2013, Orange et al. 2002, Koch et al. 2013). While CTLs are part of the adaptive immune system and kill cells by apoptosis through specific T-cell receptor interactions and co-stimulatory molecules, Natural Killer cells are associated with the innate immune system and kill cells in a tightly controlled way that involves interactions with activating and inhibitory receptors of the NK cell. For example, some inhibitory receptors recognize MHC class I molecules, which signal the NK cell to tolerate own, healthy tissue.

1.4.1 NK cell mediated target cell killing

The steps involved in NK cell mediated killing were recently reviewed in Mace et al. 2014, listing the known events that occur during target cell recognition, during the effector phase and during signal termination. The illustration in Figure 1.7 visualizes some of the reviewed events: Recognition of a target cell by an NK cell is mediated by cell surface proteins (1.7 a-d). When activating signals win over inhibitory signals in the NK cell (1.7 d-e), the (activating) immunological synapse is formed which involves actin remodeling (1.7 e-f).

Microtubuli and lytic granules reorganize prior to ion-channel activation. Different ion-fluxes have activating and inhibiting roles in the cell, while rise in intracellular calcium, first from intracellular storage and secondly through plasma-membrane channels, is associated with activation and granule exocytosis (1.7 f, and Feske et al. 2012). For the degranulation of lytic granules towards the target cell membrane, polarization of the microtubule-organizing center (MTOC) is pivotal. This step is accomplished by several proteins and requires F-actin polarization (1.7 h-o).

Finally, lytic content is exocytosed towards the target cell while intact vesicles are recycled (1.7 p).

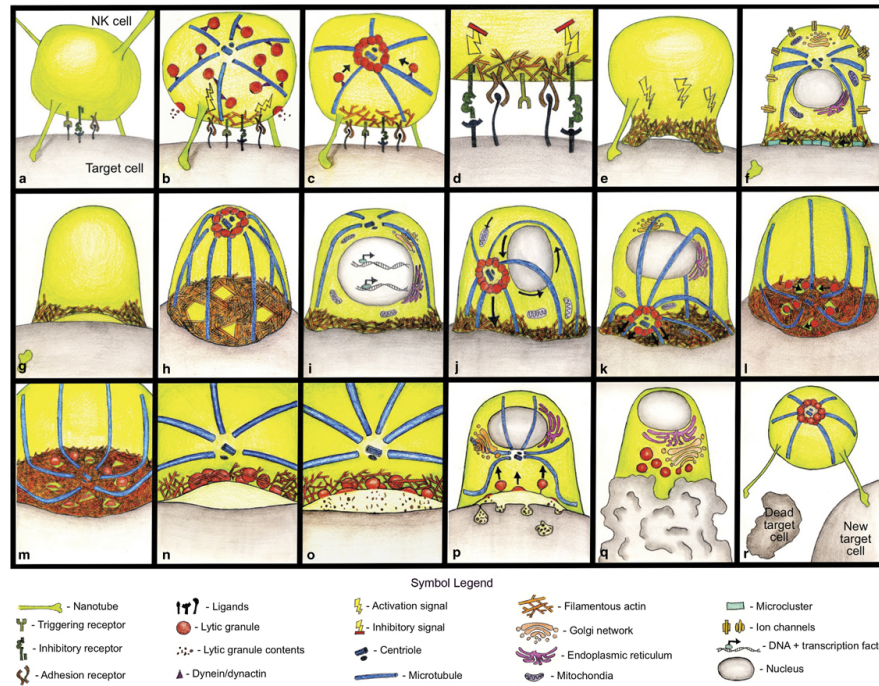


Figure 1.7: NK cell exocytosis drawing showing the reorganization of actin, vesicles and the MTOC in the NK cell. (Illustration from: Mace et al. 2014)

These events are followed by detachment from the target cell that undergoes apoptosis (1.7q-r). In the course of the NK cell mediated death response, NK cells secrete cytokines, such as IFN- γ , which can result in a positive feedback to enhanced NK cell cytotoxicity and which stimulates activity of macrophages and differentiation of T-cells (Schoenborn and Wilson 2007). NK cells also express TNF- α , TRAIL and CD95L, which can induce apoptosis by triggering caspase activation in the attacked target cell. Alternatively, NK cells kill their target cell by delivering proteases termed granzymes into the target cell (Masson and Tschopp 1987, Krzewski and Coligan 2012). This circumvents the need of caspase expression in the target cell for death induction. The volume within the immunological synapse was estimated to be less than $5 \mu\text{m}^3$ (Martinvalet et al. 2009), allowing high ligand and receptor concentrations for soluble proteins. Moreover, entire vesicles were observed to be secreted by NK cells, which might still allow high local concentration of cytotoxic agents and proteins at the plasma membrane of the target cell (Mace et al. 2014).

Granzymes

Granzyme A and B are activated by cleavage through cathepsins and stored as active enzymes in lytic granules (Kummer et al. 1996). Moreover, granzyme B is complexed with serglycin, and association to heparan sulfate enhanced granzyme A and B activity (Zhang et al. 2001, Grujic et al. 2005, Veugelers et al. 2006).

With the help of perforin, which forms transient pores at the plasma membrane (Lopez et al. 2013)

or from endosomes (Thiery et al. 2011), granzymes enter the target cell, a process that possibly also requires chymase activity (Kam et al. 2000). Fail of granzyme delivery by non-functional perforin is known to cause uncontrolled activity of lymphocytes and macrophages leading to high cytokine production, a disease termed lymphohistiocytosis (Krzewski and Coligan 2012). Similar to caspases, granzymes cleave essential proteins inside the target cell, a process that leads to cell death and that can show apoptotic or non-apoptotic signs of death (Figure 1.8).

	Granzymes						
	A	B	H	K	M	C	F
Cell lysis	Yes	Yes	Yes	Yes	Yes	Yes	Yes
z-VAD-fmk sensitive	No	Yes	Y/N	No	Y/N	No	No
Bcl-2 inhibition	No	Yes	?	No	No	?	?
MOMP	No	Yes	Y/N	Yes	Y/N	Yes	Yes
$\Delta\psi_m$	Yes	Yes	Yes	Yes	Y/N	Yes	?
ROS	Yes	Yes	Transient	Yes	Y/N	?	Yes
ATP Depletion	Yes	Later	?	?	?	?	Rapid
PS exposure	Yes	Yes	Yes	Yes	Yes	Yes	Yes
Loss plasma membrane	Rapid	Late	Rapid?	Rapid	Rapid Late	Rapid	Rapid
Chromatin condensation	Yes	Yes	Yes	Yes	Yes	Yes	Yes
DNA fragmentation	Yes	Yes	Yes	Yes	Y/N	Yes	?
	SS	DS	DS?	SS		SS	
PARP	Yes	Yes	?	?	Y/N	?	?
ICAD/DFF45	No	Yes	Y/N	?	Y/N	No	?
Bid	No	Yes	Y/N	Yes	?	No	No

Abbreviations: DS, double stranded; MOMP, mitochondrial outer membrane permeability; SS, single stranded; Y/N, reported results have been contradictory; ?, have not been reported.

Figure 1.8: Granzyme- dependent cell death characteristics. Human granzymes A, B, H, K, M and mouse granzymes C and F. (Table from: Ewen et al. 2012)

In contrast to caspases, granzymes are serine proteases belonging to the tryptase family. Five human granzymes (A, B, H, K, M) are known (Kam et al. 2000, Ewen et al. 2012). The only granzyme that cleaves its substrates after the amino acid aspartic acid (D, Asp), like caspases do, is granzyme B. In contrast, granzyme A and K cleave preferentially after arginine or lysin (tryptase), granzyme M cleaves preferentially after methionine and granzyme H prefers tyrosine (Mahrus and Craik 2005). Interestingly, it was shown that granzyme B and caspase-8 both cleave the protein Bid, however at different sites, namely at *RIEADS* and at *ELQTDG* (Figure 1.9, Li et al. 1998).

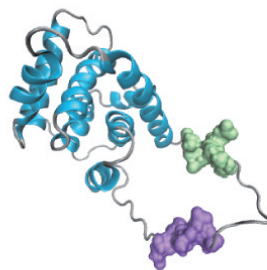


Figure 1.9: Bid can be cleaved by granzyme B and caspase-8. The PDB entry 2BID shows the protein Bid, illustrated using the program VMD (Humphrey et al. 1996). Amino acids RIEADS (green) are recognized by granzyme B while amino acids ELQTDG (purple) are preferably recognized by caspase-8.

Next to Bid, caspase-8 and -10 were reported to be cleaved by granzyme B (Barry et al. 2000). Thus, caspase-8 and granzyme B might use the same route to trigger cell death. Moreover, while caspase-8 substrates were mostly found inside the cytosol, granzyme A and B substrates were found in the cytosol and inside the nucleus. Granzyme B was reported to cleave the substrates ICAD, PARP, NUMA, ROCK-II, DNA-PK, lamin B, filamin and α -tubulin (Andrade et al. 1998, Joeckel and Bird 2014). Granzyme A cleaves substrates of the SET complex inside the nucleus which translocate there from the ER in a ROS-dependent manner. Further nuclear substrates are lamins A to C, core histones, Ku70 and PARP-1 (Ewen et al. 2012). Notably, also the mitochondrial protein NUDUFS3, component of complex I, was reported to be cleaved by granzyme A (Martinvalet et al. 2008).

In this way, granzymes take over both tasks, of initiator and of effector caspases. Though less is known of the sub-cellular localization and about substrates of granzyme M, K and H, it was found that granzyme M could enhance granzyme B function by cleaving the granzyme B inhibitor serpinB9 (Bird et al. 1998, Mahrus et al. 2004).

Expression of *serine proteinase inhibitor* serpinB9 at the protein level was originally described in dendritic cells and in immune-privileged tissues (Bladergroen et al. 2001). It is debated whether serpinB9 blocks caspase-8 on top of granzyme B (Bird et al. 1998, Kummer et al. 2007, Kaiserman and Bird 2010). But it was shown that only mutated serpin B9 (Glu 340 Asp) made serpinB9 an inhibitor of CD95 induced apoptosis similar to the viral protein CrmA, however, with a reduced ability to catalyze granzyme B (Bird et al. 1998).

It is thought that serpinB9 keeps granzyme B in check to avoid so called self-inflicted lysis of cytotoxic T cells (Bird et al. 1998, Ashton-Rickardt 2010) or destruction of healthy, next-standing cells like endothelial and mesothelial cells (Buzza et al. 2001) and mesenchymal stem cells (Haddad et al. 2011), and it might also confer resistance to tumor cells (Medema et al. 2001, Stout-Delgado et al. 2007).

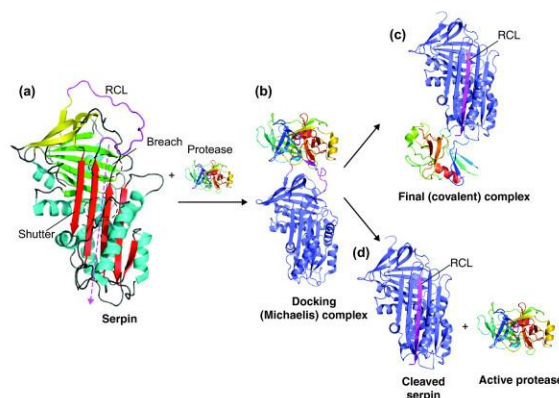


Figure 1.10: Serpin inhibitory mechanism. The protease binds serpin at the reactive center loop (RCL, a) and forms a complex with serpin (b). Serpin either is enzymatically cleaved releasing the active protease (d) or forms a covalent complex with the protease (c). Note that in both cases serpin undergoes a conformational change, the RCL forming a beta-strand (Scheme from: Law et al. 2006).

1.5 The membrane and the soluble form of CD95L

CD95L is one of the 19 members of the TNF superfamily (Aggarwal 2003). Most of the members are type II single-pass transmembrane proteins, with the N-terminus facing the cytosol (Figure 1.4). The extracellular region contains the TNF homology domain (THD), which constitutes the receptor-binding domain forming a non-covalent trimer. In some cases this domain can be cleaved off and act as cytokine, a well-known example is TNF- α . Interestingly, some of the TNF ligands bind different receptors, such as CD95L binding to CD95 and DcR3 and TRAIL binding to DR4, DR5, DcR1 and DcR2. Vice versa, different ligands bind the same receptor, such as TNF- α and TNF- β both bind TNFR1 and VEGI and LIGHT both bind DR3. CD95L, expressed by NK cells and CTLs, is stored inside the cell on lytic granules where its proline-rich domain is recognized by Src homology 3 (SH3) domain binding proteins that mediate this sorting. Interestingly, a study conducting proteom analysis on isolated vesicles revealed that CD95L and granzymes are most likely stored into distinct lytic granules, as those constituted a different protein composition (Schmidt et al. 2011).

Regarding CD95L processing, CD95L can be cleaved by SPPLA leading to the release of the cytosolic domain. Thereby, reverse signaling and activation of transcription can be induced by the N-terminal CD95L domain (Kirkin et al. 2007). Moreover, CD95L can be cleaved by the proteases ADAM10 and Plasmin, presumably from the extracellular side of the cell when the ligand is exposed at the plasma membrane (Figure 1.11, Schulte et al. 2007, Bajou et al. 2008). This cleavage leads to release of the soluble form of ligand (sCD95L) comprising the receptor binding domain. The soluble ligand is trimeric but is less potent to induce cell death than its membrane counterpart (Tanaka et al. 1995, Schneider et al. 1998). Secondary cross-linking of trimeric ligand using antibodies has been shown to enhance its apoptotic activity (Figure 1.11, Schneider et al. 1998, Holler et al. 2003).

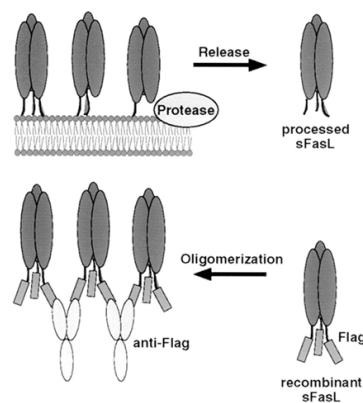


Figure 1.11: Proteolytic cleavage of FasL/CD95L and secondary cross-linking by antibodies. Proteases cleave membrane CD95L and release a soluble form of ligand termed sFasL/sCD95L. Increase of the specific apoptotic activity of sFasL/sCD95L can be achieved by "secondary" cross-linking of the ligands using antibodies. (Illustration from Schneider et al. 1998)

1.5.1 CD95-CD95L interactions

The CD95L amino acid sequence forms a jelly-roll fold with two beta-sheets. Several loops protrude the ligand trimers, those at the N- and C-terminus are stabilized intramolecularly by a disulfide-bridge and those to the side mediate binding to the receptor (Figure 1.12, right and Figure 2.3, page 33). By mutagenesis studies it was discovered that mostly charged and polar amino acids are involved in the CD95-CD95L interaction (Figure 1.12, Bajorath 1999).

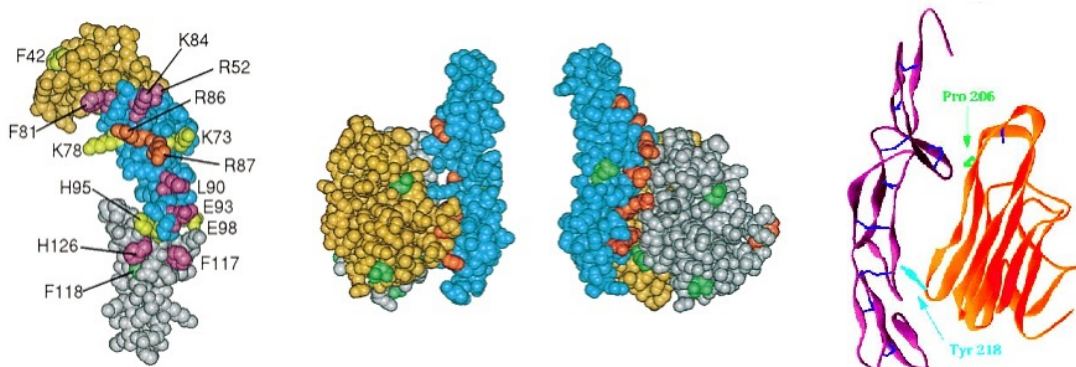


Figure 1.12: Amino acids involved in the CD95L-CD95 interaction. Illustration left and middle from: Bajorath 1999, *Left*: CD95 receptor, red: mutation abolished binding (amino acids in one-letter code), magenta: mutation significantly reduced but did not abolish binding, yellow: not important for binding, green: mutation allows no receptor expression. *Middle*: blue receptor binding in the cleft formed by two CD95L monomers in gold and gray, red: residues (CD95) critical or important for binding, green: CD95L glycosylation sites. *Right*, with inverted colors from Schneider et al. 1997: Amino acids Pro206 and Tyr218 in CD95L are involved in CD95 binding, dark blue: disulfid-bridges.

In contrast, the interaction between monomer subunits is accomplished by van der Waals forces and hydrogen bond interactions that are located between the beta-sheets. Crystallography revealed that TNF- α forms a compact trimer, while the TNF family ligand GIRTL forms surprisingly a more open, less compact trimer and coherently a weak tendency to trimerize (Mukai et al. 2010, Chattopadhyay et al. 2007). Recently, a crystal structure of the CD95L monomer (amino acids 130-280) binding to a monomer of soluble decoy receptor DcR3, a receptor form amplified in lung and colon cancer (Pitti et al. 1998), was deposit in the protein data base (PDB, entry code 4MSV). However, based on biochemical data, including gel filtration (Tanaka et al. 1997) and biochemical cross-linking (Berg et al. 2007), trimerization of sCD95L is expected.

Nevertheless, it was discovered that fusing sCD95L to trimerization domains dramatically enhanced their activity (Shiraishi et al. 2004). Those oligomerization domains include parts of the extracellular matrix protein tenascin-C (TNC) (Berg et al. 2007), parts of the protein fibrin of bacteriophage T4 (T4-domain) (Martin-Villalba et al. 2008) or the coiled-coil protein isoleucine zipper which is a mutant form of the leucine zipper found in the protein GCN4P-II of yeast (Shiraishi et al. 2004, PDB entry 1GCM).

A possible reason for the enhanced activity of the membrane and the soluble CD95L that are

fused to oligomerization domains over the activity of sCD95L might be a conformational change by at the same time keeping and possibly stabilizing non-covalent trimerization. In this way, the oligomerization-fused soluble ligand would mimic the membrane form, which is presumably less flexible or more rigid than the cleaved sCD95L form, as discussed for the human GIRTL ligand and its isoleucine-zipper fused form in Chattopadhyay et al. 2007. Notably, those differences observed for the soluble ligands and membrane counterparts reflect the importance of proteolytic processing as a way for the cell to modulate their activity.

1.5.2 Binding studies

CD95 contacts to CD95L are mainly accomplished by means of the second and third cystein rich domain (CRD) of the receptor (Edmond et al. 2012). The CD95-CD95L interactions are of electrostatic nature (Bajorath 1999). For example, the surface potential of the related receptors TNFR1 and TNFR2 differ at the contact regions to the ligand, explaining different affinities to their ligand TNF- α (Mukai et al. 2010).

The crystal structure of receptor TNFR1 with TNF- β (Banner et al. 1993) and of receptor DR4 with TRAIL (Hymowitz et al. 1999), but also the mutagenesis study (Bajorath 1999) showed that one receptor simultaneously binds to two ligand subunits of the trimeric ligand.

Surface plasmon resonance measurements revealed for binding of Flag-sCD95L to dimeric Fc-fused CD95 receptors a $k_{on} = 7.2 \times 10^4 \text{ nM}^{-1}\text{sec}^{-1}$ and $k_{off} = 2.8 \times 10^{-3} \text{ sec}^{-1}$ by fit to a 1:1 Langmuir model (Berg et al. 2007). Interestingly, Lang and co-workers developed an assay based on luciferase-bound soluble CD95L to measure the binding of CD95L to CD95 receptors on cells. They combined the advantages of non-radioactive labeling with high sensitivity detection and revealed that antibody cross-linked soluble CD95L showed similar receptor occupancies compared to soluble CD95L despite different avidities due to enhanced ligand cross-linking. This resulted in stronger accumulation of antibody cross-linked ligand than of soluble CD95L in the lipid-raft/detergent insoluble fraction. Interactions between the ligand and the receptor were assumed to occur in three-to-three mode, but a shift in equilibrium towards lipid-raft localized, ligand-bound receptors was proposed. Furthermore, the K_D for luciferase bound soluble CD95L was around 2.0 to 2.6 nM on HT1080 cells (23000 binding sites) and HaCaT (4600 binding sites) cells (Lang et al. 2012). Boschert and co-workers concluded from radioactive binding measurements at 0°C on cells that TNF- α binds to single receptors of pre-dimerized TNFR1 but binds to both of the pre-dimerized TNFR2 receptors (Figure 1.13, Boschert et al. 2010). Furthermore, while TNFR1 showed a low unbinding rate ($t_{1/2} = 33.2 \text{ min}$), TNFR2 showed a high unbinding rate ($t_{1/2} = 1.1 \text{ min}$, Grell et al. 1998, similar values obtained by Krippner-Heidenreich et al. 2002).

Notably, measurements by surface plasmon resonance spectroscopy revealed that binding of TRAIL to dimeric Fc-fused DR4 and DR5 occurs presumably in a step-wise manner and showed that binding of a trimer to a single receptor can be accomplished (Figure 1.13, Reis et al. 2011).

Common to the here briefly summarized TNF-ligand binding study results is a globally weak affinity in the nM range and a low unbinding rate except for TNFR2. Interestingly, the avidity had a smaller impact on receptor occupancy, but had a strong impact on activity (Lang et al. 2012, Reis et al. 2011).

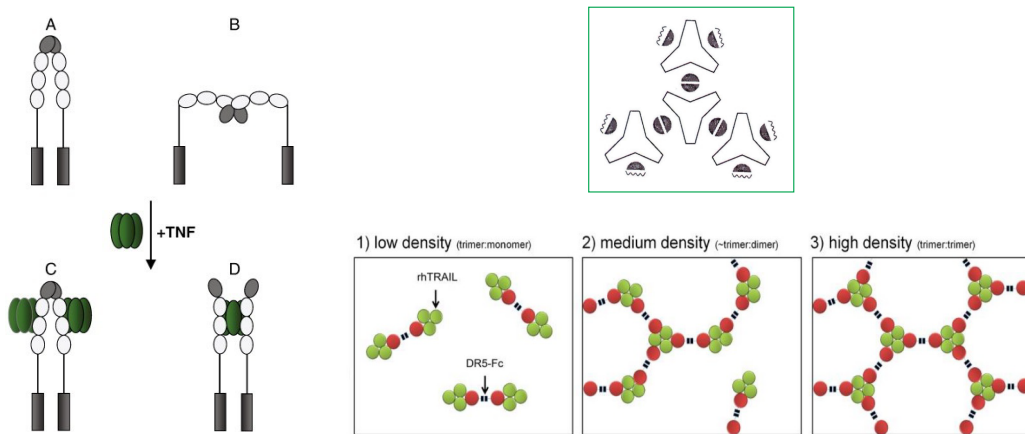


Figure 1.13: Binding models: TNF- α to TNFR1 and TNFR2 and TRAIL to DR5 Left: Illustration from Boschert et al. 2010, (A-B) Model based on crystal structure of TNFR1 (Naismith et al. 1995), (C-D) Proposed binding of TNF- α binding to TNFR1 (C) and TNFR2 (D). Green box: Illustration from Naismith et al. 1995, Proposal of receptor clustering through trimeric ligands (triangle) by dimeric receptors (semi-circles). Three boxes: Illustration from Reis et al. 2011, schematic of the sensor chip and TRAIL (green) binding at different receptor densities. The recombinant Fc-DR5 receptor (red) is a covalent dimer.

1.6 CD95L non apoptotic signaling and internalization

In some cancers, CD95 receptor levels are down-regulated which would be one explanation for how cancer cells can bypass apoptosis. However, receptor or ligand levels are frequently normal or even increased in tumors, indicating that apoptosis resistance is realized by other apoptotic regulators than CD95 (Peter et al. 2005).

It was unexpected and striking that CD95 also mediates cell death-independent pathways (Strasser et al. 2009, Paulsen and Janssen 2011, Martin-Villalba et al. 2013). Notably, it was found that tumor cells benefit from CD95 signaling and respond to CD95L with growth. Moreover, CD95 had a co-stimulatory function in T-cell activation. Strikingly, Barnhardt and co-workers found that many apoptosis resistant tumor cells respond with proliferation upon CD95 stimulation and that those also express small amounts of CD95L (Barnhart et al. 2004). CD95 dependent cell growth was confirmed by Chen and co-workers who tested various apoptosis-resistant and -sensitive cancer cell lines (Chen et al. 2010). Thus, there is now growing evidence that CD95 function goes beyond cell death induction.

Lavrik and her colleagues described this behavior and found that growth is stimulated by low doses- while death is triggered by high doses of CD95L (Lavrik et al. 2007).

Studies using mouse models confirmed the important role of CD95L pro-survival signaling in a physiological context. For example, Li and co-workers found that expression of CD95L enabled metastasis into the liver by inducing proliferation of cancer cells but death of healthy hepatocytes (Li et al. 2009). Interestingly, in hepatocellular carcinoma with p53 mutations the contrary, namely loss of CD95 expression was found (Volkman et al. 2001).

Chen and colleagues showed among others that CD95 KO mice exhibited a weaker susceptibility to diethylnitrosamine-induced hepatocellular carcinoma because of weaker CD95 dependent JNK and Jun phosphorylation (Chen et al. 2010). O'Reilly and co-workers looked at serological and cellular differences when comparing mice expressing only soluble CD95L or only membrane CD95L to *gld/gld* mice, which express non-functional CD95L (Ramsdell et al. 1994), to be able to differentiate between the function of those two ligand forms (O'Reilly et al. 2009). Mice expressing the membrane, non-cleavable form of CD95L appeared normal, while soluble ligand expressing mice developed similar pathologies to *gld/gld* mice, showing lymphadenopathy and hyper-gammaglobulinaemia and rarer autoimmune kidney disease and histiocytic sarcoma. Notably, in soluble CD95L expressing mice some of these outcomes had a significant earlier onset and showed a more severe course.

CD95 can therefore regulate both, death and proliferation of a cell. The two different routes emanating from CD95 seem to be dependent on the ligand form, soluble or membrane, the ligand dose and the target cell type, which determines the expression level of various signaling proteins.

1.6.1 Internalization of CD95 receptors

Internalization of CD95 was reported to be critically involved in *type I* apoptosis signaling, which is not dependent on the mitochondrial amplification loop of apoptosis, and where amounts of DISC formation are high.

In several *type I* cell lines commonly used in the laboratory, efficient internalization of CD95 upon ligation was observed: Algeciras-Schimmich and co-workers found that CD95 internalization was dependent on caspase-8-activity and actin in many cells (BJAB, MCF-7, SKW6.4, K50 and H9). They concluded that rapid DISC formation was followed by large CD95 aggregation, also known as capping, and subsequently internalization. Moreover, non-apoptotic pathways were induced when internalization was blocked (Algeciras-Schimmich and Peter 2003). Lee and co-workers verified this behavior in BJAB, SKW6.4, A20 and H9 cells by using different techniques to block internalization and concluded that CD95 receptor internalization is required to promote apoptosis in *type I* cells. Interestingly, in their hands non-cleavable membrane CD95L induced CD95 receptor internalization (Lee et al. 2006). In contrast, in *type II* CEM cells, internalization of CD95 was delayed compared to *type I* cells (Eramo et al. 2004), and work from Austin and co-workers revealed that block of TRAIL internalization increased cell death (Austin et al. 2006).

TNF- α but not CD95 receptor internalization could be blocked by monodansylcadaverine indicating different mechanisms of internalization of CD95 and TNFR (Algeciras-Schimmich and Peter 2003). Moreover, as mentioned, while caspase-8 activity was found localized inside the cytosol upon TNF- α stimulation of *type II* HeLa cells, IZsCD95L-induced caspase-8 activity was found at the plasma membrane stressing that receptor internalization is differently used by the cell (Beaudouin et al. 2013).

Together, this shows that internalization is regulated differently in diverse cells by the distinct TNF family ligands. Internalization of receptors undoubtedly plays an important role in pathway activation.

1.7 Aim of this work

In this work, I planned to investigate how the different death signals, CD95 ligand mediated caspase-8 activity and the different granzymes trigger cell death. For this, two main questions were explored.

The first question deals with the spatio-temporal activity of granzymes in single cells. To study the individual activities of granzymes, recombinant granzyme protein were oftentimes used in the past. Although this ensures specificity, it might not reflect the natural mechanism of NK cell dependent granzyme activity (Joeckel and Bird 2014). The work of Choi and Mitchison, using a FRET-based granzyme B reporter, elegantly showed how information on NK cells "serial killing" can be obtained (Choi and Mitchison 2013). I believe that by looking at *protease activities* rather than *protein localization*, insights into NK cell mediated cell death can be derived.

I aimed at (i) developing reporters that can be used to measure granzyme activity next to the caspase-8 activity in single cells upon NK cell stimulation to (ii) understand how the different death signals contribute to apoptosis induction.

I furthermore aimed at (iii) investigating the spatial localization of granzymes, notably of granzyme A and B at the plasma membrane, the cytosol and inside the nucleus, since the technique for the measurement of protease activity is based on single-color fluorescent reporters that allow to simultaneously measure and distinguish different protease activities within single cells (Beaudouin et al. 2013).

The second question deals with soluble CD95L mediated caspase-8 activation in apoptosis induction. Early, receptor trimerization by means of the ligand was proposed. In the years 1999 and 2000, the CD95 receptor was found to be pre-oligomerized, namely trimerized (section 1.3). Perhaps because of that, the ligand receptor interaction was often assumed to occur in a direct three-to-three stoichiometric binding. Intriguingly, IZ-fused ligands resemble trimers of ligand that are more active than the trimers that are not artificially enhanced. According to interpretation of new results (section 1.5.2, Berndt 2012), direct receptor cross-linking by the ligand might be a

mechanism for the cell to modulate receptor activation, and therefore pathway initiation.

As I have observed that soluble CD95L can induce cell death in HeLa cells that express high receptor levels, a conceivable hypothesis to start with was that receptors get activated by ligand induced receptor oligomerization.

To test this, I aimed at investigating which molecular events in apoptosis initiation are different for soluble CD95L (sCD95L) and isoleucine-zipper-fused sCD95L (IZsCD95L). By this, the mechanism of CD95 receptor activation was thought to be better understood and would (i) explain what is critical in CD95 receptor signaling that renders sCD95L into a poor inducer of apoptosis. For this, I initially planned to (ii) focus on the comparison and description of caspase-8 activity triggered by the two different ligands by applying the technique developed in the lab by Dr. Joël Beaudouin (Beaudouin et al. 2013). Furthermore, as receptor activation involves non-trivial protein oligomerization steps, I aimed at studying the kinetics of (iii) ligand binding (iv) receptor oligomerization and (v) FADD recruitment using two differently strong forms of CD95L. Those measurements were planned to be supportive for caspase-8 activation studies, since understanding the requirements for caspase-8 activation helps to describe the molecular events of apoptosis induction.

2 Materials & Methods

2.1 Molecular Biology and Biochemistry

2.1.1 Molecular cloning for the expression of proteins and shRNA

Tables 2.1, 2.4 and 2.5 list constructs used in this study. Some constructs were readily provided as stated, while I generated others by molecular cloning using the backbones of the pRESpuro2, pRESneo3 or the pEGFP vectors (Clontech laboratories, inc.). The encoded amino acid sequences made in this work are fully given. The name of the protein always reads from the N-terminus to the C-terminus. For molecular cloning I used enzymes from New England Biolabs in the appropriate buffers, agarose powder for gels from Biozym, T4-Ligase from Fermentas and selected transformed DH5 α or Top10 bacteria from Life Technologies by ampicillin or kanamycin from Sigma-Aldrich. Gel purification and DNA plasmid extraction kits were used from Qiagen.

2.1.2 Cell culture, production of ligand & transfection of plasmid DNA

Cell culture. HeLa and 293T cell lines were kept at 37°C and 5% CO₂ in a humidified atmosphere and maintained in DMEM (Gibco®) without phenol-red, supplemented with 10% FCS (Biochrom), 2 mM L-Glutamin (GlutaMAX, Gibco) and Penicillin-Streptomycin (Gibco). NK92-C1 cells (provided by Prof. Carsten Watzl) express stably IL-2 and grew in suspension forming cell clusters. They were fed with α -MEM containing 2 mM L-Glutamin (Gibco), 12.5% Horse-Serum (Biochrom), 12.5% FCS (Biochrom) and 100 units/ml penicillin plus 100 μ g/ml streptomycin (Gibco).

Production of recombinant proteins. To produce recombinant Flag-tagged (F) F-mGFP, F-mCherry, mGFP-IZ, mCherry-IZ, soluble CD95L and fluorescent fusion proteins thereof (Table 2.5), I used 293T cells as expression system. This ensured glycosylation of the ligands. Proteins encode a signal sequence that allows secretion of the protein into the cell supernatant. Transfection of plasmid DNA was made using 1-2 μ g DNA/ 2.5 \times 10⁵ cells or 10 μ g DNA/ 4 \times 10⁶ cells in cell culture dishes using jetPRIME® transfection reagent (PEQLAB GmbH/ VWR). The next day after transfection, cell supernatants were carefully replaced by fresh medium.

Table 2.1: Protein Sequences

Name of protein	Amino acid sequence + Additional information
Serpin-B9	UniProtKB P50453 Subcloned into pRESpuo2, Gateway cDNA from DKFZ
CD48	UniProtKB P09326 Subcloned into pRESpuo2, DNA provided by Prof. Carsten Watzl
mCherry ¹	<i>MVSKGEE...DELYK</i> M=start codon (Shaner et al. 2004)
mGFP ¹	<i>MVSKGEE...DELYK</i> F64L, S65T, H231L & L221K M=start codon (Roger et al. 1995, Snapp et al. 2003, Yang et al. 1996, Cormack et al. 1996)
EBFP2 ¹	<i>MVSKGEE...DELYK</i> (Ai et al. 2007)
H2B-EBFP2 ¹	<i>MPEPA...TSAK</i> (D26G, V119I) + <i>DPPVAT</i> + EBFP2 H2B type 1-J, UniProtKB P06899
mCherry-Bid-mGFP ¹	mCherry(<i>MVSKGEE...DELYK</i>) + <i>GGGGSGGGGRVGGGSRG</i> + Bid, UniProtKB P55957 + <i>GSRAQASNSAVELKLDIT</i> + Snap(DKD...PAG) + <i>DPPVAT</i> + mGFP (<i>MVSKGEE...DELYK</i>)
GFP-Rab4a & GFP-Rab4a(S27N), GFP-Rab7a & GFP-Rab7a(T22N), GFP-Rab11b & GFP-Rab11b(S25N)	GFP (F64L, S65T, H231L) + UniProtKB P20338, P51149, Q15907 Constructs provided by Dr. Vytaute Starkuviene
GFP-Rab5a & GFP-Rab5a(S34N)	UniProtKB P20339 Constructs provided by Dr. Nathan Brady
CD95 ¹	CD95 aa1-335, isoform1, UniProtKB P25445
CD95-mGFP ¹	CD95 + <i>GGGGGPVAT</i> + mGFP
CD95- Δ DD-mGFP ¹	CD95 aa 1-210 + <i>GGGPVAT</i> + mGFP
CD95-YFP ¹	CD95 + <i>GGGGGPVAT</i> + YFP
FADD-mGFP ¹	FADD (UniprotKB Q13158) + <i>PRARDPTSGGGGGPVAT</i> + mGFP

Constructs¹ provided by Dr. Joël Beaudouin

At the third day after transfection, supernatants containing the ligand were harvested and freed from eventual cell debris and floating dividing cells by centrifugation for 5 min at 900 rpm and filtering through a 0.22 μ m PVDF-filter (Millex® Syringe Filters, Millipore). No cytotoxicity of recombinant ligand to 293T cells was observed by eye.

I observed that ligands which were stored in the fridge at 4°C and which were not purified by affinity chromatography showed consistent activity for a long period. Nevertheless, ligands older than 3 to 4 more months were discarded and new batches of ligand were characterized. In contrast, I have observed that ligand which I expressed and purified by affinity chromatography showed only consistent activity within a short time. That is why purified proteins were only used for experiments performed within the following week.

Table 2.2: Protein Sequences: Ligands and fluorescent protein fusions

Short name	Amino acid sequence
Flag	DYKDDDDK
Isoleucine-zipper (IZ)	QKSKRRRTSSDRMKQIEDKIEEILSKIYHIENEIARIKKLIGER TR bold letters: PDB entry 1GCM = IZ
Secretion Signal	MGTPHLQGFLLLFPLLLRLHGASAGS, M=start codon
Secretion Signal 2	MARRLWILSLLAVTLTVALAALE, M=start codon
Fusion protein	Fusion protein of the following parts
sCD95L	Secretion Signal + Flag + SGR + CD95L ^a aa 117-281
IZsCD95L	Secretion Signal 2 + Flag + PS + IZ + CD95L ^a aa 117-281 original plasmid provided by Prof. Henning Walczak
F-mCherry ^b	Secretion Signal + Flag + KVNS + mCherry (VSK...LYK)
mCherry-sCD95L ^b	F-mCherry + LGGGGSG + CD95L ¹ aa 130-281
mCherry-IZ ^b	F-mCherry + LGGGGSGG + IZ
mCherry-IZsCD95L ^b	mCherry-IZ + CD95L ¹ aa 117-281

CD95L^a: UniProtKB/Swiss-Prot entry P48023, aa = amino acids

^b version of this recombinant protein was built the same way using mGFP

Table 2.3: shRNA

shRNA CD95	GGATCC(BamHI)CAGCGTATGACACATTGATTTTCAAGAGA AATCAATGTGTCATACGCTTGTTTTTTGGAAAGCTT(HindIII)
shRNA control	GGATCC(BamHI)AATCTCATTCGATGCATACTTCAAGAGA GTATGCATCGAATGAGATTCTTTTTTTGGAAAGCTT(HindIII)

Cell culture for microscopy experiments. To transfect HeLa cells for microscopy experiments FuGENE6® (Roche) or jetPRIME (PEQLAB GmbH/ VWR) reagent was used. One day after transfection, the cell supernatant was replaced by fresh medium. One day before microscopy, transfected cells were plated into ibidi 8-well chambers at a number of 2×10^4 per well. Experiments with transiently expressed CD95 and shRNA were performed at the third day after transfection to allow translocation of CD95 to the plasma membrane and efficient reduction of expression, respectively. Otherwise, experiments were done at the second day after transfection. Gentle transfection of GFP-Rab proteins was allowed using FuGENE6® (Roche). Microscopy of those proteins was done the day after transfection because at the second day cells started to die, presumably due to the disturbed cellular traffic by those proteins. For co-culture experiments with HeLa cells, about 10^5 to 6×10^5 NK92-C1 cells were required, depending on the number of conditions tested. For this, an estimated number of about 10^6 NK92-C1 cells were centrifuged, carefully resuspended in 10 ml fresh medium, counted, again centrifuged and resuspended in the final required volume (about 300 μ l per condition) using fresh, supplemented α -MEM.

Table 2.4: Protein sequence of fluorescent reporter

Short name	Amino acid sequence (UniProtKB/Swiss-Prot entry)
H2B	H2B.j aa 1-126 (P06899), D26G, V119I
KRas	KRas aa 166-189 (P01116)
MitoNEET-short	MitoNEET aa 1-41 (Q9NZ45)
MyrSnap2	<i>MGCIKSKRKDNLNDDDETGGSG</i> + Snap(DKD...PAG) + <i>LELKLDIT</i> + Snap(MDKD...PAG) + <i>DPPGS</i>
NES	<i>MNLVDLQKKLEELDEQQ</i> , M=start codon
Snap	(Snap protein sequence: Keppler et al. 2004)
Short name	Amino acid loop with cleavage site
ELQTD	<i>TGGGELQTDGGGGGGR</i>
RIEADS	<i>TGGGRIEADSGGGGGGR</i>
KVPL	<i>TGGGKVPLGGGGGGR</i>
IGNRS	<i>TGGGIGNRSGGGGGGR</i>
Fusion protein (reporter)	Fusion protein of the following parts, mGFP(VSK...LYK)
mGFP-ELQTD-KRas	mGFP(MVSK...LYK) + <i>GVGGSELQTDGGGGAVELKLDIT</i> + Snap(DKD...PAG) + <i>DPPGS</i> + KRas
NES-ELQTD-mGFP	NES + ELQTD + mGFP (Beaudouin et al. 2013)
MyrSnap2-ELQTD-YFP	MyrSnap2 + ELQTD + YFP (Beaudouin et al. 2013)
NES-RIEADS-mGFP	NES + RIEADS + mGFP
NES-RIEADS-mCherry	NES + RIEADS + mCherry
MyrSnap2-RIEADS-mGFP	MyrSnap2 + RIEADS + mGFP
MitoNEET-RIEADS-mGFP	MitoNEET-short + RIEADS + mGFP
H2B-RIEADS-mGFP	H2B + <i>DPPGS</i> + RIEADS + mGFP + <i>SGLRSTGSR</i>
NES-IGNRS-mGFP	NES + IGNRS + mGFP
MitoNEET-IGNRS-mGFP	MitoNEET-short + IGNRS + mGFP
H2B-IGNRS-mGFP	H2B + <i>DPPGS</i> + IGNRS + mGFP + <i>SGLRSTGSR</i>
NES-KVPL-mGFP	NES + KVPL + mGFP

2.1.3 Affinity chromatography

Flag-tagged proteins were purified using ANTI-FLAG® M2 Affinity Gel (Sigma-Aldrich). For this, filtered 293T cell supernatants were incubated with beads at 4°C over night. 50 ml supernatant typically received 350 µl - 500 µl beads. The next day, beads were loaded on an ethanol- and PBS-washed polypropylen-column (Qiagen) and washed with 50 ml ice-cold PBS. To elute the recombinant Flag-tagged protein by competition, 3x FLAG® Peptide (Sigma-Aldrich) in 2 ml PBS (100 µg/ml) was added to the beads. The first flow-through was collected and added to the beads once again because this increased the yield.

2.1.4 Chemical cross-linking of proteins

Flag-peptide in eluate of purified proteins was most removed by passing the solution through a filter by centrifugation (Millipore Amicon Ultra 0.5 ml Centrifugal Filter Units, 10K). Then, purified proteins were covalently cross-linked by adding Glutaraldehyde (0.1% f.c., 25% stock from Sigma-Aldrich), Formaldehyde (1% f.c., Methanol-free 16% stock, Thermo Scientific, Pierce®) or BS³ (1mM f.c., suberic acid bis-(3-sulfo-N-hydroxysuccinimide ester)-sodium salt freshly dissolved in PBS, Sigma-Aldrich). The reaction took place for 20 min on ice. Each reaction was stopped by adding Tris-solution (pH 8, 0.1 M f.c.), followed by the addition of Lämmli Buffer (Bio-Rad) containing 10% β-mercaptoethanol (Roth) or dithiothreitol (DTT, Fermentas). Proteins were denatured by heating at 90°C for 10 min, subjected to protein polyacrylamide electrophoresis or stored at -20°C. Alternatively, samples were not heated or not supplied with β-mercaptoethanol or DTT.

2.1.5 Separation of proteins by size and their detection

Purified proteins, cell supernatant or cell lysates were mixed with Lämmli Buffer (Bio-Rad), heated for 10 min at 90°C, cooled down to room temperature and loaded on a polyacrylamide gel (NuPAGE®10% Bis-Tris Gel and 3-8% Tris-Acetate Gel together with MOPS, MES- or Tris-Acetate SDS-Running Buffers, Life Technologies). As a reference for the protein size the Novex® Sharp Pre-Stained Protein Standard was used containing calibration proteins from 3.5–260 kDa. The separation of proteins inside the gel took place in the appropriate chamber at 180 V for 1 h. Upon separation, proteins were subsequently blotted in a wet-blot procedure. Therefore, a polyvinylidene-fluorid (PVDF) membrane (0.2 μm, Bio-Rad) was activated with 99% ethanol absolute Ph.Eur. (Sigma-Aldrich), rinsed first with water and then with borat-buffer (1 mM boric acid f.c., 50 μM EDTA f.c., pH 8.8 with NaOH) which was also used as transfer buffer. Transfer took place at 300 mA over night. To visualize blotted proteins on the membrane, the membrane was blocked for 1 h with 1% BSA in PBS-Tween (Tween 0.1% f.c., AppliChem) and finally incubated with primary antibody in fresh blocking buffer. After washing three times 10 min with PBS-Tween, the membrane was incubated for another hour with horseradish-peroxidase (HRP)-coupled secondary antibody, followed by three washing steps, 5 min each, with PBS-Tween. Finally, substrate for the enzyme (SuperSignal West Pico Chemiluminescent Substrate, Thermo Scientific) was added to the membrane for 10 min. HRP-enzyme activity yielded chemoluminescence (430nm) which was detected with a Charge-Coupled-Device(CCD)-Camera (ChemoCam Imager, Intas). Digital images of western blots were analyzed using ImageJ (Rasband 1997-2014).

2.1.6 Immunoprecipitation of ligand bound to receptors on cells

In order to compare amounts of protein recruited to mCherry-sCD95L and mCherry-IZsCD95L bound receptors, for each ligand, two cell dishes containing each about 8 Mio cells were incubated with 20 ml ligand for 20 min at 37°C. As control, two dishes were treated with conditioned, filtered 293T cell supernatant.

After ligand binding, the supernatant was removed and cells were carefully washed once with 20ml ice-cold phosphate buffered saline (PBS). Then, cell lysates were prepared. For this, 100 µl lysate buffer was added per 10⁶ cells and incubated for 15 min on ice (lysate-buffer: 20 mM Tris-HCl pH 7.4, 1% Triton X-100, 10% glycerol, 150 mM NaCl, 1mM phenylmethylsulfonyl fluoride (PMSF), 1µg/ml of leupeptin, antipain, chymostatin and pepstatin A each, freshly supplemented with Benzonase® Nuclease (99% purity, Novagen)). During the incubation, adherent cells were detached from the culture dish using cell scrapers and transferred to reaction-tubes. Cells were then centrifuged for 15min at 4°C to obtain the soluble supernatant of the lysate. An aliquot of this was taken as out as control ("Lysate", Figure 3.30).

For the immunoprecipitation, each lysate was incubated over night at 4°C with 20 µl washed ANTI-FLAG® M2 Affinity Gel (Sigma-Aldrich). The next day, beads were washed 4x with PBS, mixed 1:1 with loading dye, cooked 10 min at 90°C, then subjected to SDS-PAGE and western blotting or frozen for storage.

The expertise for immunoprecipitation came from Prof. Inna Lavrik's and Prof. Peter Krammer's group. Immunoprecipitation, SDS-PAGE and western blotting were kindly carried out by Dr. Kolja Schleich.

2.1.7 Protein quantification

I quantified relative amounts and absolute amounts of non-purified and purified proteins by western blot with Amino-terminal FLAG-BAP® Fusion Protein (Sigma-Aldrich) and Fluorescence Correlation Spectroscopy (FCS). To get absolute concentration estimates in FCS measurements, I used a labeled antibody-solution of known concentration as reference. Thereby proteins of similar molecular weight (IgG-antibody & mCherry-sCD95L each about 150 kDa) could be compared or calculated. To estimate and compare protein amounts of fluorescently labeled and non-labeled ligands, mCherry protein was quantified using FCS and used as reference protein of known concentration for the quantification of non-tagged proteins by western blot.

2.1.8 FA/GA fixation and immunostaining

For cross-linking (fixing) of proteins, cells were washed with PBS and, if appropriate, trypsinized and subsequently washed in cold PBS. Cells on ice were cross-linked for 10 min using FA/GA fixative (4% f.c. formaldehyde (Thermo Scientific, Pierce® Formaldehyde Ampules, Methanol-

Table 2.5: Antibodies for western blot and immunofluorescence

Detected protein	Antibody name (Reference)
Flag-tag	Monoclonal ANTI-FLAG® M2 antibody, mouse (Sigma Aldrich)
GFP	Anti-GFP antibody, mouse IgG1 α , clones 7.1 and 13.1 (Roche)
RFP	5F8 anti-Red, rat IgG2a (ChromoTek)
CD95	Apo-1-3, mouse IgG3 (Enzo Life Sciences)
Serpin-B9	7D8, mouse IgG1 κ , (Abcam)
FADD	Anti-FADD monoclonal antibody 1C4, mouse IgG1 (Scaffidi et al. 2000)
Caspase-8	Anti-caspase-8 monoclonal antibody C15, mouse IgG2b, recognizes the p18 subunit of caspase-8 (Scaffidi et al. 1997)
FLIP	Anti-FLIP monoclonal antibody NF6, mouse IgG1, recognizes the N-terminal part of c-FLIP (Scaffidi et al. 1999)
mouse IgG (H+L)	secondary antibody HRP-coupled (Abcam)
rat IgG (H+L)	secondary antibody HRP-coupled (Abcam)
mouse IgG (H+L)	secondary antibody Alexa488-coupled (Life Technologies, Molecular Probes)
mouse IgG (H+L)	secondary antibody Alexa594-coupled, (Life Technologies, Molecular Probes)

free), 0.1% f.c. glutaraldehyde (Sigma-Aldrich) in HBSS buffer (Hank's Balanced Salt Solution, Gibco) supplemented with 0.1 M f.c. sucrose (Sigma-Aldrich)).

For staining of proteins in fixed cells, cells were first incubated 3 x 10 min in blocking buffer alone (HBSS, 0.1 M sucrose and 1% BSA, Sigma-Aldrich). Then, cells were incubated at room temperature for 1 h with primary antibody diluted in blocking buffer. After three washing steps, each 10 min using blocking buffer, cells were incubated for 1 h with secondary antibody. For intracellular staining of proteins the buffer was supplied with 0.2% f.c. saponin (Sigma-Aldrich). Finally, cells were again washed using blocking buffer and kept in PBS for imaging.

2.2 Microscopy and F-techniques

2.2.1 Flow cytometry

Flow cytometry was performed with a modified flow cytometer FC500 MPL from Beckman Coulter which was equipped with a Sapphire 488 nm/ 20 mW and a Compass 561 nm/ 40 mW laser. Emitted GFP fluorescence and fluorescence from Alexa594-labeled secondary antibodies were separated using the dichotic mirrors T495LPXR, T580LPXR and T525LPXR with the numbers denoting the wavelength of the light where separation occurs. Emission filters were ET510/25M for GFP-fluorescence and ET632/60M for Alexa594-fluorescence.

2.2.2 Fluorescence (Cross) Correlation Spectroscopy

To assess the oligomerization state of sCD95L and IZsCD95L and the concentration of protein solutions, I applied Fluorescence Correlation Spectroscopy (FCS) and Fluorescence Cross Correlation Spectroscopy (FCCS) (Elson 2011, Digman and Gratton 2011). The fluorescence intensity of molecules within a confocal volume was measured using the Leica TCS SP2 confocal laser scanning microscope (Leica Microsystems CMS GmbH, Mannheim, Germany). Proteins in solution were brought on ibidi labtek chambers and focused around 20 μm above the bottom using a 63x/1.2 W CORR HCX PL APO CS objective. I recorded fluorescence for either 20 or 50 seconds. To obtain the temporal correlation of intensities within the confocal volume, intensity traces in time were analyzed using the ISS Vista software.

For FCS measurements of mCherry-tagged proteins, I expected to obtain differences in diffusion between trimeric mCherry-fused proteins and monomeric F-mCherry protein because their difference in size was expected to be large enough (Table 3.5, page 68). The diffusion coefficient D of a freely diffusing spherical particle is inversely proportional to the hydrodynamic radius R_h according to the Stokes-Einstein relation (Equation 2.1, left). By applying FCS, a so-called retention time τ_D can be measured, which is the time that a molecule requires on average to cross the confocal volume. This time is also inversely proportional to the diffusion coefficient and has been shown to depend on the radius ω of the beam in the xy-plane (Equation 2.1, right, Magde et al. 1974). Thus, τ_D was extracted at the half-maximal amplitude of the autocorrelation function and fold differences in τ_D were compared between different proteins. Measurements from the same day using the same microscopy settings were compared.

For FCCS measurements, the autocorrelation and cross-correlation results obtained using the software ISS Vista were only visually interpreted by comparison to control measurements.

$$D = \frac{k_B T}{6\pi\eta R_h} \quad D = \frac{\omega^2}{4\tau_D} \quad (2.1)$$

2.2.3 Confocal Laser Scanning Microscopy

Fluorescence microscopy was made using the Leica TCS SP5 confocal laser scanning microscope (Leica Microsystems CMS GmbH, Mannheim, Germany). The microscope has a motorized stage and an incubator with CO₂ supply and temperature control to maintain living cells. Fluorescence emission of mGFP and mCherry was acquired in line sequential mode. Light for the detection of EBFP2 (405 nm UV diode, detection range: 425-475 nm) was also used simultaneously with light for the detection of mCherry (561 nm, helium-neon laser, detection range: 600-660 nm), but not together with light for the detection of mGFP (488 nm, argon laser, detection range: 500-560nm) because of spectral overlaps in the detection.

I used the 40x/1.25 OIL, HCX PL APO CS objective mostly for binding measurements and the

63x/1.4 OIL, HCX PL APO CS objective for single cell fluorescence reporter measurements. Time-series images were recorded by selecting fields of cells and using the automated focusing software from Leica. Focusing was made at low resolution and using low intensity of 594 nm laser light (5%) to measure the reflection of the bottom of the 8-well chamber at each time point. Then, an offset from the maximum reflection was chosen to focus cells at the appropriate height. The resolution for time-series images was typically 512 x 512 pixel, if not stated differently.

Fluorescent reporter substrate cleavage assay

In order to measure protease activity inside single cells, I used fluorescent reporters developed by Dr. Joël Beaudouin (Beaudouin et al. 2013). Those fluorescent reporters are fusion-proteins that consist of a fluorescent protein such as GFP or Cherry which is linked to a localization domain through an unstructured loop containing the protease cleavage site. Upon cleavage of the reporter by a protease, the fluorescent protein is separated from the localization domain and small enough to freely diffuse into the nucleus, a process that can be visualized by microscopy. Conversely, in case of the nuclear reporter, upon proteolytic activity, fluorescence would be seen increasingly in the cytosol.

Obtaining intensity measures of reporter cleavage

Fluorescent reporters were analyzed manually using ImageJ. Briefly, 8-bit images were background subtracted and transformed into RGB images. The spatial redistribution of the fluorophore upon processing by proteases can be visualized as a plot of nuclear intensity over time. For this, the fluorescence intensity of probes was measured inside a region of the nucleus for each time series image and normalized to the cytosolic intensity at time $t = 0$, giving values between 0 and 0.5 assuming similar volumes of nucleus and cytosol (Eq. 2.2a). Alternatively, I typically also measured the cytosolic intensity at each time point to normalize the nuclear intensity to this value, giving normalized intensity values between 0 and 1 (Eq. 2.2b). This can be important for long time series to account for potential bleaching of the fluorophore but also for transient changes of expression. To note, using the NES-probes, the cytosolic pool contains all non-cleaved but also parts of cleaved probes. To assess the intensity of the plasma-membrane probe over time (MyrSnap2-probe or KRas-probe), an image stack of the whole cell before start of the time-series was acquired to quantify the total amount of non-cleaved probe. Derived total intensities of plasma-membrane (pm) and cytosolic probes (NES) allow then to compare both probes by normalizing to the relative difference in expression at time $t = 0$ (Eq. 2.3).

$$(a) \quad I_{NES}(t) = \frac{I_{NES}^{nucleus}(t)}{I_{NES}^{cytosol,t=0}} \quad (b) \quad I_{NES}(t) = \frac{I_{NES}^{nucleus}(t)}{I_{NES}^{cytosol}(t)} \quad (2.2)$$

$$I_{pm}(t) = \frac{I_{pm}^{nucleus}(t)}{I_{pm}^{cytosol,t=0}} \cdot \frac{I_{NES}^{total,t=0}}{I_{pm}^{total,t=0}} \quad (2.3)$$

Interpretation of reporter cleavage data

To compare caspase activities in different single cells, parameters describing the substrate cleavage such as the rate and the onset of activity were extracted by fitting single cell substrate cleavage data to the so-called *modified Gompertz function* ($F(t)$, Figure 2.1, Zwietering et al. 1990). Substrate is cleaved when enzymes, for example caspase-8 or granzymes, are active. I assumed that enzyme is saturated with substrate which makes the velocity of the reaction independent of substrate concentration. For example, substrates of caspase-8 are caspase-8 itself, Bid, caspase-3 and other proteins but also the fluorescent reporter. The velocity or rate μ_m of the reaction corresponds to the maximal temporal change of the cleaved substrate S_{cl} ($\mu_m = \frac{d[S_{cl}]}{dt}$) which is assumed to be correlated to the enzyme concentration. Substrate cleavage data showed typically a lag time where no substrate cleavage was observed. This can be observed for caspase-8 substrate cleavage (for example Figure 2.1 and Beaudouin et al. 2013) and was shown also for caspase-3 substrate cleavage (Rehm et al. 2002). In the example curve-fit (Figure 2.1), the amplitude is clearly defined and the three parameters amplitude (A), rate (μ_m) and onset (λ) can be identified well.

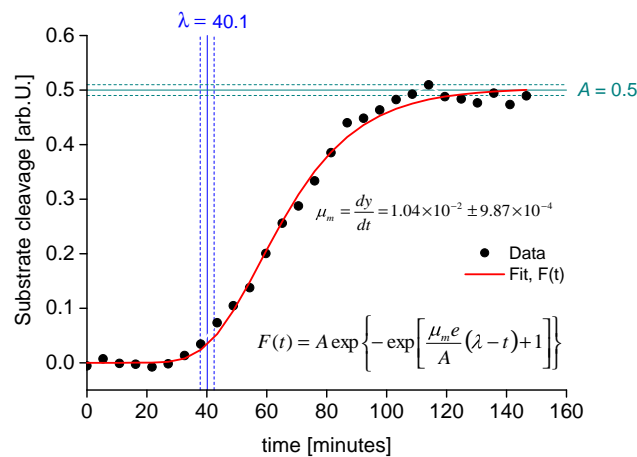


Figure 2.1: Progress curve of cleaved substrate with example of a fit to the modified Gompertz-model. Estimated parameter values (solid line) and 95% confidence intervals (dashed line) are shown for the fit of caspase-8 substrate cleavage data to the function $F(t)$ which was published in Zwietering et al. 1990. A = amplitude, μ_m = rate or velocity, λ = onset or lag time of substrate cleavage (product formation).

For data that did not clearly show an amplitude, an upper bound for the amplitude was applied to the curve fit. This was justified because substrate cleavage data were normalized. When the confidence interval of a single fit was large relative to the confidence intervals obtained from the majority of the data, then fitting results were not included in the statistics.

Binding & internalization of ligand, FADD recruitment measurements by confocal microscopy

- For binding assays, I used the 40x/1.25 OIL objective, chose a 1x zoom and the pinhole was opened to 1.7 Airy unit. The resolution was 512 x 512 pixel and I acquired 16-bit-images. The image analysis procedure is described in the results section.
- To image the lower plasma membrane of the cell (Figure 3.33) I chose the 40x/1.25 OIL objective, zoom 2.5x, pinhole size of 1.3 Airy unit, a resolution of 1024 x1024 pixel and acquired 16-bit images.
- To assess the binding strength of ligand at different pH, I prepared 50mM Tris-maleate and 50mM Tris-succinate buffers using Tris-maleate (AppliChem) and succinic acid (AppliChem) with Tris (AppliChem), respectively containing each 50mM NaCl, 2mM CaCl₂ and adjusted the pH using HCl and NaOH, respectively. Buffers were supplied with FCS 5% f.c. before the experiment.
- To measure FADD-recruitment, mGFP and mCherry fluorescence was imaged the same way as for binding assays. Before statistical analysis, to obtain an intensity-time plot of the different measured cells, data points, measured in the center of the cell, were interpolated every 10 minutes starting at time zero because the time resolution of the image series was about 10 minutes.
- Next to binding, uptake of mCherry-sCD95L and mCherry-IZsCD95L into HeLa-CD95-mGFP and HeLa-CD95- Δ DD-mGFP cells was assessed by confocal microscopy, too (Figure 3.32). For this, cells were continuously incubated for different time points (10, 20, 30, 60 minutes) or left untreated (time zero) and then put on ice. To assess total ligand bound to the plasma membrane and inside the cells, cells were washed twice with PBS and fixed by FA/GA-fixation. To measure internalized ligand, cells were washed with a buffer of low pH (25 mM glycine in PBS, 3 % BSA, pH=2.7) for 20 to 30 minutes, then washed twice with PBS and fixed by FA/GA-fixation. While surface binding was homogeneous allover the cell surface, internalized ligand was distributed in endosomes randomly over the cell. For each condition, four image-stacks containing on average 22 ± 8 cells were recorded using confocal microscopy. For this, I used the 40x/1.25 OIL objective, chose a 2x zoom, closed the pinhole to 1.1 Airy unit and recorded image-stacks (Δz systematically 0.77 μ m), each 16-bit, of fixed cells to allow

quantification of total ligand over the cell and of total internalized ligand. To compare the different conditions, the background-subtracted intensity of one image stack was measured and values were normalized to the cell number. The standard deviation was calculated from values of the different measured stacks.

2.2.4 Fluorescence Recovery After Photobleaching

To test for differences in receptor clustering on the plasma membrane when different forms of ligand were added to cells, I measured the diffusion of CD95 receptors.

While the diffusion coefficient of particles in gas-phase or in solution is correlated to the inverse of the hydrodynamic radius R_h of the particle, the diffusion coefficient of particles embedded within (cell) membranes is rather independent on the size of the protein but depends on the area of membrane that is displaced by the protein (Saffman and Delbrück 1975). How does the mobility of molecules on the cell membrane depend on the size of the transmembrane-region of the embedded protein? Philip Saffman and Max Delbrück predicted that the translational displacement or diffusion coefficient D_T is proportional to the logarithm of the inverse radius of the molecule inside the membrane with $D_T = \frac{r^2}{4t} = \frac{k_B T}{4\pi\mu h} (\log \frac{\mu h}{\mu' a} - \gamma)$, whereby $\mu \gg \mu'$ with a being the radius of the particle embedded in a membrane of thickness h and viscosity μ surrounded by aqueous liquid of viscosity μ' , r is the displacement distance, k_B is the Boltzmann constant and T is the absolute temperature and γ is the Euler's constant with 0.5772 (Figure 2.2, Saffman and Delbrück 1975). For example, the Saffman-Delbrück model was able to reproduce data by Kerstin Weiß and co-workers who measured the diffusion of proteins having a radius of up to $a \approx 8$ nm by applying two-Photon-FCS (Weiß et al. 2013, the protein density was about 1 protein/ μm^2) or data by Gernot Guigas and Matthias Weiß who included the phenomenon of hydrophobic mismatch of the protein inside the lipid-bilayer (Guigas and Weiss 2008).

The Saffman-Delbrück theory of the relation between the diffusion coefficient D and the radius a of an embedded particle has been further tested as its validity was not always observed: it was predicted and supported by data that the diffusion coefficient D can also scale with $\frac{1}{a}$ (reviewed in Rayan et al. 2010) or with $\frac{1}{a^2}$ (Guigas and Weiss 2006).

For the protein CD95, this membrane-spanning radius a can be estimated by comparison to the protein size of the related protein TNFR (Figure 2.3). The width of a receptor monomer would be around 1.5 nm. However, the transmembrane part might adopt a different size. Notably, trimerized receptors would be held apart by the trimeric ligand with a distance of about 6 nm, which would then yield a radius a of 5.5 to 11 nm depending on the assumed radius (implied grey arc, Figure 2.3 right).

I aimed at measuring the CD95 receptor mobility on cells before and after ligand stimulation to test whether qualitative differences in receptor mobility due to changes in oligomerization and consequently changes in the membrane-spanning area can be observed.

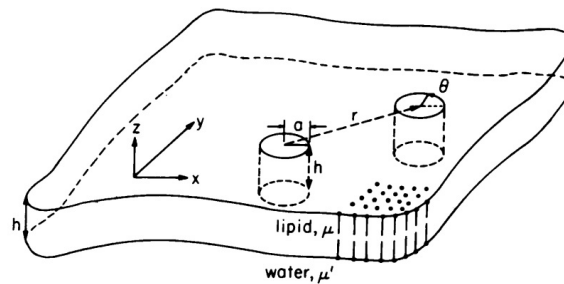


Figure 2.2: Diffusion of proteins in the membrane. a = radius of the particle, embedded in a membrane of thickness h and viscosity μ surrounded by aqueous liquid of viscosity μ' . r = displacement distance, θ = angular rotation. (Illustration from Saffman and Delbrück 1975).

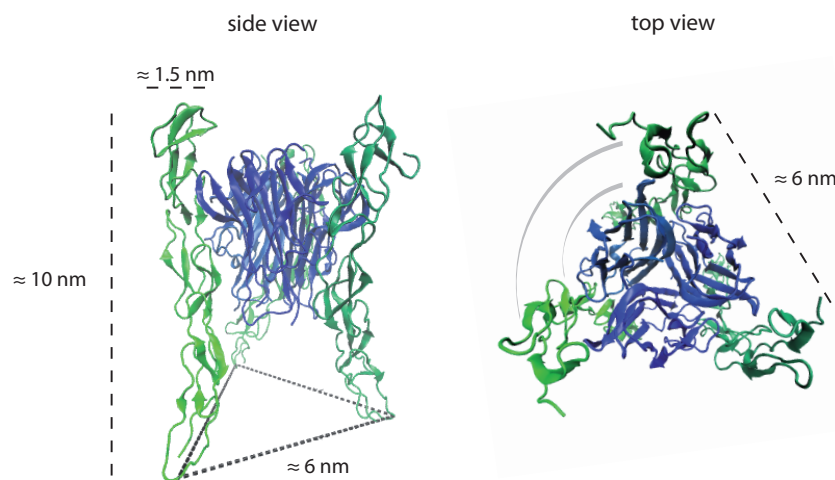


Figure 2.3: Size estimates of the TNF- α -TNFR2 complex The complex of the PDB entry 3ALQ was illustrated and measured using the program VMD (Humphrey et al. 1996).

How can the diffusion coefficient on cells be measured?

I applied Fluorescence Recovery After Photobleaching (FRAP) to measure the receptor mobility of CD95-mGFP and CD95- Δ DD-mGFP on the plasma membrane of cells. The diffusion of molecules on cell membranes is a process that is slow enough to be recorded by imaging. In FRAP, fluorescently tagged molecules are used to obtain the diffusion coefficient D . Fluorescence in a part of the cell is bleached using high laser intensities. Then, the redistribution of the fluorescence intensity is recorded. This spatio-temporal evolution of the intensity recovery is driven most by the diffusion of the molecule, which can be described by Fick's second law $\frac{\delta C(x,t)}{\delta t} = D \frac{\delta^2 C(x,t)}{\delta x^2}$, with $C(x,t)$ being the concentration of the molecule, expressed alternatively in intensity, in time and space.

To analytically describe the intensity recovery, different functions can be used. The choice depends on the underlying process of recovery which can be diffusion but it can also contain

contributions of interaction, such as association or dissociation processes (Goehring et al. 2010). Conceptually, there are two different ways of interpreting the redistribution. The first option is to directly fit the recovery curve obtained by measuring the previously bleached area over time (for example Axelrod et al. 1976). The other option is to use in addition the intensity information next to the bleached area (for example Politz et al. 1999, Srikanth and Rakesh 1989). In the second case, profiles across a spot-bleach-geometry have been measured to fit data to a Gaussian function.

Modeling the intensity recovery of FRAP data using a stripe-geometry

We applied a new analytical model, conceived by Dr. Joël Beaudouin, to analyze FRAP data with stripe-bleaching geometry. Together with Joël and two students, Julia Peukes and Sarah Kaspar, we tested this new model to estimate the diffusion coefficient of mGFP-tagged receptors on the plasma membrane of HeLa cells. We performed FRAP experiments using the Leica TCS SP2 confocal laser scanning microscope (Leica Microsystems CMS GmbH, Mannheim, Germany). Cells were measured at low spatial resolution of 256×256 pixels which corresponded to $59.64 \times 59.64 \mu\text{m}$ in our settings. The temporal resolution was 0.40 sec. We measured 20 pre-bleach images, required 6 images for bleaching by setting the 405 nm laser and the 488 nm laser to 100%, and acquired 40 post-bleach images. To model diffusion in one dimension, we applied a stripe-geometry. We designed the stripe so that it looked Gaussian at the first time point after the bleach. To do so, the stripe was chosen not too broad, about $5 \mu\text{m} \times 25 \mu\text{m}$, and with the effect of diffusion during the bleach and the point spread function of the microscope it appeared Gaussian at the first time point after the bleach (Figure 2.4 and 2.5).

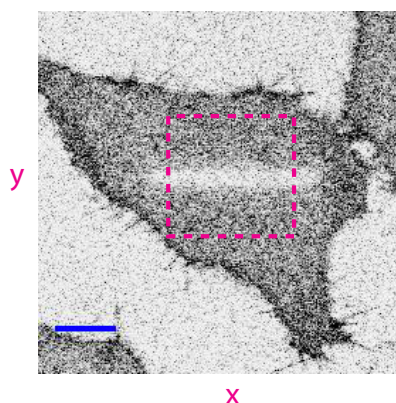


Figure 2.4: FRAP-Stripe geometry Image of the lower plasma membrane of an adherent HeLa cell expressing CD95-mGFP. Photobleaching of a geometry of about $5 \mu\text{m} \times 25 \mu\text{m}$ was made using a confocal laser scanning microscope. The bleached area is visible in this image which shows the first recorded time-point after the bleach. The pink box indicates the region of the intensity measurement, which was then averaged along the x dimension to obtain a Gaussian intensity profile along the y-dimension. The rectangle was placed in a way so that diffusion along x would not contribute to the measurement. Scale bar = $20 \mu\text{m}$.

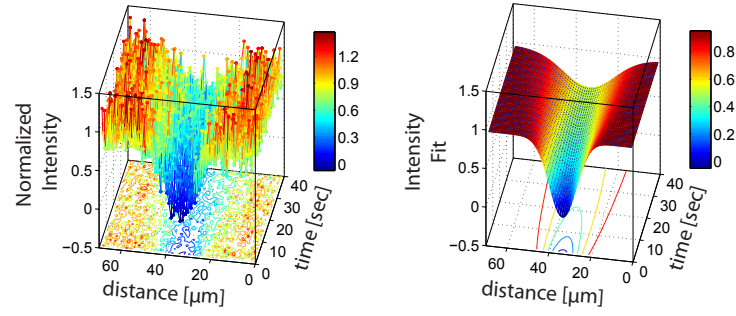


Figure 2.5: Fit of FRAP-recovery using temporal Gaussian profiles *Left:* normalized intensity of post-bleach data. *Right:* Fitted intensities to obtain the parameter D that describes the change of the width of the Gaussian in time.

When the initial condition is Gaussian, the analytical solution of the diffusion equation $\frac{\delta C(x,t)}{\delta t} = D \frac{\delta^2 C(x,t)}{\delta^2 x}$ can be modeled with a Gaussian function (Politz et al. 1999). Those spatial profiles stayed Gaussian-shaped over time whereby the variance of the Gaussian, σ^2 , increased linearly with time, having a slope of $2D$.

To obtain the spatial intensity profile we used ImageJ for the image analysis. First, the background was subtracted, then post-bleach images were normalized to the averaged intensity before the bleach. Finally, a rectangle covering the region of the bleached stripe and fluorescence was measured as illustrated (pink box, Figure 2.4). For each measured time point, the intensity of this measured rectangle was averaged along the x -axis resulting in a profile along y of Gaussian shape.

Next, the goal was to describe in a robust way the evolution of the intensity in time and space depending on the diffusion coefficient. With increasing time, the amplitude of the intensity profiles decreased together with an increase of the half-maximal width (σ in μm). To model this deformation, first, the variance of the Gaussian was described as a function of time (Equation 2.4).

$$R(x, t) = -\frac{1}{\sqrt{\sigma^2(t)2\pi}} e^{-\frac{1}{2} \frac{(x-\mu)^2}{\sigma^2(t)}} \quad (2.4)$$

The diffusion coefficient, given in $\mu\text{m}^2\text{sec}^{-1}$, can be defined as $\sigma^2(t) = 2Dt + \sigma_0^2$.

$$R(x, t) = -\frac{1}{\sqrt{(2Dt + \sigma_0^2)2\pi}} e^{-\frac{1}{2} \frac{(x-\mu)^2}{2Dt + \sigma_0^2}} \quad (2.5)$$

The decrease of the amplitude in time can be described by defining two new parameters $B = 4\pi D$ and $C = 2\pi\sigma_0^2$. This will make the estimation of the diffusion coefficient mostly dependent on the temporal evolution of the width of the Gaussian. In addition, to account for bleaching, we added

a parameter E in exponential form to the nominator of the term.

$$R(x, t) = -\frac{e^{-Et}}{\sqrt{(Bt + C)2\pi}} e^{-\frac{1}{2} \frac{(x-\mu)^2}{2Dt + \sigma_0^2}}. \quad (2.6)$$

More flexibility to this model was given by adding an offset F that can decrease with time $-Gt$.

$$R(x, t) = -\frac{e^{-Et}}{\sqrt{(Bt + C)2\pi}} e^{-\frac{1}{2} \frac{(x-\mu)^2}{2Dt + \sigma_0^2}} + F - Gt. \quad (2.7)$$

Parameter estimates were obtained by nonlinear regression using the Levenberg-Marquardt algorithm (Figure 2.5, right). For statistical evaluation of the fit, the 95% confidence interval of the parameter reflecting the diffusion coefficient D was calculated (see for example Figure 3.42, page 117).

Practically, to track the mobility of about 15 cells over time, one cell was repeatedly measured every 10 minutes as long as 50% of all selected cells from one condition were living. Fewer data points are plotted, because data were discarded because of cell division during the time course or bad confidence of the fit. Because each measurement was performed at a different time-point, data points, which each reflect a FRAP measurement, were interpolated. Cells were also measured before addition of ligand corresponding to the first time point $t = 0$ min.

2.2.5 Total Internal Reflection Fluorescence Microscopy (TIRFM)

Photobleaching measurements were kindly performed by Dr. Michael Schwering on a home-built Total Internal Reflection Fluorescence microscope in the group of Prof. Dirk-Peter Herten (Schwering 2012). Purified mGFP-tagged proteins diluted in PBS at a concentration of about 1ng/ml were placed on a labtek that was first cleaned with hydrofluoric acid and secondly with PBS. The protein concentration was an estimate: protein solutions of not more than 1 μ g/ml were obtained after purification. Those were diluted 1000- fold in PBS. This protein-solution was allowed to settle and bind for about 20 minutes. In case the density of proteins on the labtek was still to high, proteins were diluted more. Binding of mGFP-IZ, mGFP-sCD95L and mGFP-IZsCD95L to the bottom of the labtek was very stable over time. To reduce protein movements, the protein solution was removed. Practically, after bringing the fluorescent proteins in focus, Michael moved the labtek quickly to a previously not imaged field and I started immediately the time series by clicking the record button on the computer.

What are single-molecule-fluorescence photobleaching experiments?

The phenomenon of photobleaching describes an irreversible process of the light-induced chemical modification and destruction of a chromophore. In this way a molecule can lose the ability to absorb light and to emit fluorescence. Each fluorescent molecule has its own photobleaching

quantum yield, defined as the probability of photobleaching per photon absorbed (Hinterdorfer and Oijen 2009). In a single-molecule-fluorescence photobleaching experiment, molecules are imaged at normal laser intensity but with a high temporal resolution to shut off fluorophores slowly over time. For example in our experiments, set up by Dr. Michael Schwering, molecules were measured for 40 seconds every 100 millisecond, resulting in 400 images for one photobleaching series (Figure 2.6).

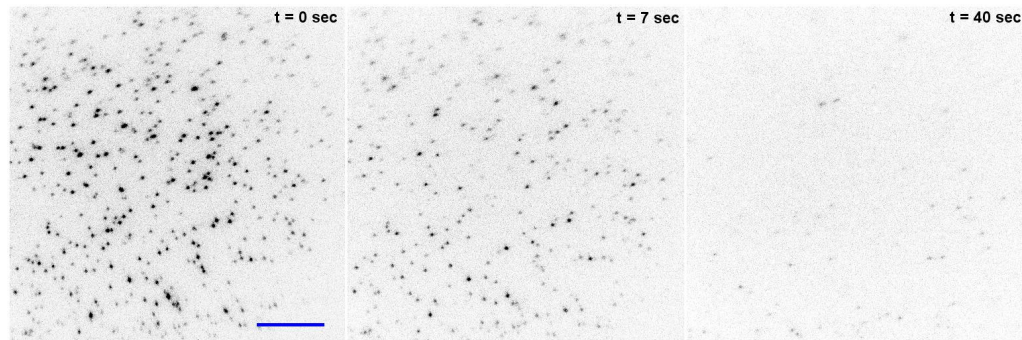


Figure 2.6: Imaging mGFP-sCD95L molecules using TIRF microscopy. Snap-shots of time series images at $t = 0, 7$ and 40 seconds. Scale bar = $5\mu\text{m}$.

Photobleaching by single-molecule-fluorescence imaging has been previously applied to resolve for example the subunit stoichiometry of the protein Cry1Aa (Groulx et al. 2011), the human Glycine Receptor (Durisic et al. 2012) or the AMPA receptor/TARP (Hastie et al. 2013), the NMDA receptor (Ulbrich and Isacoff 2007) and was also used to count TexasRed-labeled adenylate kinase proteins trapped inside a lipid vesicle (Das et al. 2007). The approach does not require super-resolution, meaning no spatially resolved fluorophores within the complex. Instead, it relies on the intensity of the unresolved molecule complex or spot.

The intensity of a single spot over time that is photobleached at a time t shows the profile of a step function (see box page 39 for background information). For more than one fluorophore within the complex, the intensity trace appears as an irregular staircase. Theoretically, the maximal number of "stairs" or steps observed reflects the number of the subunits of the complex. However, this number can be difficult to be read from the intensity trace (McGuire et al. 2012). To obtain statistically relevant results, photobleaching time-series of many spots, usually about 100-500 molecules, are interpreted. For a population of proteins with equal subunit stoichiometry and no constrain for the detection of steps, a single peak at the subunit stoichiometry in the histogram of the frequency against the step number per trace would be expected. Practically however, constrains for the detection of steps exists. One commonly used method to interpret photobleaching data was proposed by Ulbrich and Isacoff, which is based on the binomial distribution (Eq. 2.8), with the probability $P(k)$ that k steps out of n possible steps are observed, with probability p to detect the events (Ulbrich and Isacoff 2007, Arant and Ulbrich 2014).

For example, the probability P to observe three ($k = 3$) bleaching steps in a trimer ($n = 3$) increases for increasing probability p (Figure 2.7, right). In contrast, the probability P to observe three bleaching steps in a hexamer ($n = 6$) increases for probabilities $0 \leq p \leq 0.5$ and decreases for probabilities $0.5 \leq p \leq 1$ (Figure 2.7, left).

$$P(k) = \frac{n!}{k!(n-k)!} p^k (1-p)^{n-k} \quad (2.8)$$

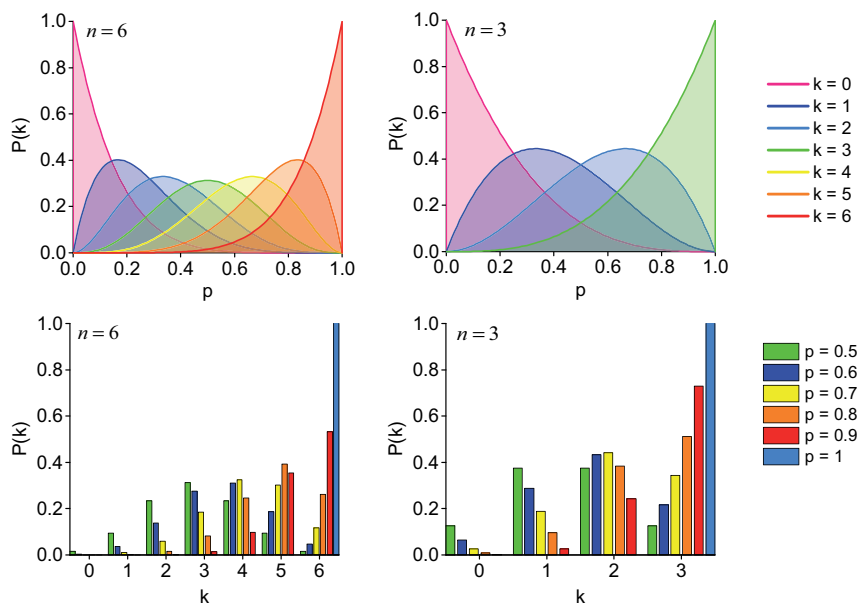


Figure 2.7: The binomial distribution. P = Probability that k out of n possible events are present. p = probability to detect the event n .

Thus, the probability p reflects the likelihood to detect the fluorescence. The value of this probability is influenced, for example, by the kinetics of fluorophore maturation, by bleaching of molecules in the population before image acquisition and by the labeling efficiency of the analyte or by the cleavage extent of the fluorescent fusion protein to be measured. This parameter p can be either fitted or estimated from a measurement of an analyte with known stoichiometry. To test whether the purified fusion proteins mGFP-sCD95L and mGFP-IZsCD95L used in my study were cleaved, I subjected those to SDS-PAGE and western blotting. For mGFP-IZsCD95L, 8% of total specific protein resembled a band corresponding to the size of mGFP on the blot (Figure 2.8), while mGFP-sCD95L exhibited no cleavage. Furthermore, there exists a likelihood that multiple steps occur at the same time, or temporally close, leading to missed detection of steps in the step-counting approach. Those can be detected from calculating the intensity change (for example McGuire et al. 2012, Durisic et al. 2012). Still, 11 to 37% (Ulbrich and Isacoff 2007) or even 50% (McGuire et al. 2012) of measured spots were formerly excluded from the analysis for different reasons. To note, photobleaching experiments have been previously analyzed

by manually counting the number of steps k observed in one time-trace (for example Ulbrich and Isacoff 2007) but also automatic step-counting was conducted (McGuire et al. 2012).

In this work, photobleaching data were not analyzed by the step-counting approach. Instead, a new method is proposed, which was tested and which was applied to own data (section 3.3).

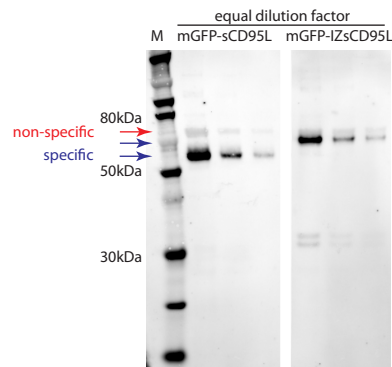


Figure 2.8: Purified mGFP-sCD95L and mGFP-IZsCD95L M = Marker. Detection using α -Flag-tag antibody. mGFP-IZsCD95L displayed 8% cleavage.

Background information: fluorescence and the exponential decay

Fluorophore excitation and fluorescence emission are fast processes that occur within femtoseconds (excitation) and nanoseconds (emission). Milliseconds of illumination allow to repeat fluorophore excitation and emission cycles many times.

In case energy is absorbed by the electron of the fluorophore, the electron is in an excited state but will return to a state of lowest energy. In this ground state, electrons are spin-paired and therefore in singlet state. Return to the ground state can occur by different processes. From the excited singlet state, the electron can lose some energy by vibrational relaxation resulting in a singlet state of lower energy but still higher than the ground state. From such an excited state, energy in form of fluorescence can be emitted resulting in return to the ground state. Instead of emitting fluorescence, the energy of the electron can also be transferred into heat, a process termed non-radiative relaxation. Alternatively, this energy can be transferred onto another molecule or electron, a process termed quenching. Third, instead of emitting fluorescence, the electron can cross from the system of spin-paired electrons into a system of unpaired spins, where the electron is termed to be in triplet state. However, this system crossing is less probable. From the triplet state the electron can return to the ground state by non-radiative relaxation or by emitting phosphorescence. As the electrons in the triplet state are more reactive, chemical reactions can be initialized from this state. This eventually can lead to damage of the fluorophore, a process termed photobleaching. At each new cycle of excitation and emission the same probability exists that the fluorophore will be excited and bleached. That is why single spots show step-wise bleaching and the fluorescence decay of a population of fluorophores can be modeled with the probability density function of an exponential distribution (see literature for example: Hinterdorfer and Oijen 2009).

3 Results

3.1 Natural killer cell mediated cell death on the single cell level

The first part of my work deals with the characterization of Natural Killer cell (NK cell)- dependent cell death. Presentation of cytotoxic proteins of the NK cell to the target cell can lead to proteolytic activity of caspases and granzymes within target cells and thereby to a controlled way of cell death. The goal was to measure the different proteolytic activities inside single cells and to correlate protease activities to cell death. I intended (i) to understand on which timescales these different activities occur, (ii) to spatially localize these activities inside the cell and (iii) to test whether these activities work together or rather exclusively inside the individual target cell.

3.1.1 Study design: measurement of proteolytic activity in HeLa cells upon NK92 cell co-culture

To directly measure protease activity from proteases such as caspases or granzymes, I worked with an assay based on fluorescent proteins for the measurement of single living cells using confocal microscopy (Beaudouin et al. 2013). Briefly, fluorescent proteins, eBFP2, mGFP or mCherry, are linked to a localization peptide or domain through an amino-acid sequence that can be recognized and cleaved by proteases. Cleavage of these localization reporters results in freeing the fluorescent protein from its localization peptide. The spatial redistribution of fluorescence over the cell in time can be measured using a confocal microscope and quantified by analyzing the intensity of the cell nucleus for non-nuclear probes, and the cytosol for nuclear probes, respectively.

As one reporter requires tagging to only one fluorescent protein, the approach allows to compare different proteases inside one single cell or to compare the different subcellular localization of proteolytic activity. The timing and strength of probe cleavages allows to deduce activation kinetics and amounts of different proteases.

HeLa cells were used as a model system to study target cell death because they can be easily transfected and followed by microscopy and because they are known to respond to CD95L, granzyme A and granzyme B with death (for example Beaudouin et al. 2013, Choi and Mitchison 2013, Martinvalet et al. 2008). Although the mode of activation might already influence the way the target cell is killed by the NK cell, activation mechanisms were not focus of this study.

I used NK92 cells which display characteristics of activated NK cells (Gong et al. 1994). The cytotoxic effect towards HeLa cells was enhanced by transient over-expression of the protein CD48 or by using a stable HeLa cell line expressing CD48 (HeLa-CD48) (Hoffmann et al. 2010).

Table 3.1: Protease activity reporters

Name of the probe (substrate/ reporter)	Cleaved by protease	Cleavage in target cells observed upon co-culture with NK92-C1 cells?
NES-ELQTD-mGFP	caspase-8	yes
NES-RIEADS-mGFP	granzyme B ¹ , caspase-10 ¹	yes
NES-RIEADS-mCherry	granzyme B, caspase-10	yes
NES-IETDG-mGFP ²	granzyme B, caspase-8	yes
NES-IGNRS-mGFP ¹	granzyme A	twice (n = 43)
NES-KVPLG-mGFP ²	granzyme M	once (n = 25)
NES-Bidloop-mGFP (ELQTD, RIEADS)	caspase-8, granzyme B, cathepsins ³	yes
NES-Bidloop-D60A-D75A-mGFP (ELQTA, RIEAAS)	cathepsins ³	no
MyrSnap2-RIEADS-mGFP	granzyme B, caspase-10	yes
MitoNeet-RIEADS-mGFP	granzyme B, caspase-10	no
H2B-RIEADS-mGFP ²	granzyme B, caspase-10	yes
MitoNeet-IGNRS-mGFP ¹	granzyme A	no
H2B-IGNRS-mGFP ²	granzyme A	yes

¹ Granzyme B cleaves caspase-10 at IEADAL (Fernandes-Alnemri et al. 1996, Talanian et al. 1997), Granzyme B and caspase-10 cleave Bid at RIEADS (Li et al. 1998, Fischer et al. 2006).

² Cleavage sites: Mahrus and Craik 2005

³ Arg65 by cathepsins B, K, L, S & Arg71 by cathepsin H (Cirman et al. 2003)

3.1.2 Potential cleavage of ELQTD, RIEADS, IGNRS and KVPLG in target cells upon NK92 cell exposure

The first objective was to find protease cleavage sites for the use as fluorescent reporters. Based on the work of Mahrus and Craik, I designed probes comprising amino acid sequence *IGNRS* to report granzyme A activity and *KVPLG* to report granzyme M activity (Mahrus and Craik 2005). Based on the study of Li and co-workers, I intended to measure granzyme B activity using the amino acid sequence *RIEADS* (Li et al. 1998). The cleavage reporter NES-*RIEADS*-mGFP containing this amino acid sequence of Bid was previously designed by Sabine Aschenbrenner in our group and used in this work. Table 3.1 summarizes different cleavage reporters that have been tested in this study.

First, I tested the frequency of NK-cell mediated protease activity in the cytosol of HeLa-CD48 cells. In a typical experiment around 25 to 50 of the transfected cells died upon NK cell exposure. The time-point of death was defined as the time when target cells shrank. Out of 37 target cells expressing the reporters for granzyme M (NES-*KVPLG*-mGFP), 25 died upon NK cell co-culture and one cell showed cleavage of this probe. Unexpectedly, out of 43 cells that expressed the cytosolic probe for granzyme A (NES-*IGNRS*-mGFP) and that died, only two cells showed probe cleavage (Figure 3.1). Target cells that expressed the reporter for granzyme B (NES-*RIEADS*-mGFP) showed an increase of nuclear fluorescence intensity in 60-100% of transfected cells that died upon NK cell contact (Figure 3.1). Target cells expressing the reporter for caspase-8 (NES-*ELQTD*-mGFP) showed cleavage in HeLa-CD48 cells up to around 40%.

Test for cathepsin cleavage

The cathepsins S, B, H, L and K have been reported to cleave the protein Bid within its flexible loop (Cirman et al. 2003). To test whether Bid might be cleaved at different sites than *RIEADS* and *ELQTD*, which are part of this loop, I compared cleavage of a reporter containing the full loop of the protein Bid (NES-Bidloop-mGFP) and a mutant of the loop where the sequences *RIEADS* and *ELQTD* were changed into *RIEAAS* and *ELQTA* (NES-Bidloop-D60A-D75A-mGFP) to cleavage of the NES-*RIEADS*-mCherry reporter. Quantification of single cell data showed that the *RIEADS*-probe was cleaved to $37 \pm 11.2\%$ short before cell death, while the Bidloop-probe was cleaved to $28.4 \pm 8.8\%$ in the same cells. In contrast, the mutant loop was cleaved only to low extent with $6.6 \pm 6.4\%$, compared to $43.6 \pm 20\%$ *RIEADS*-probe cleavage in the same cells (Figure 3.1b). This shows that in HeLa cells proteases were activated that only cleaved the protein Bid within the sites *RIEADS* or *ELQTD* upon NK92-C1 cell contact.

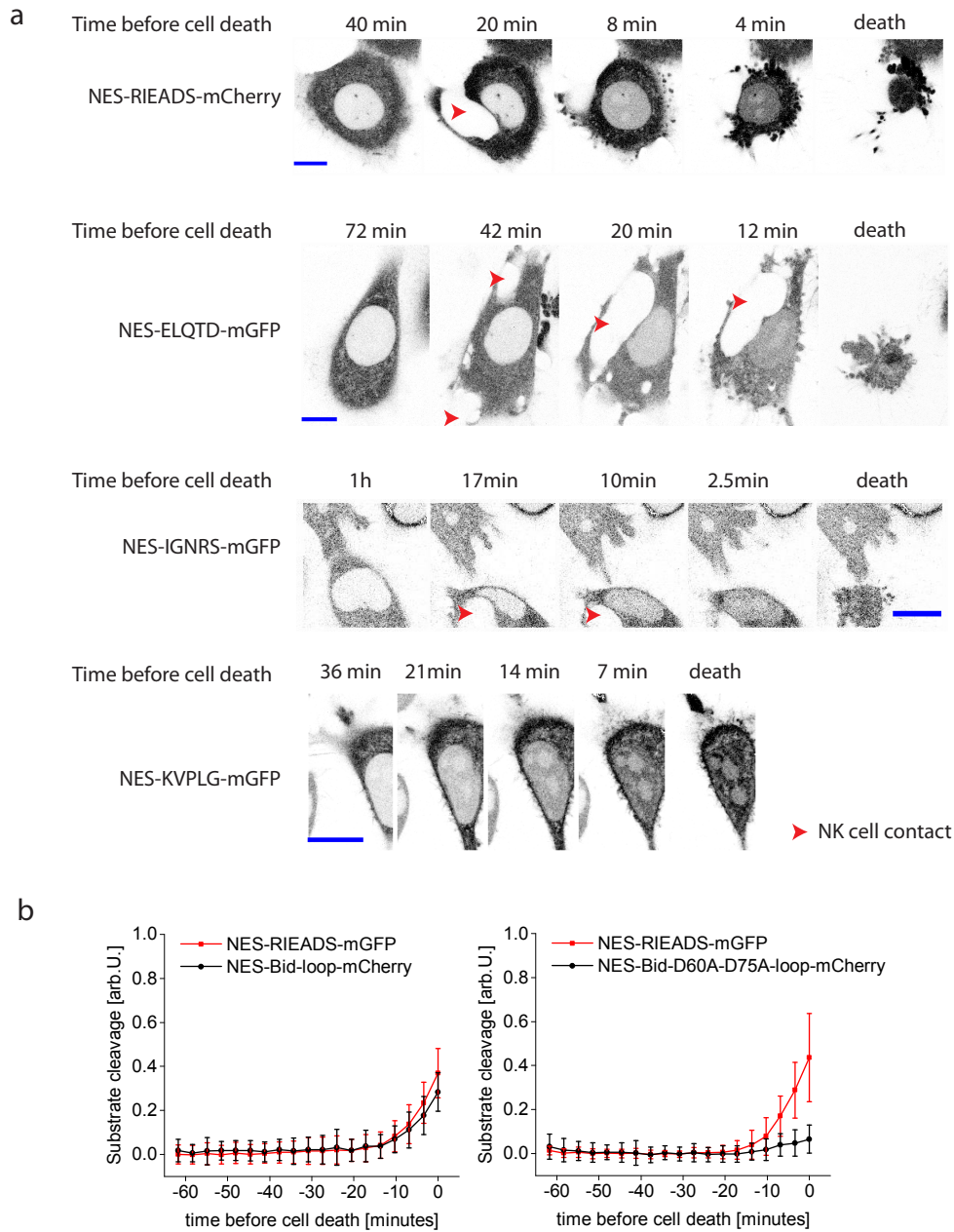


Figure 3.1: RIEADS and ELQTD-probes are cleaved in target cells upon NK92-C1 cell co-culture. (a) HeLa-CD48 cells were transfected with DNA encoding either the soluble-cytosolic protein NES-RIEADS-mCherry, NES-ELQTD-mGFP, NES-IGNRS-mGFP or NES-KVPLG-mGFP. Target cells and NK92-C1 cells were co-cultured with a NK cell to target cell ratio of 4. Non-fluorescent NK cells can be seen also in the fluorescence detection channel when the NK cell moves the fluorescent target cell out of the confocal plane. Those NK cell contacts are indicated with a red arrowhead. NES-IGNRS-mGFP and NES-KVPLG-mGFP cleavages were rarely observed (2/43 and 1/25 respectively). NES = nuclear export signal. Scale bar = 10 μ m. (b) HeLa cells expressing NES-RIEADS-mGFP with NES-Bid-loop-mCherry (left) or with NES-Bid-D60A-D75A-loop-mCherry (right). Data of single cell measurements were shifted along the time axis to compare probe cleavage relative to the cell death time. Mean and s.d. of 25 cells (left) and 26 cells (right).

3.1.3 Localization of RIEADS- and IGNRS-probe cleavage

As granzyme A has been reported to be associated with mitochondria (Martinvalet et al. 2008, Lucken-Ardjomande and Martinou 2008) the cytosolic reporter NES-IGNRS-mGFP might have been not sensitive enough to report granzyme A activity. Therefore, I also tested IGNRS-probe cleavage at the surface of mitochondria.

HeLa-CD48 cells were co-transfected with the reporters MitoNEET-IGNRS-mGFP and NES-RIEADS-mCherry and exposed to NK92-C1 cells. I observed that mitochondria systematically rounded up before undergoing cell death, suggesting that mitochondria could be targets of NK-mediated death (Figure 3.2, IGNRS-probe and boxes). I also observed that mitochondria stayed distributed in the cell and did not translocate to the plasma membrane, a process that was debated in the literature (Susanto et al. 2009). However, while the cytoplasmic RIEADS-reporter was cleaved, no cleavage of the mitochondrial IGNRS-reporter was detected (Figure 3.2a). This means that (i) granzyme A was not active at all or (ii) granzyme A was not active at the outer mitochondrial surface or (iii) that the probe is inefficiently cleaved by granzyme A and too insensitive for the use as fluorescent reporter.

In parallel to the mitochondrial IGNRS-probe, cleavage of the mitochondrial RIEADS-probe (granzyme B) was tested using MitoNEET-RIEADS-mGFP. Again, while the reporter NES-RIEADS-mCherry was cleaved, no cleavage of the reporter MitoNEET-RIEADS-mGFP was detected in cells undergoing target cell death (Figure 3.2b).

Granzyme A and B have been reported to translocate into the nucleus to cleave substrates for example lamins or PARP-1 (Susanto et al. 2012). In order to test whether RIEADS-and IGNRS-probes are cleaved inside the nucleus, I used the fluorescent reporters H2B-RIEADS-mGFP and H2B-IGNRS-mGFP. Their cleavage in HeLa-CD48 cells could be seen on images when those were strongly contrast enhanced (Figure 3.3a,b). I observed in 22 out of 42 (52%) transfected, dying cells cleavage of H2B-IGNRS-mGFP. Cleavage of this nuclear probe was measured in parallel to the NES-RIEADS-mCherry (granzyme B). When cleavage of the nuclear probe was seen, I also most of the time observed cleavage of the cytosolic RIEADS-probe (e.g. cell 1 Figure 3.3a).

These results indicate that granzyme A might potentially be active inside the nucleus in a fraction of cells. Moreover, out of 63 transfected HeLa-CD48 transiently expressing H2B-RIEADS-mGFP and NES-RIEADS-mCherry, 37 cells died upon NK92-C1 co-culture and of those 25 cells (68%) showed RIEADS-probe cleavage (Figure 3.3b). In cells showing nuclear H2B-RIEADS-mGFP cleavage, cytosolic NES-RIEADS-mCherry cleavage was systematically seen and vice versa.

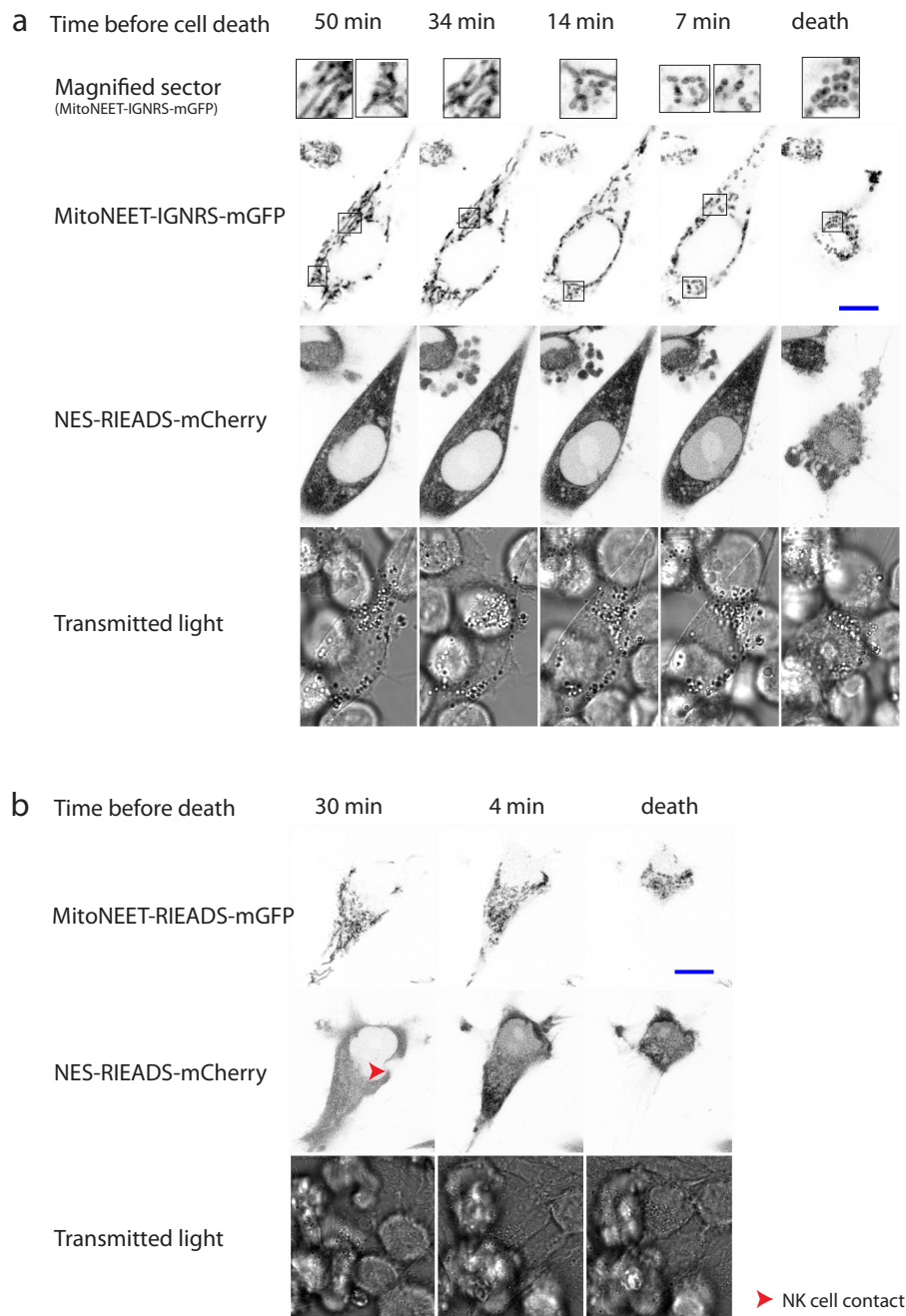


Figure 3.2: Mitochondrial surface IGNRs- and RIEADS-probes are not cleaved upon NK92-C1 cell co-culture. (a) HeLa-CD48 cells expressing NES-RIEADS-mCherry and MitoNEET-IGNRS-mGFP (presence of 10µM zVAD-fmk) or (b) NES-RIEADS-mCherry and MitoNEET-RIEADS-mGFP. NK92-C1 cell:target = 4. Snap-shots of cells at the indicated time points relative to target cell death are shown. Sections of images showing the probe MitoNEET-IGNRS-mGFP were magnified. NK cell contacts are indicated with a red arrowhead. Scale bar = 10µm.

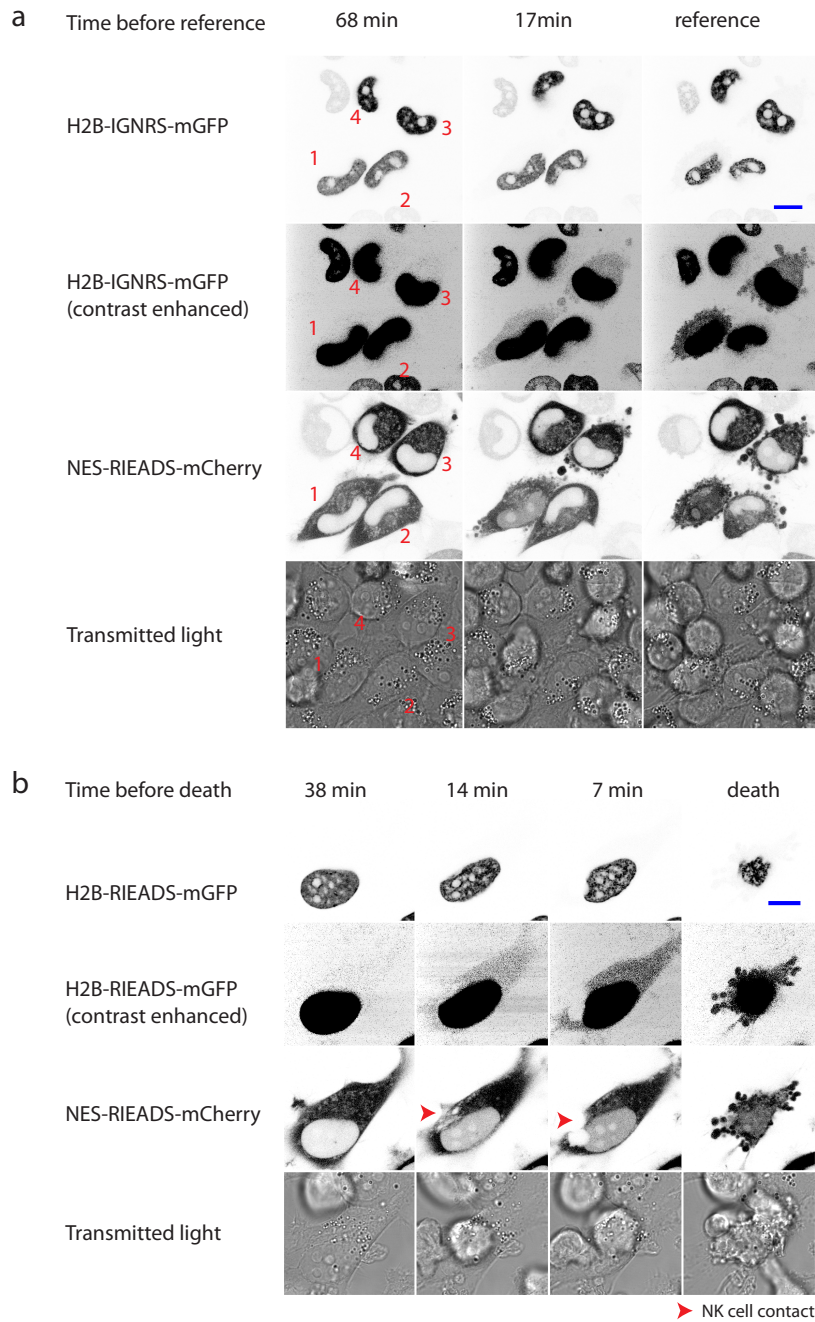


Figure 3.3: Nuclear IGNRS- and RIEADS-probes are cleaved. (a) HeLa-CD48 cells expressing NES-RIEADS-mCherry and H2B-IGNRS-mGFP and incubated with 10 μ M zVAD-fmk or (b) NES-RIEADS-mCherry and H2B-RIEADS-mGFP. NK92-C1 cell:target = 4. Snap-shots of cells at the indicated time points relative to a reference are shown. The images shown in the the first rows labeled with H2B-IGNRS-mGFP and H2B-RIEADS-mGFP, respectively are shown again in the second row with enhanced contrast. The same contrast enhancement was applied for one channel for the different time points shown. NK cell contacts are indicated with a red arrowhead. Scale bar = 10 μ m.

To conclude, the presence of NES-RIEADS-mGFP and NES-ELQTD-mGFP probe cleavage in HeLa-CD48 cells upon NK92-C1 cell exposure suggests that proteases cleaving after aspartic acid, potentially granzyme B and caspase-8, but also a protease cleaving within the IGNSR-site, potentially granzyme A, were active in the cytosol of HeLa cells. Cleavage of the IGNSR- and RIEADS-probe could not be localized at the outer leaflet of mitochondria. Nevertheless, small amounts of IGNSR- and RIEADS- probe cleavage were detected in the nucleus. Although nuclear probe cleavage looked weak, either due to inefficient accessibility to the reporter or indeed due to low amounts of proteases inside the nucleus, this activity nevertheless might have effectively participated in inducing cell death.

3.1.4 The amino acid sequence RIEADS is cleaved independently of CD95

One aim of my work was to differentiate CD95L induced caspase-8 activity from granzyme activity in single target cells. Caspase-8 activity upon soluble CD95L induction can be investigated in HeLa cells by measuring the fluorescent redistribution of the reporter NES-ELQTD-mGFP (Beaudouin et al. 2013). In order to assess the specificity of ELQTD- and RIEADS-probe cleavage to the CD95 pathway, I analyzed the cleavage of these probes in conditions where the expression of CD95 was perturbed in the target cell. For this, cells were transfected with plasmids encoding shRNA against the receptor CD95 plus a fluorescent marker H2B-eBFP2. The probes NES-ELQTD-mCherry and NES-RIEADS-mGFP were expressed transiently in HeLa-CD48 cells and probe cleavage was compared upon soluble CD95 ligand (IZsCD95L) addition and NK92-C1 co-culture.

Upon stimulation with recombinant soluble IZsCD95L, cells showed on average $46 \pm 12.8\%$ ELQTD-probe cleavage at the last measured time point before cell shrinkage (time of death). In contrast, the RIEADS-probe was cleaved to a lower extent, showing $10.6 \pm 4.8\%$ cleavage (Figure 3.4a). This means that in the context of caspase-8 activation, partial non-granzyme specific RIEADS-probe cleavage would be expected. In contrast, cells transfected with shRNA against CD95 did not die upon soluble ligand induction and neither showed ELQTD-probe nor RIEADS-probe cleavage (Figure 3.4b). In the context of NK92-C1 cell co-culture, $33.2 \pm 12.6\%$ RIEADS-probe cleavage and $7.3 \pm 6.8\%$ ELQTD-probe cleavage was measured in HeLa cells. Cells transfected with shRNA against CD95 still showed $19.8 \pm 12.9\%$ RIEADS-probe cleavage but no ELQTD-probe cleavage (Figure 3.4c and d).

To conclude, for CD95-pathway a fraction of RIEADS-probe cleavage is expected. But, in the absence of ELQTD-probe cleavage upon NK92-C1 cell exposure RIEADS-cleavage was still observed.

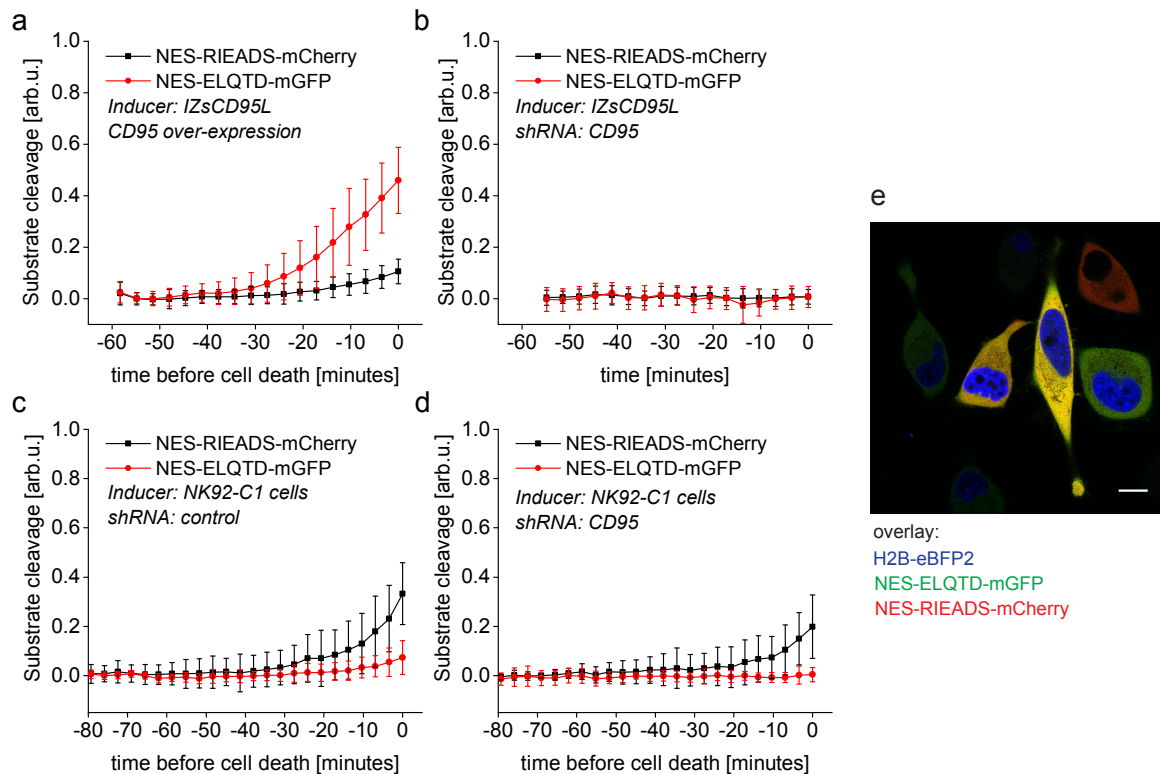


Figure 3.4: The RIEADS substrate is cleaved independent of CD95 upon NK92-C1 cell co-culture. HeLa-CD48 cells were used as target cells and transfected with two plasmids encoding the probes NES-RIEADS-mGFP or NES-ELQTD-mCherry. (a) CD95 over-expression. (b,d) shRNA against CD95 expressed with H2B-eBFP2. (c) control shRNA. (a,b) HeLa cells were stimulated with IZsCD95L. (c,d) NK92-C1 cells were added to HeLa cells with ratio 4. Data of single cell measurements were shifted along the time axis to compare probe cleavage relative to cell death time. Mean \pm s.d. of 40 cells (a), 10 cells (b), 13 cells (c) and 10 cells (d). (e) Overlay of images selected before start of the time-series for b) Scale bar = 10 μ m.

3.1.5 ELQTD-cleavage as a read-out for CD95 pathway activation

Previously, we have shown that the ELQTD-activity is more visible when localized to the plasma membrane (Beaudouin et al. 2013). To further assess ELQTD-cleavage specificity, I compared membrane-localized ELQTD-probe cleavage in HeLa-CD48 cells in a context where CD95 expression is perturbed. DNA encoding for the fluorescent reporter MyrSnap2-ELQTD-YFP was transfected alone or co-transfected either with DNA encoding shRNA against CD95 receptor and encoding the marker H2B-eBFP2 or with DNA encoding CD95-mCherry.

In CD95-mCherry over-expressing cells, 14 out of 23 (61%) selected cells showed MyrSnap2-ELQTD-YFP probe cleavage similar to control conditions where 16 out of 25 (64%) cells showed probe cleavage upon NK92-C1 cell co-culture (Figure 3.5a). In contrast, in cells with transient receptor knockdown, probe cleavage was not seen in 18 out of 20 measured cells. These results show that ELQTD-probe cleavage can be used as a read-out for CD95 pathway activation in NK-cell mediated cell death.

Next, cells were analyzed expressing membrane and cytosolic ELQTD-probes (MyrSnap2-ELQTD-mGFP and NES-ELQTD-mCherry). As expected, the membrane probe was more efficiently cleaved than the cytosolic probe showing that caspase-8 activity was activated in HeLa-CD48 cells by NK-cells, similarly to cells stimulated with soluble CD95L (Figure 3.5b, Beaudouin et al. 2013). Furthermore, I noticed that ELQTD cleavage was tendentially observed in cells that died rather late. To prove this, I measured the time point of cell death of those cells that showed membrane-probe cleavage, visible as homogeneously distributed fluorescence over the cell (e.g. Figure 3.5c, cell 3 and 4) and of those cells that did not show membrane-probe cleavage before cell death (e.g. Figure 3.5c, cell 1 and 2). Strikingly, cells which showed ELQTD-cleavage died at around 6h while cells that did not show ELQTD-probe cleavage died much earlier at around 2h (Figure 3.5d).

This could mean (i) that the CD95 apoptosis pathway is activated later than the other cell death pathway that led to quick cell death or (ii) that CD95 signal integration is merely slower than signal integration of the other cell death pathway which was probably absent in those cells.

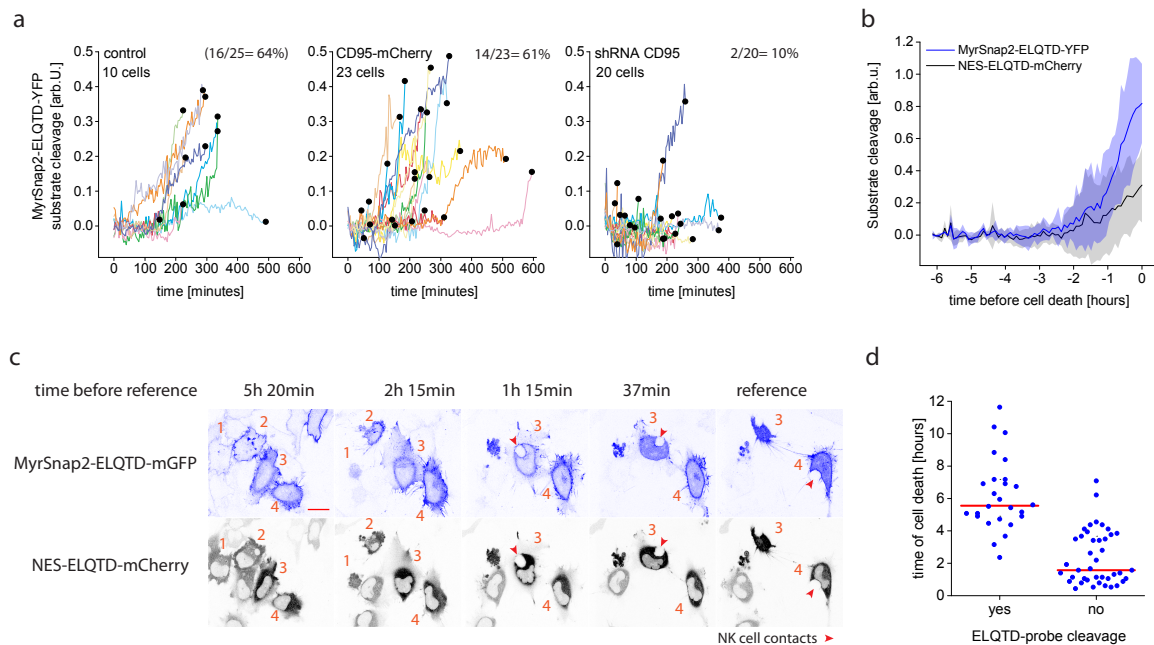


Figure 3.5: NK92-C1 mediated ELQTD substrate cleavage (a) HeLa-CD48 cells expressed the probe MyrSnap2-ELQTD-YFP. Cells co-expressed either CD95-mCherry (middle plot) or shRNA for the knockdown of CD95 and H2B-eBFP2 (plot on the right). NK92-C1:target = 3. The value of the last measured time point of one trajectory was highlighted and indicates the time of cell death. Probe cleavage could be quantified in only 10 cells in the left plot. Percentages indicate the fraction of observed cleavage of total number of transfected cells. (b-d) HeLa-CD48 cells expressed the probes MyrSnap2-ELQTD-YFP and NES-ELQTD-mCherry. NK92-C1:target = 3. (b) Quantification of probe cleavage of 10 cells. (c) Time-series snap shots. Cells 1 and 2 died earlier than cells 3 and 4, only cells 3 and 4 showed probe cleavage. Scale bar = 20 μ m. (d) Time of cell death (and median) for cells showing ELQTD-probe cleavage (yes), and cells not showing probe cleavage (no).

3.1.6 ELQTD- and RIEADS-probe cleavage correlate with target cell death

As described in the previous section, different activities are induced by NK92-C1 cells leading either to CD95-dependent ELQTD-probe cleavage or to CD95-independent RIEADS-probe cleavage in the target cell. Furthermore, I observed a correlation between cell death time and ELQTD-probe cleavage. Next, I wanted to find out whether dying cells show exclusively one of the activities, or if both activities can be observed at the same time in target cells and how this would influence cell death time. In order to investigate this, I compared NES-RIEADS-mGFP and NES-ELQTD-mCherry cleavage in HeLa-CD95 transiently expressing CD48.

Interestingly, I observed that single cells showed either (i) same probe cleavage kinetics, (ii) more ELQTD- than RIEADS-probe cleavage or vice versa (iii) more RIEADS- than ELQTD-probe cleavage (Figure 3.6). In order to test whether always one probe was cleaved the same and the second probe was cleaved to varying extent or alternatively, whether both cleavages varied, I grouped together single cell measurements that showed one of the three described relative strengths of ELQTD- and RIEADS-probe cleavage and made the statistical analysis on these subgroups (Figure 3.6a-c, Table 3.2). I noticed that relative probe cleavage amounts measured in the nucleus at the last time point before cell death were about 5% to 15% higher in a first experiment compared to values obtained in a second experiment. RIEADS-probes were cleaved on average 15% to 31% within a cell. ELQTD-probe cleavage amounts showed stronger variations, with end-point values from 9 to 59% (Table 3.2). Importantly, as seen from control experiments shown in figure 3.4a, by inducing the CD95 pathway, for 46% ELQTD-cleavage about 10.6% RIEADS-probe cleavage would be expected. This means that RIEADS-probe cleavage might be partially due to CD95-dependent activity. Hence, averaged RIEADS-probe cleavage amounts measured at the last time point were corrected for this contribution (5th and 6th column, Table 3.2). Finally, the results suggest that cells indeed showed either RIEADS cleavage, or ELQTD-probe cleavage or both and therefore that the balance of ELQTD- specific activity, presumably from caspase-8, and the RIEADS-specific activity, presumably from granzyme B, was different in individual cells.

In order to examine how the two different protease activities correlate with the cell death time, I measured this time for the three different subgroups (Figure 3.6). In the two experiments, HeLa-CD95 cells that displayed stronger ELQTD- over RIEADS- probe cleavage showed a mean cell death time of 114 ± 40 min and 95 ± 41 min, respectively. In contrast, cells showing same ELQTD- and RIEADS-probe cleavage died at a mean time of 64 ± 21 min or 57 ± 13 min upon NK92-C1 addition, similar to cells showing less ELQTD-probe cleavage than RIEADS-probe cleavage which died after 50 ± 22 min or 48 ± 15 min, respectively. This shows that cells that died at late time points were killed by a different mechanism, most likely by the CD95 pathway, than cells that died quickly upon NK92-C1 cell exposure, which potentially involved granzymes or other cytotoxic proteins. One hypothesis was that cells showing high ELQTD-probe cleavage are

killed much slower. To test whether target cells that died at different time points were hit by the NK cells at different time-points, I extracted the time of the target cell-NK cell contact from time-series images from the second experiment and for cells showing more ELQTD- than RIEADS-probe cleavage (E>R) and for cells showing less ELQTD- than RIEADS-probe cleavage (E<R). The median contact time for cells (E>R) was 40 min and therefore only 18 min delayed to the median contact time of 22 min of cells (E<R). This would not be sufficient to explain the difference in median cell death time (100 min and 44 min). While cells (E<R) required about 26 min to undergo cell death since NK cell contact, the second subgroup showing more ELQTD-cleavage required 68 min (Figure 3.6e).

Table 3.2: Percentage of NES-ELQTD-mCherry and NES-RIEADS-mGFP probe cleavage

Subgroup	Probe	% of cleavage		% of cleavage, <i>corrected</i>	
		Exp 1	Exp 2	Exp 1	Exp 2
E>R	ELQTD	59±14	44±25		
	RIEADS	24±29	15±6	10	5
E=R	ELQTD	29±29	21±5		
	RIEADS	30±30	25±13	23	20
E<R	ELQTD	19±14	9±7		
	RIEADS	31±13	22±10	27	20

Percentage of NES-ELQTD-mCherry (E) and NES-RIEADS-mGFP (R) probe cleavage (last measured time point before cell death), Exp=Experiment, mean ± s.d., *corrected* = RIEADS-probe cleavage expected when no ELQTD-cleavage present (mean values).

Together, these data show that death induced by the CD95 pathway is presumably much slower than death induced in the presence of RIEADS-probe cleavage. Furthermore, the small delay (18 min) observed in target:NK cell contact between the two groups (E<R and E>R) could indicate that the presentation of CD95L and other death-inducing molecules occurs at different time points and possibly via different granules (Schmidt et al. 2011).

A possible interpretation would be that CD95L might be still presented on the cell surface when exocytosis of lytic granules is completed. In this scenario, the NK cell might induce quick death upon release of soluble-cytotoxic molecules such as granzymes. As a "serial killer" (Bhat and Watzl 2007) the NK cell might use slow cell death by CD95L for other target cells, possibly when granzymes and other soluble factors are not available anymore.

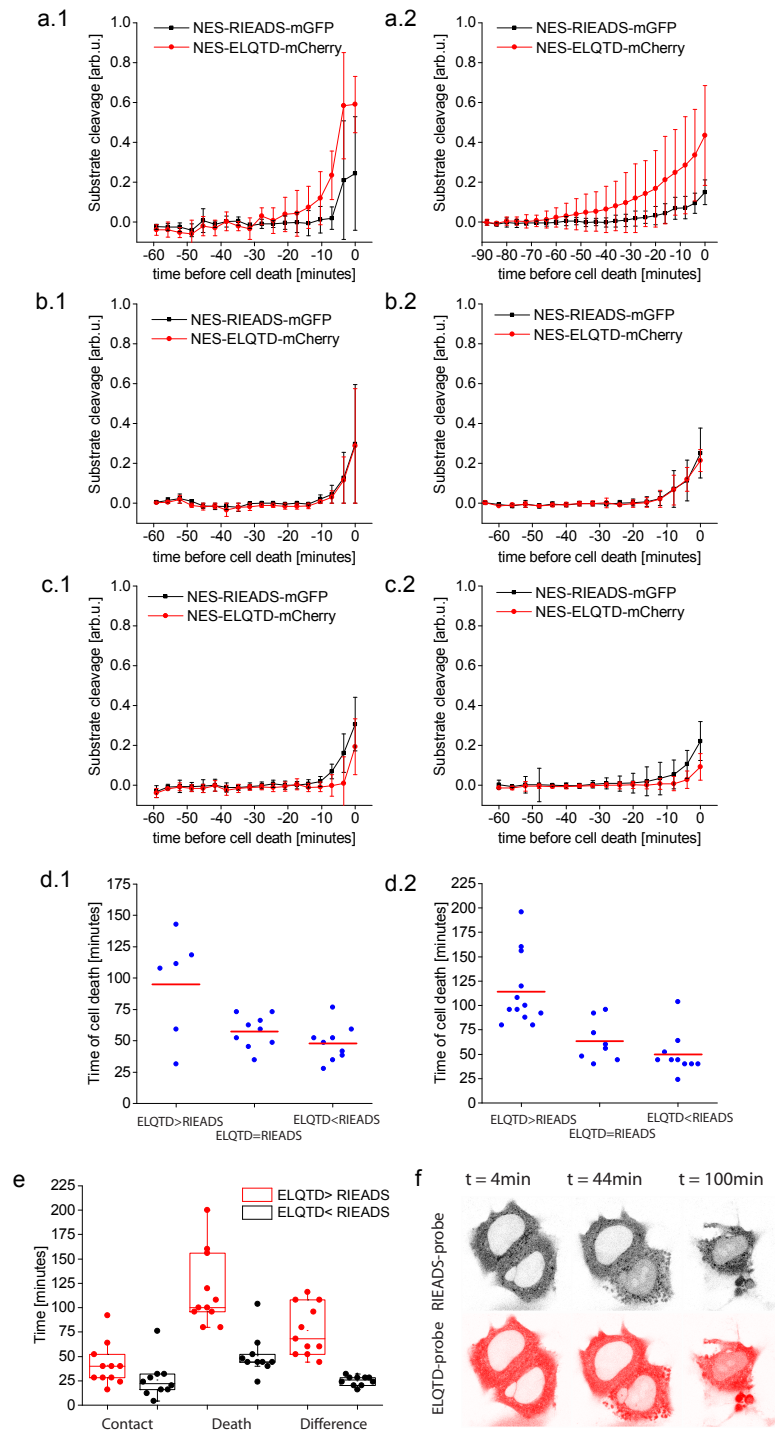


Figure 3.6: ELQTD substrate cleavage upon NK92-C1 co-culture is predictive for target cell death time. Target cells: HeLa-CD95 cells expressing transiently CD48 and the probes NES-ELQTD-mCherry and NES-RIEADS-mGFP. NK92-C1:HeLa cell ratio was 3. Confocal imaging was done two days after transfection. Mean and s.d. of single cell measurements for different subgroups, plotted towards same cell death time point and classified as follows. (a) Single cell measurements showed more ELQTD-probe cleavage than RIEADS-probe cleavage. (b) Equal ELQTD- and RIEADS-probe cleavage. (c) Less ELQTD- than RIEADS-probe cleavage. (d) Target cell death time and mean values plotted for the different subgroups a-c. Data from two independent experiments are shown (.1 and .2). (e) The time of target cell contact after addition of NK cells, the time of cell death and the difference between these two measures is plotted for the subgroups a and c of experiment two (and median). (f) Example images showing two cells expressing the probes NES-RIEADS-mGFP and NES-ELQTD-mCherry at different time points after addition of NK92-C1 cells.

Bcl-X_L over-expression slightly delays cell death

Both caspase-mediated caspase-8 activation and granzyme B activity can lead to cleavage of Bid. Truncated Bid (tBid) can trigger pore formation of Bax and Bak on mitochondria by either directly interacting with these proteins or by sequestering inhibitors of Bax and Bak, for example Bcl-X_L. Eventually, mitochondrial outer membrane permeabilization (MOMP) can lead to activation of executioner caspases and thereby to apoptosis (Kantari and Walczak 2011).

To test whether CD95-independent activity in NK92-C1-mediated target cell death involves MOMP, the effect of Bcl-X_L over-expression on target cell death time and RIEADS-probe cleavage was measured. For this, HeLa-CD48 cells were transiently transfected with plasmids encoding for Bcl-X_L-eBFP2 and the probe NES-RIEADS-mGFP (Figure 3.7b) or as control transfected with the probe alone. To prevent caspase activity, target cells and NK cells were incubated with 50µM z-vad in both conditions.

HeLa-CD48 control cells which showed NES-RIEADS-mGFP cleavage died 71 min upon addition of NK92-C1 cells, while Bcl-X_L-eBFP2 over-expressing cells died slightly delayed after 110 min (Figure 3.7a). In both conditions NES-RIEADS-mGFP substrate cleavage started around 25 min after NK92-C1 cell exposure. Cleavage rates looked similar in both conditions. (Figure 3.7c, d). However, a clear shift of the averaged cleavage trajectories for each condition can be observed (Figure 3.7e). The time window between onset of activity and cell death in control cells was about 15 min and the one in Bcl-X_L-eBFP2 expressing cells was about 30 min (Figure 3.7e, f). Moreover, control cells showed $54 \pm 25\%$ cleavage and Bcl-X_L-eBFP2 expressing cells showed $79 \pm 30\%$ substrate cleavage at the last time-point before cell death. Interestingly, in five individual cells which over-expressed Bcl-X_L-eBFP2, the time-window between onset and activity and cell death was increased up to 150 min, indicating a weak induction of the mitochondrial cell death pathway in those cells (Figure 3.7f).

Together, these data indicate that BH3-only proteins (like BAX, BAD, Bim, Bid) could be activated in target cells by NK92-C1, perhaps directly by Bid cleavage or potentially indirectly by granzyme B-mediated Mcl-1 cleavage (Kantari and Walczak 2011, Han et al. 2004).

3.1.7 Cell death and RIEADS-probe cleavage can occur independently of caspase activity

Measurements of cell death by microscopy do not only allow the observation of protease activity and cell death time but also to classify dying cells according to their morphology. In the course of the different experiments performed in this study, partially presented in the previous sections, I noticed that the shape of the dead cell killed by NK92-C1 cells differed among cells.

In order to understand the potential contribution of caspases to the cell death morphology, I visually classified those morphologies into three different categories. The first category includes

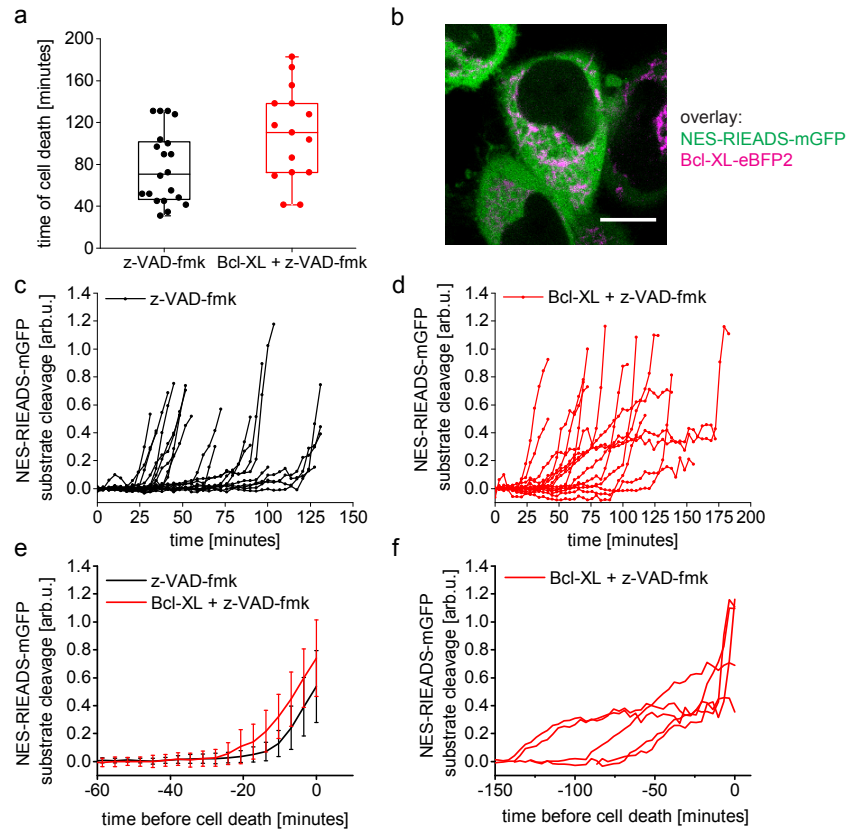


Figure 3.7: Bcl- X_L over-expression slightly delays cell death HeLa-CD48 cells were used as target cells and transfected with a plasmid encoding for NES-RIEADS-mGFP alone or together with a plasmid encoding for Bcl- X_L -eBFP2. Two days after transfection, 50 μ M of the drug zVAD-fmk was applied to target cells and NK92-C1 cells for 30 min. Target cells were then co-cultured with NK92-C1 cells with a cell number ratio of 3 (NK cell:target). (a) Median time of target cell death. (b) Example cell expressing NES-RIEADS-mGFP (green) and Bcl- X_L -eBFP2 (blue), Scale bar = 10 μ m. (c,d) NES-RIEADS-mGFP substrate cleavage data for control cells and Bcl- X_L -eBFP2 expressing cells. (e) Mean and s.d. of NES-RIEADS-mGFP substrate cleavage data presented in c and d, excluding five trajectories from Bcl- X_L over-expressing cells that are separately shown in f). In plot e) averaging was made after aligning data according to cell death time.

cells showing typical signs of apoptosis like membrane blebbing and cell shrinkage (Figure 3.8a) (Wickman et al. 2013, Ziegler and Groscurth 2004). The second phenotype describes cells that showed no membrane blebbing and no shrinkage. In this case, the NES-probes showed accumulation of fluorescent protein in the nucleus indicating signs of death. The third morphology appeared to me neither the first nor the second, but rather something in between, showing signs of blebbing but less visible shrinkage compared to apoptotic cells. This classification was done by eye and is therefore subjective. The three categories are specified in the figure with differently shaded boxes (Figure 3.8).

Furthermore, the occurrence of the different morphologies was counted and is presented in pie charts for different cellular target cell conditions: control, incubation with 50 μ M zVAD-fmk, over-expression of Bcl- X_L or over-expression of Bcl- X_L plus incubation with 50 μ M zVAD-fmk (Figure 3.8).

For cells in control condition, about 65% of the cells showed membrane blebbing (first category) and only 9% of the cells did not show membrane blebbing at all (second category). In the absence of caspase-8 activity using 50 μ M zVAD-fmk, when over-expressing Bcl-X_L or when over-expressing Bcl-X_L plus using zVAD-fmk, then only 19%, 24% and 24% of cells showed signs of membrane blebbing, respectively. In those cells, 40%, 54% and 58%, respectively of the cells showed no blebbing. Thus, by blocking caspases in target cells using the pan-caspase inhibitor zVAD-fmk or by over-expressing Bcl-X_L, less membrane blebbing was observed in dying cells. Next to cell death, block of caspase activity did not prevent RIEADS-cleavage, indicating that a protease different from caspases was active (graph, Figure 3.8).

Mahrus and co-workers have found that effector caspases (caspase-3) have preferential target proteins and destroy and cleave a limited set of cellular processes and proteins, respectively (Mahrus et al. 2008). NK92-C1 cells probably not only mediate death by activating caspases but also by delivering other cytotoxic proteins such as granzymes. Effector caspases and granzymes can have different substrates but might also share them.

These results on the cell death morphology indicate that potentially different cell death mechanisms occurred in parallel in target cells because the different observed cell death morphologies might be consequence of cleavage of distinct subsets of target proteins.

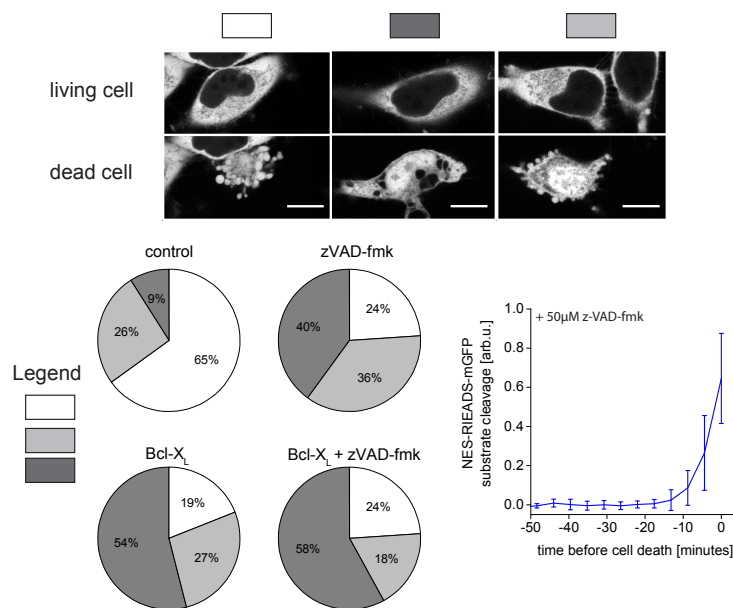


Figure 3.8: NK92-C1 mediated cell death leads to different target cell death morphologies. (a) HeLa cells expressing the probe NES-RIEADS-mGFP are shown alive and dead. Boxes indicate the three different categories of cell death morphologies that were distinguished by eye. Scale bar = 10 μ m. Pie charts: quantification of classification of cell death morphologies observed in HeLa-CD48 (and additionally HeLa-CD95 cells in control and zVAD-fmk condition) upon NK92-C1 cell co-culture. Different treatments of target cells were 50 μ M zVAD-fmk (n=43 HeLa-CD48 + 37 HeLa-CD95), Bcl-XL over-expression (n=37), Bcl-XL over-expression plus 50 μ M zVAD-fmk (n=38) or control (n=67 HeLa-CD48 + 47 HeLa-CD95). Graph: NES-RIEADS-mGFP substrate cleavage in presence of 50 μ M zVAD-fmk in HeLa-CD95 cells transiently expressing CD48 and co-cultured with NK92-C1 cells (ratio 2).

3.1.8 SerpinB9 over-expression reduces RIEADS-probe cleavage in HeLa cells

SerpinB9 is an intracellular *serine-/cysteine-proteinase inhibitor* that inhibits granzyme B by blocking the active site by forming a covalent, irreversible complex with granzyme B. SerpinB9 may also act as a substrate for granzyme B that can be released without affecting the function of the enzyme (Kaiserman and Bird 2010, Law et al. 2006). SerpinB9 capacity to also inhibit caspases was debated but it seems to more efficiently inhibit granzymeB (Bird et al. 1998).

In order to test if the amino acid sequence *RIEADS* is cleaved by granzyme B, I expressed serpinB9 together with the fluorescent probe NES-RIEADS-mCherry and the protein CD48 in HeLa cells and measured probe cleavage upon addition of NK92-C1 cells. In target cells, over-expressed serpinB9 can then directly compete with the fluorescent reporter for binding to granzyme B. By lowering the concentration of active granzymeB enzyme, one would expect a smaller rate or even block of RIEADS-probe cleavage.

I observed that NES-RIEADS-mCherry-cleavage was systematically reduced in serpinB9 over-expressing cells compared to control cells, but probe cleavage was not always completely abolished (Figure 3.9a-d). Median and mean values of substrate cleavage measured at the last time-point before cell death were higher in control cells than in those cells over-expressing serpinB9 (Figure 3.9f).

To see whether the time of target cell death was influenced by serpinB9, this time point was plotted for those cells that showed RIEADS-probe cleavage (Figure 3.9e). For a cell ratio of 1 the median cell death time was 2 h 42 min in control cells and 4 h 20 min in serpinB9 expressing cells and for a cell ratio of five 1 h and 1 h 30 min, respectively. The median and the mean cell death times were not exactly the same, nevertheless mean values showed the same tendency as median values (Figure 3.9e). To visually amplify this difference in time of death between control cells and serpinB9 over-expressing cells, log₂-transformed data points were plotted (Figure 3.9g). As a control, to test whether the difference in time of death was caused by differences in NK-target cells contact times, this time was extracted from time-series images. For a cell ratio of one, the time of contact was similar and the difference between the time of contact and the time of target cell death was larger with serpinB9 over-expressing cells (Figure 3.9e). This shows that cell death was delayed in those cells due to serpinB9 over-expression.

Together with the observation that induction of CD95 inefficiently cleaves the probe NES-RIEADS-mGFP (Figure 3.4), I concluded from this data, that granzyme B activity can be measured with the RIEADS-probe because this cleavage was blocked in serpinB9 over-expressing cells.

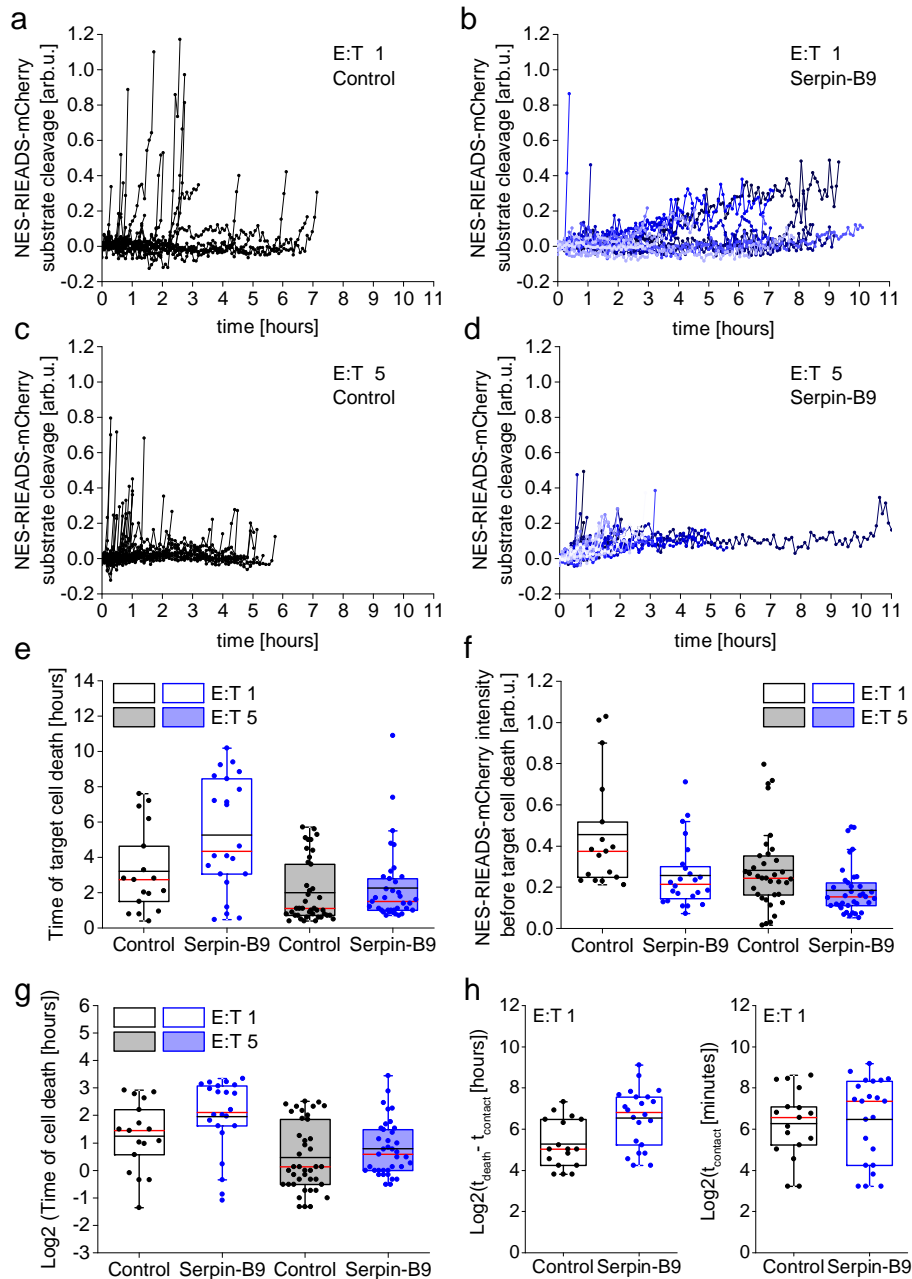


Figure 3.9: SerpinB9 blocks RIEADS-probe cleavage (a,c) HeLa cells were transfected with a plasmid encoding NES-RIEADS-mCherry and a plasmid encoding CD48. (b,d) HeLa cells were transfected with a plasmid encoding both, serpinB9 and NES-RIEADS-mCherry and a plasmid encoding CD48. (a-d) Quantification of NES-RIEADS-mCherry substrate cleavage in target cells upon addition of NK92-C1 cells. (e) Cell death time of cells measured in a-d. (f) Nuclear intensities before cell death entry replotted from data presented in a-d. (g) Log2 transformed cell death time points from plot e. (h) Time between first NK cell contact $t_{contact}$ and cell death t_{death} plotted as log2 transformed number for target cells incubated with NK92-C1 cells with a ratio 1. Likewise, the time of NK and target cell contacts $t_{contact}$ is plotted. For box-plots: median values plotted in red, mean values plotted in black. E:T=Effector to target cell ratio.

3.1.9 The proteinase inhibitor serpinB9 localizes to the cell membrane

In this work, I found that RIEADS-probe cleavage can be blocked in target cells by serpinB9 over-expression. To test the subcellular localization of over-expressed serpinB9 in HeLa cells, the protein was stained by indirect immunofluorescence and examined by confocal microscopy. As a co-marker to stain the cytosol, the fluorescent reporter NES-RIEADS-mCherry was expressed from the same plasmid as serpinB9.

I observed no specific staining in cells that were incubated with antibody in the absence of the detergent saponin or in cells that did not show mCherry fluorescence (Figure 3.10, lower panel and black arrows in middle row of upper panel). However, in NES-RIEADS-mCherry expressing cells, staining using serpinB9 antibodies was strong and showed that the inhibitor constitutes near the cell membrane (Figure 3.10 upper three panels).

These data suggest that serpinB9 either actively binds to the cell membrane in target cells or binds to another membrane-localized protein.

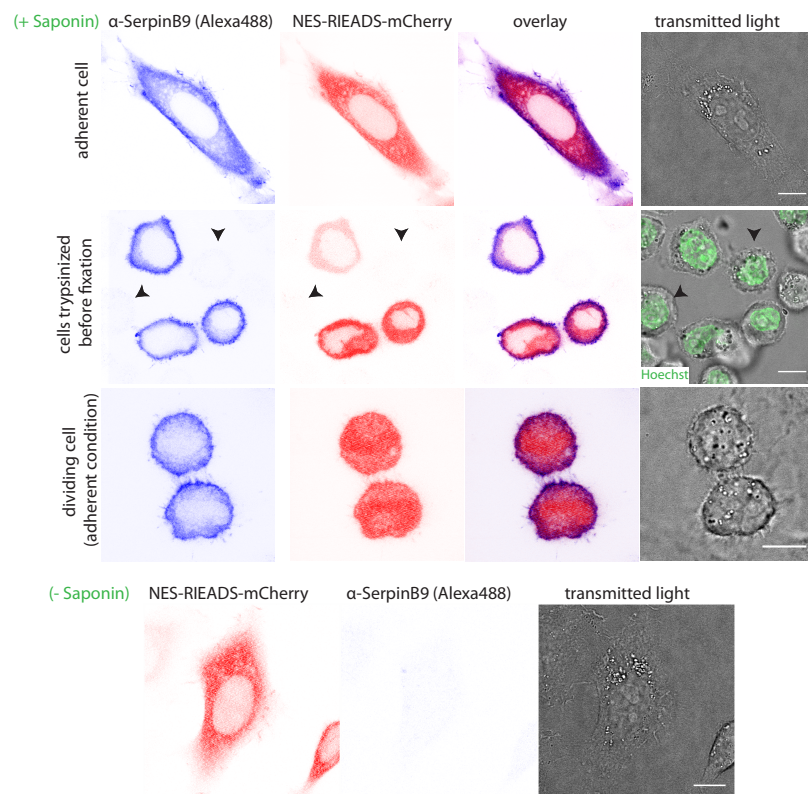


Figure 3.10: SerpinB9 localization. Adherent HeLa cells (first and third row) or trypsinized cells (middle row) were cross-linked by FA/GA-fixative and stained intracellularly for serpinB9 by indirect immunofluorescence using 0.2% saponin. mCherry fluorescence can be measured after fixation and served as a marker for the cytosol in non-dividing cells (red). Alexa-488 labeled secondary antibody was used to detect binding of serpin-antibody (blue). Nuclei of trypsinized cells were also stained with Hoechst (green). No serpinB9 staining was seen in the absence of the detergent saponin (lower panel). Scale bar = 10 μ m.

3.1.10 RIEADS and ELQTD- cleaving proteases from NK cells are active at the cell membrane in target cells

Known substrates of granzyme B are soluble-cytosolic proteins, for example Bid, or nuclear proteins, for example lamin B (at site *VEVD*, Zhang et al. 2001). Soluble-cytosolic and nuclear reporters containing the cleavage site *RIEADS* were indeed cleaved in target cells upon NK92-C1 cell co-culture (Figure 3.3, page 47).

Interestingly, the protein Mcl-1 which can be cleaved by granzyme B (Han et al. 2004) has been located to the plasma membrane when over-expressed in HeLa cells (Herrant et al. 2004). Moreover, I found that that the mitochondrial reporter MitoNEET-RIEADS-mGFP was not cleaved (Figure 3.2b, page 46) and that over-expressed serpinB9 is located near the plasma membrane in HeLa cells (Figure 3.10).

Therefore I asked if granzyme B would be active at the plasma membrane. To test this, I compared the temporal behavior of RIEADS-cleavage in the cytosol to the one at the membrane. For this, I expressed the probes MyrSnap2-RIEADS-mGFP and NES-RIEADS-mCherry in HeLa cells. Moreover, to exclude cleavage owing to CD95 activity, measurements were performed in comparison to cells expressing shRNA against CD95 (Figure 3.11b,d,e) or in cells over-expressing CD95 receptor (Figure 3.11a,c). To control how much RIEADS-cleavage would be expected when caspase-8 activity through the CD95 pathway would be induced, cells were first stimulated with soluble IZsCD95L (Figure 3.11a,b).

In cells over-expressing CD95, short before cell death, I observed $29\pm 11\%$ of membrane- and $7\pm 3\%$ of cytosolic RIEADS-probe cleavage (Figure 3.11a). In contrast, cleavage of membrane and cytosolic RIEADS-probes and cell death were completely absent in cells expressing the marker H2B-eBFP for the transient knockdown of CD95 receptor (Figure 3.11b).

Strikingly, target cells co-cultured with NK92-C1 cells showed stronger membrane than cytosolic cleavage of the substrate RIEADS probe. This was observed in cells which over-expressed CD95 receptor ($66\pm 16\%$ membrane- and $19\pm 9\%$ cytosolic-probe cleavage short before cell death) and in cells having transient CD95 receptor knockdown ($53\pm 20\%$ membrane- and $19\pm 10\%$ cytosolic-probe cleavage short before cell death) (Figure 3.11a and b).

These data indicate that the RIEADS- cleaving protease which corresponds likely to granzyme B, is active at the plasma membrane.

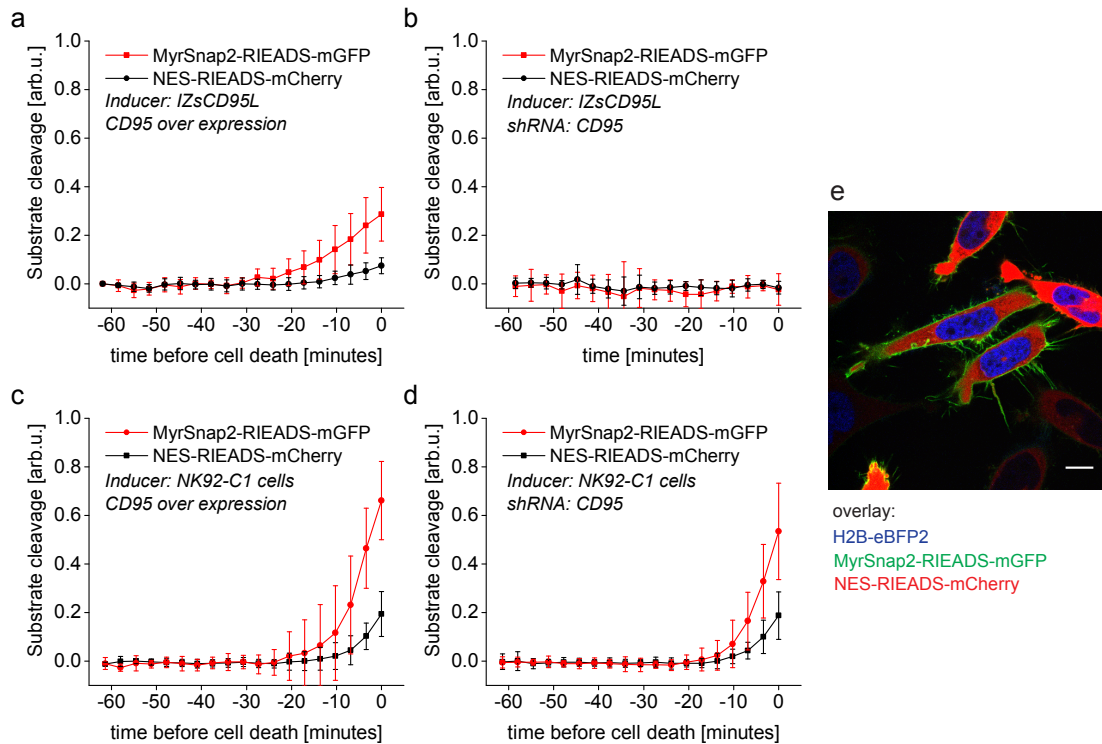


Figure 3.11: The RIEADS-probe is cleaved at the plasma membrane. HeLa-CD48 cells were used as target cells and transfected with a plasmid encoding NES-RIEADS-mCherry and MyrSnap2-RIEADS-mGFP together with a plasmid encoding for either CD95 alone (a,c) or shRNA for the knockdown of CD95 and H2B-eBFP2 (b, d). Three days after transfection IZ-sCD95L (a, b) or NK92-C1 cells were added to target cells in ratio 3 (c, d) and images were acquired with the SP5 confocal microscope from Leica repeatedly over time. Mean \pm s.d. of 20 cells (a), 10 cells (b), 17 cells (c) and 17 cells (d). (e) Overlay of images selected and measured before start of the time-series, for b) and d) cells expressing H2B-eBFP2, MyrSnap2-RIEADS-mGFP and NES-RIEADS-mCherry were analyzed. Fluorescence from eBFP2 was measured once before addition of ligand or NK cells. Scale bar = 10 μ m.

3.1.11 Conclusion - Cell death by NK cells

In this part of my work I studied how NK92-C1 cells induce death of target cells. The following points highlight the main findings that I presented.

1. By using the pan-caspase inhibitor zVAD-fmk or by over-expressing the protein Bcl-X_L, target cell death induced by NK92-cells could not be blocked but the fraction of cells showing a typical apoptotic morphology was reduced. Dead cells then showed a different morphology. This indicates different mechanisms used by the NK cell to destroy the individual target cell (Figure 3.8).
2. The fluorescent reporter comprising the RIEADS-cleavage site was presumably recognized by granzyme B because over-expression of serpinB9 reduced this cleavage (Figure 3.9).
3. The RIEADS- (granzyme B) proteolytic activity was most present at the cell membrane. Activity was also detected inside the nucleus before cell death but not at mitochondria (Figures 3.11, 3.2 and 3.3).
4. The granzyme B specific inhibitor serpinB9 localized to the plasma membrane in HeLa cells (Figure 3.10).
5. The IGNS- (granzyme A) proteolytic activity was detected inside the nucleus but was absent in the cytosol or on mitochondria of HeLa target cells before cell death (Figures 3.1 and 3.3).
6. NK92-C1 cell mediated CD95-dependent caspase-8 activity was measured specifically by the ELQTD-reporter in target cells and proteolytic activity was most present at the plasma membrane (Figure 3.9).
7. Caspase-8 activity (ELQTD-probe) and granzyme B activity (RIEADS-probe) seem to mediate death on different time-scales. While cells that died early in the population showed RIEADS-probe cleavage, those cells that died later showed mainly ELQTD-probe cleavage. (Figures 3.5 and 3.6)

Towards understanding why soluble CD95L is a weak inducer of apoptosis

Soluble CD95L (sCD95L) is a natural form of CD95L that is produced by proteolytic cleavage of the membrane form of CD95L, a process termed shedding. Cleavage leaves a remnant of CD95L at the plasma membrane and frees sCD95L containing the receptor binding domain into the extracellular space. This sCD95L is known to be a weak inducer of apoptosis but is able to trigger non-apoptotic responses (Martin-Villalba et al. 2013).

By studying CD95 pathway activation upon soluble CD95L binding and by understanding why soluble CD95L is a poor activator of CD95, I believe that insights into the mechanism of CD95 receptor activation can be obtained. Where it was possible, sCD95L was compared to a more potent inducer of apoptosis, IZsCD95L which is sCD95L fused to a trimerization domain isoleucine-zipper (IZ). This not only allowed to understand differences between the ligands but also to better characterize CD95 pathway activation.

In the following sections, results on oligomerization state measurements, ligand-receptor binding and caspase-8 activation measurements are presented.

Oligomerization state measurements at different protein concentrations

sCD95L forms a trimer in solution, as seen by gel filtration and biochemical cross-linking (Schneider et al. 1998, Berg et al. 2007). Though, it has been clearly shown that fusing soluble ligand forms of the TNF-family ligands to trimerization domains restores or enhances their signaling capabilities (for example Schneider et al. 1998). Possible explanations for the different activities of the two different soluble ligands might be changes in avidity for the ligand to the receptor or alternatively dissociation of sCD95L trimers into dimers or monomers. Dissociation of TNF- α trimers into monomers has been reported to occur at pM concentration (Corti et al. 1992) and partial dissociation of GIRTL trimers into dimers was observed by gel filtration (Zhou et al. 2008, Chattopadhyay et al. 2007).

In order to measure the oligomerization state of sCD95L and fluorescently tagged sCD95L, I performed chemical cross-linking experiments, FCS and FCCS as well as single molecule photobleaching experiments. Using the aforementioned, complementing biochemical and biophysical assays, the subunit stoichiometry was assessed at different protein concentrations ranging from nM to pM.

3.2 The subunit stoichiometry of soluble CD95L is three

3.2.1 Biochemical cross-linking indicates that sCD95L and mCherry-sCD95L do form trimers

The molecular weight of proteins can be measured by polyacrylamid gel electrophoresis (PAGE) and western blotting. Non-covalent interactions are typically not kept during this procedure. To stabilize oligomeric structures, proteins can be chemically (covalently) cross-linked, for example using bis-(sulfosuccinimidyl)-suberate (BS^3) or formaldehyde (FA). The cross-linking efficiency depends mainly on the amino acid composition of the proteins and the size of the cross-linker. Table 3.3 lists the expected sizes of monomeric, dimeric and trimeric assemblies in kDa of non-glycosylated proteins which were studied.

Table 3.3: Expected molecular weight (MW) of recombinant proteins

Protein	MW, non-glycosylated protein [kDa]		
	monomer	dimer	trimer
sCD95L	20	40	60
IZsCD95L	26	52	78
mCherry	28	/	/
mCherry-IZ	34	68	102
mCherry-sCD95L	46	92	138
mCherry-IZsCD95L	53	106	159

Using the cross-linker(BS^3), trimeric and dimeric chemical adducts of sCD95L and IZsCD95L were detected next to monomeric proteins (Figure 3.12a,b). This indicates, that both forms of ligand do form trimers. Unexpectedly, also two thin bands of about 160 and 140kDa were detected in a IZ-sCD95L protein preparation, shown in plot a). Those were seen in both conditions, with and without cross-linker, but were absent in a repetition experiment. I concluded that these bands are probably unspecific and constitute perhaps transferred antibody from the protein purification. Furthermore, in the absence of cross-linker, purified IZsCD95L which was mixed with SDS-buffers not containing reducing agent showed trimeric protein species next to dimeric and monomeric ones (Figure 3.12c). Those protein preparations that contained dithiothreitol (DTT) showed monomeric and dimeric protein species. sCD95L protein preparations showed monomeric species. Only the sample of purified sCD95L that was not heated and not treated with DTT showed also faint band resembling dimeric species. Together, this strongly supports the view that IZsCD95L forms trimers and sCD95L forms potentially less stable trimers.

Next, the composition and oligomerization of mCherry-tagged proteins was addressed because mCherry- tagged proteins were used in binding experiments. For this, purified mCherry-IZ,

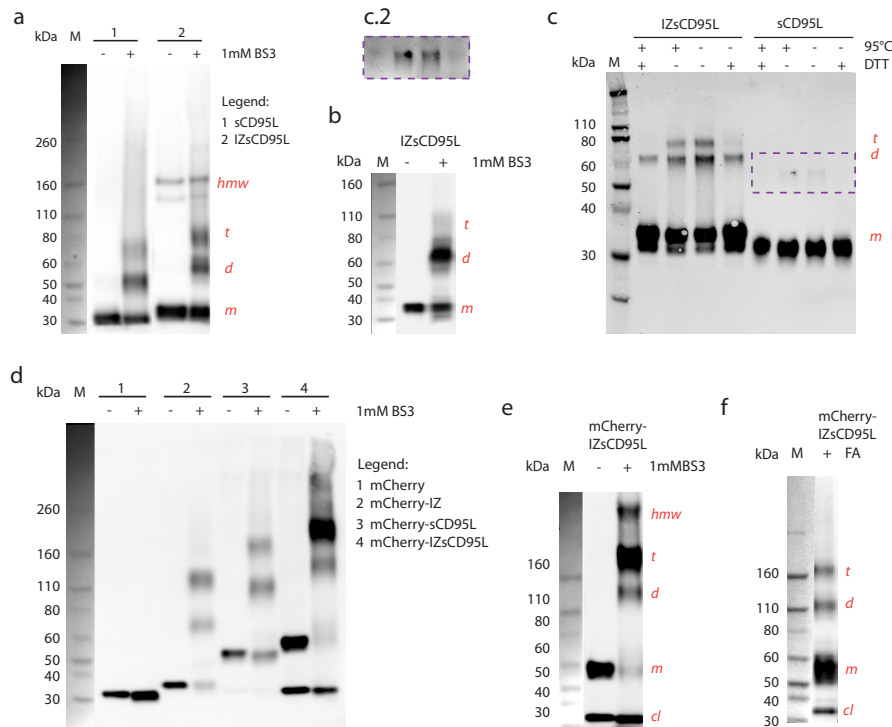


Figure 3.12: Biochemical cross-linking of purified proteins. Flag-tagged proteins were expressed in 293T cells and purified using ANTI-FLAG affinity gel. Proteins were cross-linked with 1mM bis-(sulfosuccinimidyl)-suberate (a,b,d,e) or 1% Formaldehyde (f) to stabilize non-covalent protein-interactions. All except c) made with 7% Tris-Acetate-PAGE. (c) 10% Bis-Tris-PAGE, DTT=denaturing agent dithiothreitol, 95°C=heating of samples. c.2 shows presumable dimeric species of purified sCD95L of the contrast enhanced image c). M=protein size marker. hmw=high-molecular-weight, t=trimer, d=dimer, m=monomer, cl=cleavage product.

mCherry-sCD95L and mCherry-IZsCD95L as well as the monomeric control mCherry were cross-linked with 1mM BS^3 (Figure 3.12d,e).

I observed that the Flag-tagged mCherry showed a band at the expected size of the monomer, while the other three proteins mCherry-IZ, mCherry-sCD95L and mCherry-IZsCD95L showed each bands which would correspond to monomeric, dimeric and trimeric adducts. Similarly, mCherry-IZsCD95L, cross-linked using 1% FA, showed trimeric and dimeric adducts next to monomeric species with the majority being monomeric species (Figure 3.12f). Besides, using BS^3 cross-linker in mCherry-IZsCD95L preparations, I also saw protein adducts of higher molecular weight than trimers, with the majority being trimeric species (Figure 3.12e).

Together, these data show that by using different chemical cross-linker mCherry-IZ, mCherry-sCD95L and mCherry-IZsCD95L can form trimers. Furthermore, purified mCherry-IZsCD95L unfortunately showed also a band of the size of mCherry, indicating cleavage of the protein (Figure 3.12). For purified mCherry-IZsCD95L, the mCherry-cleavage product was potentially over-represented. I assessed the amount of protein cleavage in non-purified protein preparations as explained in the following.

Assessment of mCherry-IZsCD95L cleavage extent

To estimate cleavage of the non-purified protein mCherry-IZsCD95L I intended to use western blot. Cleavage of this protein occurred probably between the mCherry and the IZsCD95L domain. However, no such cleavage was observed for the protein mCherry-IZ, which was built the same way. The goal was to compare the amount of cleaved mCherry to a known amount of mCherry. I used Fluorescence Correlation Spectroscopy (FCS) to quantify the total amount of mCherry molecules in the protein solutions of mCherry-IZsCD95L, mCherry-sCD95L and mCherry, to be able to load the same total amount of mCherry on a gel. On the western blot, non-purified mCherry and mCherry-cleavage product can be detected well in contrast to non-purified full-length proteins of around 50-60kDa because proteins from the medium seem to interfere with the blotting and detection procedure. This was visible as so-called "smiling bands" and was expected from previous western blot results. Moreover, comparison of mCherry and mCherry-cleavage product is more justified because those proteins showed similar sizes. Non-purified mCherry-sCD95L and mCherry-IZsCD95L, both at 2.4 $\mu\text{g}/\text{ml}$, showed similar fluorescence intensities by FCS (Figure 3.13a). Expressed, recombinant flag-tagged mCherry proteins were diluted in cell culture medium until similar fluorescence intensities of mCherry to mCherry-sCD95L and mCherry-IZsCD95L were measured and indicated that same mCherry molecule numbers are present. Subsequently, protein solutions, showing same amount of fluorescence were prepared to detect flag-tagged proteins by western blot. For technical replicates, proteins were loaded and detected in duplicates (Figure 3.13b). The mean amount of cleaved mCherry in mCherry-sCD95L and mCherry-IZsCD95L preparations was here 0.5% and 1.9% respectively, obtained by quantifying F-mCherry and cleavage product bands by using ImageJ. For binding assays using non-purified mCherry-tagged ligands, ligand preparations were used when cleavage did not exceed 5%.

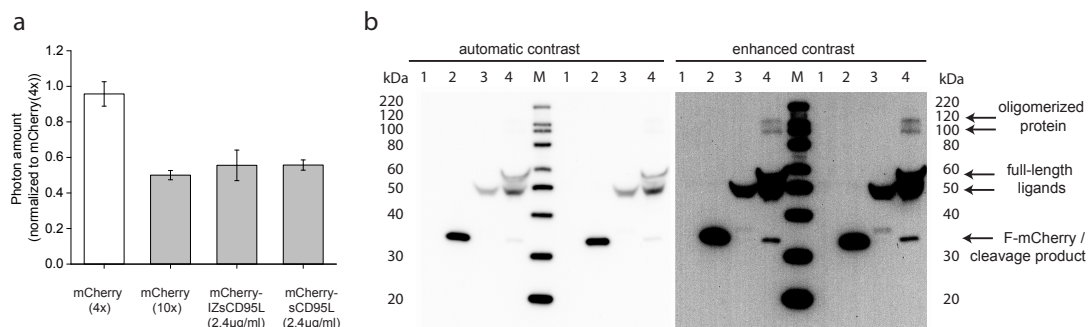


Figure 3.13: Assessing mCherry-IZsCD95L cleavage extent on non-purified protein preparations.

(a) Comparison of the fluorescence intensity of mCherry-protein dilutions (in medium) to 2.4 $\mu\text{g}/\text{ml}$ mCherry-sCD95L and 2.4 $\mu\text{g}/\text{ml}$ mCherry-IZsCD95L. (b) Western blot, Detection of non-purified flag-tagged proteins. The blot is shown contrast enhanced to visualize mCherry-cleavage. M = protein size marker. 1 = medium, 2 = mCherry, 3 = mCherry-sCD95L, 4 = mCherry-IZsCD95L.




3.2.2 FCS measurements indicate that sCD95L form trimers

To verify results from the chemical cross-linking experiment, I used the method Fluorescence Correlation Spectroscopy (FCS). By using FCS, the diffusion time or the diffusion coefficient of native, non-purified proteins in solution can be measured in the nM range. For this, proteins need to be fluorescently labeled. Genetically fusing mCherry to the proteins IZ, sCD95L and IZsCD95L allowed tagging each protein subunit with one fluorophore.

The goal was to distinguish monomeric proteins from trimeric proteins by their diffusion time. For this, the difference in the hydrodynamic radius of the monomer and the trimer must be sufficiently different (Materials and Methods section 2.2.2).

In order to estimate relative differences in diffusion time of the different fusion-proteins, I estimated their hydrodynamic radii. For this, one assumption was that the structure of those fusion proteins is rather cylindrical than spherical judged by comparison to the structure of human glucocorticoid-induced TNF receptor ligand (GITRL) fused to the IZ-domain (Chattopadhyay et al. 2007). Next, the length and width of the proteins isoleucine-zipper, GFP and sCD95L were measured using the program VMD (Humphrey et al. 1996) (Table 3.4).

Table 3.4: Size estimates for proteins

	IZ (1GCM)	mGFP (1EMA)	sCD95L (4MSV)
Protein Database (pdb) structure			
Length [nm]	4.2	5.0	4.2
Width [nm]	1.8	2.5	2.2

Protein structures were taken from pdb entries and illustrated using the program VMD. IZ=Isoleucine-zipper, three molecules assembling a trimer. CD95L, amino acids 130-281, one molecule.

The length of the IZ-domain and of sCD95L is about 4.2 nm, and that of mGFP about 5.0 nm. The IZ-domain is the slimmest protein of those having a width of about 1.8 nm, followed by sCD95L with about 2.2 nm and mGFP with about 2.5 nm. Secondly, the radii and lengths for the different fusion proteins F-mCherry, mCherry-IZ, mCherry-sCD95L and mCherry-IZsCD95L were estimated (Table 3.5).

Next, the radius R_s of a sphere having the same volume as the assumed cylinder was calculated (Bloomfield et al. 2000). Then, the fold change of these expected hydrodynamic radii $\frac{R_s}{R_{s,mCherry}}$ of the fusion protein and mCherry monomer was calculated (Table 3.5).

Using these assumptions and size estimates, monomeric mCherry is expected to have a two-fold smaller diffusion coefficient than trimeric mCherry-IZ or trimeric mCherry-sCD95L and a 2.29 fold

smaller diffusion coefficient than trimeric mCherry-IZsCD95L. In contrast, assuming monomers for all the different fusion-proteins, the diffusion coefficient of mCherry-IZ and mCherry-sCD95L is expected to be 1.26 fold higher and for mCherry-IZsCD95L about 1.44 fold higher ($\frac{R_s}{R_{s,mCherry}}$, Table 3.5). These estimates suggest that monomeric and trimeric species of those fusion proteins would be distinguishable.

Table 3.5: Hydrodynamic radius estimates of proteins and relative fold difference to monomeric mCherry

Protein	monomeric F-mCherry	t (m) mCherry-IZ	t (m) mCherry-sCD95L	t (m) mCherry-IZsCD95L
radius, r [nm]	1.25	2.5 (1.25)	2.5 (1.25)	2.5 (1.25)
Length, L [nm]	5.0	10.0	10.0	15
$p = \frac{L}{2r}$	2	2 (4)	2 (4)	3 (6)
$R_s = \left(\frac{3}{2p^2}\right)^{\frac{1}{3}} \frac{L}{2}$	1.8	3.61 (2.27)	3.61 (2.27)	4.13 (2.6)
$\frac{R_s}{R_{s,mCherry}}$	1	2 (1.26)	2 (1.26)	2.29 (1.44)

R_s =radius of a sphere having the same volume as the assumed cylinder (Bloomfield et al. 2000),
m=monomer, t=trimer

For FCS measurements, non-purified proteins were used. The confocal volume was not measured because proteins were compared relative to each other. Data of measurements acquired on the same day and with the same microscopy settings were compared. I measured mCherry-fusion proteins of the IZ-domain and of the TNF-family ligands sCD95L and TNF- α , which are assumed to have similar sizes, but also their IZ-forms, IZsCD95L and IZ-TNF- α . Autocorrelated data of 4 to 9 subsequent measurements were normalized to the amplitude, averaged and plotted with the standard deviation. The diffusion time is the value of τ at half-maximal amplitude and it reflects the average time that the fluorescent molecule required to cross the confocal volume. For mCherry this diffusion time was 100 μ sec and for mCherry-IZ about 220 μ sec, as read from the plot (Figure 3.14).

Based on the calculated expected relative differences in hydrodynamic radii, I concluded that mCherry-IZ is trimeric. Moreover, mCherry-sCD95L, mCherry-sTNF α , mCherry-IZsCD95L and mCherry-IZsTNF α showed autocorrelation curves that were overlapping with the autocorrelation curve of mCherry-IZ (Figure 3.14). Because the maximal expected relative difference in diffusion time was measured, I concluded that sCD95L, TNF- α and IZ-fused proteins of them do form trimers.

Fluorescence Cross Correlation Spectroscopy indicates that trimers are stable

Based on measurements of the diffusion time of mCherry-tagged sTNF- α , sCD95L, IZsTNF- α , IZsCD95L and IZ-domain, I concluded that there is a strong affinity for trimerization.

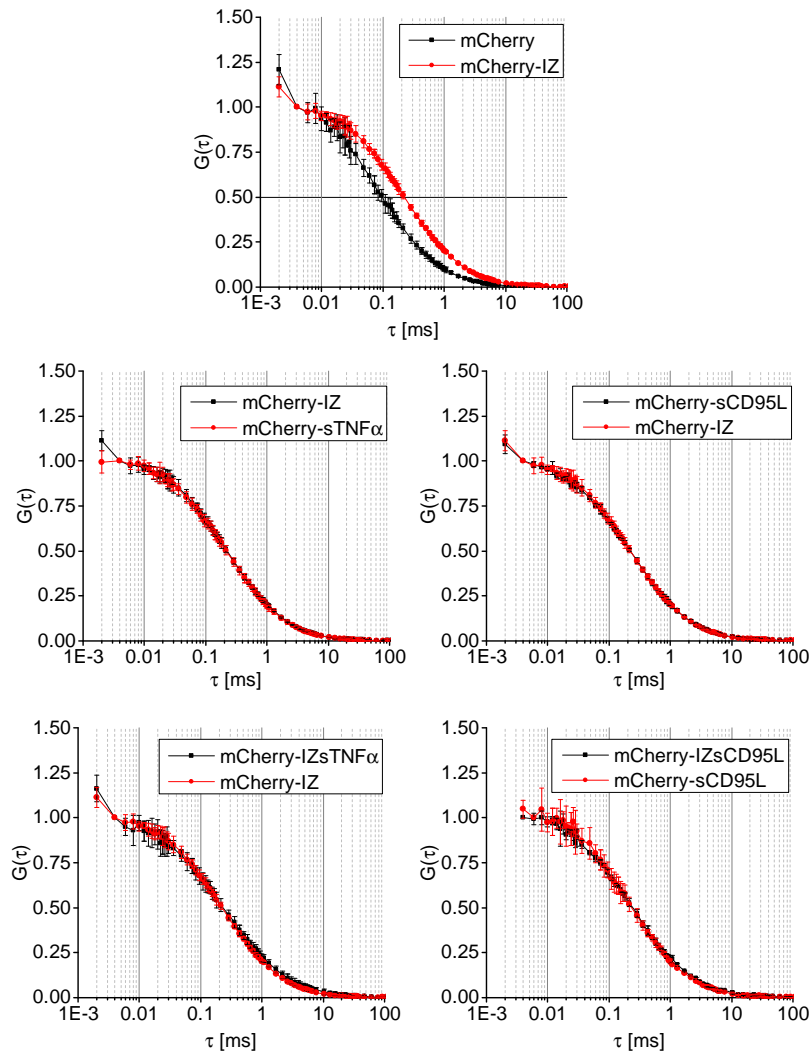


Figure 3.14: Diffusion times of mCherry tagged proteins. Autocorrelation curves were calculated from the measurements using the software ISS Vista and normalized to the amplitude (here always the second time point τ was chosen). Protein concentrations ranged from 1 to 6 $\mu\text{g/ml}$.

However, this does not exclude the possibility that this interaction is unstable with a strong off-rate combined with a strong on-rate. In case the trimeric assembly of sCD95L is unstable, trimer subunits would exchange over time.

To test if subunits of trimers exchange, Fluorescence Cross Correlation Spectroscopy (FCCS) was applied. For this, mGFP and mCherry proteins and fusion proteins thereof were expressed either together by co-transfection of the DNA in 293T cells or expressed separately.

As expected, co-expressed mGFP and mCherry did not show cross-correlation. Similar, preparations of mGFP and mCherry that were expressed separately, then mixed for 24h at 37°C and measured did also not show cross-correlation (Figure 3.15a). A positive control showing cross-correlation was the protein Bid fused N-terminally to mCherry and C-terminally to mGFP which was expressed in HeLa cells and measured in the cytosol (Figure 3.15e).

While protein preparations from co-expression of mGFP- and mCherry-tagged isoleucine-zipper, sCD95L, sTNF- α and IZ-sCD95L showed cross-correlation, no cross-correlation was found in the mixed protein preparations (Figure 3.15b-e).

Complementing biochemical cross-linking studies and FCS measurements of diffusion times, the presence of cross-correlation in preparations of mGFP and mCherry tagged proteins demonstrates that the different proteins isoleucine-zipper, sCD95L, sTNF- α and IZ-sCD95L do oligomerize. Based on FCCS measurements of mGFP and mCherry-tagged proteins, I would conclude that sCD95L, IZsCD95L and isoleucine-zipper (IZ) as well as TNF- α do form stable trimers on a time scale of 24 hours.

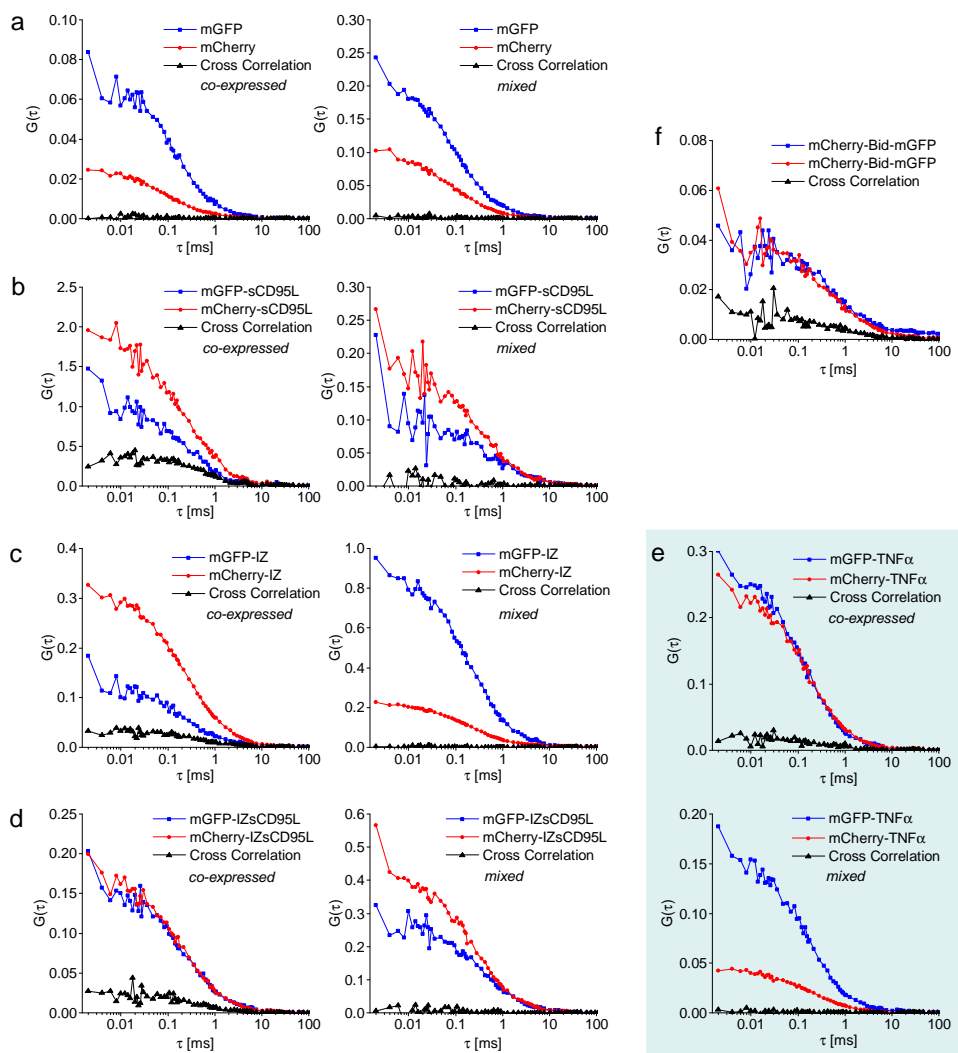


Figure 3.15: Oligomerization of sCD95L measured by FCCS. mGFP-tagged and mCherry-tagged proteins were either co-expressed in 293T cells or separately expressed and then mixed for 24h at 37°C. (a) mGFP and mCherry (negative control for cross-correlation) (b) mGFP-sCD95L and mCherry-sCD95L (c) mGFP-IZ and mCherry-IZ (d) mGFP-IZsCD95L and mCherry-IZsCD95L (e) mGFP-TNF α and mCherry-TNF α (f) Fusion protein mCherry-Bid-mGFP (positive control for cross-correlation) expressed in HeLa cells.

3.3 Inferring subunit stoichiometries from TIRFM data

Biochemical cross-linking studies and Fluorescence Correlation Spectroscopy measurements allowed verifying sCD95L trimerization in a concentration range of about 1 to 6 μ g/ml. Trimerization of the sCD95L subunits at these concentration speaks therefore for a strong affinity. To test the possibility of subunit dissociation at concentrations one to two orders of magnitude lower, I aimed at identifying their subunit stoichiometry at low, pM concentration. For this, with the kind help of Dr. Michael Schwering, I applied Total Internal Reflection Fluorescence Microscopy (TIRFM) to record photobleaching time-series images of fluorescently labeled sCD95L, IZ-domain and IZsCD95L at pM concentration. To label the different proteins, I genetically fused them to flag-mGFP, allowing one-to-one tagging of proteins with a fluorophore. As a monomeric control for photobleaching experiments, flag-mGFP alone was used.

As introduced in the section Materials & Methods, photobleaching data can be analyzed by plotting a histogram of the occurrence of the number of steps in each trace (section 2.2.5). However, because steps were rarely clearly identifiable and can be subjective (see for example Figure 3.16d) and is time-consuming, I wanted to analyze photobleaching data without the need of counting bleaching steps. For this, I first used a tool to obtain the intensity information and secondly, I developed a statistical model to relate the intensity decay to the distribution of the time points of last bleaching steps.

3.3.1 Automated extraction of intensity profiles from photobleaching data

To quantify spots from photobleaching data, we fitted a 2D Gaussian intensity model to the intensity profile of each spot in each image of the time-series using the cell segmentation approach developed by Dr. Stefan Wörz and co-workers (Wörz et al. 2010). Apart from simplifying the measurements, this had the advantage that intensity values can be obtained for individual spots that are free of background intensity. The default initial parameters for the fit were optimized by Dr. Stefan Wörz and used to analyze spots of the different fusion-proteins.

Photobleaching of a trimeric protein assembly can show in principle up to three bleaching steps. Example intensity profiles from acquired data indeed showed three "steps" for the proteins mGFP-sCD95L, mGFP-IZ and mGFP-IZsCD95L (see red arrows in Figure 3.16). This indicates that those proteins can form trimers also at pM concentration. For mGFP spots, no photobleaching "stairs" but only a single "step" were observed (see red arrow in Figure 3.16).

The hypothesis was that IZ, sCD95L and IZsCD95L fusion proteins do form also trimers at low concentration. Alternatively, in case dissociation occurs, the average subunit stoichiometry should be less than three. In order to test these hypotheses, the whole ensemble of imaged and fitted spots was analyzed. To simplify the analysis to obtain the subunit stoichiometry, I propose a different method that I termed Last identifiable Step-Analysis (*LiSA*).

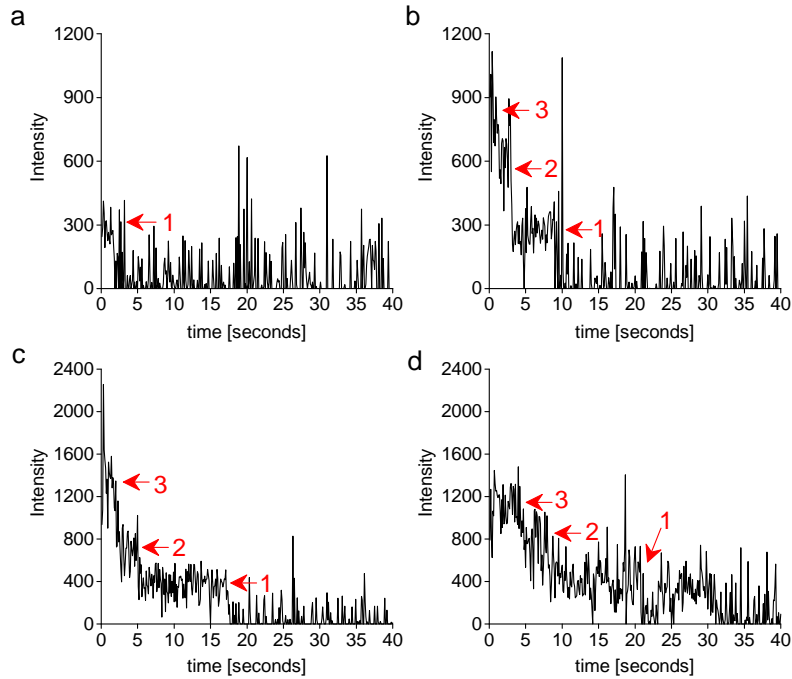


Figure 3.16: Spot number per image and example result of fits of photobleaching time-series. Intensities of a single fluorescent spot over time estimated from the amplitude of fitted gaussians of the spot. The arrows indicate fluorescence originating from three, two and one mGFP molecule(s), respectively.

3.3.2 Last identifiable Step-Analysis (LiSA)- to infer subunit stoichiometries from photobleaching data

In order to determine the subunit stoichiometry of mGFP, mGFP-sCD95L, mGFP-IZ and mGFP-IZsCD95L from single molecule photobleaching data, I developed and tested a strategy based on a statistical model. The model relates the time-points of the last bleaching event of a population of photobleached spots (hence the name "last identified steps") to the intensity decay. The number of fluorophores within the spot determines when a spot is likely to be completely bleached. In other words, the higher the number of subunits in the complex is, the higher the chance that at least one molecule in the complex is still fluorescent at time t and therefore, that a spot is still visible. The assumption is to deal with a population of molecule complexes composed each of u subunits fused each to one fluorescent molecule. As each fluorescent molecule, for example mGFP, has at each time point the same probability to be bleached, the time of the bleaching event follows a random number of the exponential distribution.

The total fluorescence of a population of fluorophores decays exponentially with time t , with the rate b , due to bleaching events occurring *somewhere* in the population (Eq.: 3.1).

$$I(t) = I_0 \exp^{-bt} \quad (3.1)$$

In other terms, the probability density function is $P(t) = b \exp^{-bt}$. The cumulative

distribution function (Eq.: 3.2) of the exponential distribution describes the probability with time that a bleaching event has occurred. The more time elapses, the higher the probability that bleaching has occurred.

$$P_{Cum}(t) = 1 - \exp^{-bt} \quad (3.2)$$

Knowing from equation 3.2 the probability that one fluorophore is bleached, we can describe the probability for all of them to be bleached as follows:

$$P_{Cum,bl}(t) = (1 - \exp^{-bt})^u \quad (3.3)$$

Conversely, the chance that at least one out of u present subunits of the complex is still fluorescent decreases with time (Eq.: 3.4).

$$P_{Cum,fl}(t) = 1 - (1 - \exp^{-bt})^u \quad (3.4)$$

$P_{Cum,fl}(t)$ describes the probability of observing a complex composed of u subunits at a time t . In the experiment, the counting of spots over time should follow this probability ($N_{measured}(u; t)$). The total fluorescence intensity from all spots of the image over time ($I(t; b)$) contains the information on the photobleaching rate, which is independent on the subunit stoichiometry of the proteins. By normalizing this intensity to one, one can replace the exponential term in equation 3.4 by this intensity measurement.

For a stoichiometry number k , the expected number of dots over time $N_{exp}(t)$ can be calculated from this intensity measurement.

$$N_{exp}(t) = 1 - (1 - I(t; b))^k \quad (3.5)$$

Finally, in order to find the true subunit stoichiometry value u , the expected probabilities for different k ($N_{exp}(k; t)$) can be compared to the actual measured number of detected spots over time ($N_{measured}(u; t)$). The value of k that minimizes the sum of the difference between the expected spot number decay and the measured spot number decay (sum of the squared errors, SSE) is the likely subunit stoichiometry number of the measured complexes. The timepoint of the last bleaching event over the whole spot population is denoted by t_{last} .

$$\min_k SSE = \sum_{t=1}^{t_{last}} (N_{exp}(k; t) - N_{measured}(u; t))^2 \quad (3.6)$$

Dealing with inhomogeneous illumination.

In a TIRFM experiment, photobleaching of molecules visibly occurs at different rates over the observed field because of inhomogeneous illumination (visible at $t = 0$ sec in Figure 2.6). That is why the probability to observe fluorescence differs in principle within one time-series image. Nevertheless, by assuming the same underlying bleaching probability for the intensity decay $I(t)$ and for the expected distribution of last-bleaching steps, the *LiSA*-method is virtually self-normalizing. Though, the probability to observe fluorescence and bleaching events might be biased by the spatial inhomogeneity. In order to minimize this bias, I proposed to subdivide the image into regions where bleaching appears to be illuminated similarly. Then, to find the value k that best fits the data and which corresponds to the average subunit stoichiometry value, one can use a statistic of the obtained SSE values over the different analyzed sub-images originating from one sample and over the different replicates. Thereby, for the different test of k , a mean and standard deviation can be given.

Analysis of simulated TIRFM photobleaching data by the *LiSA*-method

To test this method, theoretical last-step distributions were calculated from simulated bleaching data. First, I simulated photobleaching of trimers ($u = 3$) having different amount of noise. Noise reflects here the intensity fluctuations typically seen in the photobleaching time trace of a spot. In the experiment, this noise originated on the one hand from differences in fluorescence yield at each measured time point and on the other hand potentially also from the fitting procedure. Noise was added as a uniform random number (Figure 3.17a,b).

Then, the sum of squared errors of the difference between theoretical (for different k) and the true distribution of complexes over time, was calculated and plotted together with the mean of 19 replicates containing each 10 trimers (Figure 3.17c). As expected, the smallest SSE values in these plots were obtained for $k = 3$. For simulated monomers using 10 replicates containing 8 molecules each the smallest SSE-values in these plots were obtained for $k = 1$. The number of trimers and monomers was here chosen close to the experimental values.

Next, to test the influence on the spot number per image and the noise on the correct determination of the subunit stoichiometry number, photobleaching was simulated 19 times. The number of spots per image was varied from 1 to 20 and the amount of added noise varied from 0 to 380%. Mean values were calculated from the different replicates and the value of k with the smallest SSE value was kept (Figure 3.17d). The plot shows that the number of spots per image influenced the correct determination of the subunit value k . Strikingly, with a relatively small number of spots per image, 5 in this simulation, one would get already a reliable estimate of the subunit stoichiometry up to noise values of 180%. The more spots per image analyzed, the less the subunit number determination is biased.

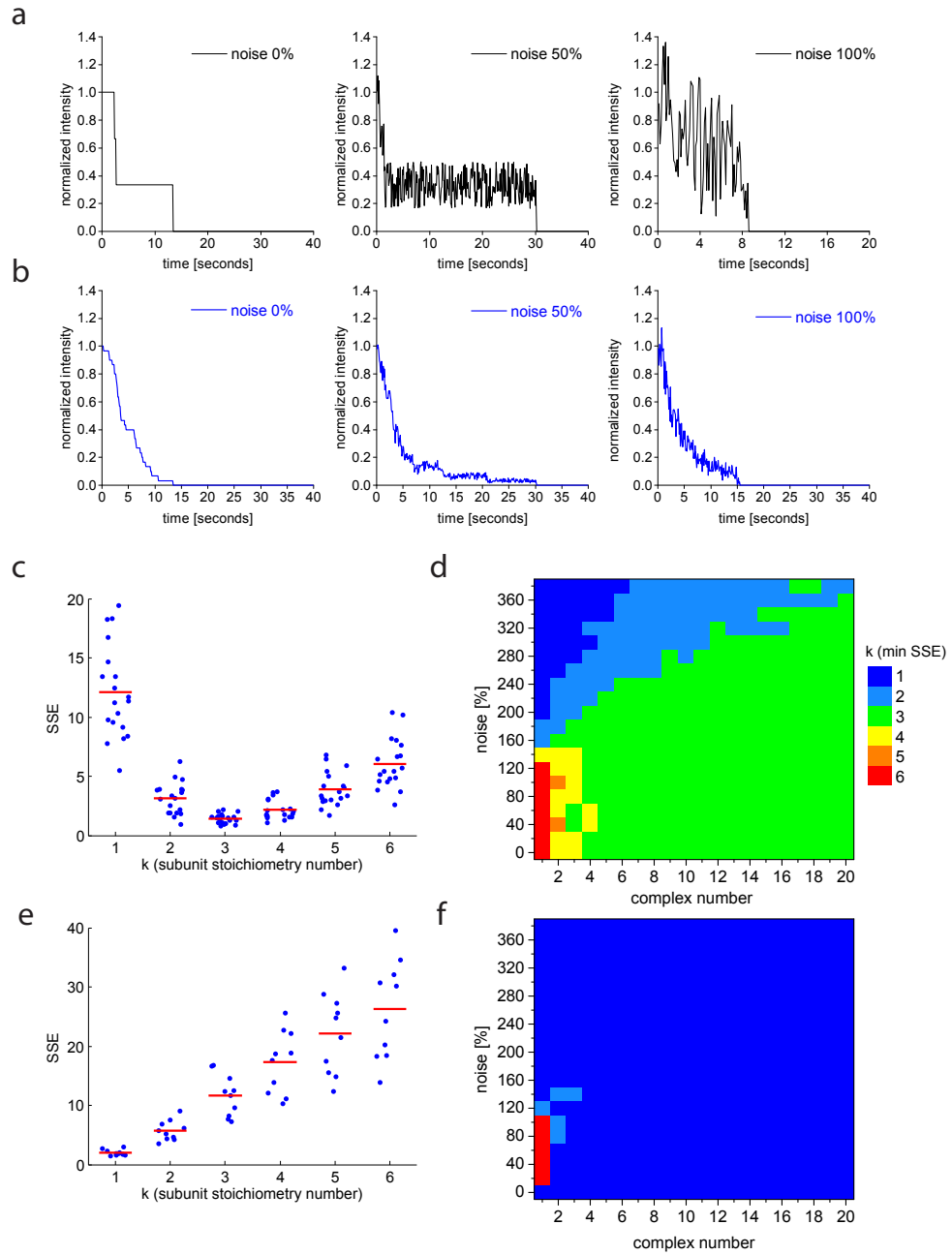


Figure 3.17: TIRFM photobleaching time-series simulation and analysis. (a-d) Simulation of complexes with subunit number $u = 3$. (a) Photobleaching of one trimeric complex having 0, 50 or 100% noise. (b) Average of photobleaching of 10 trimeric complexes having 0, 50 or 100% noise. (c) Photobleaching was simulated 19 times for 10 trimers, 100% noise was added. Theoretical number of complexes per image over time were calculated for different values of k . The sum of squared error ($SSE = \sum_{t=1}^{t_{last}} (N_{exp}(k; t) - N_{measured}(u; t))^2$) for each simulation is plotted together with the mean value of the replicates. (d) Photobleaching was simulated 19 times for different amount of noise. The value of k with the smallest SSE value is plotted in color-code. (e) Same as (c) but for subunit number $u = 1$, 10 replicates and 8 complexes each. (f) Simulations as in (d) and same color code, but for subunit number $u = 1$, 10 replicates and 8 complexes each.

Fluorescence probability or maturation of GFP

It can happen that within the population of mGFP molecules not all molecules display the ability to fluoresce. Reasons for this can be incomplete maturation or folding of the protein and the chromophore. This might be particularly present for proteins expressed on the plasma membrane where the photobleaching experiment is performed at a time where proteins are constantly expressed and the kinetics of protein maturation are coming into play. Another source would be the extraction of recombinant proteins from bacteria, which might result in partial destruction of the fluorescent protein due to potentially harsh mechanical and detergent dependent stresses. These problems might be less apparent in the here studied system where proteins were expressed and secreted in a human cell line and gently purified by affinity chromatography.

Nevertheless, to test the robustness of the LiSA method, I simulated trimers for different probabilities p to be fluorescent (for p see Figure 2.7, page 38). I found that the LiSA method would predict the correct subunit-stoichiometry of trimers for values of p in the range of 0.9 and 1.0 when no known fluorescence probabilities p are introduced to the model (Figure 3.18). For known fluorescence probabilities or maturation fractions, the LiSA method can also be applied by simply calculating the theoretical expected subunit stoichiometry and comparison to the data.

Another source would be cleavage of the fluorescent protein. In Figure 2.8 I have measured that purified mGFP-IZsCD95L showed partial cleavage of 8%. This value lies within the range of fluorescence probability values that would allow correct prediction of the subunit stoichiometry. However, different sources of lower p values cannot be excluded here. Nevertheless, the mGFP-IZ protein served as a reference for a trimeric protein to which flag-tagged mGFP, mGFP-sCD95L and mGFP-IZsCD95L proteins were compared.

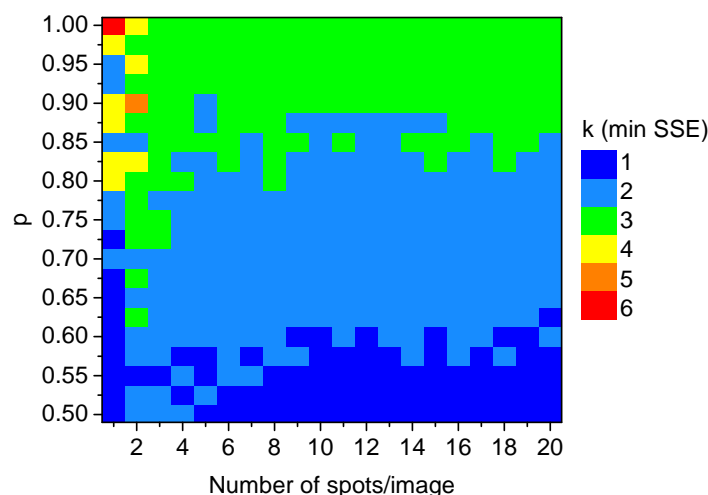


Figure 3.18: LiSA robustness. Photobleaching was simulated 20 times for different number of trimers "per image" and for different fluorescence probabilities p and by adding 100% noise. Theoretical number of complexes per image over time were calculated for different values of k . The value of k with the smallest mean SSE value is plotted in color-code.

Analysis of single molecule photobleaching data using LiSA

For the analysis, time-series images of 512x512 pixel were divided into smaller images so that 8 spots per image were present for mGFP, with a total number of 110 spots, and 10 spots per image were on average present for mGFP-sCD95L, mGFP-IZ and mGFP-IZsCD95L with total numbers of spots of 421, 261 and 196, respectively (Table 3.6). In order to determine the time-point when the spot is fully bleached (the "last step"), I chose the time-point when the fit failed twice in a row. I found that completed bleaching of the complex was thereby identified sufficiently reliably (see for example Figure 3.16).

By applying the LiSA method, I obtained theoretical dot-number distributions derived from the intensity decay. As an example, I overlaid those with the corresponding measured dot-number distribution for the different proteins (of each one image with 10 spots Figure 3.19). In those examples, the best match of the theoretical with the measured spot-number-decay was obtained with $k = 1$ for mGFP, and with $k = 3$ for mGFP-IZ, mGFP-sCD95L and mGFP-IZsCD95L (Figure 3.19). Furthermore, by analyzing all spots, for flag-mGFP spots the smallest mean SSE-value was obtained for a value of $k = 1$ while for the other three proteins mGFP-IZ, mGFP-sCD95L and mGFP-IZsCD95L a value of $k = 3$ best fit the data (Table 3.6, Figure 3.20). This indicated that flag-mGFP was identified as a monomer using this approach and revealed that those proteins form stable trimers at pM concentration.

To conclude, using the information of the time point of the last bleaching step from single molecule photobleaching data, a distribution can be generated that correlates to the intensity decay kinetic of the measured spots. Thus, to infer the subunit stoichiometry, knowledge of prior occurring bleaching steps becomes dispensable. Not least, the analysis was facilitated by using a powerful tool to extract intensities of photobleaching data in a straight-forward and fully automated manner so that finally, no measured trace was discarded.

Table 3.6: LiSA method results

k	mGFP	mGFP-IZ	mGFP-sCD95L	mGFP-IZsCD95L
1	3.2±1.6	9.7±5.5	14.9±14.8	8.4 ±6.4
2	3.3±2.4	3.0±2.2	5.2±6.8	2.4 ±2.1
3	5.4±4.6	1.5±1.0	3.7±3.2	1.8±2.0
4	7.8±6.8	2.0±1.5	4.9±3.6	2.9±3.1
5	10.0±8.8	3.3±2.5	7.0±5.5	4.7±4.2
6	12.0±10.5	5.0±3.5	9.6±7.4	6.9±5.2
c	7.9±2.9	10.0±2.9	10.0±2.9	9.8±3.0
n_t	110	261	421	196

k = tested subunit number, mean \pm s.d. of SSE.

c = number of complexes per image, mean \pm s.d., n_t = total number of spots quantified.

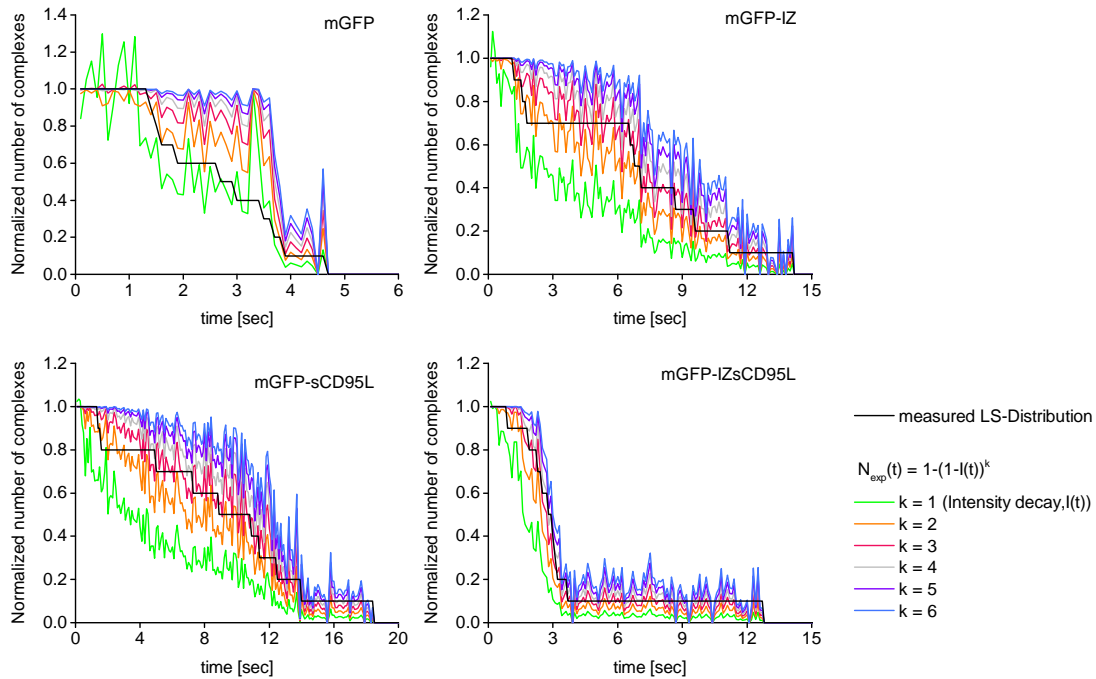


Figure 3.19: LiSA method results - spot numbers over time. One analyzed sub-image with mGFP, mGFP-sCD95L, mGFP-IZ or mGFP-IZsCD95L, respectively. Each of these images contained 10 fluorescent spots. The last-step (LS)-distribution is the number of detected complexes on the image over time (black line). Colored lines = expected LS-distributions calculated from the average fluorescence intensity decay of the spots $I(t)$ using the formula $N_{exp}(t) = 1 - (1 - I(t))^k$ for different values of k .

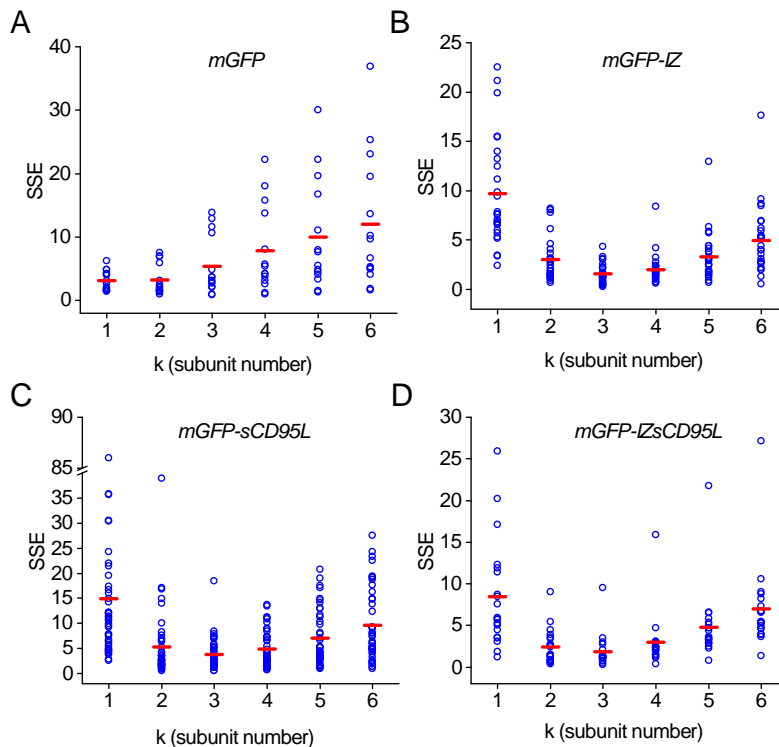


Figure 3.20: LiSA method results - SSE values. (a) mGFP, (b) mGFP-IZ, (c) mGFP-sCD95L and (d) mGFP-IZsCD95L, SSE = Sum of Squared Errors. Blue circles indicate SSE result of one sub-image, the red bar indicates the mean of those values.

3.4 Measurement of caspase activity, cell death and ligand-receptor binding kinetics by time-lapse confocal microscopy

In the next sections of my work, results on CD95L affinity, CD95 receptor occupancy and apoptosis induction and the impact of internalization on cell death of CD95L in HeLa cells are presented. The motivation was to understand how CD95L transmits the apoptotic signal to the cell. In line with the loss of apoptotic activity of CD95L upon cleavage into sCD95L, it was reported that low doses of CD95 activation can induce non-apoptotic pathways while high doses of ligand rather lead to cell death (Lavrik et al. 2007). Thereby both, the membrane and soluble form of CD95L are thought to bind the receptor CD95 but transmit different signals to the cell. Moreover, we observed that apoptosis can be triggered in HeLa that expresses ten times more CD95 receptor than HeLa cells (HeLa-CD95) not only by the strong inducer IZsCD95L, but also by sCD95L. By investigating why sCD95L is a weak inducer of apoptosis, I aimed at contributing to the understanding of CD95 apoptosis induction.

3.4.1 The relation between caspase-8 onset time and strength to cell death is independent on the affinity and cross-linking state of ligand

The definition of an activated receptor in the context of CD95 is not unique. For example, one can define an activated receptor as a receptor that is bound to ligand. Alternatively, an activated receptor could be defined as a receptor that is able to recruit downstream molecules such as FADD and caspase-8. In turn, recruitment of FADD must not necessarily result in caspase-8 activation. However, the presence of active enzyme implies ligand-receptor binding and receptor activation. As a first step, I assumed that the amount of active enzyme, measured by cleavage of reporter proteins, is correlated to the amount of activated receptors.

I tested whether sCD95L and IZsCD95L differently activate the pathway through CD95 by comparing caspase-8 substrate cleavage rates, onset times and cell death kinetics. Different receptor activation mechanisms would be concluded if cell death times were the same but one ligand shows a late onset together with a strong cleavage rate while the other ligand shows an early onset together with a modest rate. Equal receptor activation mechanisms should show the same onset time of activity and the same cleavage rate for equal cell death times.

To test these possibilities, I assessed caspase-8 activity in HeLa cells and HeLa-CD95 cells upon sCD95L and IZsCD95L stimulation by using a fluorescent reporter containing the ELQTD-cleavage site of the protein Bid. I first used the membrane-localized probe MyrSnap2-ELQTD-YFP because this reporter was shown to be more sensitive to caspase-8 activity (Beaudouin et al. 2013). I applied three to four different doses of sCD95L, IZsCD95L and antibody-cross-linked sCD95L as a continuous stimulus to cells.

While IZsCD95L efficiently induced caspase-8 activity in both cell lines, sCD95L only activated caspase-8 in HeLa-CD95 cells but not in HeLa cells at concentrations up to 2.8 µg/ml (Figure 3.21a-c). As expected (Holler et al. 2003), secondary cross-linking of sCD95L trimers using FLAG-antibody led to efficient caspase-8 induction of HeLa cells (Figure 3.21d,h).

The following paragraph describes details of these results. Using 0.1, 1.0 and 2.8 µg/ml of IZsCD95L, HeLa-CD95 cells and HeLa cells showed mean substrate cleavage rates of 0.11, 0.41 and 0.41 arb.u./minute and 0.05, 0.21 and 0.22 arb.u./minute, respectively (Figure 3.21a-b). The observed constant mean rate values for increasing ligand concentration imply that the maximal possible amount of active enzyme was reached. Besides the substrate cleavage rate, the onset of caspase-8 activity was also extracted from the fit (Figure 3.21e-f). For increasing concentrations using 0.1, 1.0 and 2.8 µg/ml IZsCD95L, the onset of caspase-8 activity in HeLa-CD95 cells were measured at 61, 25 and 20 min and in HeLa cells at 80, 37 and 21 min. This shows that the receptor level of the cell determined the amount of activated caspase-8.

Regarding the weak inducer sCD95L, mean rates of caspase-8 substrate cleavage in HeLa-CD95 cells using 0.1, 1.0 and 2.8 µg/ml continued increasing from 0.04 to 0.18 to 0.25 arb.u./minute, respectively (Figure 3.21c). sCD95L neither induced cell death nor MyrSnap2-ELQTD-YFP substrate cleavage at these concentrations in HeLa cells.

Nevertheless, the activity of sCD95L could be increased by secondary cross-linking. The mean rates using 0.1 µg/ml and 1 µg/ml were 0.04 and 0.1 arb.u./minute, respectively. For higher concentrations, 1.8 µg/ml and 2.8 µg/ml, the mean rates dropped to 0.09 and 0.08 arb.u./minute, respectively (Figure 3.21d). This inverse correlation of concentration and caspase-8 substrate cleavage rate, resulting in a bell shaped response, indicates that with increasing concentration less receptor on the cell membrane contributed to pathway activation. This behavior can be seen for multivalent ligand-receptor interactions: several receptors can be cross-linked with each other by one single multivalent ligand. However, saturation of receptor binding sites at high ligand concentrations can block their cross-linking (Lauffenburger and Lindermann 1996).

An inverse correlation was not observed for the onset of activity and increasing ligand doses: HeLa-CD95L and HeLa cells stimulated with increasing concentrations of sCD95L and secondary cross-linked sCD95L, respectively, showed caspase-8 activity continuously earlier, namely at 187, 56 to 35 min and at 95, 50, 43 to 43 min, respectively (Figure 3.21g-h). This suggests that not the binding but the formation of active receptor species was limited with increasing ligand concentrations.

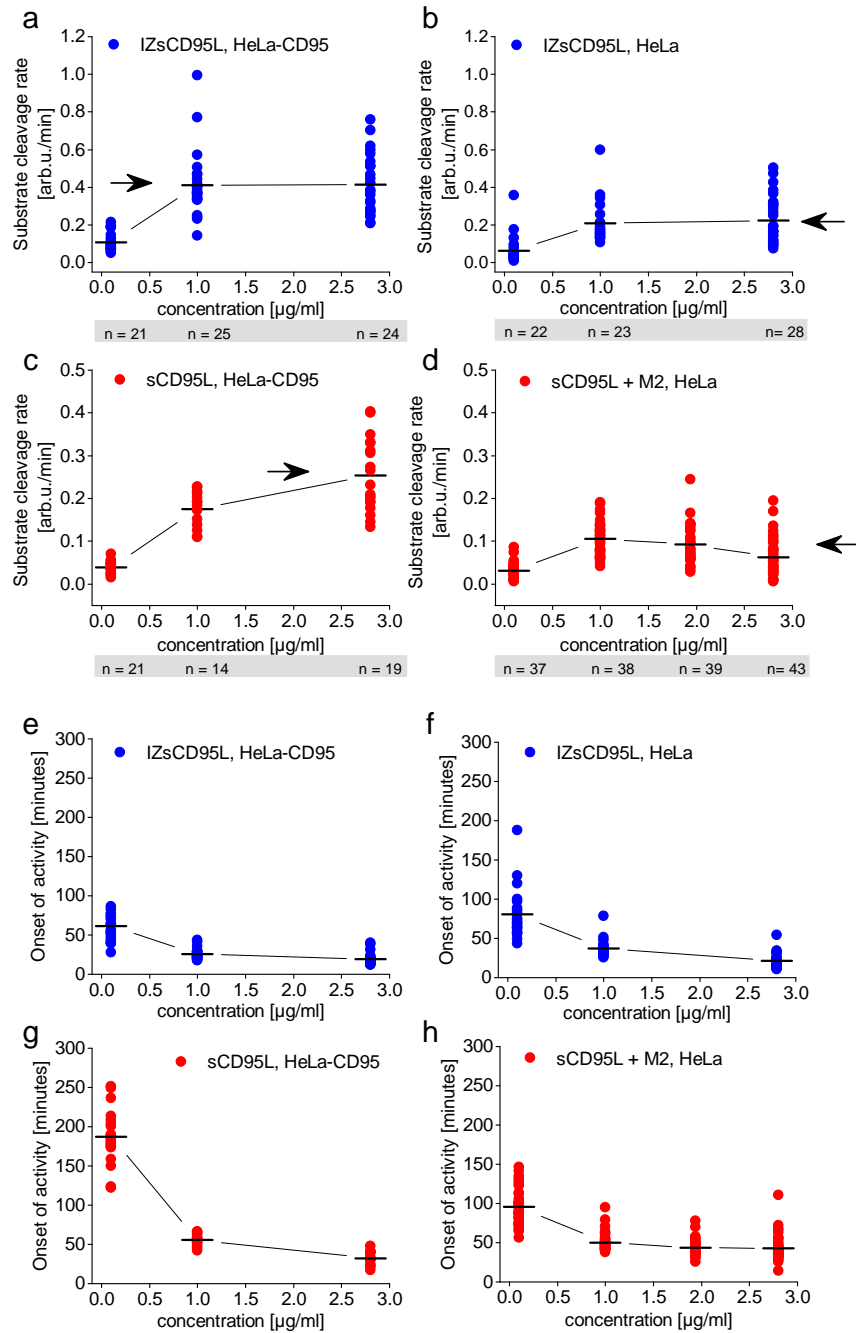


Figure 3.21: caspase activity upon sCD95L and IZsCD95L in HeLa and HeLa-CD95 cells. HeLa or HeLa-CD95 cells transiently expressing MyrSnap2-ELQTD-YFP were stimulated with different doses (0.1 μg/ml, 1 μg/ml or 2.8 μg/ml) of sCD95L, IZsCD95L or sCD95L plus 5 μg/ml Flag-M2 antibody and imaged using a confocal microscope over time. (a-d) ELQTD-substrate cleavage rates and (e-h) onset of ELQTD-substrate cleavage obtained from fit of time-series data (section 2.2.3). The number n of analyzed cells is indicated. (a,e) HeLa-CD95 cells were induced with IZ-sCD95L. (b,f) HeLa cells induced with IZsCD95L. (c,g) HeLa-CD95 cells induced with sCD95L. (d,h) HeLa cells induced with sCD95L plus M2 antibody.

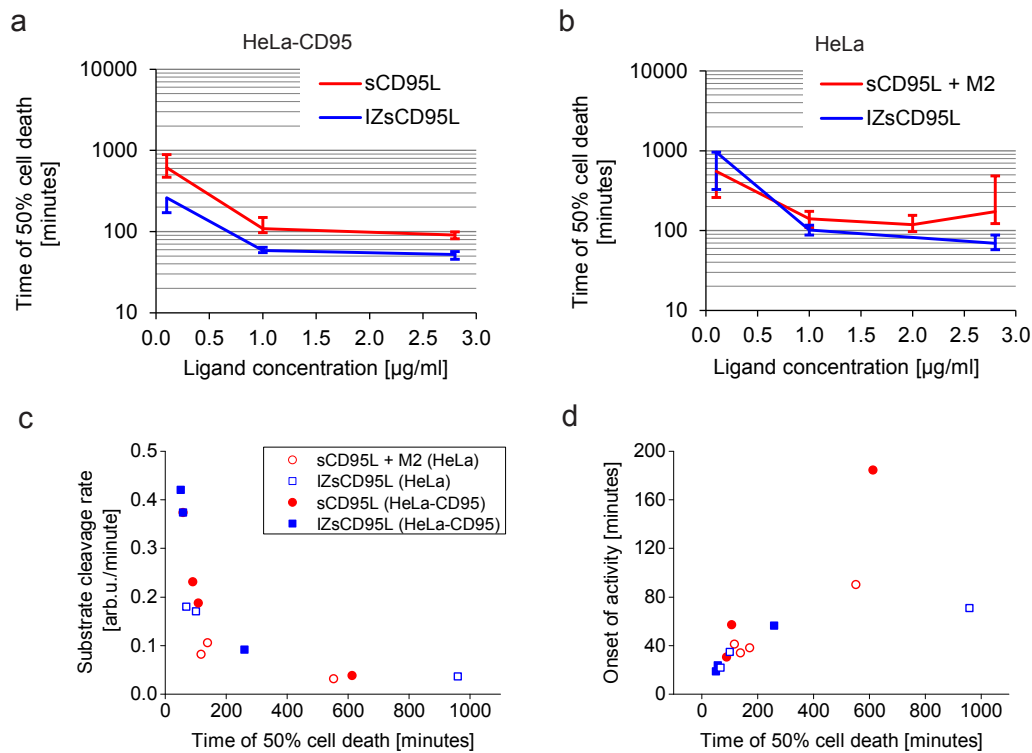


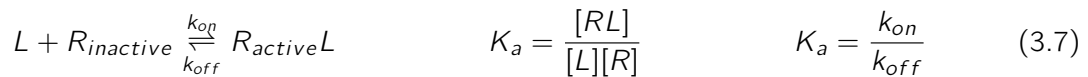
Figure 3.22: Correlation between caspase-8 activity with time of death. (a-b) Time of 50% cell death in HeLa-CD95 and HeLa cells plotted against ligand concentration. (c-d) The mean values of caspase-8 substrate cleavage rate or the onset of activity plotted against the measured time of 50% cell death for the different ligand stimuli and different cell lines.

Strikingly, the mean caspase-8 substrate cleavage rates measured for sCD95L induced cells compared to the mean rates for IZsCD95L induced cells seem to converge towards different values, namely 0.3 and 0.4 arb.u./minute in HeLa-CD95 cells and 0.2 and 0.1 arb.u./minute in HeLa cells, respectively (see black arrows in Figure 3.21). Similarly, the time of death seemed to converge towards a different, later time point with increasing concentrations of sCD95L compared to IZsCD95L (Figure 3.22a). While IZsCD95L induced death in HeLa-CD95 cells within 50 min, sCD95L required at least 100 min. Together with the observations of caspase-8 substrate cleavage, this indicates that the rate of caspase-8 cleavage, but not the onset time, determined the time of death.

To check whether sCD95L and IZsCD95L killed cells through different mechanisms, I correlated the median time of death with caspase-8 cleavage rates and onset times for both ligands (Figure 3.22). While the functional relationship between the rate of substrate cleavage and time of 50% cell death was hyperbolic (Figure 3.22c), the relation between the onset of caspase-8 activity and the time of death looked linear for short time of cell death (Figure 3.22d). This indicated that the amount of caspase-8 (rate) and the start of activity (onset) correlated with the time of cell death independently of the form of ligand.

These data would speak against a simple binding mechanism, with a single on-rate and a single off-rate, in which bound receptors correspond to activated receptors (Eq.: 3.7). In a simple binding-receptor activation model, increasing concentrations of sCD95L can lead to same cell death time as with IZsCD95L on HeLa-CD95 cells because for high concentrations, binding is mostly dependent on the on-rate, which, if different for the two different ligands, can be compensated by adjusting the ligand concentration.

Simple binding-activation model



To confirm these data and to test whether a simple binding can be excluded, the experiment has been repeated with a broader concentration range, using purified IZsCD95L and mCherry-sCD95L and also non-purified mCherry-IZsCD95L. To measure caspase-8 activity, the soluble-cytosolic probe NES-ELQTD-mGFP was used in this experiment which is easier to quantify while the sensitivity of the probe is sufficiently high.

I was able to confirm the linear correlation between the onset of activity and cell death time as well as the hyperbolic shape of the relation between the rate of substrate cleavage and time of death (Figure 3.23a,b). By covering a broader concentration range, I observed that 4 µg/ml of mCherry-sCD95L induced 50% of the HeLa cells after 8 hours and using 50 µg/ml after 3.5 hours (Figure 3.23g). Moreover, I observed that HeLa-CD95 cell death times showed a plateau of the median cell death time at 38 min with IZsCD95L using concentrations between 1 and 15 µg/ml (Figure 3.23g), consistent with data from the first dose-response experiment. In line, HeLa-CD95 cells exposed to sCD95L or mCherry-sCD95L required at least 70 min to undergo cell death with concentrations up to 50 µg/ml (Figure 3.23g).

This saturation behavior was also reflected in single cell measurements of the fluorescent reporter NES-ELQTD-mGFP. With increasing ligand concentration, mean substrate cleavage rates in HeLa-CD95 cells saturated at a value of 0.04 and 0.02 arb.u./minute using IZsCD95L and mCherry-sCD95L, respectively (Figure 3.23c). The corresponding onsets showed a plateau at 15 and 35 min, respectively (Figure 3.23d). Similarly, rates and onsets showed a plateau at lower values in HeLa cells than in HeLa-CD95 cells treated with IZsCD95L, namely at 0.025 arb.u./minute and at about 30 min. This can be explained by the lower receptor level of HeLa cells (Figure 3.23e,f). Together, this indicated that the apparent weak affinity of soluble CD95L cannot be compensated by using higher ligand concentrations to reach the activity observed with IZsCD95L. From this, a simple-binding model in which bound receptors correspond to activated receptors would be excluded (Figure 3.24a).

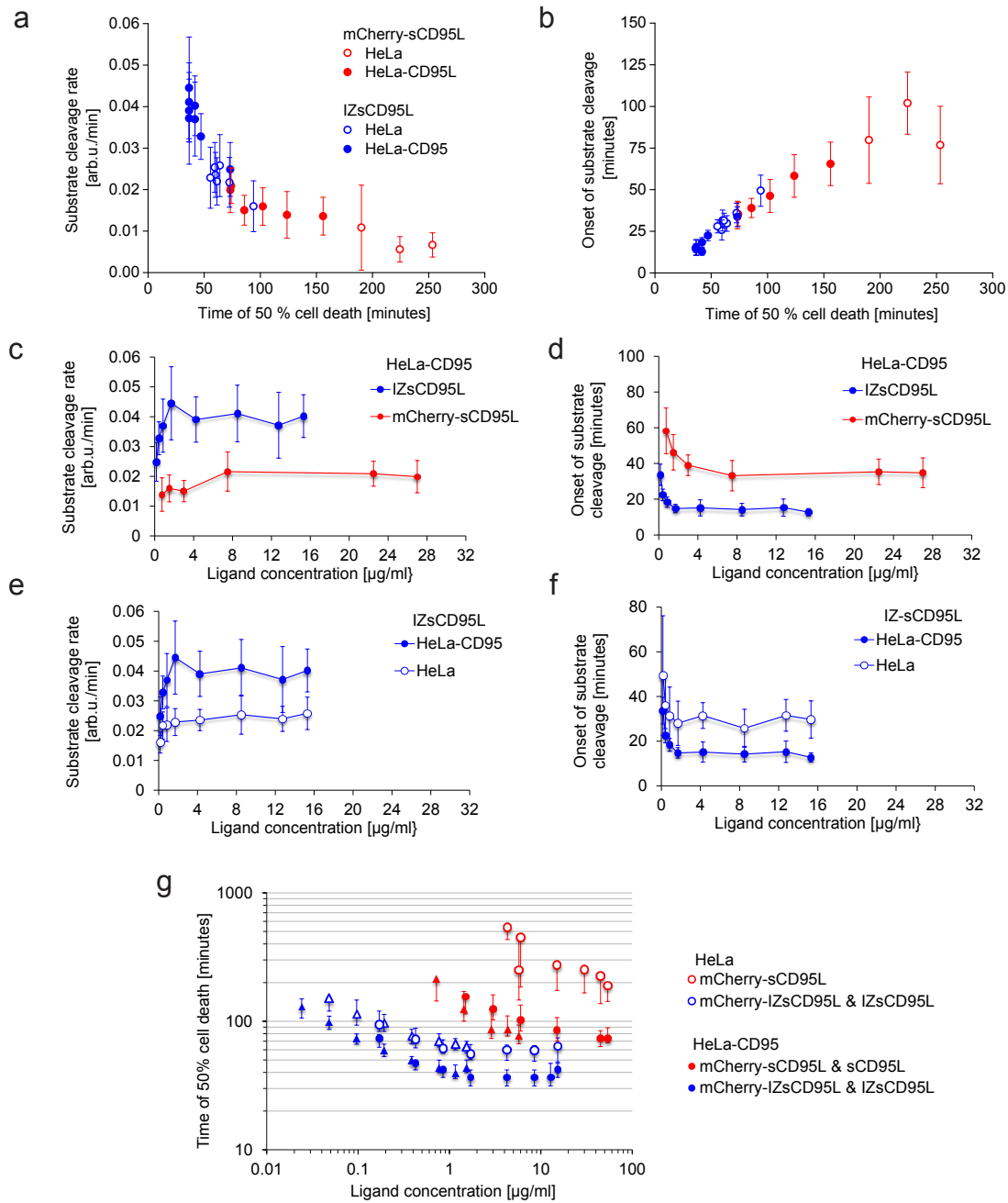


Figure 3.23: sCD95L-mediated caspase-8 substrate cleavage and cell death are confined HeLa and HeLa-CD95 cells expressing transiently the reporter NES-LQTD-mGFP were stimulated with different doses of mCherry-sCD95L or IZsCD95L. (a-f) The mean and s.d. of estimates (fit) of the substrate cleavage rate (a,c,e) and onset of activity (b,d,f) of $n=15$ to 25 cells for each concentration. (g) HeLa cells or HeLa-CD95 cells, stimulated with non-purified mCherry-IZsCD95L or purified preparations of sCD95L, mCherry-sCD95L or IZsCD95L. Shown is the time of 50% (circle), 25% and 75% (bars) cell death (% of total cells, $n = 150$ to 250 cells per condition, 75% shown in case data were available).

How could sCD95L and IZsCD95L differently activate the receptor?

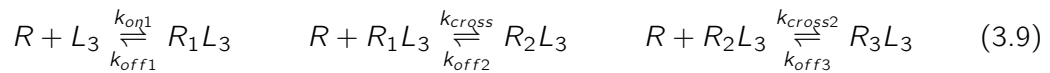
With the previous data it has been realized that caspase-8 was much less efficiently activated with sCD95L than with IZsCD95L. The ability of sCD95L to activate caspase-8 seemed to be limited by events upstream of caspase-8 in the signaling cascade, for example receptor binding or FADD-recruitment.

The simple binding model does not exclude the possibility that binding and activation of single receptors are two different events. Thus, receptors can be assumed to be present in two different ligand-bound states. Equation 3.8 describes such a case, with a simple ligand-receptor interaction followed by a reaction for receptor activation for example by a conformational change k_{conf} . For IZsCD95L this reaction might be more favorable than for sCD95L and would allow more efficient FADD recruitment (Figure 3.24b).

Simple binding-two receptor states model (SB2RS)



Ligand-induced receptor trimerization model (LIRT)



As sCD95L is a trivalent ligand, a stepwise binding of monomeric CD95 receptors to ligand was another conceivable model for receptor activation (Equation 3.9, Figure 3.24c).

The hypothesis was that sCD95L potentially inefficiently trimerizes or cross-links receptors on the cell membrane. Defining only cross-linked receptors R_2L_3 or R_3L_3 but not singly bound ligand R_1L_3 as active species that are able to recruit FADD, the ligand-induced receptor trimerization model can be seen as a form of a two-state receptor model.

Compared to the simple binding model, in the ligand-induced trimerization model, six parameters appear, for the first reaction namely k_{on1} and k_{off1} that describe the binding of a trimeric ligand L_3 from the solution to a single receptor R on the membrane resulting in a ligand-bound receptor R_1L_3 on the membrane. Subsequent binding events on the plasma membrane can be described as follows: For the recruitment of another receptor to the ligand-receptor couple R_1L_3 , a parameter for the binding k_{cross} and for the unbinding k_{off2} can be assigned.

As a trivalent ligand, a third receptor can be recruited to the ligand on the membrane described by the parameters k_{cross2} and unbinding k_{off3} . A smaller trimerization model could be proposed by having a minimum of three parameters: assuming that unbinding events occur equally, one k_{off} value for all unbinding events can be assigned. For the binding a parameter k_{on} and for the two receptor recruitment events k_{cross} can be assumed.

Alternatively, assuming CD95 receptor dimers, binding of trimeric ligands can lead to receptor-clusters of indefinite size (Figure 3.24d).

In order to better describe why sCD95L is a weak inducer of apoptosis, I tested how CD95L binds to CD95 by conducting binding and unbinding experiments on cells.

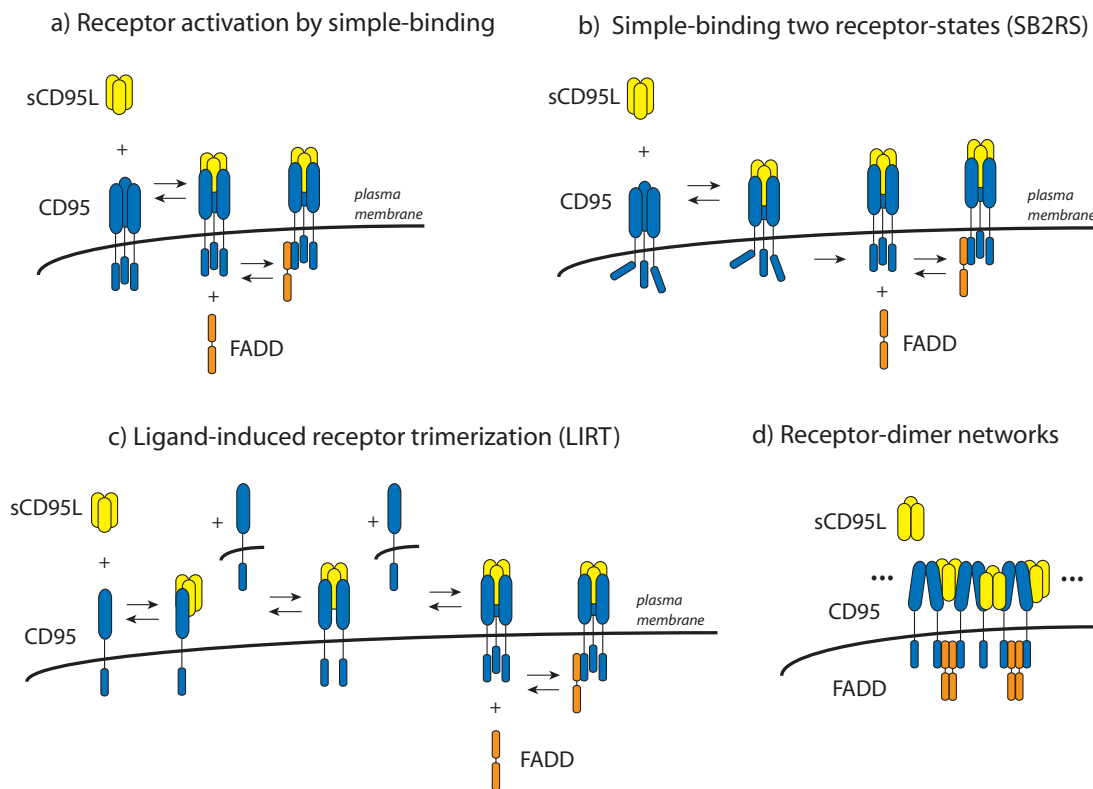


Figure 3.24: Models of CD95 receptor binding. (a) Simple 3:3 binding may directly lead to FADD recruitment. (b) Simple 3:3 binding and assuming that the receptor can be present in two different states. For example, for FADD recruitment a conformational change of the receptor might be required. (c) Ligand-induced receptor trimerization. Trimeric ligand could bind one receptor monomer. Step-wise recruitment of receptors would occur on the membrane. Only oligomerized, for example trimerized, receptor would recruit FADD. (d) Dimeric receptors cross-linked by trimeric ligands can lead to large receptor networks, as proposed in Naismith et al. 1995.

3.5 Binding affinity of soluble CD95L

Insights obtained from correlating cell death and caspase-8 activity measurements to different doses of the two forms of ligand showed that sCD95L inefficiently activates caspase-8, potentially by inefficient binding to the receptor. To test this hypothesis, I aimed at quantitatively characterizing the ligand-receptor interaction.

3.5.1 Set-up and analysis of binding experiments using confocal microscopy

To assess the binding strength of a ligand-receptor interaction, I used fluorescent proteins fused to the receptor and the ligand. Receptors tagged with mGFP at the cytosolic domain stably expressed in HeLa cells (HeLa-CD95-mGFP cells) can be well detected by confocal microscopy. Differences in cell death and caspase-8 activation of HeLa-CD95 cells between the two ligand forms were observed in the range of 1 µg/ml of ligand. Thus, for purposes of correlating binding data to activity data, ligand and receptor concentration ranges were suitable for binding experiments by fluorescence microscopy.

Concentration range: Assuming a molecular weight of about 150 g/mol for a trimer of mCherry-sCD95L, 1 µg/ml corresponds to about 6.7 nM. In a typical experiment, about 3×10^4 cells were exposed to 0.3 ml ligand. Thus, 0.3 ml of a 1 µg/ml ligand solution contained about 12×10^{14} ligand molecules. Assuming a cell surface of about $2000 \mu\text{m}^2$ and a receptor density of 100 molecules/ μm^2 , total cell surfaces encompassed about 6×10^9 receptor molecules. For the here given values, one would obtain a ratio of 2×10^5 ligand molecules per receptor. Therefore, ligand molecules were most likely in large excess in my experiments. Limited binding due to ligand depletion was not expected and the binding rate was assumed to be not diffusion-limited.

Calibration: As fluorescence of different spectra can be distinguished simultaneously on living cells, the receptor on the cell as well as the ligand in solution were tagged with mGFP and mCherry, respectively. A one-to-one labeling of the ligand or receptor allowed quantifying amounts of ligand relative to receptor amounts. For such ratio-metric measurements, the microscope needed to be calibrated. This was achieved by expressing a protein fused to both, mGFP and mCherry in HeLa cells. Among different tested constructs, the fusion protein mCherry-Bid-mGFP containing the full length protein Bid was used and the microscope was set-up so that fluorescence from both, mCherry and mGFP, looked similar in brightness. With the transient expression of proteins usually different protein levels among different cells are obtained. Quantification yielded a very clean linear correlation between mGFP and mCherry fluorescence (see for example Figure 3.30). Quantification of the calibration measurements, fit to a linear model ($Intensity_{mGFP} = a \times Intensity_{mCherry} + b$) and correction of the receptor occupancy

using the slope a was made offline. This also allowed to compare experiments from different days and to quantify the ligand-receptor ratio in an absolute way.

Background intensity: My goal was to measure the ligand bound to the receptor on the surface of the cell. Importantly, the ligand can also be seen next to the cells in solution (Figure 3.25). This means that the ligand signal on the cell is contaminated with signal of ligand in solution, which cannot be easily subtracted. Specific binding of ligand was therefore assessed by washing cells twice with medium before imaging. Otherwise, in time series images, only intensities above levels detected next to the cell were considered to be specific binding.

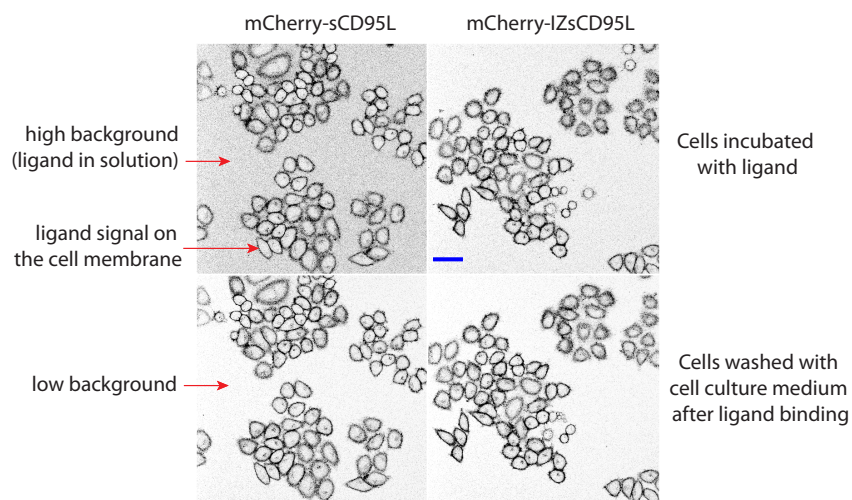


Figure 3.25: Ligand binding measurements by confocal microscopy - ligand background. Fluorescence of mCherry detected by confocal microscopy (40x objective, zoom1 and pinhole 1.8). The optical section visualizes ligand staining on the cell (signal), but also ligand in the solution next to the cell. Having high background, the signal on the cell is in principle not unambiguously identified. Washing of cells removes non-receptor bound ligand. mCherry-sCD95L = 6.4 $\mu\text{g/ml}$, mCherry-IZsCD95L = 1.8 $\mu\text{g/ml}$. Scale bar = 50 μm .

Image Analysis: Receptor and ligand intensities were analyzed by a semi-automated image segmentation sequence that I wrote as a Plugin for ImageJ. Briefly, in the image analysis, receptor intensities were segmented using the default thresholding algorithm from ImageJ which iteratively finds the threshold value t that is larger than the sum of the average value of pixels smaller than t and the average value of pixels greater than t , divided by 2 (Rasband 1997-2014).

For the analysis of an image containing about 40 cells, I chose several fields of cells displaying each similar receptor intensities (Figure 3.26). This guaranteed not to bias the thresholding towards bright cells within the image.

From those sub-images, a mask was created reflecting the area where binding of ligand would be expected. Receptor and ligand intensities of the image as well as the area of the mask were then extracted to calculate the mean intensities. I noticed that in stable cell lines, the mGFP-tagged CD95 receptor is also visible in the endoplasmic reticulum. When binding estimates only for the

cell membrane were required, the interior of the cell was excluded manually from the segmented image samples.

To conclude, using this approach the amount of ligand bound to receptor on the surface could be measured from images acquired by confocal microscopy. The ratio of those reflects the receptor occupancy or the apparent binding of the ligand to the receptor.

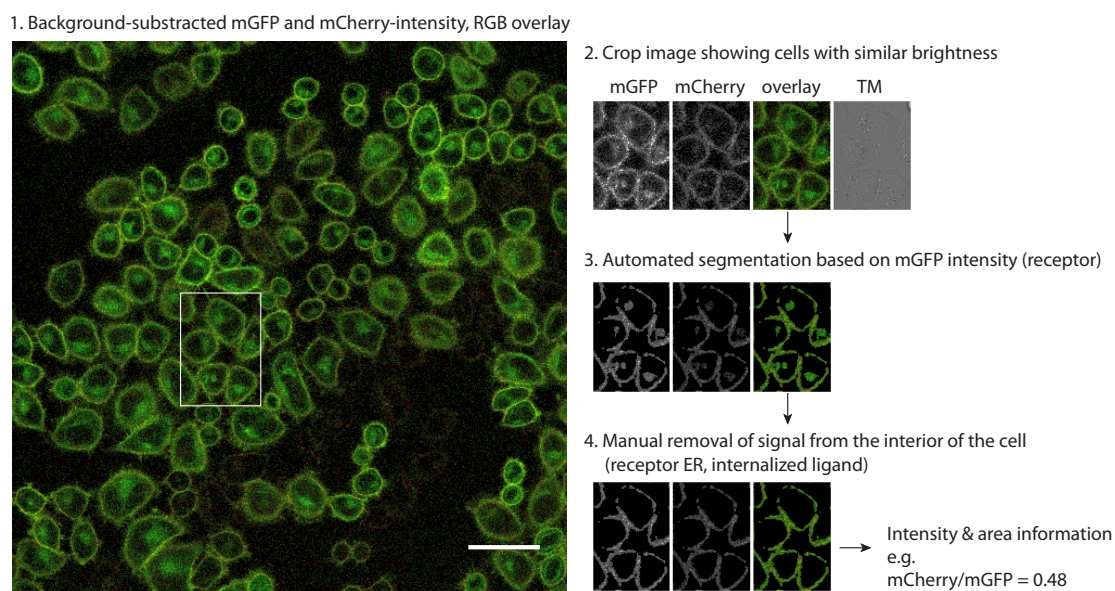


Figure 3.26: Binding measurements by confocal microscopy - image analysis. Fluorescence of CD95-mGFP and mCherry-sCD95L detected by confocal microscopy (40x objective, zoom1 and pinhole 1.8). Different steps are described to obtain the ratio of ligand over receptor from images. Scale bar = 50 μ m.

3.5.2 Binding of mCherry-sCD95L is efficient

CD95L is a trivalent ligand able to bind three CD95 molecules. The binding of the ligand can therefore be described by an apparent affinity that relates to the receptor occupancy for a multivalent binding mechanism. First, in order to estimate this receptor occupancy for the two different ligands mCherry-sCD95L and mCherry-IzCD95L, time-series data were acquired for different concentrations of ligand. For example, by using 1.4 μ g/ml mCherry-sCD95L and 0.4 μ g/ml mCherry-IzCD95L binding of the ligands to HeLa-CD95-mGFP cells looked similar (Figure 3.28a). Overall, the kinetics of binding looked like an exponential recovery and no difference in the shape of binding between the ligands could be observed.

Furthermore, I observed in time-series images that a portion of ligand gradually appeared inside the cell indicating internalization of ligand. In order to obtain the receptor occupancy at the plasma membrane for the two different ligands, I measured binding after 10 min of a continuous ligand stimulus when ligand internalization was visibly low.

Figure 3.27 shows the receptor occupancy as a function of ligand concentration. The data clearly

show that lower concentrations of mCherry-IZsCD95L were required than of mCherry-sCD95L to reach the same receptor occupancy. The factor in concentration required to obtain same apparent binding was around 3. Strikingly, this factor was small compared to the observed differences in activity that were shown in the previous part (see Figure 3.23g).

In order to test whether binding of the ligand is enforced by recruitment of downstream signaling proteins such as FADD, binding was assessed in HeLa cells stably expressing the receptor CD95- Δ DD-mGFP at equal receptor levels as HeLa-CD95-mGFP cells (Figure 3.27a). Interestingly, no difference in binding compared to HeLa-CD95-mGFP cells was observed in this cell line for mCherry-sCD95L and mCherry-IZsCD95L, respectively (pink and green data points compared to black and blue data points Figure 3.27b). This indicates that the avidity of the ligand is independent of downstream events.

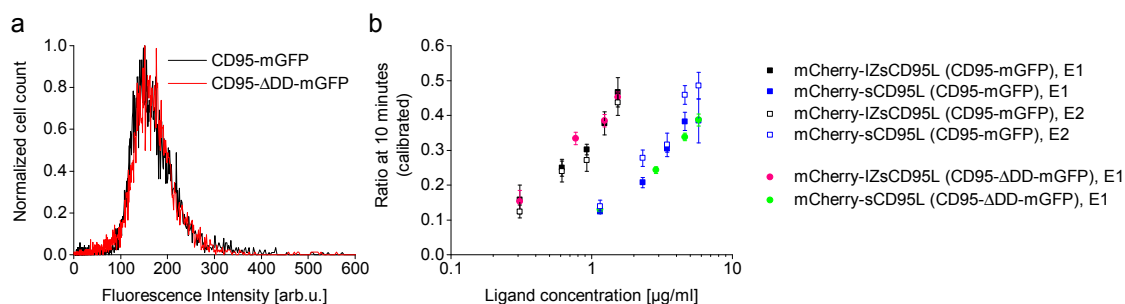


Figure 3.27: CD95-mGFP and CD95- Δ DD-mGFP bind the two different ligands equally well. (a) Flow cytometry detecting mGFP fluorescence, HeLa-CD95-mGFP = black, HeLa-CD95- Δ DD-mGFP = red (b) HeLa cells stably expressing CD95-mGFP or CD95- Δ DD-mGFP were incubated for 10 min with different concentrations of mCherry-sCD95L or mCherry-IZsCD95L at 37°C. Specific binding was measured after washing cells twice with medium followed by image acquisition. E1 = Experiment1, E2 = Experiment2.

Together with knowledge from the previous parts, it was expected that the activities of mCherry-sCD95L and mCherry-IZsCD95L are still different at concentrations used where apparent binding looked equal. To confirm this in HeLa-CD95-mGFP cells, caspase-8 and cell death activities were measured in such conditions. By using a new batch of the two ligands, same apparent binding of the two ligands was assessed. To do so, binding was first measured for different amounts of ligand at time point $t = 10$ min and then using about 1.8 μ g/ml mCherry-IZsCD95L and 6.4 μ g/ml mCherry-sCD95L at 2.5 min, 5 min and 15 min (Figure 3.28b,c). 50% cells stimulated with 1.8 μ g/ml mCherry-IZsCD95L died after 50 min and showed an early onset of reporter cleavage at 10 min (Figure 3.28d,e). In contrast, mCherry-sCD95L induced cells died clearly much later, the median cell death time being 2h 30 min, and showed an onset of reporter cleavage at 50 min (Figure 3.28e). Besides, also the rate at which the reporter was cleaved was higher in cells stimulated with mCherry-IZsCD95L. This indicated that less caspase-8 was activated with mCherry-sCD95L despite efficient binding. Moreover, the delay in caspase-8 activation cannot be explained by a simple delay in binding.

To summarize, the observed difference in activity could not be compensated by ligand concentrations that lead to equal apparent binding. Together with the observation that increasing concentrations of sCD95L did not reach same cell death times as with IZsCD95L, these data speak against a simple binding-activation model in which bound receptors would reflect activated receptors.

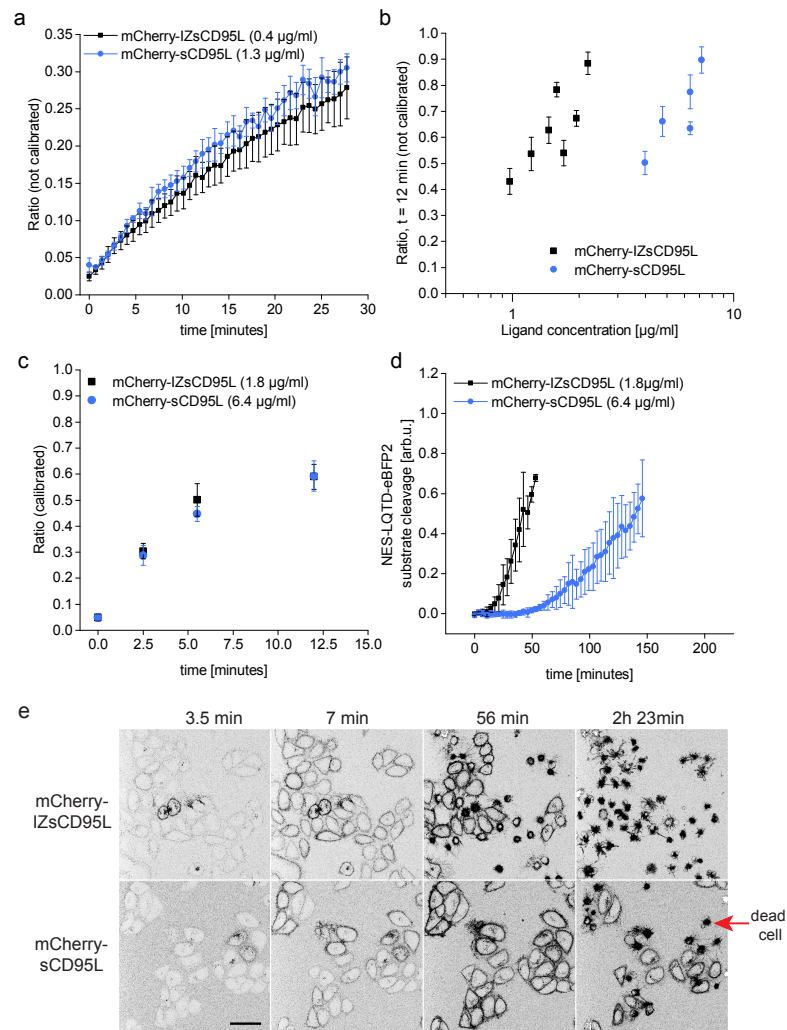


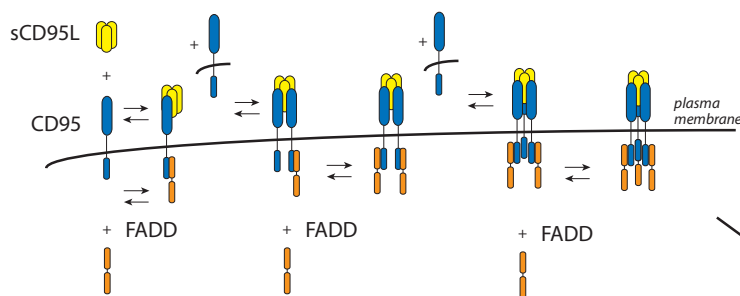
Figure 3.28: Different activities despite same apparent binding. (a) Receptor occupancy over time with continuous ligand stimulation, image quantification was not background corrected, note the similar binding behavior of the two ligands. (b) Receptor occupancy for different ligand concentrations at time point $t = 12$ min. (c) Receptor occupancy over time for higher ligand concentrations than shown in (a) and measured for individual time points after washing cells twice with medium. Intensities were calibrated. (d) Quantification of NES-LQTD-eBFP2 redistribution, mean and s.d. of 12 (mCherry-sCD95L) and 15 (mCherry-IZsCD95L) single cell measurements using HeLa-CD95-mGFP cells. The mean end point reflects approximately the median time of cell death. (e) Snap-shots of time-series data, indicated is the time upon addition of ligand, continuous ligand stimulation, 1.8 $\mu\text{g/ml}$ mCherry-IZsCD95L and 6.4 $\mu\text{g/ml}$ mCherry-sCD95L was used. Scale bar = 50 μm .

3.5.3 The adaptor protein FADD is inefficiently recruited by sCD95L

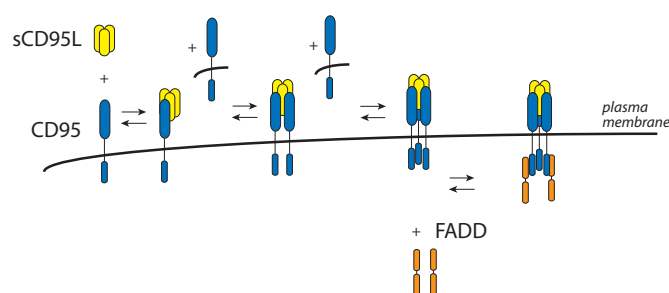
Results obtained from binding measurements suggest that the weak capacity of sCD95L to induce apoptosis is potentially caused by a lack of ability to induce further rearrangements of the receptor upon binding to the receptor. In line, eventual CD95 conformational changes were proposed next to the observation of high-order interactions between the death domains of CD95 and FADD (Hymowitz and Dixit 2010, Sandu et al. 2006, Scott et al. 2009, see also Figure 1.5). As close proximity of CD95 receptor and FADD clusters are thought to be required for efficient caspase-8 activation, two different models of FADD recruitment are conceivable: Assuming the ligand-induced trimerization model for ligand binding, one idea was that every bound receptor can recruit one FADD molecule (Illustration 1a in Figure 3.29). In this model, the resulting CD95L/CD95/FADD-cluster size would define caspase-8 activation efficiency. The alternative hypothesis was that FADD is only recruited to ligand-bound receptors that are at the same time sufficiently activated (Illustration 1b in Figure 3.29). In this model, receptor oligomerization would cause FADD recruitment and as a consequence of this caspase-8 activation.

Ligand-induced receptor trimerization (LIRT)

1a) FADD is recruited to ligand-bound receptors



1b) FADD binds only to receptor clusters



2) Caspase-8 recruitment to and activation in CD95/FADD-clusters

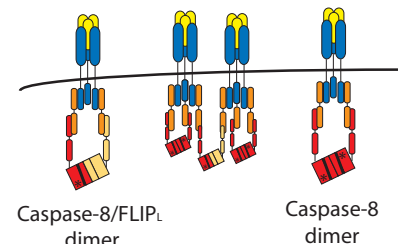


Figure 3.29: Models of FADD recruitment. Ligand binding to receptors on the cell surface is assumed to occur stepwise. (1a) Model assuming that each ligand-bound receptor can recruit FADD molecules. (1b) Model assuming that FADD is recruited only to receptors that are sufficiently cross-linked. (2) Caspase-8 and FLIP_L would be recruited to and activated in CD95-FADD complexes that are sufficiently oligomerized not excluding cooperative binding of those molecules.

In both models, only close proximities of FADD would allow dimerization of caspase-8 with another caspase-8 molecule or with FLIP_L which is necessary for activation and processing of caspase-8 (Illustration (2) in Figure 3.29). In order to test the two hypothesis for FADD-binding, I aimed at quantifying the amount of FADD recruited to the receptor upon ligand induction. For this, I applied two different approaches. The first approach was immunoprecipitation of ligand bound to cells and the second approach was time-lapse microscopy of FADD-mGFP.

Immunoprecipitation of ligand-bound receptors

By comparing the relative amounts of FADD recruited to receptors for cells showing same apparent binding of mCherry-sCD95L and mCherry-IZsCD95L to HeLa-CD95-mGFP cells, the two models should be discriminated: In case FADD is recruited independent of receptor activation, same amounts of FADD should be immunoprecipitated. Otherwise, in case of receptor-activation dependent FADD recruitment, different amounts of FADD relative to receptor would be expected.

Compared to microscopy-based experiments, about 250 times more cells (8×10^6 cells) are required for one experimental condition in immunoprecipitation (IP) experiments. Thus, equal apparent binding at 20 min was assessed by testing different dilutions of ligand using microscopy. Then, I chose ligand concentrations of mCherry-sCD95L and mCherry-IZsCD95L that showed a receptor occupancy of 30% within 20 min on HeLa-CD95-mGFP cells (Figure 3.30a,b). Two technical replicates were then performed for the stimulation of cells for the ligand-immunoprecipitation experiment.

Receptor amounts for the two different ligand were similar in the different ligand precipitates and absent in the control, verifying same apparent binding of the two ligands to the cells (Figure 3.30c). However, the amounts of mCherry-tagged ligand in the IP were different on the blot probably due to the differences in blotting efficiency known to occur for proteins of different size.

By having very similar receptor levels in the ligand precipitates, the different proteins FADD, caspase-8 and FLIP can be compared between the different treatments. Notably, mCherry-sCD95L precipitates contained much less FADD compared to mCherry-IZsCD95L precipitates (Figure 3.31a). In line, much less cleaved FLIP (p43) and much less caspase-8 were detected in those precipitates. Together, these data suggest that FADD is recruited only to a subset of ligand-bound receptors.

Next, relative amounts of proteins recruited to the receptor were compared to test for differences in caspase-8 processing. While FADD- relative to CD95 receptor amounts (FADD/CD95) were about 4 to 5 times higher in cells treated with mCherry-IZsCD95L compared to cells treated with mCherry-sCD95L, relative protein amounts of FADD to caspase-8 (FADD/C8) were equal in those cells (Figure 3.31b). In cells treated with the weak agonist mCherry-sCD95L, slightly more

processed caspase-8 (p43/41) relative to FADD was detected. This indicates that despite lower FADD recruitment, caspase-8 processing was efficient and relative to FADD amounts similar in both conditions (Figure 3.31b).

Notably, higher amounts of cleaved FLIP_L (p43) relative to FADD were found in mCherry-sCD95L treated cells. Full-length FLIP_L protein could not be determined because of the presence of an unspecific band (indicated by a star (*) in Figure 3.30). Amounts of FLIP_S were overall very low and relative to FADD similar in both conditions.

To summarize this part, these results show that despite same amounts of receptor binding, different amounts of FADD were recruited by the two different ligands. Presumably, as a consequence of inefficient FADD recruitment, less total and less processed caspase-8 was detected in mCherry-sCD95L immunoprecipitates. Nevertheless, processing of caspase-8 was equally efficient with both ligands. Thus, lower rates of caspase-8 substrate cleavage observed in mCherry-sCD95L-induced cells (Figure 3.23) can therefore be explained by inefficient recruitment of FADD.

FADD-mGFP recruitment by microscopy

To confirm these findings, I applied a microscopy-based assay. In the study of Neumann and co-workers, FADD-eGFP recruitment was visible upon TNF- α or TRAIL treatment of cells expressing receptor chimeras in form of dot-like structures at the cell membrane (Neumann et al. 2012). I wanted to quantify and compare the amounts of recruited FADD relative to total amounts of FADD by microscopy. Furthermore I aimed at excluding the possibility that only a small fraction of potentially higher oligomerized mCherry-IZsCD95L led to recruitment of higher amounts of FADD. To do so, mGFP- tagged FADD was transiently over-expressed in HeLa-CD95 cells. Upon induction with mCherry-tagged ligand, fluorescence of both, FADD-mGFP and mCherry-ligands, was imaged by confocal microscopy repeatedly over time. To note, over-expression of FADD-mGFP led to spontaneous aggregation of the protein inside the cell appearing as filament-like structures (Figure 3.31c). Those cells were not chosen for time-lapse microscopy. Upon ligand addition, binding of 1.8 $\mu\text{g/ml}$ mCherry-IZsCD95L (or 6.4 $\mu\text{g/ml}$ mCherry-sCD95L, not shown) to cells was rapidly visible, within 5 min, which further increased until 46 minutes (Figure 3.31d). Moreover, regarding FADD-mGFP localization over time, in many cells FADD-mGFP fluorescence redistribution could be observed by eye from the image. In the chosen example one can see that the bright and homogeneously distributed cytosolic and nuclear staining changed into a pattern of bright dots and a decrease in cytosolic and nuclear intensity (Figure 3.31d).

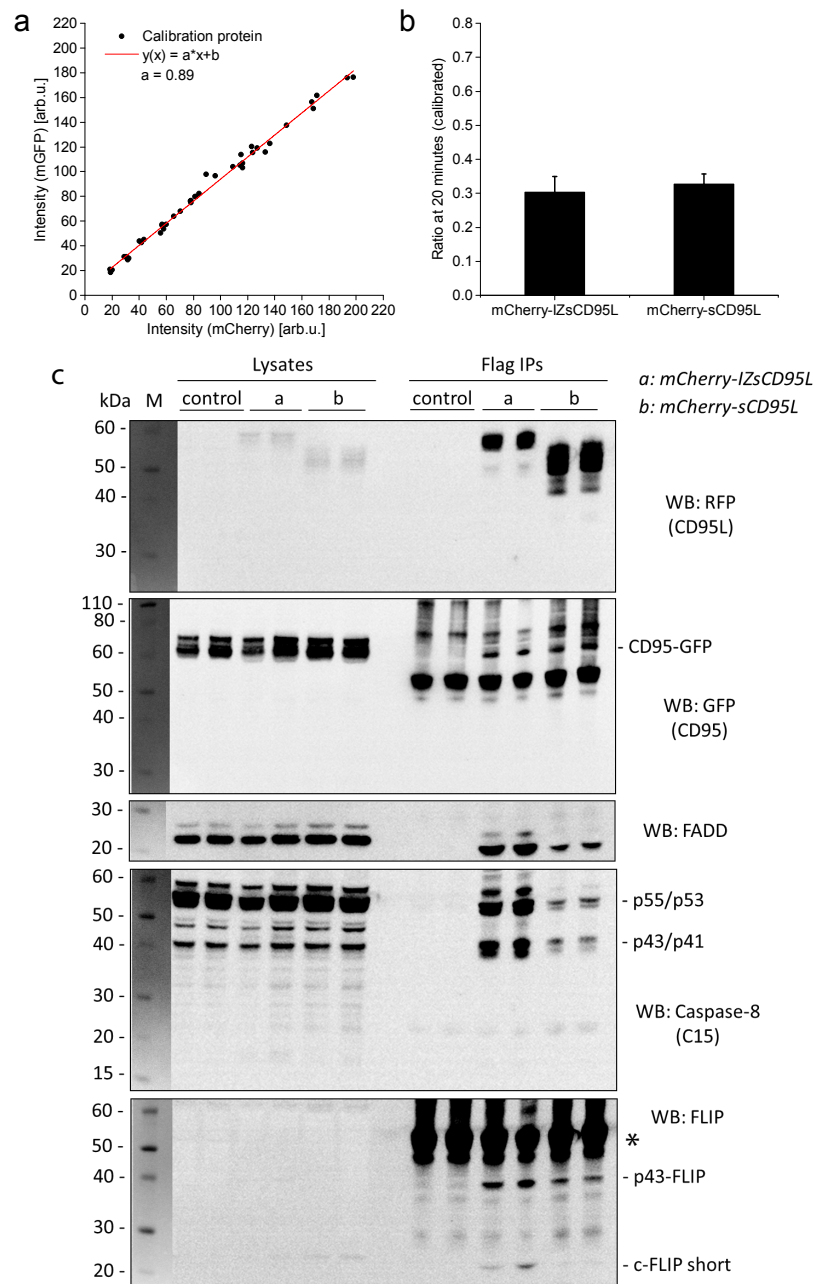


Figure 3.30: Immunoprecipitation of mCherry-IZsCD95L and mCherry-sCD95L. (a) Calibration of fluorescence intensities. mCherry-Bid-mGFP was transiently expressed in HeLa cells. Intensities originating from fluorescence of mGFP and mCherry in the same region of a cell were measured and plotted against each other. (b) Quantification of mCherry-IZsCD95L and mCherry-sCD95L bound to HeLa-CD95-mGFP cells (mean \pm s.e.m.). The ligands were allowed to bind for 20 min at 37°C, washed twice with medium (room temperature) and then immediately (<1 min) imaged. Three technical replicates were performed to control pipetting errors. (c) Western blot images. Ligand amounts showing after 20 min 30% of apparent binding in the control experiment were used and applied for 20 minutes on HeLa-CD95-mGFP cells. As control, cell culture medium was used. Flag-tagged ligands were immunoprecipitated and aliquots of lysates and immunoprecipitates from two replicates were loaded on the same polyacrylamide gel. IP = Immunoprecipitate, M = Protein size marker, WB = western blot.

Those FADD-mGFP dots, corresponding potentially to recruited FADD molecules, were mostly visible near to the cell membrane but also inside the cell, and were detected in 41% of mCherry-sCD95L (n = 32) and in 49% (n = 34) of mCherry-IZsCD95L- treated cells. To note, ligand only partially co-localized with FADD-mGFP (see arrows Figure 3.31d).

In Figure 3.31e mCherry-IZsCD95L binding and FADD-mGFP fluorescence redistribution is shown for another pair of cells. These images show a very clear accumulation of FADD-mGFP to the cell membrane and a decrease of fluorescence inside the cytosol and nucleus. This pattern was observed in 5 out of 34 cells of mCherry-IZsCD95L treated cells but not in mCherry-sCD95L treated cells. In cells which did not show this described pattern or the mentioned dots, fluorescence redistribution was difficult to see by eye from the images.

To anyway compare FADD-mGFP levels relative to total FADD-mGFP amounts in cells treated with the two different ligands, I quantified FADD-mGFP amounts in the nucleus of all imaged cells at the measured time-points. Strikingly, within 50 min, the mean FADD-mGFP fluorescence intensity dropped from 100% to 74% in mCherry-sCD95L induced cells and to 46% in mCherry-IZsCD95L induced cells (Figure 3.31f). Notably, the decrease in fluorescence was not exponential, but displayed a shoulder at short times. Differences in fluorescence redistribution between the ligands became particularly apparent only after 30 min, a time when binding of ligand was already strong at these receptor levels (Figure 3.28). The time of death was similar to HeLa-CD95-mGFP cells treated with same ligand concentrations shown in Figure 3.28. In particular, in those cells the onset time of caspase-8 activity was around 20 min with mCherry-IZsCD95L and around 50 min with mCherry-sCD95L. At these time-points FADD staining in the nucleus of HeLa-CD95 cells was reduced to about 80% with both ligands.

To conclude, these data confirm immunoprecipitation experiments in that more FADD was recruited to receptors at the cell surface at a time by mCherry-IZsCD95L than by mCherry-sCD95L, despite same apparent binding of those ligands. On top, using time-lapse microscopy this approach had the potential to visualize kinetics of FADD recruitment, which was previously not reported. Strikingly, despite quick binding of ligands to cells, FADD recruitment was delayed. This indicates that FADD recruitment is limited by a process which occurs after ligand binding, supposedly conformational changes of receptors or receptor oligomerization kinetics. In view of the two-state receptor theory, the events related to ligand-receptor interaction were further explored experimentally.

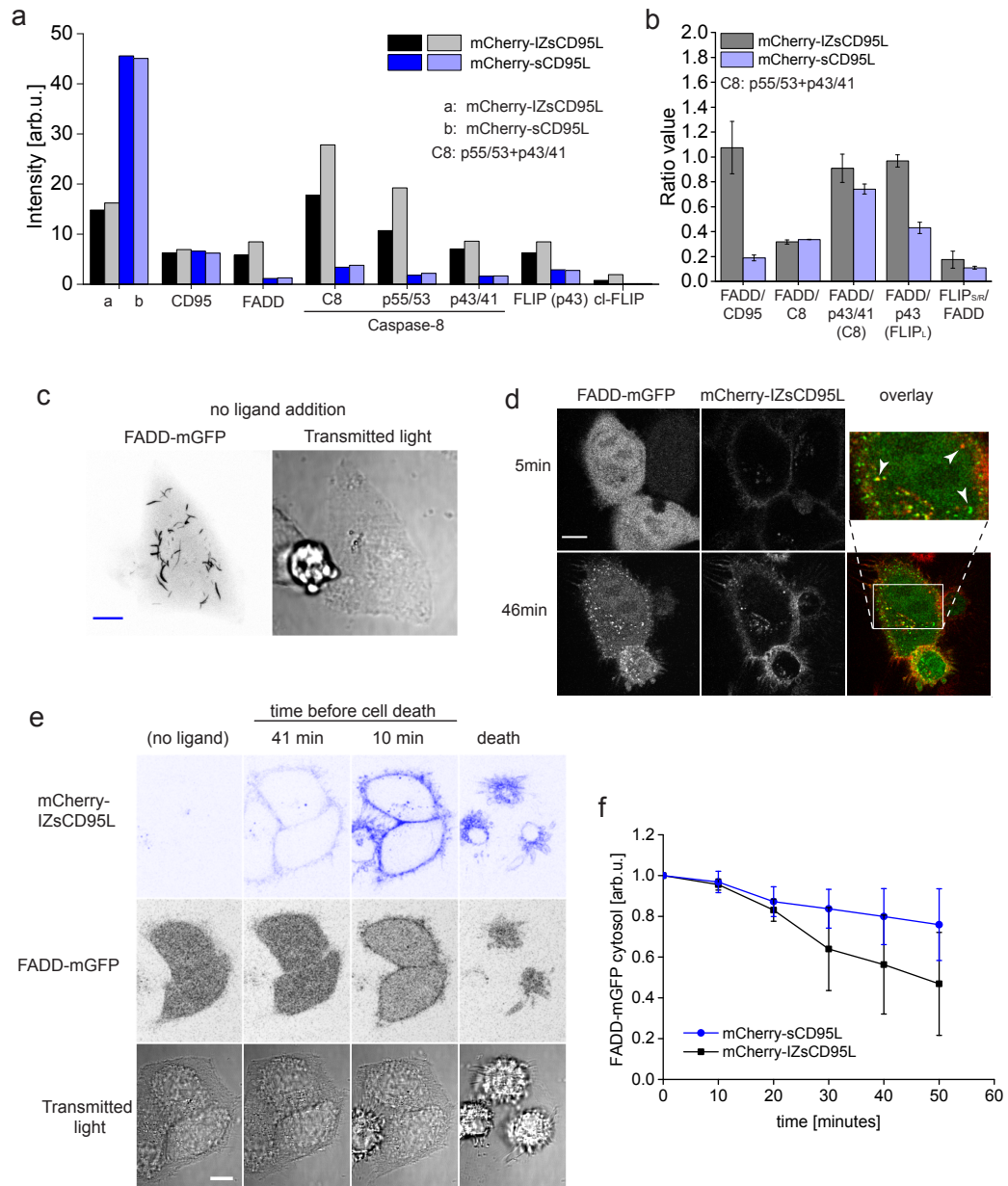


Figure 3.31: FADD is inefficiently recruited to mCherry-sCD95L bound receptors. (a) Quantification of western blot images from immunoprecipitation of mCherry-IZsCD95L and mCherry-sCD95L from HeLa-CD95-mGFP cells for the comparison of proteins of the same size detected by the same antibody. (b) Ratio values were calculated from mean values of results shown in plot a) for the comparison of relative amounts recruited to CD95 receptors. (c-f) HeLa-CD95 cells, transient FADD-mGFP expression, Scale bars = 10 μ m. (c) FADD-mGFP filaments spontaneously formed upon transient expression, as expected for over-expressed DED-containing proteins (Siegel et al. 1998). No ligand was added, projection sum of a z-stack. (d) Snap-shots of a time series, 1.8 μ g/ml mCherry-IZsCD95L, FADD-mGFP dots formed over time, white arrows indicate that FADD-mGFP inside the cell do not always colocalize with internalized mCherry-IZsCD95L. Contrast settings were kept equal for the different time points of one channel. (e) Another example of the spatial localization of FADD-mGFP upon ligand induction. Here, no FADD dots but FADD recruitment to the plasma membrane is visible. (f) Quantification of nuclear/cytosolic FADD-mGFP upon induction with 1.8 μ g/ml mCherry-IZsCD95L (34 cells) or 6.4 μ g/ml mCherry-sCD95L (32 cells).

3.6 Internalization of soluble CD95L

As introduced, internalization might be relevant for cell death signaling by CD95L (section 1.6.1) but internalization is also generally an important consideration when modeling binding (Beck and Goren 1983-1984, Shankaran et al. 2007, Becker et al. 2010). Therefore, I studied CD95 internalization by imaging mCherry-tagged ligands and mGFP-tagged CD95.

Because we observed CD95-driven caspase-8 activity mainly at the cell membrane (Beaudouin et al. 2013), I tested the hypothesis that internalization affects signaling by removing receptor species from the cell membrane and thereby counteracting receptor activation kinetics and tested the possibility that the two ligands have different internalization behaviors.

To do so, first, the extent of internalization was estimated. Second, internalization was investigated by live cell imaging using co-markers for endocytosis. Third, the effect of block of internalization on cell death, by using over-expression of inactive mutants of Rab4a, Rab5a, Rab11b and Rab7a or by applying drugs to cells was measured. Finally, the specificity of the effect on cell death was assessed by measuring caspase-8 activity.

Soluble CD95L slowly internalizes in HeLa cells independent on caspase-8 activity

A suitable way to distinguish cell membrane bound from internalized ligand is to wash away all cell membrane bound ligand rigorously in a buffer of low pH of 2.7 (section 2.2.3). This would allow to efficiently disturb electrostatic interactions between ligand and receptors. To test if internalization kinetics are dependent on FADD recruitment and DISC-formation, I measured a HeLa cell line expressing a death domain truncated version of the receptor CD95 (HeLa-CD95- Δ DD-mGFP) next to HeLa-CD95-mGFP cells. Before the internalization assay, equal apparent binding of the two forms of ligand mCherry-IZsCD95L and mCherry-sCD95L was assessed the same way as shown in Figure 3.27.

The total amount of ligand, bound at the plasma membrane and inside the cell, I_{total} and the fraction of internalized ligand $I_{cytosol}$ were measured from 3D-stacks of fixed cells (section 2.2.3). Total and internalized ligand amounts were slightly higher for cells stimulated with mCherry-IZsCD95L than for cells stimulated with mCherry-sCD95L (Figure 3.32). To confirm the equal binding of ligand I derived the ligand surface amounts by calculating $I_{surface} = I_{total} - I_{cytosol}$, which confirmed an equal receptor occupancy (Figure 3.32c). Internalization occurred most likely independent of the death domain because no difference between HeLa-CD95-mGFP and HeLa-CD95- Δ DD-mGFP cells was observed (Figure 3.32c). With a continuous ligand stimulus, after 30 min about 15% of total mCherry-sCD95L signal was internalized, while for mCherry-IZsCD95L, about 35% of total ligand resided inside the cell. To estimate the rate of internalization, its kinetics was then calculated as percentage of total ligand from both cell lines.

mCherry-sCD95L internalized with an initial rate of $0.5\% \text{ min}^{-1}$ and mCherry-IZsCD95L with an initial rate of $1.2\% \text{ min}^{-1}$ (Figure 3.32d). Different internalization rates for the two different ligands might correlate to the amount of activated receptors. Since mCherry-IZsCD95L activates more caspase-8 at these concentrations compared to mCherry-sCD95L despite same apparent surface binding, more receptors were potentially activated and internalized by mCherry-IZsCD95L. The internalization process could lead to the extinction of receptor activity. Alternatively, as proposed in the context of type I cells (Lee et al. 2006), it might be also tempting to speculate that those internalized ligands actually reflect active receptor species.

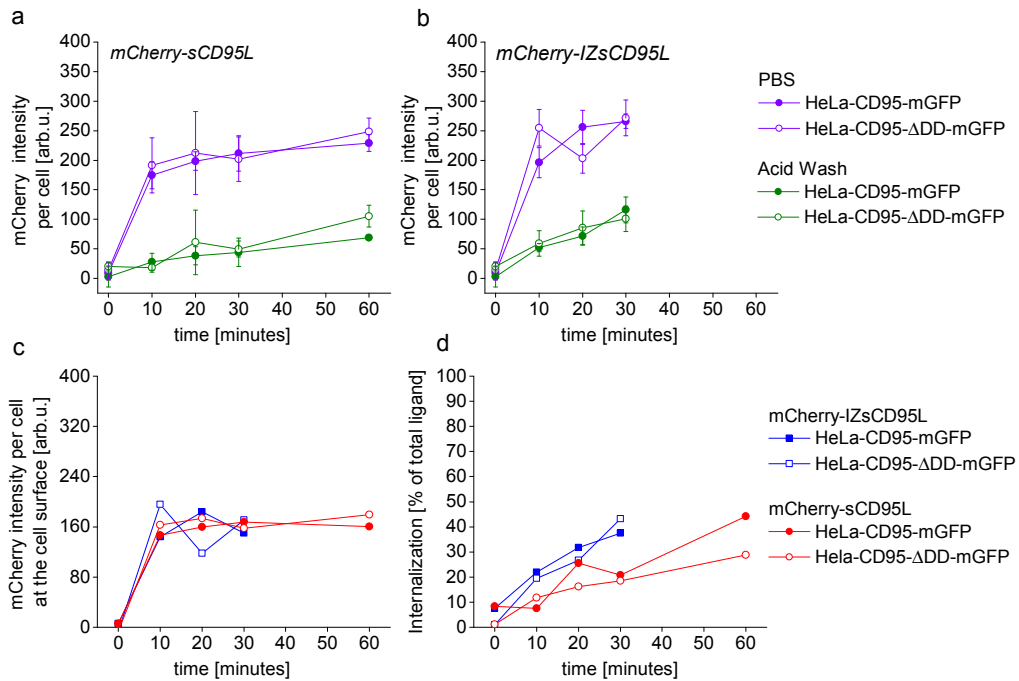


Figure 3.32: Internalization of mCherry-tagged ligands. HeLa-CD95-mGFP cells and HeLa-CD95 Δ DD-mGFP were continuously incubated with mCherry-tagged ligand for 10, 20, 30 or 60 min or left untreated. Concentrations of ligand were used that lead to 40% occupied receptors within 10 min. Ligand amounts of PBS-washed or acid-buffer washed cells which were cross-linked by FA/GA-fixative and were quantified using confocal microscopy. (a,b) black: PBS washed cells, red: Acid-buffer washed cells. (a) mCherry-sCD95L. (b) mCherry-IZsCD95L. (c) Fluorescence intensity at the cell surface calculated from mean values of data shown in a) and b). (d) Internalized ligand in percentage calculated from mean values of a) and b) by normalization to the highest value.

3.6.1 CD95L might signal from early endosomes but not from late endosomes in HeLa cells

In case receptors would signal from endosomal structures upon internalization, a prerequisite would be that the death domain of the receptor must face the cytosol to be able to recruit FADD, caspase-8 and FLIP proteins. This would not be fulfilled in a context of multivesicular structures, in which endosomes are engulfed in so-called carrier vesicles (Raiborg et al. 2003, Gruenberg and Stenmark 2004).

The localization of receptors and ligands was evaluated by time-lapse microscopy which allowed to track the localization of mCherry-tagged ligands and mGFP-tagged receptors in living cells. As ligands and receptors travel through compartments of different pH during internalization, I tested whether mGFP fluorescence from the receptor co-localizes with mCherry-fluorescence from the ligand inside the cell. In contrast to mCherry, light absorbance by mGFP and fluorescence emission is reduced at low pH. More precisely, the fluorescence-yield of GFP(S65T), which has a pK_a of 6.0, is around 50% at pH 6.0 and drops to less than 20% at pH 5.0. MCherry has a pK_a of less than 4.7 and still about 75% fluorescence-yield can be obtained at pH 5.0 (Kneen et al. 1998, Shaner et al. 2005, Doherty et al. 2010). The cytosol has a neutral pH of about 7.2. The luminal environment of early endosomes displays a pH of about 6.2, the one of large endosomes (late endosomes) about 5.0-5.6 and the one of lysosomes of about 4.8-5.2 (Kneen et al. 1998, and references within). The idea was to use mGFP as a marker for the orientation and localization of the receptor inside the cell. In case receptors would be engulfed into bigger, multivesicular endosomes, fluorescence of mCherry, but not of mGFP would be expected together with a loss of signaling ability.

As anticipated from binding experiments, cell surface staining was observed quick after ligand addition ($t = 2$ min, Figure 3.33a). With increasing time, mCherry fluorescence gradually appeared inside the cell. In some cases, I observed that mCherry-fluorescence inside the cell first took a tube-like shape before appearing as more rounded endosomal structures (compare $t = 30$ min to $t = 1$ h 30 min, Figure 3.33a). Interestingly, stably expressed mGFP-tagged receptors showed the same tube-like structures which co-localized with those of seen in the mCherry-detection channel ($t = 30$ min, Figure 3.33a,b). As those receptors might directly stay in touch with the cytosol, signaling from those tube-like structures would in theory be possible. Notably, mGFP-fluorescence did not co-localize with the large mCherry-positive round endosomal structures (Figure 3.33a,b). This suggests that apoptotic signaling would not take place from these structures. Presumably, tube-like structures reflected small early endosomes traveling potentially along microtubules and subsequently fused with and engulfed into larger endosomes which finally led to pH-dependent impediment of GFP-fluorescence. Internalization was not blocked with the receptor mutant CD95- Δ DD-mGFP or by zVAD-fmk. From that I concluded that this internalization was not dependent on the amino acids 1-210 of the receptor and also not dependent on caspase activity (Figure 3.32

and 3.33a,b).

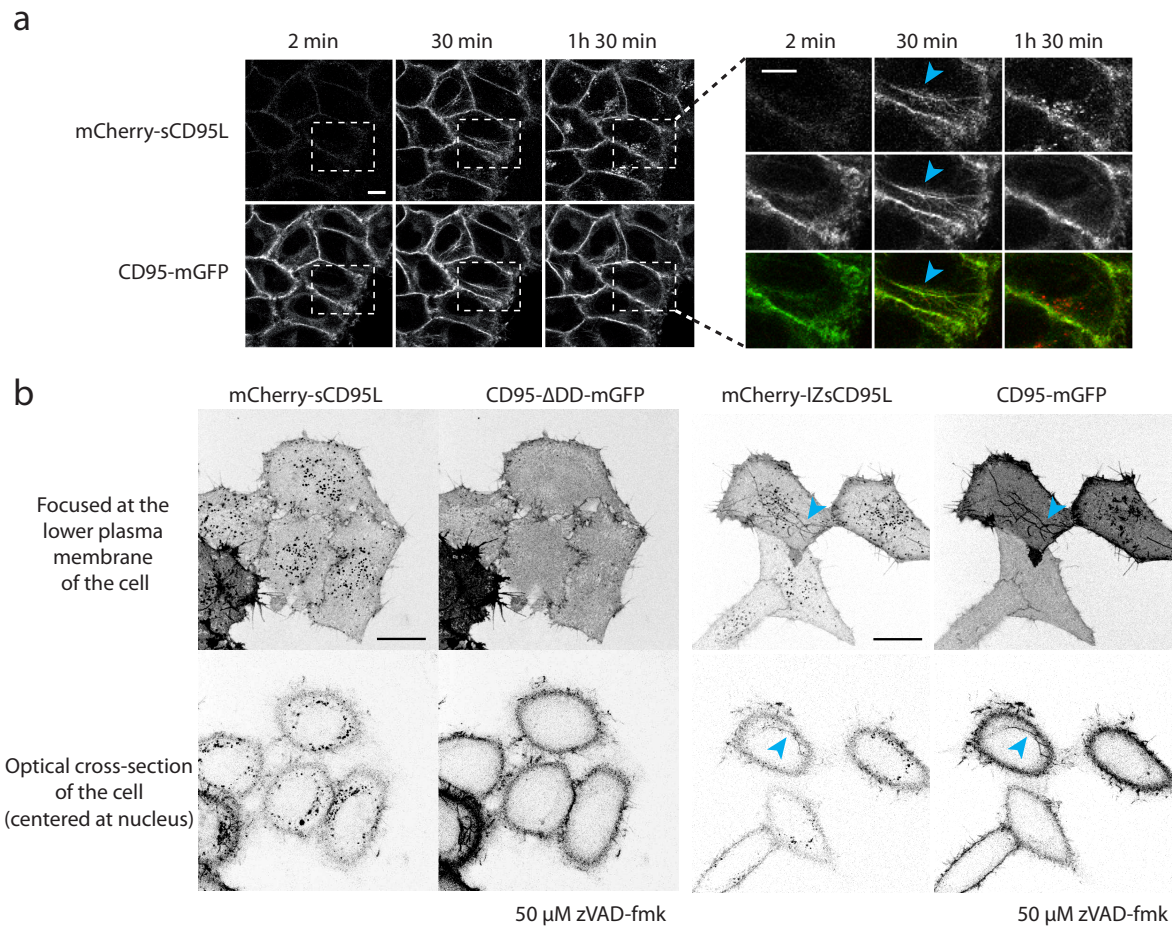


Figure 3.33: Ligand internalization. (a) HeLa-CD95-mGFP cells were stimulated with 0.1 $\mu\text{g}/\text{ml}$ mCherry-sCD95L. Scale bar = 10 μm . Intensities were not calibrated. On the right: magnified images. (b) Cells expressing transiently CD95- ΔDD -mGFP or CD95-mGFP were incubated with 6.4 $\mu\text{g}/\text{ml}$ mCherry-sCD95L or 1.8 $\mu\text{g}/\text{ml}$ mCherry-IZsCD95L in the presence of 50 μM zVAD-fmk, snapshots of images at $t = 4\text{h}$ and 1h 30 min, respectively after ligand addition. Optical sections of the cell were made at the lower cell surface and at the center of the cell. Note the presence of mCherry- fluorescent spherical and tube-like structures. Tube-like structures but not spherical ones are also visible in the GFP-detection channel. Scale bar = 20 μm . Intensities were calibrated. Blue arrowheads point to tube-like structures.

3.6.2 mCherry-sCD95L localizes to Rab4a- and Rab5a-positive endosomes

The uptake of extracellular ligand into the cell can be mediated by different proteins reported as follows: actin-dependent phagocytosis or macropinocytosis, clathrin-dependent internalization, caveolin-dependent internalization and lastly clathrin- and caveolin-independent internalization (Mayor and Pagano 2007). Among other proteins, small GTPases mediate the intracellular traffic of endosomes. Regarding early endosomes, Rab5a is thought to be involved in clathrin-mediated endocytosis, Rab4a function is rather associated with fast recycling of early endosomes (Stenmark 2009).

In order to test whether the observed CD95L internalization might be clathrin-mediated, I checked whether mCherry-sCD95L staining would co-localize with GFP-tagged Rab-proteins in HeLa-CD95 cells.

Strikingly, I observed that mCherry- positive endosomal structures co-localized to vesicles of GFP-Rab4a and GFP-Rab5a (Figure 3.34a and b). More precise, mGFP formed a ring-like structure as expected for proteins adhering to the outer membrane of endosomes while mCherry fluorescence was detected from the whole vesicle (Figure 3.34, magnified images). Consistent with the observations from Roberts and co-workers, Rab4a-mGFP and Rab5a-mGFP over-expression led to enlarged vesicles, most likely because these proteins mediate fusion of early endosomes (Roberts et al. 1999). Fluorescence from the equivalent inactive proteins GFP-Rab4a(S27N) and GFP-Rab5a(S34N) showed a more homogeneously distributed pattern over the cytosol and mCherry-sCD95L fluorescence was less visible in the cytosol compared to conditions of GFP-Rab4a and GFP-Rab5a over-expression.

Interestingly, I have observed the opposite, namely bigger vesicles containing mCherry-sCD95L in cells expressing the inactive mutant mGFP-Rab7a(T22N) compared to cells expressing the wild type form mGFP-Rab7a, GFP-Rab4a or GFP-Rab5a (Figure 3.34c). This suggests that dysfunctional Rab7a lead to accumulation of mCherry-sCD95L potentially because the fusion of endosomes to lysosomes and subsequent degradation might be blocked.

Although over-expression of these proteins might have also artificially enhanced the direction into those endosomal pathways, these data suggest that internalization occurs through a Rab4a and Rab5a controlled endocytic pathway.

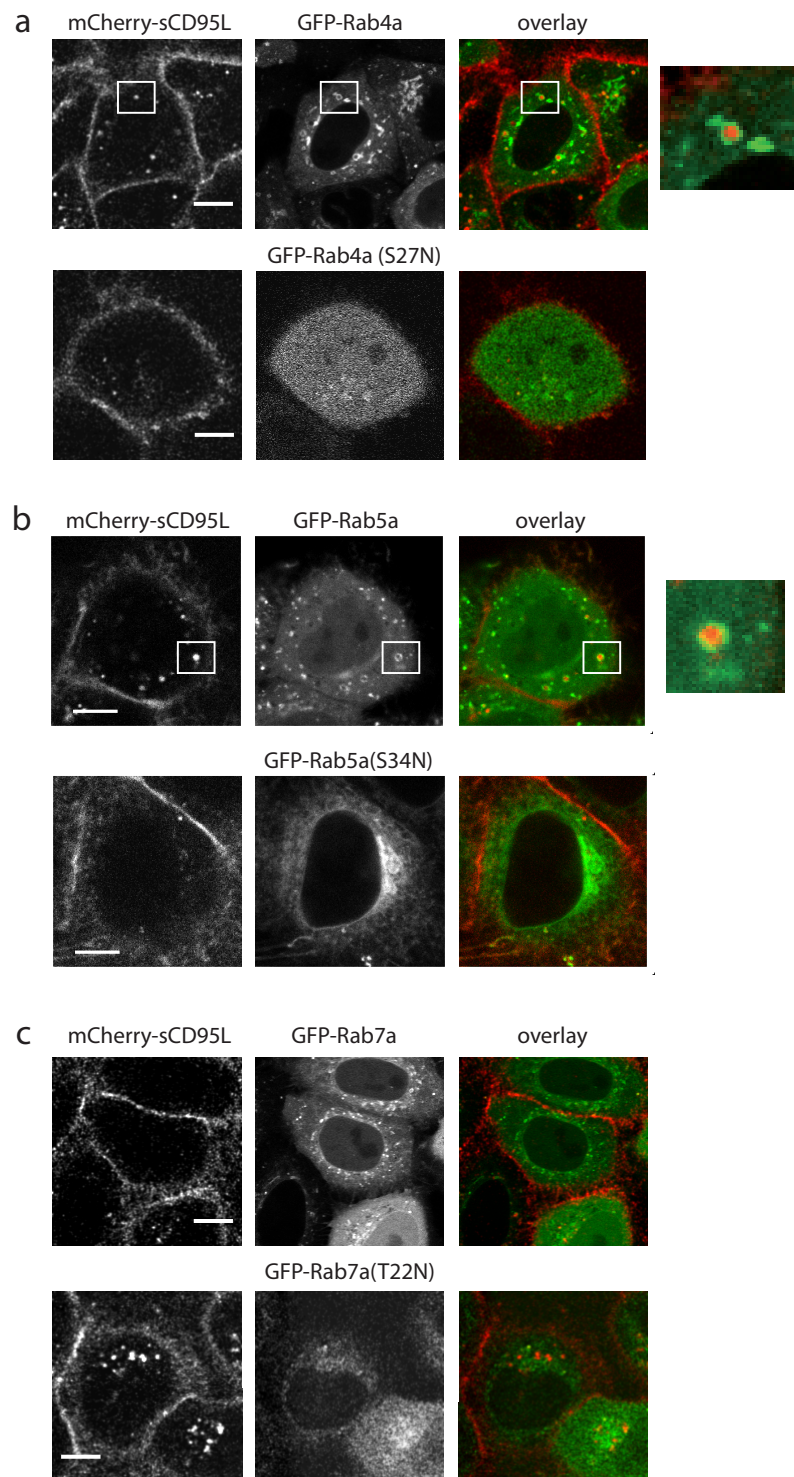


Figure 3.34: Co-localization of mCherry-sCD95L with Rab4a and Rab5a. HeLa-CD95 cells expressing different N-terminally tagged Rab proteins and induced with mCherry-sCD95L, $t = 70$ min. (a) first row: Rab4a, second row: Rab4a(S27N) (b) first row: Rab5a, second row: Rab5a(S34N) (c) first row: Rab7a, second row: Rab7a(T22N). The magnified images on the right show the internalized ligand inside Rab-positive vesicles of the white-bordered boxes. Scale bar = $10\mu\text{m}$.

3.6.3 Block of ligand internalization by methyl- β -cyclodextrin and monensin

As mentioned in the previous section, internalization may affect ligand-receptor interaction and DISC assembly. Therefore, the receptor activation kinetics might stand in competition with the receptor internalization kinetics. To test the effect of internalization on pathway activation, I intended to block mCherry-sCD95L internalization at the uppermost stage of the internalization cascade, namely at the cell membrane.

It is known that lipids play a major role in the different internalization pathways because protein recruitment to the cell membrane occurs via lipid-binding domains such as the ANTH domain in the protein AP80 or the PH- domain in the protein dynamin (Roy and Wrana 2005). Disturbing the lipid composition of the cell can therefore block internalization, and different drugs have been developed to do so, as summarized in the book by Ivanov (Ivanov 2008). For example, the drug methyl- β -cyclodextrin ($M\beta$ CD) was reported to specifically block lipid-raft/caveolin- dependent internalization and also non-specifically block clathrin-mediated internalization of transferrin. Next to $M\beta$ CD, monensin is a drug that does not directly affect cell surface receptor internalization but as an ionophore it blocks intracellular traffic, renders endosomes less acidic and can prevent receptor recycling (Mollenhauer et al. 1990).

To verify cell surface staining and intracellular staining, cells were washed on ice in a buffer of low pH (acid buffer) before fixation and examination by confocal microscopy. I could prove that the ring-like staining of mCherry-fluorescence on the cell (Figure 3.35a) measured by optical sectioning presents outer cell surface staining because after applying acid-buffer wash, this membrane staining but not intracellular staining disappeared (Figure 3.35a, 2nd column). Furthermore, cells incubated on ice with ligand did not show intracellular staining as low temperature prevents endocytosis (Figure 3.35a, 3rd column). Internalization of mCherry-sCD95L in HeLa-CD95-mGFP cells was efficiently delayed by treatment of cells with 3 mM $M\beta$ CD for 1h (Figure 3.35a, b). Similarly, treatment of cells with 10 μ M monensin or a mixture of 10 μ M monensin and 3 mM $M\beta$ CD visually blocked internalization (Figure 3.35b). For another read-out, to test whether internalization is blocked by these drugs, the occurrence of the described tube-like structures was counted in images showing CD95-mGFP fluorescence. A time-series capturing cells upon ligand or control medium addition was analyzed until start of cell death (1h 40 min). Formation of these structures was seen in 31.5% of cells incubated with ligand and in 5.3% in control cells that did not received ligand (Figure 3.35c). Cells treated with same amount of ligand and incubated on top with 1 μ M, 2 μ M or 10 μ M monensin showed a reduction of these structures to 10.3, 12.7 and 12.1% of the cells, respectively, while treatment with 3 mM $M\beta$ CD completely abolished formation of those tube-like structures. Moreover, this treatment did not affect the receptor level on the surface of HeLa, HeLa-CD95 or HeLa-CD95-mGFP cells measured by immunostaining and flow cytometry (Figure 3.35d). To conclude, these experiments show that internalization of mCherry-sCD95L can be efficiently blocked using the drugs monensin and $M\beta$ CD.

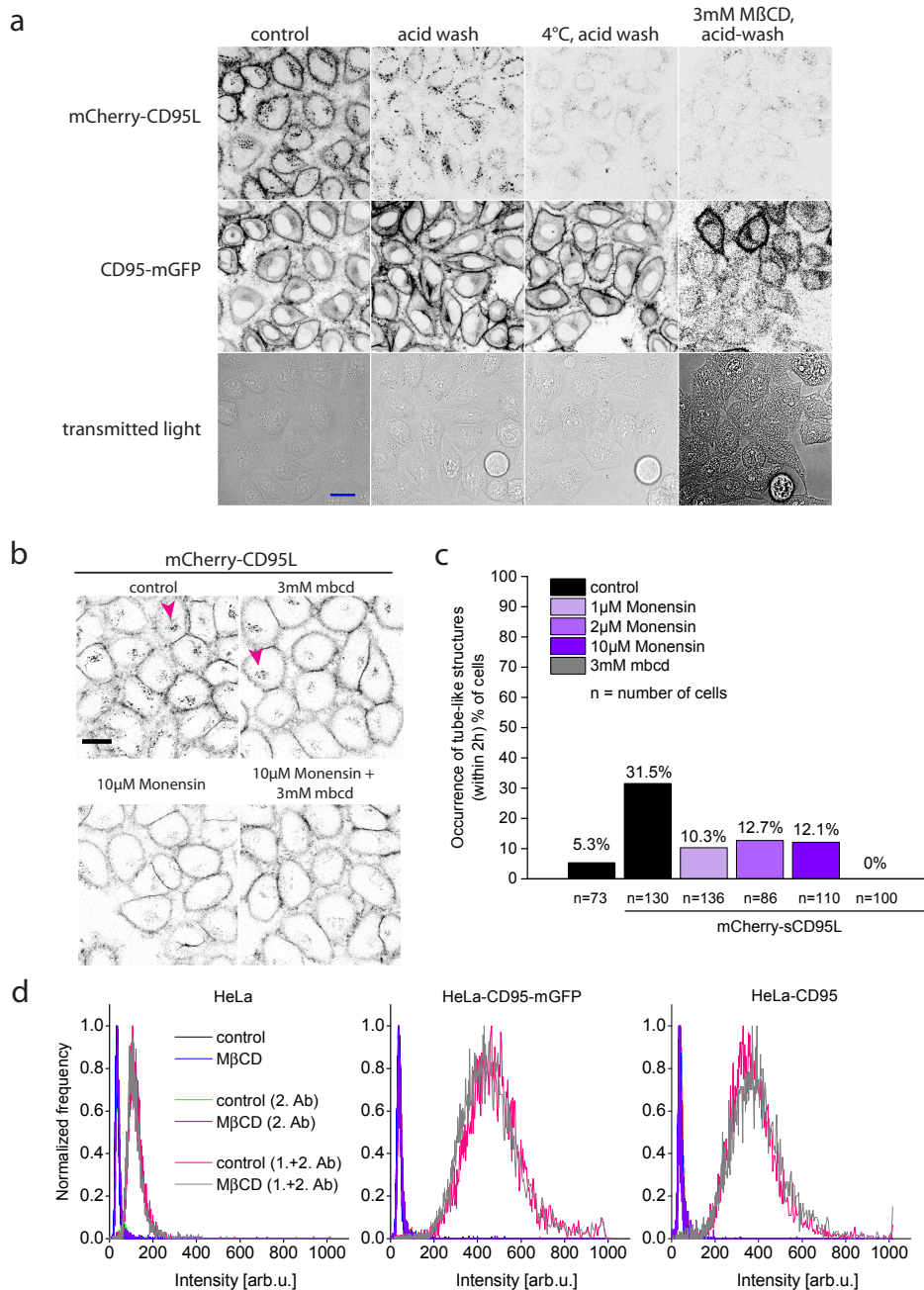


Figure 3.35: Monensin and MβCD delay internalization and reduce the amount of tube-like structures in HeLa-CD95-mGFP cells. (a) HeLa-CD95-mGFP cells incubated for 1h with 3mM MβCD or left untreated, stimulated for 40 min with mCherry-sCD95L at 4°C (3rd column) or at 37°C (1st, 2nd and 4th column). Cells were washed for 30 min on ice with PBS or acid-buffer and subsequently fixed using 4% FA fixative. Scale bar = 20μm. Note that with MβCD fewer black dots are visible inside the cells and that acid-wash removed cell surface staining. At 4°C less intracellular staining is visible. (b) HeLa-CD95-mGFP cells treated 1h with 3 mM MβCD, 10 μM monensin, or both or left untreated (control). Induced with equal amounts of mCherry-sCD95L. Snap-shots of time-series data t = 1h 30 min. Scale bar = 20μm. Arrows indicate that fewer black dots are visible inside cells with MβCD. (c) Quantification of tubular structures counting. (d) HeLa, HeLa-CD95 and HeLa-CD95-mGFP cells were either incubated for 1h in 3 mM MβCD or left untreated. Cells were fixed by FA/GA and stained using the Apo1-3 antibody and α-IgG(Alexa 594).

3.6.4 Block of internalization enhances sCD95L mediated cell death in HeLa cells

To study the effect of CD95 ligand internalization in HeLa-CD95 cells on apoptosis induction, cell death kinetics were first assessed for cells treated with different amounts of monensin and mixtures of monensin and M β CD. With increasing concentrations of monensin, cells responded increasingly faster to ligand with death (Figure 3.36). 50% of cells treated with M β CD or 1 μ M Monensin together with ligand died after 4h, while only 10% of control cells treated only with ligand were dead at this time point. Using 2 μ M or 10 μ M monensin, the median cell death time was 3h. The effect of monensin could be enhanced when M β CD was added on top. Cells treated with 3mM M β CD plus 1 μ M, 2 μ M or 10 μ M monensin died after 2h 12 min.

These data show that internalization counteracts activity of CD95 potentially by competing with receptor activation kinetics in HeLa-CD95 cells.

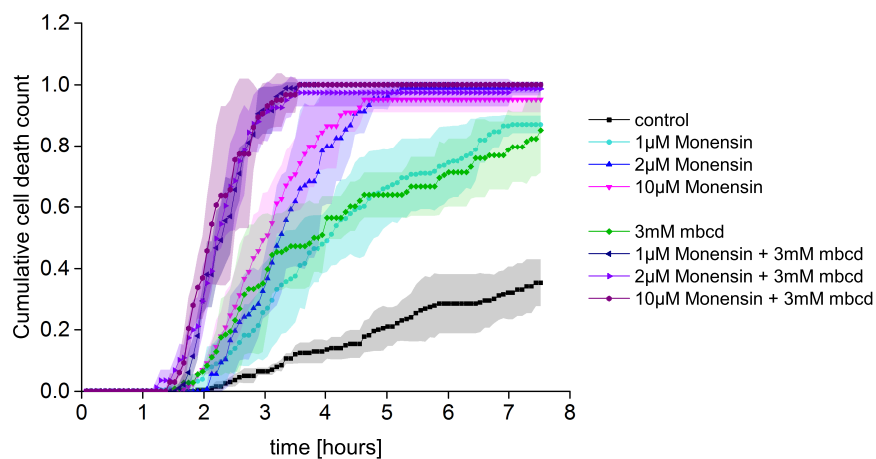


Figure 3.36: Cell death of HeLa-CD95-mGFP cells treated with Monensin and M β CD. HeLa-CD95-mGFP cells were incubated for 1h with the indicated drugs and then stimulated with equal amounts of mCherry-sCD95L with the indicated drugs.

To complement these results, cell death was addressed in a cellular context where the normal internalization route was altered. By the over-expression of inactive mutants of Rab4a, Rab5a, Rab11b or Rab7a, the function of the respective endogenous Rab protein can become in principle vanishingly small. As specific Rab proteins have been assigned to different stages of the internalization route, internalization can be blocked, in theory, at these specific stages by using over-expression of mutants of Rab.

Figure 3.37 shows cell death kinetics obtained from two independent experiments where four different Rab mutants were transiently over-expressed in HeLa-CD95 cells which were then exposed to mCherry-sCD95L. mGFP transfected control cells showed the slowest death kinetics with 50% cell death after 2h 30 min. A fast death kinetic with 50% cell death after 1h 40 min was observed when mGFP control cells were treated with M β CD. Expression of Rab5a(S34N) accelerated cell death most by inducing 50% cell death after 1h 30 min upon ligand addition and

showing an earlier onset of cell death compared to cells treated with $M\beta$ CD. Expression of Rab11b(S25N) showed 50% cell death after 2 hours, and thus more compared to control cells but with a similar onset and similar cell death kinetics at early time-points. Cell death kinetics were unchanged compared to control conditions when Rab7a(T22N) was expressed (Figure 3.37). Cells transiently transfected with Rab4a(S27N) showed in one experiment 50% cell death 50 min earlier than control cells, but in the other experiment more than 25 min later than control cells. To summarize, these results suggest that Rab4a mediated endocytosis possibly but that Rab5a mediated endocytosis definitely competed with receptor activation kinetics. A fraction of potentially active endosomes could be presumably kept intact inside the cell by blocking Rab11b mediated fusion events. At late stages of the internalization route, activity from endosomes would not be expected since block of lysosome formation using Rab7a(T22N) did not change cell death kinetics.

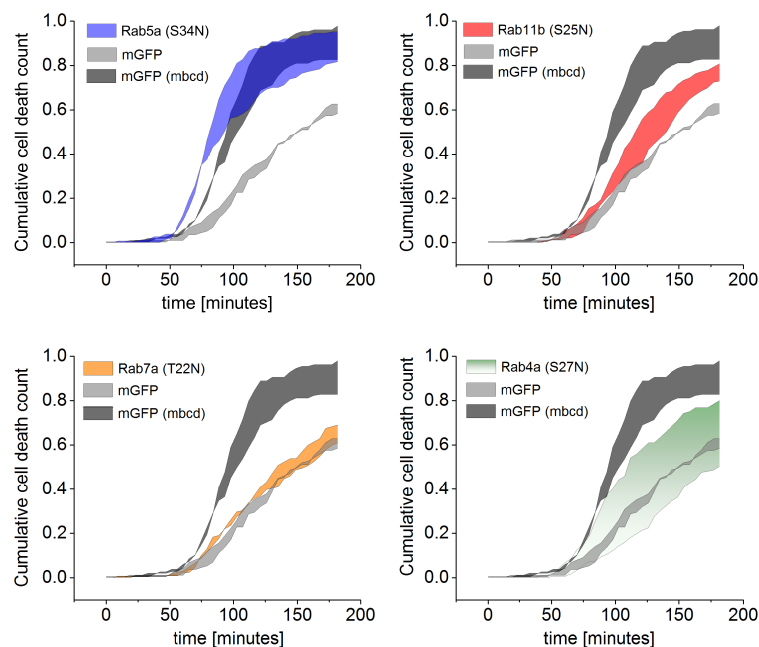


Figure 3.37: Cell death of HeLa-CD95 cells expressing an inactive mutant of Rab4a, Rab5a, Rab7a or Rab11b. HeLa-CD95 cells were transiently transfected with the mGFP-tagged proteins Rab4a(S27N), Rab5a(S34N), Rab7a(T22N) or Rab11b(S25N), or mGFP alone as control. Cells were induced with equal concentrations of mCherry-sCD95L. Cell death of transfected cells was counted. The area between cumulative cell death counts of two experiments is shaded with a color. Results from control and $M\beta$ CD-treated cells are re-plotted in the four graphs for the comparison to cell death kinetics with the different Rab proteins.

In order to test whether accelerated death kinetics in $M\beta$ CD-treated cells was pathway specific, cell death and caspase-8 activity upon mCherry-sCD95L stimulation were measured in HeLa-CD95 cells. An effect that would not be related to the pathway would let caspase-8 cleavage amounts unchanged in control and $M\beta$ CD conditions. For a pathway specific effect, I expected higher caspase-8 substrate cleavage rates and earlier onsets of caspase-8 activity in $M\beta$ CD-treated cells compared to control conditions.

To test these two possibilities, caspase-8 activity was measured using the probes mGFP-ELQTD-KRas and NES-ELQTD-mCherry (Figure 3.38). In case strong activity would originate from the endosomes, block of internalization should lower NES-probe cleavage and favor membrane-probe cleavage. I have used the localization sequence of the protein K-ras, because localization of this protein was shown to be insensitive to M β CD (Prior et al. 2003).

When cells were stimulated with mCherry-sCD95L in the presence of M β CD, I observed 50% cell death after 1h 30 min and after 3h 20 min in control conditions (Figure 3.38a). Five cells in the M β CD-condition (plots d and f, colored in pale red) died much faster compared to the bulk of cells. In order not to bias the results towards these cells, parameter estimates from these cells were taken out from the statistics.

Regarding the substrate cleavage rate, for control and M β CD, median rates were 0.00485 and 0.01049 arb.u./minute using the NES-probe and 0.0065 and 0.01068 arb.u./minute using the KRas-probe, respectively (Figure 3.38g). Differences were also seen when comparing the fitted values for the onset of probe cleavage between the two conditions. In cells treated with M β CD, the median onset of NES-probe activity was 62 min, and therefore 13 min earlier compared to control cells. Similarly, the median onset of KRas-probes started at 37 min, 11 min earlier than in control cells (Figure 3.38h).

Figure 3.38b shows the mean probe cleavage plotted against the normalized time. By setting the end-point time to 1, probe cleavage could be compared independent on cell death time which showed no difference between control and M β CD treated cells. This means that the effect of the drug is very likely a pathway specific event, because cells die faster with stronger caspase-8 activity. Taken together, these data support the view that CD95L internalization competes with receptor activation kinetics on the cell membrane of HeLa cells because the delay of internalization by the drugs M β CD led to stronger caspase-8 activity. Moreover, monensin treatment and intervention with the endosomal pathway by dominant inactive Rab proteins led to increased cell death kinetics.

How stable is the ligand-receptor interaction at different pH?

To get an insight into the binding behavior of the ligand within endosomes but also to assess the ligand-receptor interaction itself, I measured the strength of the ligand-receptor interaction at different pH. For this, I assessed the binding stability of ligand on living cells upon washing cells with Tris-Maleate (pH 7.2, 6.5, 6.0 or 5.5) and Tris-Succinate (pH 5.0) buffers by using confocal microscopy as a read-out.

I added mCherry-sCD95L or mCherry-IzsCD95L for 12 min to HeLa-CD95-mGFP cells to obtain a receptor occupancy of 30%. Subsequently, cells were washed twice with the respective buffer, so that one minute afterwards, images were acquired. Binding of mCherry-IzsCD95L was stable over the range of the different tested pH: The receptor occupancy decreased at pH 6.5 only to 20%, at pH 6.0 and 5.5 to 15% and at pH 5.0 to 20% (Figure 3.39a, black bars, see also c).

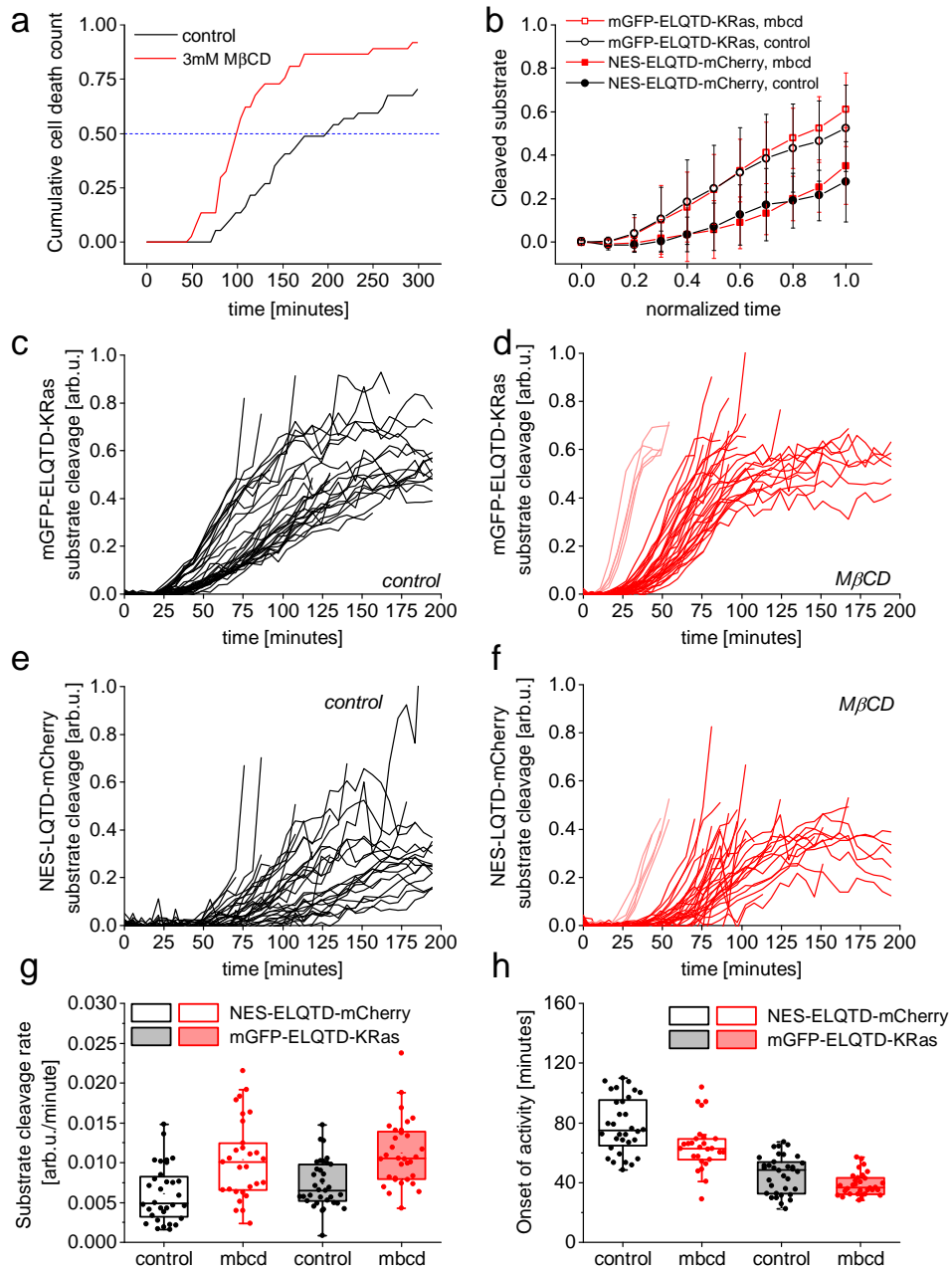


Figure 3.38: CD95L mediated cell death was accelerated when HeLa cells were treated with MβCD. Fluorescent reporters mGFP-ELQTD-KRas and NES-ELQTD-mCherry were transiently expressed in HeLa-CD95 cells. For control and MβCD-treated cells each, two wells were treated with equal amounts of mCherry-sCD95L. (a) Cumulative cell death count. (b) Probe-cleavage normalized to cell death time (mean ± s.d.) (c-d) mGFP-ELQTD-KRas substrate cleavage in single cells (control n=34, MβCD n= 37). (e-f) NES-LQTD-mCherry substrate cleavage in single cells. (g-h) Substrate cleavage measurements of single cells b-f were fitted to extract substrate cleavage rates (g) and the onset (h) of caspase-8 activity (section 2.2.3).

In contrast, binding of mCherry-sCD95L was less stable. At pH 6.5, binding dropped to 15% and at pH 6.0, 5.5 and 5.0 to less than 5% , reflecting background signal (Figure 3.39a, blue bars, see also c). Prolonging the binding phase of mCherry-sCD95L to 20 min and 40 min resulted in a receptor occupancy of 40% and 50% respectively. Nevertheless, washing at pH 6.0 resulted again in loss of ligand binding to 5% (Figure 3.39b). Conversely, reducing the concentration of mCherry-IZsCD95L by factor two, giving 20% binding at pH 7.2, washing at pH 6.0 resulted still in 10% binding (Figure 3.39a, striped bars). It should be noted that living cells maintained at 37°C incubated with buffers of pH lower than 6.0 systematically shrank- most likely due to an osmotic shock.

From these data, it seems possible that the interaction of mCherry-IZsCD95L to CD95 receptors is stable in late endosomes and in recycling endosomes. In contrast, for mCherry-sCD95L unbinding of the ligand would be expected in endosomes of pH 6.0. More general, because the ligand-receptor interaction is based on charged interactions, this experiment shows that the interaction of CD95 receptor to mCherry-IZsCD95L is more stable than the interaction of CD95 to mCherry-sCD95L.

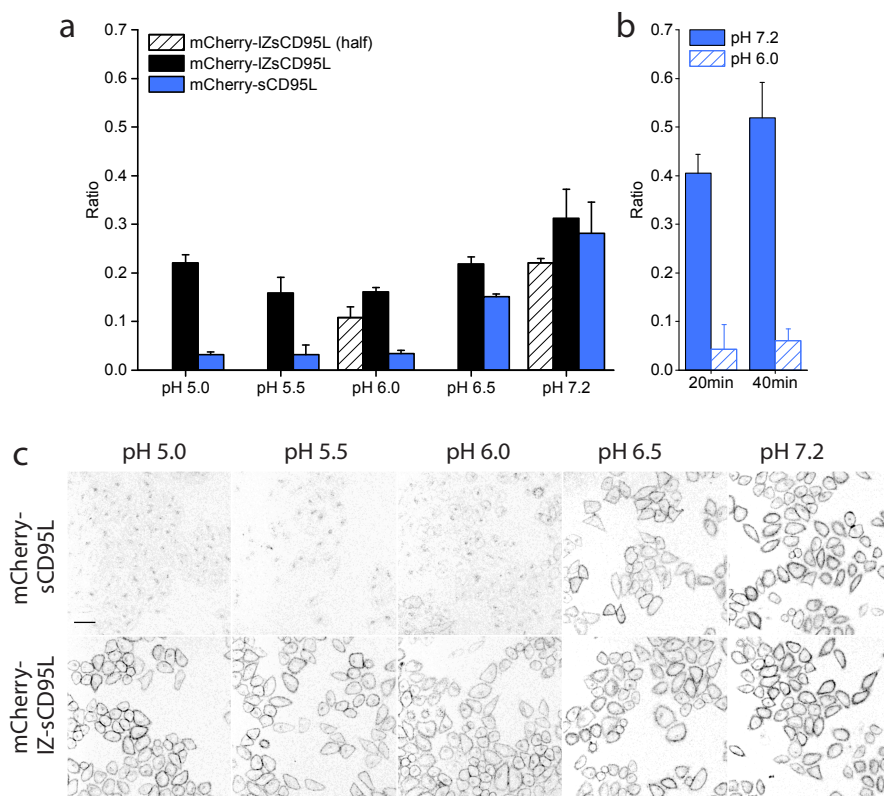


Figure 3.39: Binding of mCherry-tagged ligands at different pH. (a-b) Ratio=mCherry-sCD95L or mCherry-IZsCD95L binding relative to CD95-mGFP. mean \pm s.d. (a) Ligands were allowed for 10 min to bind to HeLa-CD95-mGFP. Ratios reflect binding after washing with Tris-Maleate (pH 5.5 to 7.2) or Tris-Succinate (pH 5.0) buffers. Striped bars: half-concentrated mCherry-IZsCD95L. (b) mCherry-sCD95L was allowed to bind HeLa-CD95-mGFP for 20 min or 40 min. Cells were then washed with Tris-Maleate buffer of pH 7.2 or 6.0 and imaged immediately. (c) Sample images of quantification shown in a). Scale bar = 50 μ m.

3.7 IZsCD95L, but not sCD95L efficiently cross-links CD95

3.7.1 Measurements of the unbinding kinetics - Minimal models of receptor activation

In this work I showed that sCD95L and mCherry-sCD95L present stable trimers that display a low avidity to CD95 receptor while trimers of mCherry-IZsCD95L showed a high avidity. Increasing the concentration of mCherry-sCD95L achieving same apparent binding on cells as with mCherry-IZsCD95L did not result in same activities, as measured by FADD-recruitment and caspase-8 substrate cleavage kinetics. Moreover, at same apparent binding, mCherry-sCD95L bound with lower strength to receptors on cells compared to mCherry-IZsCD95L as seen by measurement the interaction in the presence of buffers of different pH. In addition, ligand internalization antagonized apoptosis induction potentially by consuming activated receptors.

From this data, one would conclude that ligand bound receptors do not reflect activated receptors. This means that ligand-bound receptors must exist in at least two different states, an inactive one and an active one. This might be accomplished by assuming for example a reaction of a conformational change that would lead to activation of the receptor (SB2RS-model in cartoon Figure 3.24, page 86). Alternatively, as the ligand is trivalent, one can assume step-wise oligomerization of the receptor together with the hypothesis that only trimerized receptors are active (LIRT-model in cartoon 3.24, page 86). Those models are not mutually exclusive. Furthermore, as receptors might exist as dimers or higher oligomers, networks of receptor trimers are conceivable.

To test whether the ligand-receptor interaction shows indeed oligomerization behavior, I conducted unbinding experiments. Thereby, simple binding can be in principle distinguished from cooperative binding or oligomerization reactions (Lauffenburger and Lindermann 1996). In an unbinding experiment, first ligand is allowed to bind to receptors. Then, the key is to measure the loss of ligand on the cell in the presence and in the absence of non-labeled ligand and to compare both unbinding kinetics. To note, the concentration of the non-labeled competitor influences the unbinding kinetics. In the absence of non-tagged ligand the cell is washed, in my study cell culture medium was used, to replace all the labeled ligand in solution.

If we consider at the moment a simple binding mechanism, with a single on-rate and a single off-rate, unbinding of the ligand is only dependent on one parameter: the off-rate. Once the ligand is unbound, the chance that this ligand will rebind is theoretically as low in the presence as in the absence of non-labeled ligand. Unbound ligand is principally lost in the solution. Therefore, in a simple binding model, the unbinding kinetics will look the same for both conditions. Then, the measured off-rate would reflect the real off-rate.

In contrast, we assume several on- and off- reactions in an oligomerization model. Then, the measured unbinding rates reflect apparent off-rates and should be interpreted in the context of a

model. In the presence of non-labeled competitor, this competitor will bind free receptors and thereby lower the chance that rebinding of labeled ligand to free receptors will occur. Thus, the higher the concentration of the competitor, the faster the unbinding kinetics will occur. At the same time, a strong cross-linking reaction, meaning a high ratio of on-rate and off-rate for a single cross-linking reaction, the more difficult the ligand will unbind. If the cross-linking reactions are favored a lot, then unbinding might not happen neither in the presence nor in the absence of competitor. Therefore, the difference in unbinding kinetics between the two conditions, wash- or competition- condition, depends on the parameter values for the individual on-rates and off-rates.

Unbinding kinetics in view of a ligand induced receptor oligomerization model

In order to distinguish between the two different binding modes, simple binding and ligand-induced receptor oligomerization, I performed unbinding experiments for the two different ligands mCherry-sCD95L and mCherry-IZsCD95L. For this, the measurement and the analysis was carried out exactly as in binding experiments. Fluorescently tagged ligand, mCherry-sCD95L or mCherry-IZsCD95L, were added for 10 min or 30 min to cells in presence of 10 μ M zVAD-fmk. Then, the fluorescently tagged ligand was either replaced by non-labeled ligand (*competition*) or control medium alone (*wash*). Thereupon, fluorescence was measured repeatedly over time.

Internalization competes with unbinding of ligand from the membrane for the loss of membrane fluorescence. Hence, unbinding kinetic measurements were also performed in presence of 3mM M β CD (Figure 3.40c-f). Cell death measurements confirmed the acceleration of cell death with the drug M β CD upon mCherry-sCD95L stimulation observed in previous experiments (section 3.6.4). For competition assays, concentrations of mCherry-tagged and non-fluorescently tagged ligands sCD95L and IZsCD95L were determined that show equal median cell death times (Figure 3.40h). Under control conditions, median cell death times (50% cell death) occurred with sCD95L and mCherry-sCD95L at 163 \pm 19 min and 152 \pm 17 min, respectively (Figure 3.40h). Cell death times were reduced using these ligands in the presence of M β CD to 111 \pm 12 min and 117 \pm 10 min, respectively. For IZ-sCD95L and mCherry-IZsCD95L, median cell death times in control conditions were 52 \pm 4 min and 58 \pm 4 min, respectively. In the presence of M β CD cell death times for those ligands were 47 \pm 4 min and 57 \pm 5 min.

Upon competition with non-tagged ligands, mCherry-ligand fluorescence intensities declined over time. In contrast, receptor intensities globally remained constant for mCherry-sCD95L treated cells and slightly increased sometimes for mCherry-IZsCD95L treated cells (Appendix A, Figure A.1 and A.2). To compare the different conditions, the calibrated ligand intensity relative to receptor intensity was calculated and denoted as *Ratio* in the graphs (Figure 3.40). Comparing the different unbinding kinetics for cells that were only washed after ligand binding (*medium wash*), no striking differences in the ratio and in the ligand binding between the two ligands and in the presence or absence of M β CD were observed (black lines, Figure 3.40 and Figure A.1 and A.2).

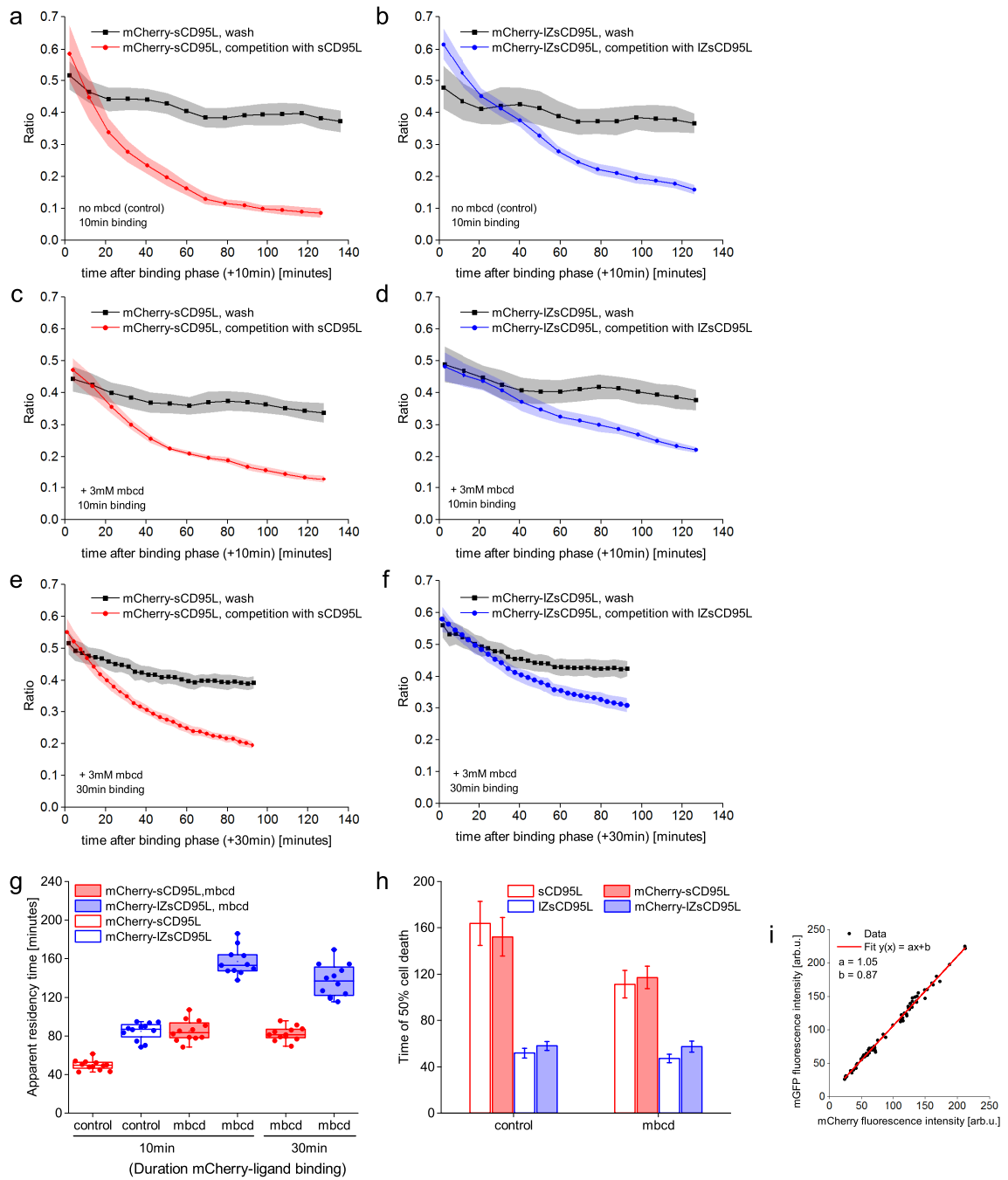


Figure 3.40: Unbinding kinetics upon medium wash or competition with non-labeled ligand. HeLa-CD95-mGFP cells were treated with mCherry-sCD95L (a,c,e) or mCherry-IZsCD95L (b,d,f) for 10 min (a-d) or 30 min (e,f). (a-f) Unbinding kinetics upon washing cells rapidly (<2 min) twice with medium (*wash*) or upon a washing step followed by addition of non-labeled ligand (*competition*). Of each of 3 fields (from one well) 4 sub-images were analyzed, mean \pm s.d. (g) Estimated apparent residency times of ratio data (a-f). (h) Median cell death time from three experiments using the same batch and concentration of ligand as for binding measurements, mean \pm s.e.m. of three experiments. (i) Calibration measurement of mCherry-Bid-mGFP protein, one data point = one cell. Linear fit of data to the model $y(x) = ax+b$.

Notably, clear differences between the wash- and the competition- unbinding kinetics were measured for each ligand condition (red and blue lines, Figure 3.40). This shows that ligand-bound CD95 receptors are present in different states on the cell. In order to facilitate comparison between different competition-unbinding kinetics, those kinetics were fitted to the exponential decay function $y(t) = a * \exp(-t/t_r)$ to obtain the apparent residency time t_r (Figure 3.40g). mCherry-sCD95L showed a median apparent residency time of 50 min when internalization was allowed, while block of internalization prolonged the residency time on the cell surface to 84 min (Figure 3.40a,c,g). For mCherry-IZsCD95L a similar behavior was obtained. This ligand resided in presence of internalization 87 min and in the absence of internalization 153 min (Figure 3.40b,d,g). This difference shows that ligand internalization contributes to signal loss at the cell surface over time in binding-competition experiments performed at 37°C. Moreover, mCherry-IZsCD95L showed a stronger avidity to the receptor than mCherry-sCD95L because addition of competitor resulted in longer residency times in the presence of M β CD (153 min compared to 84 min).

To test whether receptor oligomerization is stronger at later time-points, unbinding measurements in the presence of M β CD were also conducted upon binding of mCherry-tagged ligands for 30 min to the cells (Figure 3.40e,f). However, prolonging the binding phase did not increase the residency times as compared to data obtained with ligands incubated for 10 min. mCherry-sCD95L showed an unchanged residency time of 81 min and mCherry-IZsCD95L showed rather a slight decrease in the apparent residency time to 136 min.

To summarize, results obtained from unbinding measurements underscore a model in which CD95 receptors exists in at least two different states upon ligand binding. Moreover, the different receptor states were most likely formed to varying extent by the two ligand forms, with an increased avidity of mCherry-IZsCD95L to receptors compared to mCherry-sCD95L to receptors.

ODE-based description of binding kinetics

To test whether the ligand-induced trimerization (LIRT) model could explain the data, binding data and unbinding data were fitted at once to this model using the tool PottersWheel (Maiwald and Timmer 2008). I assumed three parameters for binding and cross-linking of the receptors: k_{on} and k_C for the forward reactions of binding ligand in solution and on the membrane, respectively. One parameter k_{off} was chosen for the three reverse reactions. To allow some freedom, offsets were included for binding data and a factor between 0.9 and 1.1 to account for the ligand concentrations (The PottersWheel code is documented in appendix B).

First, this model was not able to fit the data: this was due to the fact that a binding equilibrium was systematically reached below a ratio of one, at a ligand-receptor ratio of around 60%. To allow more freedom, the fraction of receptors that can be bound by ligand was described as a parameter and was fitted.

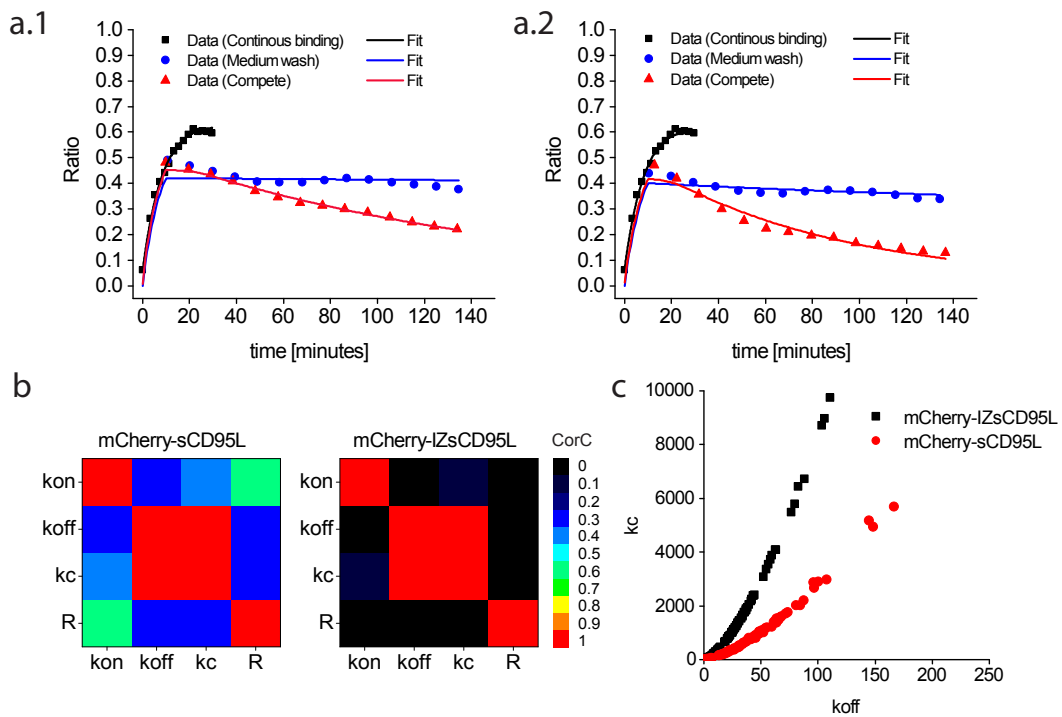


Figure 3.41: Ligand-induced receptor trimerization (LIRT) -model fit Data points were fitted 100 times to the LIRT model using PottersWheel (Maiwald and Timmer 2008). (a) Best fits, black: binding (data used for a.1 and a.2 from mCherry-IZsCD95L binding, same apparent binding was expected), blue: wash, red: competition with non-labeled ligand (a.1) mCherry-IZsCD95L (a.2) mCherry-sCD95L. (b) Correlation matrix showing the correlation coefficients (CorC) of the covariance matrix from obtained fitted parameter values of 80% best fits. Note the correlation between the k_c and k_{off} parameters (c) Parameter values of k_c and k_{off} obtained from the best 80% fits of 100.

One justification why only a fraction of receptors was bound came from the literature: It has been reported that the receptor can be cleaved through metalloprotease activity, releasing a small, about 10kDa fragment leading to partial loss of CD95 receptor apoptotic activity (Strand et al. 2004). Perhaps this might account for the observed, restricted binding behavior.

Next, I again performed parameter estimation by repeating the fitting procedure 100 times. For each fitting procedure the initial values for individual parameters were newly guessed. This time, including the parameter accounting for a fraction of receptors that can be bound, the LIRT-model was able to capture the data (Figure 3.41a).

For both ligands, a fraction of about $58\% \pm 0.99\%$ of receptors that can be bound was estimated. Given the ligand concentration, the parameter k_{on} was for mCherry-sCD95L $k_{on} = 1.17E+6 \pm 7E+4$ and for mCherry-IZsCD95L $k_{on} = 3.99E+6 \pm 1E+4$.

However, for both ligands, the two parameters k_c and k_{off} were not identifiable (Figure 3.41b,c). For mCherry-sCD95L treated cells the k_c was 999 ± 1105 and the k_{off} was 45 ± 33 , including results of the 80% of 100 best fits. Similarly, for mCherry-IZsCD95L treated cells the k_c was 2193 ± 2048 and the k_{off} was 39 ± 21 . Nevertheless, to illustrate the relation between the

non-identifiabilities of the parameter values, I plotted the obtained k_{off} against obtained k_c values of those 80% best fits (Figure 3.41b,c). By doing so, two different curves for the two different ligands were obtained, whereas mCherry-sCD95L showed systematically lower k_c values for a given k_{off} (Figure 3.41c).

To summarize, although not all kinetic parameters were identified, the LIRT-model captures the behavior of the kinetics of ligand binding and unbinding. The model would suggest, that cross-linking of receptors by ligand would be stronger with mCherry-IZsCD95L than for mCherry-sCD95L. Besides, the SB2RS-model was not able to capture the data because no parameter combination could be found that explain the difference between the wash- and competition-condition. In both models, LIRT and SB2RS, the same number of parameter and data-points were present. Using the SB2RS-model fitting mCherry-IZsCD95L data, best fits gave a value of $\chi^2/N = 0.71$, p-value $(N-p) = 0.62$, which were higher than the one obtained for the LIRT model with $\chi^2/N = 0.07$. Using the LIRT-model to fit mCherry-sCD95L data, I obtained similarly good fits with $\chi^2/N = 0.09$. Thus, unbinding measurement data would disprove the SB2RS-model or a simple binding mechanism as a possibility for receptor activation.

3.7.2 mCherry-sCD95L lowers the CD95 receptor mobility on living cells less than mCherry-IZsCD95L

To further test the potential difference in receptor cross-linking with the two ligands, I measured receptor clustering through receptor mobility.

The mobility of the receptor can be expressed by the diffusion coefficient of the receptor. It is dependent on the number of transmembrane regions of the protein complex spanning the lipid bilayer and the radius of the trans-membrane protein (see section 2.2.4, page 32). Receptor aggregates with higher subunit number would in theory diffuse slower than single receptors or those with lower subunit number. On top, association processes with other membrane proteins might lower the mobility of the receptor of interest. For example, depletion of the cadherin FAT1 has been shown to sensitize cells to CD95L, TRAIL and TNF- α induced cell death by increasing pro-caspase-8 recruitment (Kranz and Boutros 2014).

I assessed the mobility of CD95 receptors by performing FRAP experiments at different time-points upon ligand addition and by fitting the diffusion coefficient to the spatio-temporal intensity profile for each cell (see section 2.2.4, page 32). From unbinding experiments it was expected that the potential receptor-cross-linking equilibrium would be generated within 10 min after ligand addition (section 3.7.1) and would be maintained over time. Further, mCherry-sCD95L would potentially not cross-link receptors as much as compared to mCherry-IZsCD95L and therefore not lower the mobility of the receptor as strong.

First, the receptor mobility was assessed for equal concentration of 0.6 $\mu\text{g/ml}$ for

mCherry-sCD95L and mCherry-IZsCD95L. For this, HeLa stably expressing an shRNA against CD95 were used that expressed transiently CD95-YFP (Figure 3.42a). As equal ligand concentrations were used, differences in binding and receptor mobility were expected because the receptor occupancy should be higher for mCherry-IZsCD95L induced cells.

For mCherry-IZsCD95L induced cells, the receptor mobility dropped from $0.31 \pm 0.08 \mu\text{m}^2 \text{sec}^{-1}$ before induction to $0.11 \pm 0.02 \mu\text{m}^2 \text{sec}^{-1}$ after 40 min and for mCherry-sCD95L induced cells from $0.29 \pm 0.05 \mu\text{m}^2 \text{sec}^{-1}$ before induction to $0.17 \pm 0.01 \mu\text{m}^2 \text{sec}^{-1}$ after 110 min. Control cells showed a constant receptor mobility from $0.33 \pm 0.06 \mu\text{m}^2 \text{sec}^{-1}$ before induction to $0.30 \pm 0.09 \mu\text{m}^2 \text{sec}^{-1}$ at 70 min. The diffusion coefficients were estimated from curve fits with good confidence (Figure 3.42b).

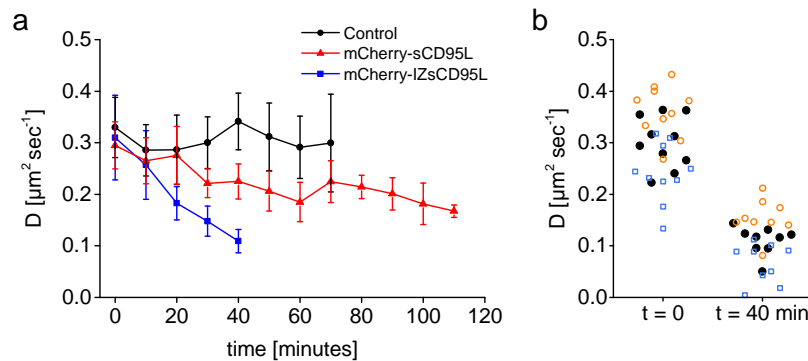


Figure 3.42: Fluorescence Recovery After Photobleaching. (a) HeLa-shRNA:CD95 cells expressing transiently CD95-YFP, stimulated with $0.6 \mu\text{g}/\text{ml}$ mCherry-sCD95L ($n=9$ cells) or mCherry-IZsCD95L ($n=10$ cells) or control medium ($n=10$ cells). (b) Estimated diffusion coefficients with corresponding upper (orange) and lower (blue) confidence level (95% interval) for time points $t = 0$ and $t = 40$ min of data obtained from cells induced with mCherry-IZsCD95L.

Next, I tested whether the two different ligands might induce receptor cross-linking differently, even with ligand concentrations that lead to same apparent binding kinetics. HeLa cells stably over-expressing CD95-mGFP were used and measured upon addition of control medium, $1.8 \mu\text{g}/\text{ml}$ mCherry-IZsCD95L or $6.4 \mu\text{g}/\text{ml}$ mCherry-sCD95L. MCherry-IZsCD95L-induced cells showed a median cell death time of around 60 min, and with mCherry-sCD95L around 2h 25 min. Because even smaller differences were expected than in the previous experiment and because the variation between single cells was high, experiments were repeated three to four times (Figure 3.44a-i). Then, to compare the receptor mobility of the different treatments, the mean of replicated FRAP time-series experiments was calculated and plotted together with the standard error of the mean. Cells induced with mCherry-sCD95L, showed a mean receptor mobility of $0.22 \pm 0.02 \mu\text{m}^2 \text{sec}^{-1}$ before induction which decreased to $0.13 \pm 0.02 \mu\text{m}^2 \text{sec}^{-1}$ at 110 min upon induction (Figure 3.44j).

Similarly, with mCherry-IZsCD95L induced cells, a decrease of receptor mobility from $0.25 \pm 0.03 \mu\text{m}^2 \text{sec}^{-1}$ before induction to $0.12 \pm 0.03 \mu\text{m}^2 \text{sec}^{-1}$ at 50 min upon ligand addition was observed. Control cells showed a receptor mobility of $0.27 \pm 0.06 \mu\text{m}^2 \text{sec}^{-1}$ before exchange of medium and a receptor mobility of $0.28 \pm 0.01 \mu\text{m}^2 \text{sec}^{-1}$ after 60 min. This shows that receptor mobilities decreased to same values with both ligands. However, the receptor mobility decreased with slower kinetics using mCherry-sCD95L than with mCherry-IZsCD95L (Figure 3.44j and Figure 3.43).

In order to test whether the receptor mobility is dependent on the interaction of CD95 to proteins inside the cytosol, I used CD95 that lack the cytosolic death domain (CD95- Δ DD-mGFP). The hypothesis was that formation of the DISC and recruitment of downstream signaling proteins might help receptor cross-linking. Deletion of the death domain was therefore thought to lead to milder receptor mobility changes than with wild type receptors. The diffusion coefficient for mCherry-sCD95L induced CD95- Δ DD-mGFP receptors declined from $0.27 \pm 0.02 \mu\text{m}^2 \text{sec}^{-1}$ before induction to $0.09 \pm 0.04 \mu\text{m}^2 \text{sec}^{-1}$ at 90 min. For mCherry-IZsCD95L induced cells, the mean receptor diffusion coefficient was $0.28 \pm 0.04 \mu\text{m}^2 \text{sec}^{-1}$ before induction and dropped to $0.09 \pm 0.02 \mu\text{m}^2 \text{sec}^{-1}$ at 60 min (Figure 3.45i). Again, mCherry-IZsCD95L-induced receptors showed a slightly faster or stronger decline in mobility than mCherry-sCD95L induced receptors (Figure 3.45i). Surprisingly, for both ligands, I observed a stronger decrease in receptor mobility upon ligand addition with receptors that lack the death-domain compared to full-length receptors (Figure 3.43). This might indicate that this deletion mutant of the receptor can be better cross-linked. Speculatively, receptor cross-linking might be hindered by proteins binding to the cytosolic part of the domain. Deleting this part of the receptor might cancel out this constrain and thereby facilitate further ligand induced receptor cross-linking.

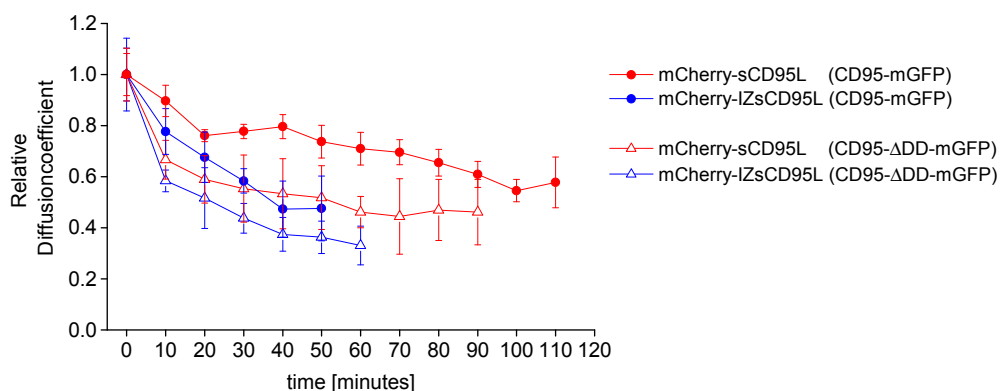


Figure 3.43: Relative diffusion-coefficient Mean data from diffusion-coefficient estimates were normalized to the value measured before ligand addition ($t = 0$). From this, the mean and \pm s.e.m. were calculated.

By applying FRAP, all receptor species on the cell are measured, namely all non-bound and bound receptors. Therefore, the measurement of the diffusion coefficient reflects an average value of all receptors. To test the sensitivity of the method to detect changes in receptor mobility, concentrations of mCherry-IZsCD95L were used (1.8-5.4 ng/ml) that led to same cell death time as with 6.4µg/ml mCherry-sCD95L. The fraction of bound ligand per receptor was expected to be very low. However, this has not been determined. Notably, the average mobility of receptors induced with low concentrations of mCherry-IZsCD95L remained constant over time. Systematically, but to a lesser extent than using higher concentrations, the average diffusion coefficient dropped shortly before the time of 50% cell death (Figure 3.45j).

This shows that the detection of changes in receptor mobility in FRAP experiments depended on the quantity of cross-linked receptor species formed. By using around 5ng/ml mCherry-IZsCD95L and around 6µg/ml mCherry-sCD95L, leading to same median cell death times, presumably highly different receptor occupancies would be obtained. The observation, that mCherry-sCD95L, but not mCherry-IZsCD95L led to strong changes in receptor mobility at the indicated concentrations shows that the vast majority of species that contributed to receptor mobility decrease are not consequently active receptor species, consistent with a ligand-induced receptor trimerization or oligomerization model.

To conclude, the CD95 mobility was reduced upon binding of mCherry-sCD95L and mCherry-IZsCD95L, respectively. Small differences in the kinetics of the mobility reduction could be observed for the two ligands for concentrations where equal apparent binding is observed. Presumably, not all receptors that were cross-linked and that led to a decrease in receptor mobility were at the same time active receptors. Thus, based on the small differences in the receptor mobility decrease that I observed, I would predict that only a small fraction of ligand-bound and cross-linked receptors exist in a cross-linking state that is sufficient to recruit FADD.

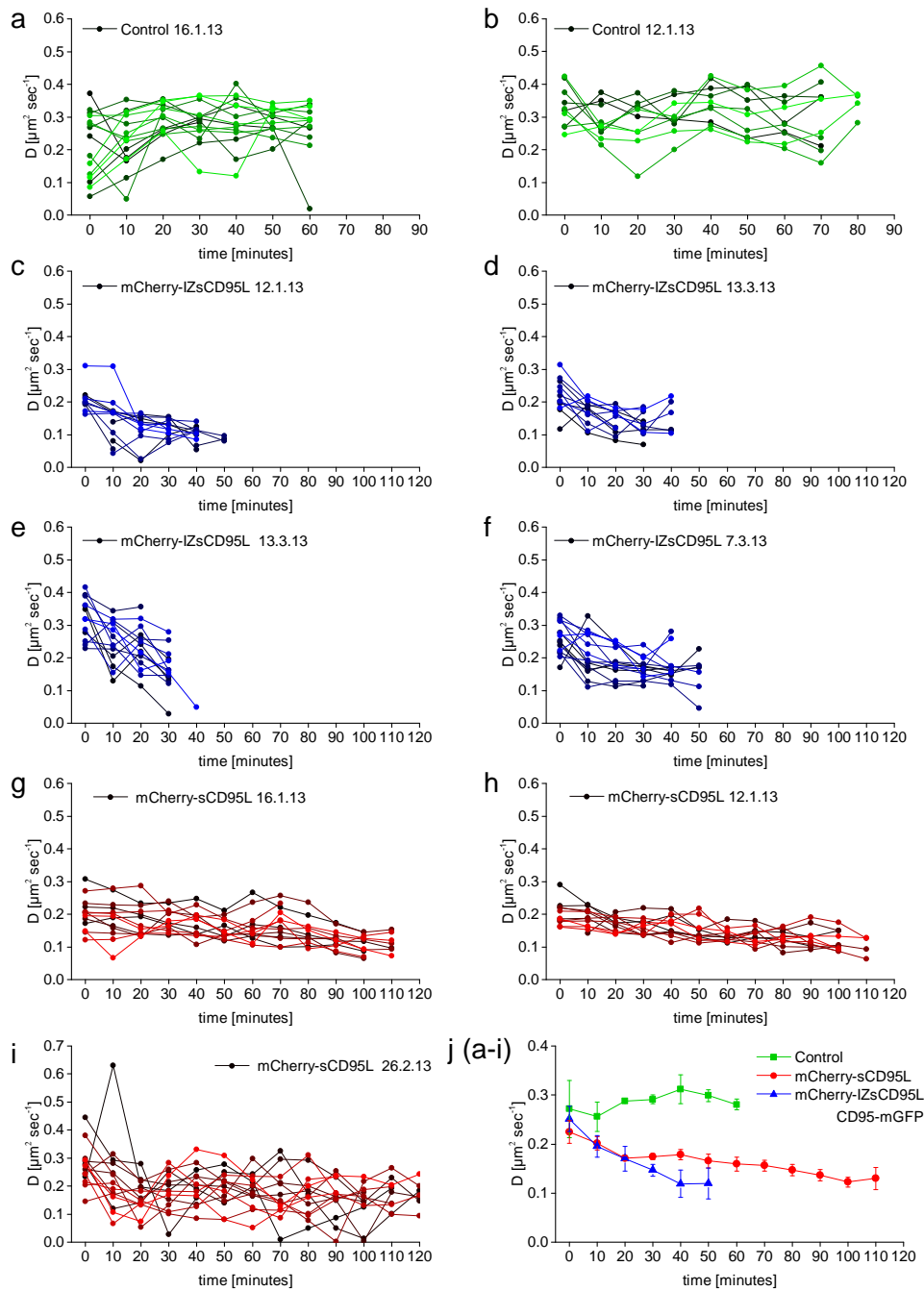


Figure 3.44: Diffusion-coefficient estimates of CD95-mGFP measured by Fluorescence Recovery After Photobleaching. (a-i), Each plot reflects one experiment consisting of multiple FRAP-experiments. One diffusion coefficient estimate was obtained by measurement of one HeLa-CD95-mGFP cell. Cells were measured repeatedly over time. (a,b) Medium exchange, no addition of ligand. (c-f) 1.8 $\mu\text{g/ml}$ mCherry-IZsCD95L. (g-i) 6.4 $\mu\text{g/ml}$ mCherry-sCD95L. Concentrations of the two different ligands led to same apparent binding. (j) Mean \pm s.e.m. for data shown in plots a-i).

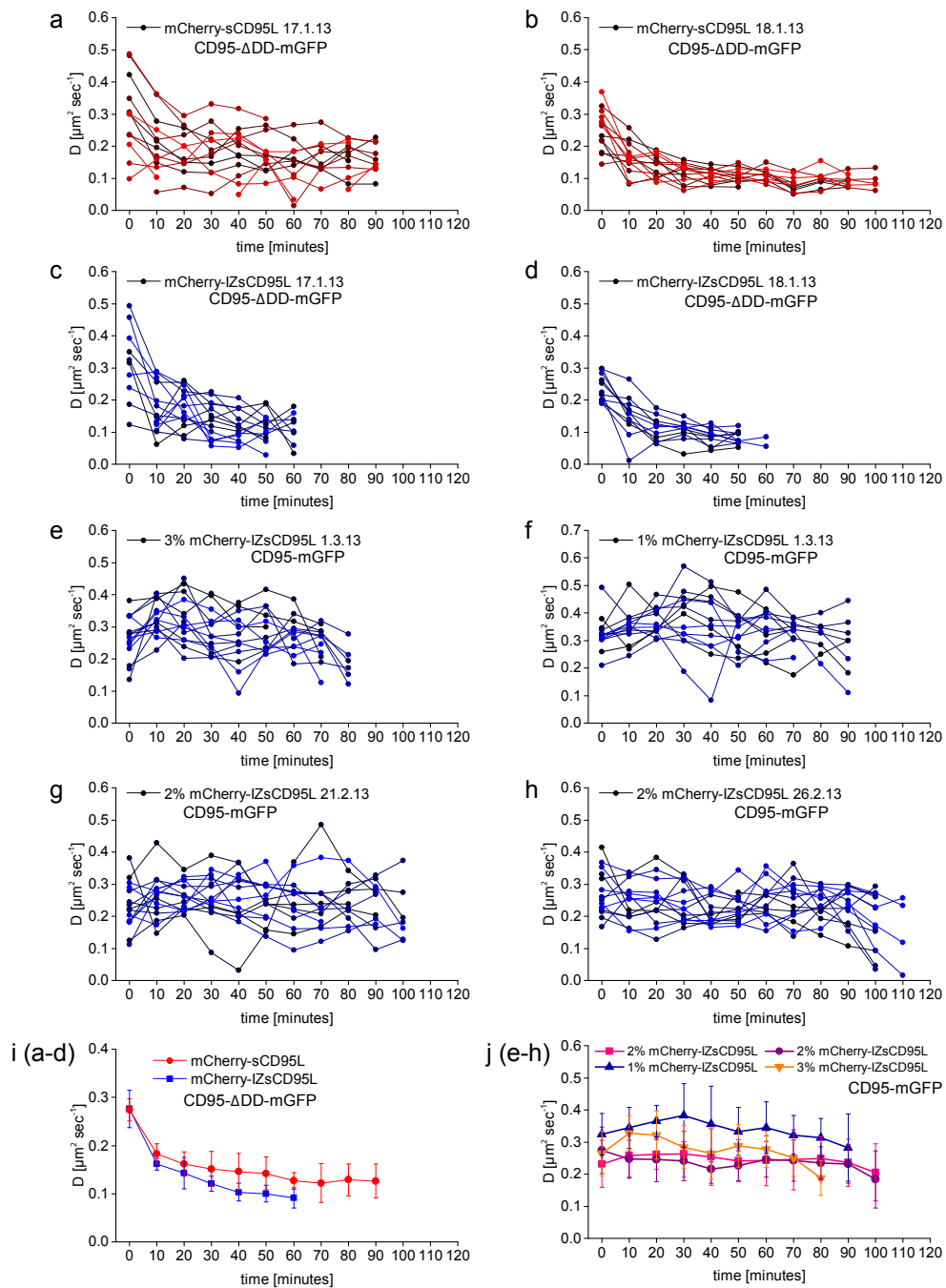


Figure 3.45: Diffusion-coefficient estimates of CD95- Δ DD-mGFP and CD95-mGFP. (a-h) Each plot reflects one experiment consisting of multiple FRAP-experiments. (a-d) HeLa cells transiently expressing CD95- Δ DD-mGFP. (e-f) HeLa-CD95-mGFP cells. (a,b) 6.4 μ g/ml mCherry-sCD95L. (c,d) 1.8 μ g/ml mCherry-IZsCD95L. (g-h) 1.8-5.4 ng/ml mCherry-IZsCD95L. (i) Mean \pm s.e.m. for data shown in plots a-d. (j) Mean \pm s.d. for data shown in plots e-h.

3.7.3 Summary: why sCD95L is a weak inducer of apoptosis

In order to induce apoptosis, the receptor CD95 needs a stimulus that enables the assembly of the death-inducing signaling complex (DISC). This signaling complex is known to contain FADD and caspase-8/-10. However, the molecular events that allow FADD and caspase recruitment are not fully understood. A better understanding of CD95L apoptosis induction was gained from combining cell death- and caspase-8 activity measurements with binding data. I set-up experimental workflows to measure binding kinetics of fluorescently tagged ligand to living cells. This allowed to estimate the receptor occupancy. As expected, sCD95L, inferred from mCherry-sCD95L measurements, had a low avidity to the receptor CD95. Although the increase of mCherry-sCD95L concentration led to a comparable receptor occupancy as with mCherry-IZsCD95L, this did not lead to the same activity. Cell death and caspase-8 activity were restricted not only by the receptor level but also by the avidity of the ligand. To recapitulate, for the two different ligands, two different "limits" were reached: cell death of HeLa-CD95 cells could be seen earliest at around 40 min using IZsCD95L and earliest at around 80 min using sCD95L. Thus, binding and activity data excluded the hypothesis that a simple ligand-receptor interaction (3:3 stoichiometry) directly leads to receptor activation. Moreover, using the two different ligands at concentrations where binding kinetics looked the same, I showed that FADD was recruited less by mCherry-sCD95L but that (processed) caspase-8 levels relative to FADD levels were the same for both ligands at the DISC. Thus, the ability to activate caspase-8 was likely dependent on the ability to recruit FADD to the receptor. By this, I have excluded the hypothesis that FADD is recruited to any ligand bound receptor and would exclude that caspase-8 processing is limiting and inefficient.

Then, why FADD was inefficiently recruited to sCD95L bound receptors? Ligand-bound receptors likely exist in at least two different states. A model assuming simple binding followed by a second reaction (SB2RS-model) was compared to the ligand-induced receptor trimerization model (LIRT-model): I performed unbinding kinetic experiments and concluded that the LIRT-model, but not the SB2RS-model, is likely to occur. Measurements of the mobility of the receptor underlined these findings. Thus, FADD may be recruited to a subset of sufficiently cross-linked receptors, a kinetic process that was slower with sCD95L than with IZsCD95L. Notably, FADD recruitment kinetics were generally slow compared to ligand binding and displayed a non-exponential or "shoulder"-like shape. Moreover, by using dominant inactive mutants of Rab as well as the drugs monensin and M β CD, I observed that block of ligand internalization augments cell death and caspase-8 activity. One explanation might be that internalization competed with receptor cross-linking kinetics. My data furthermore show that the cytosolic domain was not required for ligand internalization, ligand binding or receptor cross-linking. Still, a stronger decrease in receptor mobility with this receptor mutant was observed. This indicated that proteins associated to the cytosolic domain impeded or that a conformational change slowed down receptor cross-linking of full-length CD95.

4 Discussion

4.1 NK cell mediated protease activity measurements

In this study, fluorescent probes have been tested for their functionality to report NK92-C1 cell mediated proteolytic activity inside HeLa cells. The involvement of Granzyme A, B and M in NK92 cell mediated cell death of HeLa cells was expected based on previous observations (Mahrus and Craik 2005; Martinvalet et al. 2009; Choi and Mitchison 2013). In this work, different fluorescent reporters containing the amino-acid sequences *RIEADS*, *ELQTD*, *IETD*, *IGNRS* and *KVPLG* were tested to study CD95-dependent and independent protease activity as well as their subcellular localization.

Among others, I was able to confirm the localization CD95-dependent caspase-8 activity at the plasma membrane in target cells by applying NK92-C1 cell as stimulus. This shows that the caspase-8 activation mechanism is determined by the cell and not by the form of ligand, consistent with results from this work using sCD95L, IZsCD95L and antibody cross-linked sCD95L (section 4.3.5).

4.1.1 Granzymes

Pinkoski and colleagues showed that recombinant, FITC-labeled granzyme B can enter cells by internalization in the absence of perforin and that the presence of perforin led to release of granzyme B into the cytosol (Pinkoski et al. 1998). This would not exclude the possibility that granzyme B entry occurs from the plasma membrane when pore formation is efficient.

Strikingly, in this work granzyme B activity showed a similar activity pattern as caspase-8: the membrane-standing probe MyrSnap2-RIEADS-mGFP (granzyme B) was more efficiently cleaved compared to the cytosolic probe (NES-RIEADS-mGFP) and the nuclear probe (H2B-RIEADS-mGFP). These findings would support data from Lopez and others in that granzyme entry can occur through the cell membrane (Lopez et al. 2013). However, a partial endosomal activity would still be consistent with my data. Though, as granzyme B is not a membrane protein, I would have anticipated that proteases delivered by NK cells would be soluble. In this case, equal membrane-probe and cytosolic-probe cleavage would have been expected. In this context, the RIEADS-cleaving protease delivered by the NK cell might eventually not diffuse freely into the target cell cytosol. Substrate cleavage at the membrane could be a consequence of trapping of the enzyme close to the cell membrane.

Intriguingly and in line with the observation that the membrane reporter for granzyme B was most efficiently cleaved, I found that its inhibitor serpinB9 was accumulated at the cell membrane. For the cell, targeting the inhibitor at the site of granzyme entry and activity would provide an efficient strategy to block protease activity. Consistently, Mcl-1, which is another substrate for granzyme B, was shown to be located at the plasma membrane (Han et al. 2004; Herrant et al. 2004). Notably, the subcellular localization of Mcl-1 changed upon cleavage, since a deletion mutant of Mcl-1 imitating cleavage by granzyme B (Herrant et al. 2004), or a GFP-Mcl-1 fusion protein (Akgul et al. 2000) showed localization of the protein to mitochondria. It might be interesting to find whether serpinB9 localizes in both states, the active or the latent one, to the membrane. Furthermore, the subcellular localization of other inhibitors, like CrmA, which is a viral protein that inhibits caspase-8 and granzyme B (Tewari et al. 1995, Zhou et al. 1997), might be similarly localized at compartments where the active protease would be expected, in this case possibly the plasma membrane.

Hypothetically, serpinB9 localization in the cell could be accomplished by posttranslational modification of the protein that enables the protein to tether itself to the membrane, for example by palmitoylation. Another way would consist in binding to a protein that is located to the cell membrane. For example, interactions of serpinB9 to several proteins were found by screenings (Database BioGRID). Among them, CD81 has been shown to interact with serpinB9 by affinity capture followed by mass spectrometry (Perez-Hernandez et al. 2013). CD81 is a transmembrane protein (a tetraspanin), which expression has been shown in HeLa cells (Bartee et al. 2010).

Granzyme B mediated probe cleavage in the cytosol and at the cell membrane are consistent with models in which granzyme B was shown to cleave predominantly cytosolic substrates such as Bid at the site *IEADS* and caspase-10 at the site *IEADA* (Talanian et al. 1997, Barry et al. 2000). Nevertheless, cleavage of cytosolic substrates such as caspase-8 or Bid by granzyme B might be not as effective to promote cell death as the direct cleavage of nuclear targets. Despite nuclear RIEADS-probe cleavage was visibly small in my experiments, this might have efficiently resulted in cell death induction without necessity of caspase activation. Indeed, granzyme B cleavage of the protein DNA-PK at the amino acid sequence *VGPDF* with $2.5 \pm 0.8 \cdot 10^6 \text{ M}^{-1} \text{ sec}^{-1}$ seemed to be particularly efficient (Andrade et al. 1998). Caspase-independent activity is supported by my data which showed different cell death morphologies under control, Bcl-X_L and zVAD-fmk condition. However, this death might have been also attributed to granzyme A activity for example.

In my study, the incubation of cells using 50µM zVAD-fmk did not prevent RIEADS-probe cleavage. Indeed, by applying 50µM zVAD-fmk and 2µM (or around 60µg/ml) recombinant granzyme B plus addition of lytic agent, Thomas and co-workers found that granzyme B can induce caspase-independent MOMP (Thomas et al. 2001). However sensitivity of granzyme B to zVAD-fmk was reported (reviewed in Ewen et al. 2012). Notably, the strength of granzyme B

activity would determine whether MOMP or transient loss of the mitochondrial membrane potential effectively leads to cell death or not, in a caspase- dependent or independent manner (discussed in Waterhouse et al. 2006). The apparent contradiction granzyme B inhibition by zVAD-fmk require further investigation. Importantly, granzyme B might bind and cleave different peptide sequences with different efficiencies: $\frac{k_{cat}}{K_M}$ ratios in the range of 10^4 to 10^6 $M^{-1} sec^{-1}$ have been measured (reviewed in Kam et al. 2000). The cleavage sequence VGPDFGR has been used recently in a FRET-based reporter assay to measure granzyme B activity in HeLa cells (Choi and Mitchison 2013) and earlier in a fluorescence-quenching based assay to measure granzyme B activity in Jurkat, Ramos, and Daudi cells (Packard et al. 2007). By comparing the different reported cleavage sites with one assay, including the cleavage site VAD, from zVAD-fmk, one might yield insights into the mechanism of granzyme B substrate binding.

In order to measure granzyme A activity in single living cells, the cleavage site *IGNRS* (Mahrus and Craik 2005) was used in fluorescent reporters. While cytosolic (NES-IGNRS-mGFP) and mitochondrial (MitoNEET-IGNRS-mGFP) cleavage could not be verified, the cleavage of the nuclear probe H2B-IGNRS-mGFP was observed. This would be consistent with the observation of nuclear targets of granzyme A and at the same time rule out the possibility that granzyme A is active in the cytosol. Concluding, it is tempting to speculate that activation, or a putative release of inhibition, of granzyme A occurs inside the nucleus or in mitochondria where substrates of granzyme A have been found. An alternative explanation might be that granzyme A is active but brought by a cargo to those compartments shielding granzyme A from the probes and other substrates present in the cytosol.

4.1.2 Timing of RIEADS-probe and ELQTD-probe cleavage

One of my aims was to investigate on the single cell level how caspase-8 and granzyme B activities would coordinate cell death. After assessing specificities for the ELQTD-probe and the RIEADS-probe, the two reporters were used in combination in one single cell in order to distinguish the two different protease activities, one caspase-8, the other granzyme B.

Strikingly, CD95-dependent ELQTD-probe activity was systematically observed in those cells that were dying later than those cells showing RIEADS-probe cleavage despite similar timing of NK-cell contacts. In principle, one explanation would be that CD95L has activated an activity that prevents or hampers cell death, however, because both caspase-8 and granzyme B were known to induce death in HeLa cells, I would rule out this possibility. The rate of RIEADS-probe cleavage was typically very high and thus indicates high concentration of the probe-cleaving protease. Cells that showed RIEADS-probe cleavage also died quickly. The data would support the idea that CD95-dependent caspase activity required simply more time to integrate the death signal and when RIEADS-proteolytic activity was present, cells subsequently died early. For the fraction of

cells that died late, the CD95 pathway possibly served as a back-up mechanism for NK91-C1 mediated target cell death in a case where granzyme activity is not present. Importantly, the CD95 receptor level had no visible impact on ELQTD-cleavage rates and transient knockdown of CD95 had to be tight in my experiments in order to block this cleavage, which was achieved by expressing the shRNA for three days. Why would CD95 pathway require more time to induce cell death than granzymes? Granzyme amounts should be compared relative to amounts of active caspase-8. While binding of CD95L to CD95 might be fast processes within the synapse, activation of the receptor, FADD recruitment and caspase-8 activation are steps that might take time and that do not play a role in granzyme B mediated death. The description of the temporal behavior of these processes in dependence on the CD95 ligand dose and avidity are topic of section 4.3. Furthermore, activation of the mitochondrial pathway is a limiting step (Albeck et al. 2008). While caspase-8 and caspase-3 activation in the CD95 pathway are controlled by other proteins, granzyme B is thought to be delivered by the NK cell as an active enzyme and might encounter less regulatory proteins. Eventually, the limiting step for granzyme B dependent cell death in HeLa cells might be only its efficient delivery in high doses.

4.2 TIRFM photobleaching analysis to derive the stoichiometry of labeled complexes

To investigate the oligomerization state of sCD95L, TIRF microscopy of single molecules was applied in this study. By having the control protein IZ in hand and the knowledge that sCD95L proteins should be trimeric at nM concentration, one motivation was to measure the subunit stoichiometry of proteins at much lower protein concentration, namely in the the picomolar range, a concentration that might be relevant in a physiological context. Thus, I took advantage of the property that sCD95L, the IZ-domain and to a lesser extent also mGFP bind unspecifically, and therefore randomly, to the glass of the labtek chamber. For proteins that do not bind to glass, TIRF measurements could be carried out on an artificial support. However, the capturing method must not affect the oligomerization status or bring species too close together.

To simplify the analysis, we developed and tested a method, termed *Last identified Step-Analysis* (LiSA) to derive the subunit stoichiometry of soluble protein complexes from single molecule photobleaching data. Typically photobleaching data were analyzed by counting the number of steps in each single time-trace (Ulbrich and Isacoff 2007). In theory, for homogeneous complex stoichiometries, each trace should show the same number of steps reflecting the subunit number. However, oftentimes a distribution of observed steps is determined. This was interpreted to mean that a significant fraction of the molecules may not be fluorescent. This occurs for example, when expressing receptors that are genetically tagged with fluorescent proteins on cells, because of the maturation kinetics of the chromophore or when fluorophores are bleached before image

acquisition or for labeling efficiencies lower than 100%. Together, this reduces the probability to detect fluorophores that should however be present. Thus, a generally accepted bottleneck in analyzing photobleaching data is that molecules are only fluorescent with a probability p that is smaller than one (section 2.2.5). Using the method of counting all steps, this probability can in theory be fitted to the data, but it is of advantage to know this probability from measurements, for example by using control proteins of known subunit stoichiometry. This probability p should be relatively easy quantifiable by applying FCS measurements, because the relation of the measured molecule number N and the brightness B_N of this measured molecule number composed of subunits u having each a fluorophore brightness b , $\frac{B_N}{b} = u \cdot N$, is typically used to assess the subunit stoichiometry of proteins. This requires to measure several molecule dilutions in the range of 1 to 100 molecules per $1 \mu\text{m}^3$ (confocal volume). It also implies that this work-flow for the estimation of p would be especially suitable for soluble proteins and for plasma membrane proteins of which expression level can be easily varied and which diffusion is fast enough, because this way of estimating the fluorescence probability p can be biased by bleaching of molecules during the detection of the immobile or slowly diffusing molecule.

In theory, the LiSA method should be in no way inferior to the step-counting method. I observed that by having a probability p of 90 -100%, at the tested complex number and noise values, the LiSA method robustly predicted the correct subunit stoichiometry. As I worked with proteins that were expressed and secreted by 293T cells, I would assume that perhaps cleavage of the fluorophore from the protein, but not necessarily incomplete maturation of the fluorophore, could have led to a suboptimal fluorescence yield. Indeed, 8% of cleavage of mGFP-IZsCD95L, but no cleavage of mGFP-sCD95L, was observed (page 39). Nevertheless, this value lies within the range where the LiSA method should have detected the correct oligomerization state without including the probability p in the analysis, as done in this work. Moreover, my strategy was to compare the oligomerization degree of the mGFP-tagged ligands sCD95L and IZsCD95L to a known trimeric protein. As the same pattern in the analysis for mGFP-IZ, mGFP-IZsCD95L and mGFP-sCD95L proteins was observed, I concluded that those proteins form trimers. In the LiSA method, the probability p cannot be fitted, but the theoretical last-step-distribution can be simulated for known values of the probability p , which could be determined in a separate experiment, and eventually compared to the measured last-step-distribution.

To conclude, the LiSA method has some attractive advantages. One is that it relies on counting only the last bleaching step of the photobleaching time series of a single protein trace instead of counting all visible bleaching steps. Moreover, regarding the settings of photobleaching and comparison of measurements of different days, the illumination power determines how fast proteins are being bleached and therefore how many steps of bleaching are likely to be observed. As the LiSA method is based on a simple model that relates the temporal behavior of the intensity decay to the last-step-distribution of proteins or protein-complexes, protein

measurements should be comparable from experiments that were acquired with different laser intensities. Finally, another clear advantage is that the LiSA method showed to be very robust to intensity fluctuations, which are typically more apparent when using protein based fluorophores but less when using organic dyes. Thus, even when no clear bleaching steps would be observable, the subunit stoichiometry would be reliably identified.

4.2.1 Oligomerization state of sCD95L

In this study, I showed by using TIRFM that soluble CD95L is trimeric at pM concentration. Previously, Berg and her colleagues have found by using gel filtration and biochemical cross-linking assays that human sCD95L (amino acids 137-291) constitutes a trimer (Berg et al. 2007). To verify the oligomerization state of soluble CD95L and their corresponding fluorescent fusion proteins mCherry-sCD95L and mGFP-sCD95L, I applied biochemical protein cross-linking, FCS/FCCS next to TIRF microscopy. In this study, trimerization of the different non-tagged and tagged proteins sCD95L, IZ and IZsCD95L was confirmed. In biochemical cross-linking studies, mCherry-IZsCD95L, but not mCherry-sCD95L adducts showed also high-molecular-weight (HMW) assemblies for strong cross-linking conditions using 1 mM BS³ next to the majority of trimeric adducts. This is similar to the study of Berg and colleagues who measured trimeric but also HMW-adducts of TNC-sCD95L. They found that those assemblies constituted inactive proteins. Even if this fraction would have resembled active species, I concluded that the difference in avidity of mCherry-IZsCD95L and mCherry-sCD95L and other observations (section 4.3.5) cannot be solely explained from this low fraction of potentially misfolded proteins. To test the possibility that sCD95L subunits dissociate and reassemble, FCCS measurements of mCherry- and mGFP tagged soluble CD95L or TNF- α in the range of 0.5 to 6 μ g/ml were performed. Subunit exchange of the mCherry- or mGFP- tagged ligands sCD95L and IZsCD95L or of the IZ-domain was not detected. Although these measurements represent only a qualitative way to assess dissociation, they had the advantage to be easily measured and controlled. Moreover, by applying FCS, the average molecule number and the average diffusion time of the fluorescent protein in a solution can be measured. Thereby, dissociation of the different trimeric proteins into monomers was excluded from the observation that the maximal expected difference in diffusion time of mCherry and the mCherry-tagged ligands was measured. Together with the results from TIRFM, soluble CD95L most likely exist as a stable trimer at pM concentration.

4.3 sCD95L signal integration

The threefold stoichiometric binding of TNF family ligands and receptors serves as a platform on the extracellular side of the cell which signal is transmitted and sensed by cytosolic protein.

Though, in the absence of ligand-receptor clusters by microscopy, still differences in activity between the two ligand forms, sCD95L and IZsCD95L, were observed. With a trimerized ligand, up to three receptors can meet, but it is not precisely known whether receptor trimerization is sufficient to recruit the adaptor molecule FADD to the receptor. Potentially, a conformational change of the receptor precedes recruitment of FADD (Scott et al. 2009). Moreover, FADD dimerization or self-association was shown to help FADD binding to the receptor (Sandu et al. 2006). As a consequence, FADD binding to the receptor might occur in a cooperative manner. As caspase-8 is known for inter-dimer cleavage (Chang et al. 2003), next to the three receptors at least one other receptor is required to recruit a second caspase-8 dimer, indicating that receptors must be cross-linked, at least transiently, more than into trimers to allow inter-dimer cleavage. This is consistent with the observation that secondary, antibody cross-linked trimers are potent inducers of apoptosis (Holler et al. 2003).

In this work, I wanted to understand the kinetics of pathway activation, starting from the ligand binding.

4.3.1 Ligand-binding kinetics by confocal microscopy

Addressing ligand-receptor binding by using radioactive labeled ligand has the unique advantage of comparing broad ligand concentration ranges as this labeling is still very sensitive towards lower concentrations. With the development of fluorescence based assays ligand binding measurements by microscopy are possible, though in a more confined range.

In this study, binding kinetic measurements of ligand to adherent cells was established by using confocal fluorescence microscopy. This had the advantage that the receptor occupancy was quantifiable by labeling the receptor and the ligand in a one-to-one manner. Though receptor levels were artificially increased for this approach using stable HeLa cell lines stably over-expressing the receptor, similarly high CD95 receptor levels can be found in a patho-physiological context in the *type II* hepatocellular carcinoma cell line HepG2 (unpublished measurements from Dr. Johanna Berndt).

Differences in pathway activation for sCD95L and IZsCD95L were measurable at high receptor levels. This allowed to relate binding with pathway initiation kinetics such as FADD recruitment and caspase-8 activation.

Moreover, using imaging it was possible to distinguish binding from internalization events. Separate experiments using wash-buffers at low pH confirmed internalization and outer membrane binding. Importantly, specificity was guaranteed by working under optimized signal to noise conditions and control experiments. Therefore, the approach to measure binding by fluorescently labeled ligands and receptors by confocal microscopy represented a suitable and attractive method.

4.3.2 CD95L-CD95 interaction strengths

By applying binding experiments at different pH, binding and unbinding experiments and FRAP-measurements, ligand-driven receptor changes by the two forms of ligand could be observed.

At equal concentration using confocal microscopy, ligand binding of mCherry-IZsCD95L was much stronger than with mCherry-sCD95L showing that trimeric IZsCD95L has a higher avidity. Over this receptor range of about 10^5 per cell, an about three-fold higher concentration of mCherry-sCD95L was necessary to achieve same apparent binding as with mCherry-IZsCD95L.

The difference in avidity to CD95 between the two forms of ligand was underscored by binding experiments at different pH, which suggested that between IZsCD95L and CD95 receptors more stabilizing electrostatic interactions were formed than in mCherry-sCD95L:CD95 interactions.

With respect to the study of Boschert and co-workers (Boschert et al. 2010), it would be interesting to find which of the amino acids in the three sCD95L receptor binding clefts promote the binding to receptors most? Mutagenesis of amino acids within the IZsCD95L that might mediate binding to CD95 and comparison of the binding by these mutants to sCD95L could provide this information. Moreover, the characterization of the receptor-ligand interaction at different pH served as a tool to get insights into the potential binding behavior in the different compartments of the cell, namely the cell surface, endosomes and lysosomes. Notably, for mCherry-sCD95L, signaling from the plasma membrane and from early endosomes, at pH 6.5, would be conceivable. For mCherry-IZsCD95L, binding to CD95 would be moreover theoretically possible in endosomes and late endosomes as binding was stable at pH 5.0.

4.3.3 Fluorescence recovery after photobleaching: measurements of CD95 mobility

In order to assess the oligomerization of CD95 receptors upon CD95L addition, the kinetics of the receptor mobility decrease upon soluble CD95L addition was assessed. FRAP measurements of the receptor mobility showed a high cell-to-cell variation, possibly due to the different receptor mobilities themselves but possibly also due to the analysis and fitting procedure. Although a decrease in diffusion coefficient can be measured relatively easily upon ligand addition, it was difficult to judge from single experiments whether average receptor mobilities over time between the two forms of ligand were indeed different. That is why many FRAP experiments were performed upon ligand addition. Perhaps the comparison of only two time points, before ligand addition and at a defined time point, would have also provided these informations of receptor mobility decrease. However, by looking at the binding kinetics, more insight could be obtained: the receptor mobility decrease appeared immediately after ligand addition and looked like an exponential decay, contrasting to the slow and delayed activity of caspase-8. This means, that the receptor mobility decrease comes along with binding, which looks like an exponential recovery, and thus ligand binding has induced an increase in the membrane spanning area associated to the

receptor CD95. One interpretation is that binding leads to efficient CD95 cross-linking, with both ligands mCherry-sCD95L and mCherry-IZsCD95L, respectively. The relatively fast receptor mobility decrease for the two ligands would indicate that the majority of receptors were already clustering, but that, according to the differences in activity, only a fraction of those were signaling-competent. Alternatively or in addition, another putative interaction of the receptor, driven by the ligand, might have led to the decrease in receptor mobility, for example a putative interaction to FAT1. It was found that the atypical cadherin FAT1, a single-spanning transmembrane protein, antagonized CD95 dependent caspase-8 activation (Kranz and Boutros 2014). By calculating the mean and the s.e.m. of repeated FRAP experiments a difference between the two ligand forms could be determined. Receptors induced with mCherry-sCD95L were on average more mobile than receptors induced with mCherry-IZsCD95L at concentrations with same apparent binding. This supports the view that clustering of receptors by sCD95L is inefficient.

Strikingly, the receptor that lacked the death domain showed a faster decrease in receptor mobility than the wild type receptor for cells induced with mCherry-sCD95L and mCherry-IZsCD95L, respectively. How might this be accomplished? Excluding sterical differences due to mGFP-fusion as a reason for that, this would mean that death domain binding proteins would slow down ligand-driven receptor clustering as proposed in the following.

Importantly, the receptor CD95 binds also to proteins inside the cell in its non-ligated state: Segura and co-workers found that the long form of protein *Fas Apoptosis Inhibitory Molecule* (FAIM, Schneider et al. 1999) is released from the receptor upon receptor ligation (Segura et al. 2007). In their work, FAIM_L protected PC12 cells and cortical neurons from apoptosis. The same group also showed that FAIM_L especially influenced death of type II cells and found that the protein moreover interacts with XIAP (Moubarak et al. 2013). The authors proposed that FAIM_L would have a dual role, first at the DISC, and secondly by interfering with caspase-3 activity. Consistently, another study showed that the microRNA MiR-133b reduced FAIM expression and sensitized HeLa cells to CD95-induced apoptosis (Patron et al. 2012). A non-related protein with similar name, FAIM2/LFG (Lifeguard), was also reported to bind intracellularly to the receptor CD95 without disturbing the interaction of CD95 to FADD (Somia et al. 1999). Interestingly, FAIM2/LFG was shown to be over-expressed in breast cancer cell lines and in high tumor grades of primary breast tumors (Bucan et al. 2010). Another example is the protein *Apoptosis-linked gene 2* (ALG-2), which binds the receptor and dissociates from it after induction with the anti-CD95 antibody CH11 (Jung et al. 2001). In contrast, the protein F1A α (Protein fem-1 homolog B) is an oligomeric death receptor-binding protein homologous to the *Caenorhabditis elegans* sex-determining protein FEM-1, which can be cleaved by a caspase-like protease, was found to help apoptosis induction by association to the receptor (Chan et al. 1999).

Based on FRAP data, I suggest that CD95 receptor clustering kinetics are potentially *impeded* by

dissociation processes that precede FADD recruitment and caspase-8 activation. Thus, replacement processes, rather than only recruitment processes at the CD95 receptor upon ligand binding might contribute to the observed delay between ligand binding and FADD recruitment and could explain the different observed kinetics of CD95-mGFP and CD95- ΔDD -mGFP receptor mobility (Figure 4.1).

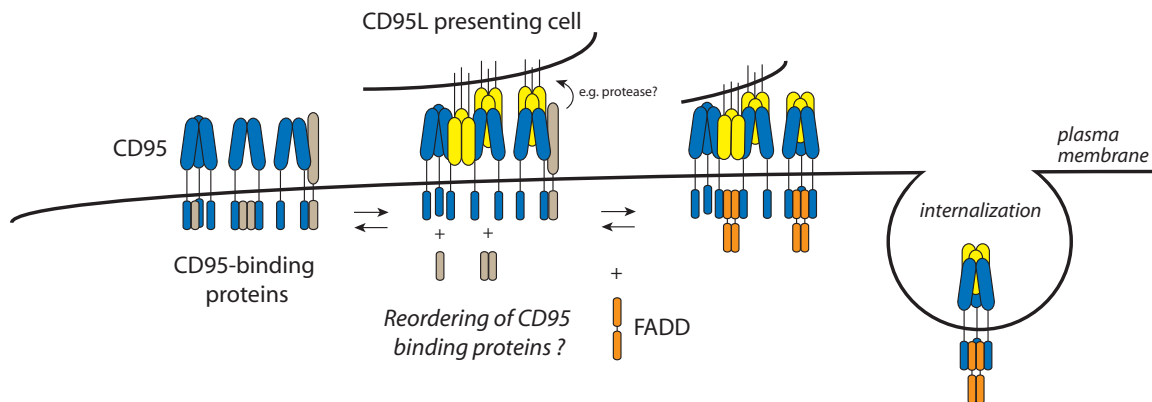


Figure 4.1: Reorganization rather than recruitment? CD95 receptor can bind to proteins when not ligated (see text for references). Ligand binding might induce dissociation and association processes, rather than recruitment processes only. Cleavage of the ligand, for example by ADAM10 (Schulte et al. 2007), could allow ligand internalization.

4.3.4 Unbinding kinetics

In this work, CD95 ligand unbinding kinetics were interpreted with the help of an ODE-based model. It is well accepted that the CD95 receptor exists in a pre-oligomerized state. Because of that, the formation of ligand-receptor networks is conceivable (Figure 1.13 green box, Goldstein 2000, Chan 2007).

To differentiate simple one-to-one interactions followed by clustering from stepwise receptor trimerization, I measured the unbinding kinetics of the two ligand forms using confocal microscopy. The here modeled ligand-induced receptor trimerization using the LIRT-model presented a way to mathematically describe trimerization kinetics, while the SB2RS-model described simple three-to-three binding kinetics followed by a clustering event, resulting in the same number of parameter, namely three, to model the binding kinetics. The modeling of networks would have required several further assumptions to be made, like the size of the network (Goldstein and Perelson 1984), that cannot be given by my data.

Indeed, the LIRT-model, but not the SB2RS-model could reproduce the data. However, we failed in the attempt to identify the parameter k_C , for cross-linking of receptors on the cell membrane, and the parameter k_{off} describing unbinding events of the ligand from the receptor. Nevertheless, the observation of slower unbinding kinetics for the IZ-form of ligand compared to the weaker

binding ligand form can be explained by assigning different receptor cross-linking parameter values for a given k_{off} value ("dissimilar non-identifiability", Figure 3.41). This illustrated that, in the frame of this model, sCD95L would cross-link the receptor less than the ligand IZsCD95L. The range of values found for the parameter k_c and k_{off} was large. Values of k_c higher than $1 \mu\text{m}^2 \text{molecules}^{-1} \text{min}^{-1}$ already would lead to very fast trimerization kinetics of receptors compared to binding. Most of the bound ligand would then reflect trimerized ligand. Such a model would be supported by the observation that the unbinding kinetics did not change when comparing unbinding kinetics at 10 and 30 minutes (half-life of mCherry-sCD95L ≈ 81 min, half-life of mCherry-IZsCD95L ≈ 153 min) and would be further backed up by the observation that the receptor mobility decreased for both ligand forms immediately, without delay, upon ligand addition. Nonetheless, in this model, based on the data, trimerization of CD95 by sCD95L should be less efficient than trimerization with IZsCD95L.

Notably, the quantitative description of binding using ODE-based modeling predicted that not all receptors on the plasma membrane could be bound by ligand. This prompted me to check whether extracellular cleavage of the receptor was reported. The work of Strand and co-workers would indeed support this hypothesis (Strand et al. 2004). They found that CD95 can be cleaved at two sites by MMP-7 metallo-protease activity, resulting in a truncated receptor form that either lacks the first amino acids 1 to 35 or 1 to 49 and that transmitted the ligand signal less efficiently at comparable receptor levels. Importantly, cleavage at amino acid 49 would remove a small part of the PLAD (amino acids 42-66, Edmond et al. 2012), and might thus interfere with receptor self-assembly. Indeed, in different reports (for example Algeciras-Schimmich and Peter 2003, Lavrik et al. 2008, and in this work Figure 3.30, page 95), two bands corresponding to the full-length form of CD95 and a putative cleaved form were detected. In my work, the size difference was about 10 kDa. However, those bands might also correspond to differently glycosylated receptor molecules. Furthermore, the amino acid sequence of CD95 contains a signal sequence for localization that is potentially cleaved after amino acid 25, resulting in a protein size difference of about 2.7 kDa (Database UniprotKB information). Therefore, the composition of these two bands seen by western blot remains to be determined but may correspond to receptor cleavage.

To conclude, regarding the binding mode, the following arguments speak against a simple one-to-one/three-to-three binding mode of CD95L to CD95: (i) Cell death of the two different ligands reached different median death times at saturation, (ii) compensating ligand concentration towards same apparent binding of both ligands did not result in same cell death kinetics, (iii) for both ligands unbinding measurements using non-labeled competitor showed faster kinetics compared to medium-wash conditions (*accelerated unbinding*, Lauffenburger and Lindermann 1996) and (iv) the mobility of the receptor decreased over time upon ligand addition.

4.3.5 FADD recruitment and caspase-8 activation

In this study, CD95L dose-response measurements showed that the concentration of active caspase-8, seen in form of substrate cleavage rates, could predict the median cell death time in a non-linear manner. This was because for high ligand concentrations and thus small cell death times, caspase-8 cleavage rates reached saturation. However, a linear correlation of caspase-8 onset of activity and median cell death was drawn (page 84). A relation between the shape of the progress curve of caspase-8 substrate cleavage and the time of cell death from single cell data was already shown in Beaudouin et al. 2013, as normalization of substrate cleavage data to end time points, where cell death occurred, typically showed overlapping curves. Remarkably, I observed in this work that this relation was independent of the form of ligand. This emphasizes that the mechanism of caspase-8 activation, and therefore potentially also receptor activation, follows the same mechanistic events for the different forms of ligand. Assuming that the rate of substrate cleavage was proportional to the amount of enzyme being activated, my data showed that caspase-8 was activated in a ligand dose dependent and receptor level dependent manner. With increasing ligand doses, for both forms of ligand, the rate first increased but then showed saturation. Similarly, with increasing ligand concentration, the cell death time first decreased and then showed saturation. As caspase-8 substrate cleavage reached higher values and cell death times reached lower values, respectively, for IZsCD95L than for sCD95L, I concluded that sCD95L ligand has a limited capacity to activate caspase-8 enzymes.

I would exclude the possibility that only a small fraction of higher oligomerized and active IZsCD95L contributed to increased cell death kinetics, as (i) FRAP measurements reflect measures of the average mobility of many hundreds to thousands receptors on the membrane, (ii) binding of mCherry-tagged IZsCD95L reflect binding of the majority of ligands which are trimeric and (iii) FADD recruitment kinetics showed strong membrane recruitment of FADD to the plasma membrane. The latter observation could be reproduced in the meantime by Dr. Joël Beaudouin in the lab, by using stable HeLa cell lines lacking endogenous expression of FADD and reconstituted with GFP fusions of FADD.

Krippner-Heidenreich and colleagues used protein chimeras containing the extracellular domain of TNFR1 and TNFR2, respectively, fused each to the cytosolic domain of CD95. In their study it was found that FADD recruitment is controlled by the ligand receptor interaction because soluble TNF- α efficiently clustered at the cell surface on TNFR1 chimeras and efficiently recruited FADD (for FADD recruitment, two time points were compared). While efficient binding, but no clustering and no FADD recruitment was observed in TNFR2 chimeras with soluble TNF- α , secondary cross-linking of the ligand finally induced clustering on TNFR2 chimeras and FADD recruitment. This was supported by their observation that soluble TNF- α bound to TNFR2 showed a short half-life of 1.2 min and an extended half-life of 14.5 min for binding to cells when the ligand was secondary cross-linked (Krippner-Heidenreich et al. 2002).

Similarly, I aimed at interpreting both, ligand-unbinding kinetics and FADD-recruitment. However, I was particularly interested in FADD recruitment kinetics. Strikingly, I observed that FADD-mGFP recruitment kinetics did not follow an exponential behavior like ligand binding and receptor diffusion-coefficient decrease but displayed a shoulder-like form in *type II* HeLa cells (Figure 3.31f, page 97). This indicated that binding of FADD possibly relies on the efficient receptor activation, presumably by receptor clustering by the ligand. This view is further supported by the observation that much less FADD was immunoprecipitated in mCherry-sCD95L treated cells than in mCherry-IZsCD95L treated cells. Furthermore, in line with the observation that mCherry-sCD95L treated cells show faster unbinding kinetics and a weaker decrease in receptor mobility than mCherry-IZsCD95L treated cells, FADD-mGFP recruitment to receptors was delayed with mCherry-sCD95L compared to mCherry-IZsCD95L treated cells, when ligand concentrations of same apparent binding were used.

Notably, by relating FADD-mGFP recruitment to the onset of caspase-8 activity under these experimental conditions, I noticed that the time when caspase-8 activity begun corresponded to the time when cytosolic FADD decreased about 20% for both ligands (Figure 3.31f and 3.28d). Moreover, FADD-levels correlated well with levels of processed caspase-8 indicating that caspases can be efficiently activated once FADD is recruited to the receptor. This suggests that FADD recruitment, and as a prerequisite also receptor cross-linking, but not caspase-8 processing, are limiting steps in sCD95L induced caspase-8 activity and apoptosis.

Despite quick DISC formation was reported in *type I* Hut78 and CD95 over expressing K50 cells and SKW6.4 cells using 2 µg/ml Apo1-3 antibody as a stimulus (Kischkel et al. 1995), less efficient DISC formation was systematically observed in a panel of *type II* tumor cell lines induced with Apo1-3 or IZsCD95L (Algeciras-Schimmich et al. 2003). Thus, my data would suggest that one component that constitutes the difference between *type I* and *type II* cells is the recruitment efficiency of FADD to the receptor, which most likely is linked to CD95 oligomerization efficiency.

4.3.6 CD95L internalization competes with receptor activation kinetics in HeLa

Internalization of CD95 has been observed and was shown to impact CD95 signal transduction, as reviewed in Schütze et al. 2008.

In this work, I observed that at same apparent surface binding, more mCherry-IZsCD95L than mCherry-sCD95L was internalized. This could indicate that *activated* receptors were internalized because more caspase-8 activity and more FADD recruitment was observed with mCherry-IZsCD95L.

Moreover, tube-like structures of CD95-mGFP were observed that also co-localized with mCherry-sCD95L. Perhaps, those structures resemble small early endosomes traveling along the cytoskeleton or resemble tube-formed early endosomes (Figure 4.2). As CD95-mGFP, mGFP fused to the cytosolic domain, was visible, I would predict that recruitment of FADD to those

tube-like structures is possible. In the here studied *type II* cells, internalization concerned only a small proportion of ligand-bound receptors, in line with the observation, that the membrane probe was stronger cleaved than the cytosolic probe. Nevertheless, in *type I* cells, which show more internalization (Schütze et al. 2008), those proportions might switch towards recruitment of FADD to intracellular structures. Finally, signaling from the observed larger, presumably multi-vesicular endosomes (Raiborg et al. 2003), would be physically prohibited, as receptors have no access to the cytosol. This was visualized by mCherry-fluorescent endosomal structures, which at the same time did not show mGFP fluorescence anymore, most likely due to pH-quenching (Figure 4.2).

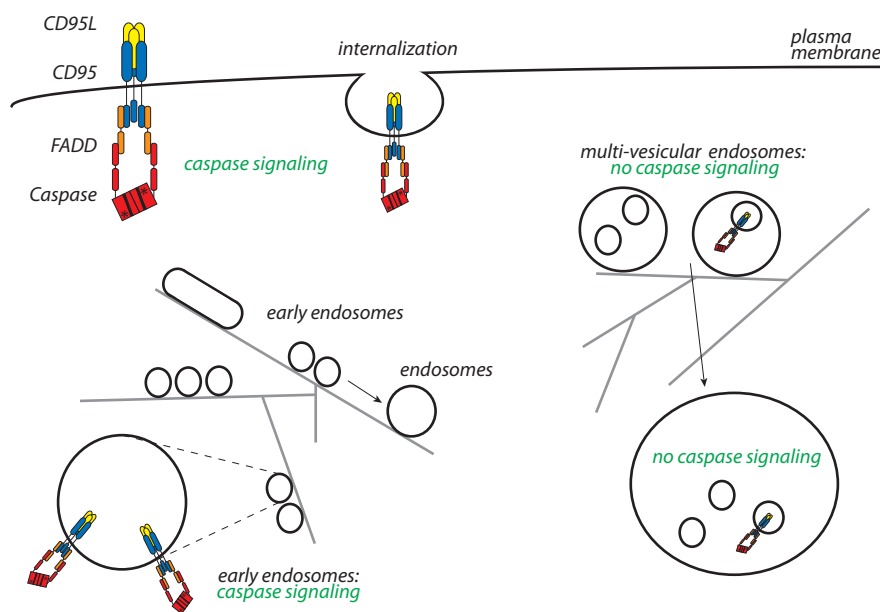


Figure 4.2: Endosomal CD95 receptor signaling might only occur from early endosomes. In HeLa cells signaling from the plasma membrane was mostly observed. Imaging and binding results would indicate that signaling from early endosomal structures would theoretically be possible. Black lines: plasma membrane and endosomes, grey lines: cytoskeleton.

To summarize, I concluded that internalization of CD95L in HeLa cells quenches the ligand signal, because (i) block of internalization by M β CD, monensin or expression of Rab-inactive mutants enhanced cell death, (ii) caspase-8 activity correlating with cell death was enhanced upon block of internalization, (iii) ligand-containing vesicles (mCherry) did not co-localize with pH sensitive mGFP-CD95 fluorescence. I would like to point out that the over-expression of Rab-inactive mutants can lead to spontaneous cell death independently of CD95L induction. Transfection for Rab protein expression in HeLa cells was optimized so that spontaneous death of Rab-mutants was only observed at the second day after transfection but not at the first day. Still, a sensitizing effect cannot be completely excluded. Moreover, the cell surface receptor level was not tested for

Rab-inactive mutant over-expressing cells.

With the drug monensin, receptor signaling is presumably prolonged by preventing the endocytic traffic of early endosomes to late endosomes and lysosomes. This was underlined by results obtained from over-expression of Rab inactive mutants. Since Rab5a mediates the fusion of the plasma membrane to early endosomes, receptor inactivation by internalization was possibly blocked by over-expression of Rab5a(S34N).

The fine tubular-like network which was sensitive to M β CD, and to a lesser extent also to monensin, could reflect small early endosomes that were not fused yet. Incorporation of small endosomes into larger endosomes then could have led to quenching of the mGFP signal while keeping and enlarging the mCherry signal (Figure 4.2). It remains unclear to which extent inactive or active, bound or unbound receptors are internalized, therefore, a full model describing binding and internalization was not attempted.

Regarding the mechanism of internalization, clathrin but also caveolin-mediated endocytosis is conceivable based on the observation that the ligand co-localizes with Rab5a and Rab4a and that pathway activation is hampered by M β CD treatment. This drug is also known to disrupt lipid rafts (Ivanov 2008). Involvement of lipid-rafts in CD95 receptor activation was predominantly expected in *type I* cells but exists also in *type II* cells as it is thought to promote pathway initiation at the plasma membrane by helping receptor clustering (Eramo et al. 2004). In case accumulation of receptors into lipid-rafts would have enhanced receptor activation kinetics in the here studied HeLa cells, this enhancing effect was potentially surpassed by the diminishing effect of ligand internalization and resultant signal quenching.

Appendix

A Unbinding measurements using confocal microscopy

The following two figures contain supportive information for results presented in section 3.7.1, page 112.

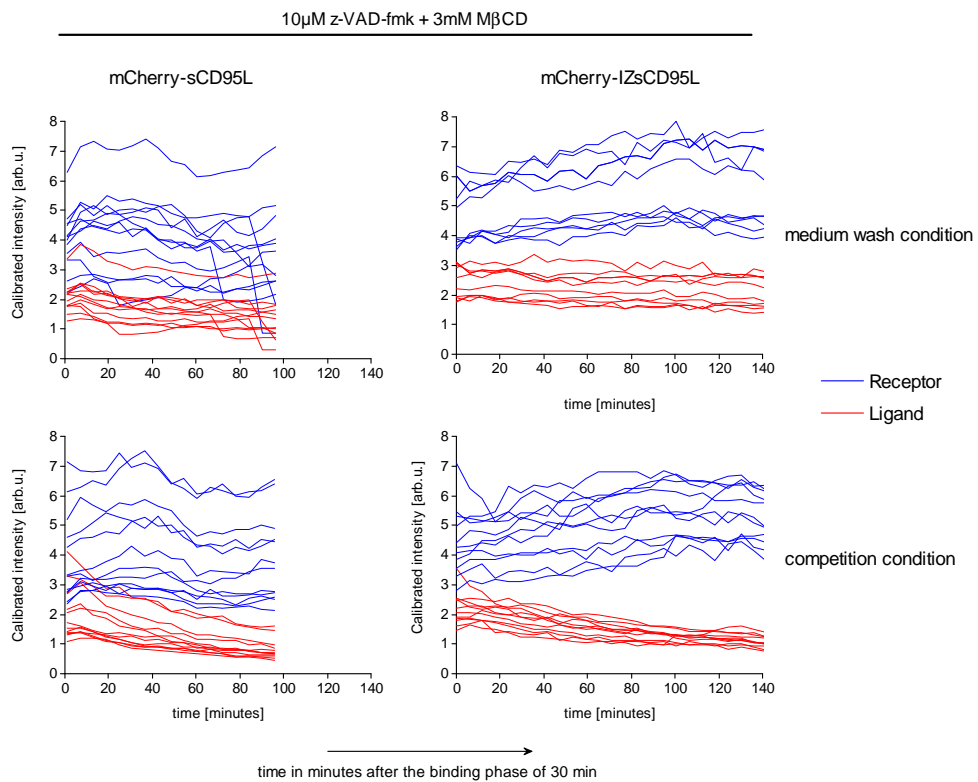


Figure A.1: Unbinding kinetics supplementary data 1. The different plots show calibrated fluorescence intensity data of mCherry-ligand and CD95-mGFP. Each trace represents a field of about 2 to 5 cells analyzed as reported in this work (section 3.5, page 87).

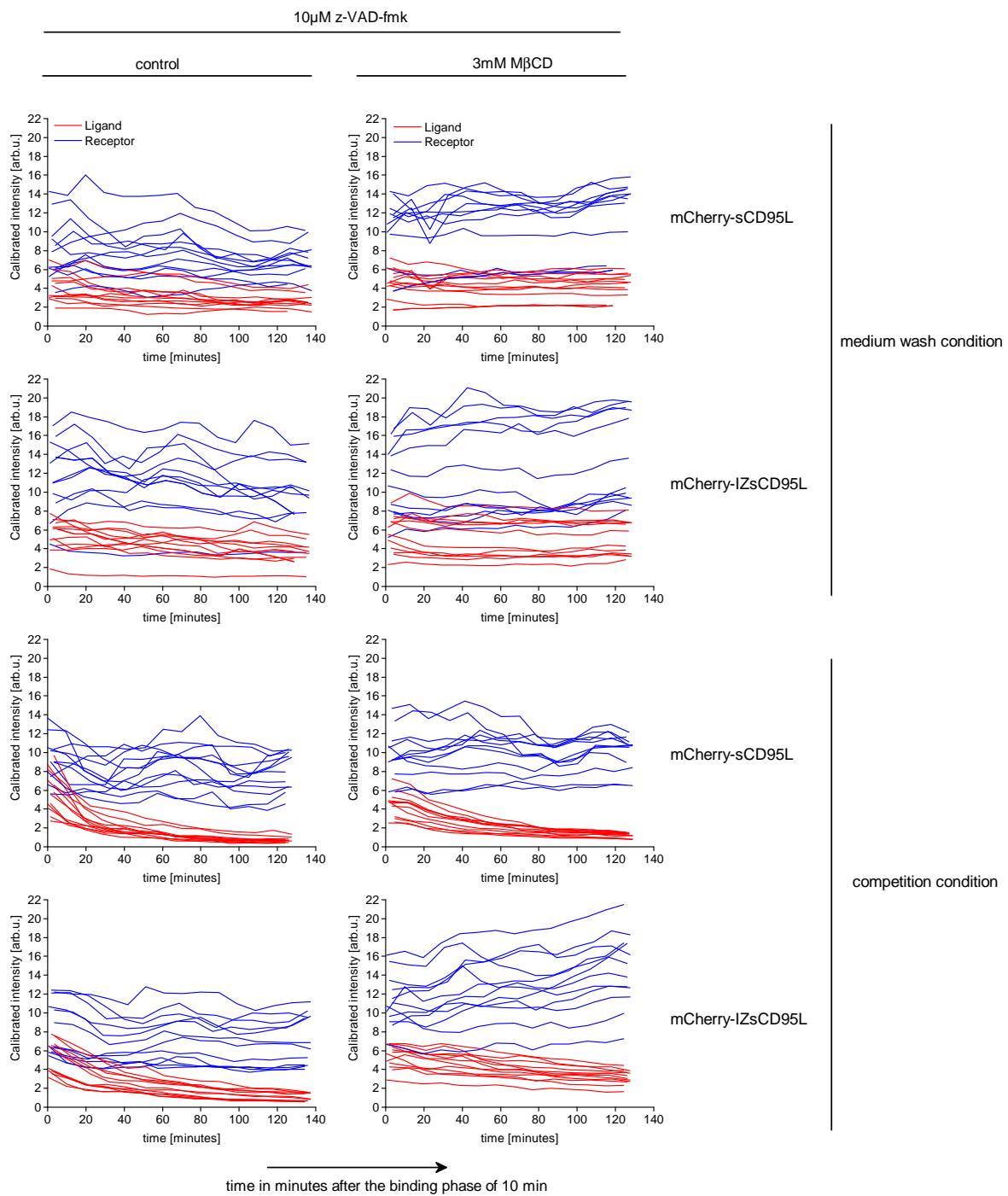


Figure A.2: Unbinding kinetics supplementary data 2. The different plots show calibrated fluorescence intensity data of mCherry-ligand and CD95-mGFP. Each trace represents a field of about 2 to 5 cells analyzed as reported in this work (section 3.5, page 87).

B Modeling binding kinetics

The Matlab® toolbox PottersWheel (Maiwald and Timmer 2008) was used to describe and fit at once the kinetic binding and unbinding data, including wash- and competition- conditions for a given ligand. Simulations are based on ordinary differential equations. The following table lists values for constants according to the experimental set-up and lists parameters used for the model. In the PottersWheel-code, L denoted trimerized, fluorescent ligand. L_c denoted trimerized non-fluorescent ligand.

Table B.1: Parameter and unit conversions

Parameters & constants	Value and unit
Reaction volume V_r	$1\text{E}+9\mu\text{m}^3$ ($1\text{cm} \cdot 1\text{cm} \cdot 10\mu\text{m}$) = $1\text{E}-6$ liter
Number of cells	30000 cells
Cell surface A	$2000 \mu\text{m}^2/\text{cell}$
Receptor, R	100 molecules/ μm^2
Ligand, L (constant stimulus)	$1 \mu\text{g}/\text{ml} \approx 1\text{E}-8 \text{ mol}/\text{liter} \approx 100 \text{ molecules}/\mu\text{m}^2$
k_{on}	$\text{liter mol}^{-1}\text{min}^{-1}$
k_c	$\mu\text{m}^2 \text{ molecules}^{-1}\text{min}^{-1}$
k_{off}	min^{-1}
$factlig$	$0.92 \leq factlig \leq 1.09$
$offset$	$\ll 0.06$

The following code was used for the ligand-induced receptor trimerization (LIRT) model (section 3.4.1, page 85 and section 3.7.1, page 114).

```

1 % PottersWheel model definition file
2 % For more information visit www.potterswheel.de
3 function m = trimer_rcleaved_LIRT()
4 m = pwGetEmptyModel();
5
6 % Meta information
7 m.name = 'trimerm';
8 m.modelFormat = 3.0;
9
10 % Default sampling time points
11 m.t = 0:5:200;
12

```

```
13 % X – Dynamic variables
14 m = pwAddX(m, 'R', 100, 'global', 0, 100, [], 'membrane');
15 m = pwAddX(m, 'RL', 0, 'fix', 0, [], [], 'membrane');
16 m = pwAddX(m, 'R2L', 0, 'fix', 0, [], [], 'membrane');
17 m = pwAddX(m, 'R3L', 0, 'fix', 0, [], [], 'membrane');
18 m = pwAddX(m, 'RLc', 0, 'fix', 0, [], [], 'membrane');
19 m = pwAddX(m, 'R2Lc', 0, 'fix', 0, [], [], 'membrane');
20 m = pwAddX(m, 'R3Lc', 0, 'fix', 0, [], [], 'membrane');
21
22 % K – Dynamic parameters
23 m = pwAddK(m, 'kon', 3000000.0, 'global');
24 m = pwAddK(m, 'koff', 0.30, 'global');
25 m = pwAddK(m, 'kc', 0.05, 'global');
26 m = pwAddK(m, 'offset', 0.0002, 'local');
27 m = pwAddK(m, 'factlig', 1, 'local', 0.9, 1.1);
28
29 % R – Reactions
30 m = pwAddR(m, 'R01', {'R'}, {'RL'}, {'L'}, 'C', [], 'k1*k2*r1*m1', {'kon', 'factlig'});
31 m = pwAddR(m, 'R02', {'RL'}, {'R'}, {}, 'C', [], 'k1*r1', {'koff'});
32 m = pwAddR(m, 'R03', {'RL', 'R'}, {'R2L'}, {}, 'C', [], '2*k1*r1*r2', {'kc'});
33 m = pwAddR(m, 'R04', {'R2L', 'R'}, {'R3L'}, {}, 'C', [], 'k1*r1*r2', {'kc'});
34 m = pwAddR(m, 'R05', {'R3L'}, {'R2L', 'R'}, {}, 'C', [], '3*k1*r1', {'koff'});
35 m = pwAddR(m, 'R06', {'R2L'}, {'RL', 'R'}, {}, 'C', [], '2*k1*r1', {'koff'});
36
37 m = pwAddR(m, 'R07', {'R'}, {'RLc'}, {'Lc'}, 'C', [], 'k1*k2*r1*m1', {'kon', 'factlig'});
38 m = pwAddR(m, 'R08', {'RLc'}, {'R'}, {}, 'C', [], 'k1*r1', {'koff'});
39 m = pwAddR(m, 'R09', {'RLc', 'R'}, {'R2Lc'}, {}, 'C', [], '2*k1*r1*r2', {'kc'});
40 m = pwAddR(m, 'R10', {'R2Lc', 'R'}, {'R3Lc'}, {}, 'C', [], 'k1*r1*r2', {'kc'});
41 m = pwAddR(m, 'R11', {'R3Lc'}, {'R2Lc', 'R'}, {}, 'C', [], '3*k1*r1', {'koff'});
42 m = pwAddR(m, 'R12', {'R2Lc'}, {'RLc', 'R'}, {}, 'C', [], '2*k1*r1', {'koff'});
43
44 % C – Compartments
45 m = pwAddC(m, 'membrane', 1);
46
47 % Y – Observables
48 m = pwAddY(m, 'Ratio', 'offset + 3*(RL+R2L+R3L)/100');
49
50 % Input
51 m = pwAddU(m, 'L', 'steps', [-10 0 10], [0 3e-8 0], [], [], [], [], {}, []);
52 m = pwAddU(m, 'Lc', 'steps', [-10 0 12], [0 0 3e-8], [], [], [], [], {}, []);
53
54 % Designer layout properties
55 m.designerPropsM = [1 1 1 0 0 0 400 250 600 400 1 1 1 0 0 0 0 0 0];
```

The PottersWheel code for the Simple binding two receptor states (SB2RS) model differed in the definition of the variables, parameters, reactions and the observables as follows:

```

1 % X – Dynamic variables
2 m = pwAddX(m, 'R', 100, 'global', 0, 100, [], 'membrane');
3 m = pwAddX(m, 'RL', 0, 'fix', 0, [], [], 'membrane');
4 m = pwAddX(m, 'RaL', 0, 'fix', 0, [], [], 'membrane');
5 m = pwAddX(m, 'RLc', 0, 'fix', 0, [], [], 'membrane');
6 m = pwAddX(m, 'RaLc', 0, 'fix', 0, [], [], 'membrane');
7
8 % K – Dynamic parameters
9 m = pwAddK(m, 'kon', 3000000.0, 'global');
10 m = pwAddK(m, 'koff', 0.1, 'global');
11 m = pwAddK(m, 'kc', 0.05, 'global');
12 m = pwAddK(m, 'offset', 0.000000001, 'local');
13 m = pwAddK(m, 'factlig', 1, 'local', 0.9, 1.1);
14
15 % R – Reactions
16 m = pwAddR(m, 'R01', {'R'}, {'RL'}, {'L'}, 'C', [], 'k1*k2*r1*m1', {'kon', 'factlig'});
17 m = pwAddR(m, 'R02', {'RL'}, {'R'}, {}, 'C', [], 'k1*r1', {'koff'});
18 m = pwAddR(m, 'R03', {'RL'}, {'RaL'}, {}, 'C', [], 'k1*r1', {'kc'});
19 m = pwAddR(m, 'R07', {'R'}, {'RLc'}, {'Lc'}, 'C', [], 'k1*k2*r1*m1', {'kon', 'factlig'});
20 m = pwAddR(m, 'R08', {'RLc'}, {'R'}, {}, 'C', [], 'k1*r1', {'koff'});
21 m = pwAddR(m, 'R09', {'RLc'}, {'RaLc'}, {}, 'C', [], 'k1*r1', {'kc'});
22
23 % Y – Observables
24 m = pwAddY(m, 'Ratio', 'offset + (RL+RaL)/100');

```


List of Abbreviations

arb.u.	arbitrary unit
DISC	death inducing signalling complex
DTT	dithiothreitol
Eq.	Equation
FADD	Fas associated death domain containing protein
FA/GA	Formaldehyde/Glutaraldehyde
f.c.	final concentration
FCCS	Fluorescence Cross Correlation Spectroscopy
FCS	Fluorescence Correlation Spectroscopy, method
FCS	Fetal Calf Serum, supplement in growth medium
Flag/ Flag-tag	Polypeptide of the amino acids DYKDDDDK
FRAP	Fluorescence Recovery After Photobleaching
FRET	Fluorescence Resonance Energy Transfer
H2B	Histone H2B, protein of the nucleosome
IZ	Isoleucine-Zipper
M β CD	methyl- β -cyclodextrin
mGFP	monomeric green fluorescent protein
M	molar, mol L ⁻¹
NES	nuclear export signal
NK cell	Natural Killer cell
PBS	phosphate buffered saline
PDB	Protein Data Bank by the RCSB (Research Collaboratory for Structural Bioinformatics)
sCD95L	soluble CD95L
s.d.	standard deviation
s.e.m.	standard error of the mean
shRNA	short hairpin RNA
SSE	Sum of Squared Errors
TIRFM	Total Internal Reflection Fluorescence Microscopy
zVAD-fmk	carbobenzoxy-valyl-alanyl-aspartyl-[O-methyl]-fluoromethylketone

List of Tables

2.1	Protein Sequences	22
2.2	Protein Sequences: Ligands and fluorescent protein fusions	23
2.3	shRNA	23
2.4	Protein sequence of fluorescent reporter	24
2.5	Antibodies for western blot and immunofluorescence	27
3.1	Protease activity reporters	42
3.2	Percentage of NES-ELQTD-mCherry and NES-RIEADS-mGFP probe cleavage	52
3.3	Expected molecular weight (MW) of recombinant proteins	64
3.4	Size estimates for proteins	67
3.5	Hydrodynamic radius estimates of proteins and relative fold difference to monomeric mCherry	68
3.6	<i>LiSA</i> method results	77
B.1	Parameter and unit conversions	141

List of Figures

1.1	Apoptosis drawing by Kerr, Wyllie and Currie	2
1.2	The intrinsic and extrinsic apoptosis pathway	3
1.3	Caspase activation platforms	4
1.4	Protein informations on CD95L, CD95, FADD, Caspase-8 and FLIP	6
1.5	Models of FADD binding to CD95 receptor	7
1.6	The active site of caspase-8 formed at the large and the small subunit	8
1.7	NK cell exocytosis	11
1.8	Granzyme- dependent cell death characteristics	12
1.9	Bid can be cleaved by granzyme B and caspase-8	12
1.10	Serpin inhibitory mechanism	13
1.11	Proteolytic cleavage of FasL/CD95L and secondary cross-linking by antibodies	14
1.12	Amino acids involved in the CD95L-CD95 interaction	15
1.13	Binding models: TNF- α to TNFR1 and TNFR2 and TRAIL to DR5	17
2.1	Progress curve of cleaved substrate with example of a fit to the <i>modified Gompertz</i> - model.	30
2.2	Diffusion of proteins in the membrane	33
2.3	Size estimates of the TNF- α -TNFR complex	33
2.4	FRAP-Stripe geometry	34
2.5	Fit of FRAP-recovery using temporal Gaussian profiles	35
2.6	Imaging mGFP-sCD95L molecules using TIRF microscopy	37
2.7	The binominal distribution.	38
2.8	Purified mGFP-sCD95L and mGFP-IZsCD95L	39
3.1	RIEADS- and ELQTD-probes are cleaved in target cells upon NK92-C1 cell co- culture.	44
3.2	Mitochondrial surface IGNRS- and RIEADS-probes are not cleaved.	46
3.3	Nuclear IGNRS- and RIEADS-probes are cleaved.	47
3.4	NK92-C1 mediated RIEADS substrate cleavage is independent of CD95.	49
3.5	NK92-C1 mediated ELQTD substrate cleavage.	50

3.6	ELQTD substrate cleavage upon NK92-C1 co-culture is predictive for target cell death time.	53
3.7	Bcl-X _L over-expression slightly delays cell death	55
3.8	NK cell mediated cell death- death morphologies	56
3.9	SerpinB9 blocks RIEADS-probe cleavage	58
3.10	SerpinB9 localization	59
3.11	The RIEADS-probe is cleaved at the plasma membrane	61
3.12	Biochemical cross-linking of purified proteins	65
3.13	Assessing mCherry-IZsCD95L cleavage extent	66
3.14	Diffusion times of mCherry tagged proteins	69
3.15	Oligomerization of sCD95L measured by FCCS	70
3.16	Spot number per image and example result of fits of photobleaching time-series	72
3.17	TIRFM photobleaching time-series simulation and analysis	75
3.18	LiSA robustness	76
3.19	LiSA method results - spot numbers over time	78
3.20	LiSA method results - SSE values	78
3.21	caspase activity upon sCD95L and IZsCD95L in HeLa and HeLa-CD95 cells	81
3.22	Correlation between caspase-8 activity with time of death.	82
3.23	sCD95L-mediated caspase-8 substrate cleavage and cell death are confined	84
3.24	Models of CD95 receptor binding	86
3.25	Binding measurements using confocal microscopy - ligand background	88
3.26	Binding measurements using confocal microscopy - image analysis	89
3.27	CD95-mGFP and CD95- Δ DD-mGFP bind the two different ligands eqally well.	90
3.28	Different activities despite same apparent binding	91
3.29	Models of FADD recruitment	92
3.30	Immunoprecipitation of mCherry-sCD95L and mCherry-IZsCD95L	95
3.31	FADD is inefficiently recruited to mCherry-sCD95L bound receptors.	97
3.32	Internalization of mCherry-tagged ligands	99
3.33	Ligand internalization	101
3.34	Co-localization of mCherry-sCD95L with Rab4a and Rab5a	103
3.35	Monensin and M β CD delay internalization	105
3.36	Cell death of HeLa-CD95-mGFP cells treated with Monensin and M β CD	106
3.37	Cell death of HeLa-CD95 cells expressing an inactive mutant of Rab4a, Rab5a, Rab7a or Rab11b	107
3.38	CD95L mediated cell death was accelerated when HeLa cells were treated with M β CD	109
3.39	Binding of mCherry-tagged ligands at different pH	110

3.40	Unbinding kinetics upon medium wash or competition with non-labeled ligand . . .	113
3.41	Ligand-induced receptor trimerization (LIRT)-model fit	115
3.42	Diffusion-coefficient of transiently expressed CD95-YFP upon ligand binding	117
3.43	Relative diffusion-coefficient	118
3.44	Diffusion-coefficient of CD95-mGFP upon ligand binding	120
3.45	Diffusion-coefficient of transiently expressed CD95- Δ DD-mGFP upon ligand binding	121
4.1	Reorganization rather than recruitment?	132
4.2	Endosomal CD95 receptor signaling might occur from early endosomes	136
A.1	Unbinding kinetics supplementary data 1	139
A.2	Unbinding kinetics supplementary data 2	140

Bibliography

- Aggarwal BB (2003) *Signalling pathways of the TNF superfamily: a double-edged sword*. Nat. Rev. Immunol. 3, 745–756.
- Ai HM, NC Shaner, Z Cheng, RY Tsien, and RE Campbell (2007) *Exploration of new chromophore structures leads to the identification of improved blue fluorescent proteins*. Biochemistry 46(20), 5904–10.
- Akgul C, DA Moulding, MRH White, and SW Edwards (2000) *In vivo localisation and stability of human Mcl-1 using green fluorescent protein (GFP) fusion proteins*. FEBS Letters 478(1-2), 72–76.
- Albeck JG, JM Burke, SL Spencer, DA Lauffenburger, and PK Sorger (2008) *Modeling a snap-action, variable-delay switch controlling extrinsic cell death*. PLoS Biol. 6(12), 2831–52.
- Alberts B, ed. (2008) *Molecular Biology of the Cell*. 5th ed. Garland Science.
- Algeciras-Schimmich A and ME Peter (2003) *Actin dependent CD95 internalization is specific for Type I cells*. FEBS Letters 546, 185–188.
- Algeciras-Schimmich A, EM Pietras, BC Barnhart, P Legembre, S Vijayan, SL Holbeck, and ME Peter (2003) *Two CD95 tumor classes with different sensitivities to antitumor drugs*. Proc. Natl. Acad. Sci. U.S.A. 100(20), 11445–50.
- Andrade F, S Roy, D Nicholson, N Thornberry, A Rosen, and L Casciola-Rosen (1998) *Granzyme B Directly and Efficiently Cleaves Several Downstream Caspase Substrates: Implications for CTL-Induced Apoptosis*. Immunity 8, 451–460.
- Arant RJ and MH Ulbrich (2014) *Deciphering the subunit composition of multimeric proteins by counting photobleaching steps*. Chemphyschem. 15(4), 600–5.
- Ashton-Rickardt PG (2010) *Serine protease inhibitors and cytotoxic T lymphocytes*. Immunol Rev. 235, 147–158.
- Austin C, D Cary, D Lawrence, A Peden, E Varfolomeev, K Totpal, AM DeMazière, J Klumperman, D Arnott, V Pham, RH Scheller, and A Ashkenazi (2006) *Death-receptor activation halts clathrin-dependent endocytosis*. Proc. Natl. Acad. Sci. U.S.A. 103(27), 10283–8.

- Axelrod D, DE Koppel, J Schlessinger, E Elson, and WW Webb (1976) *Mobility measurement by analysis of fluorescence photobleaching recovery kinetics*. *Biophys J.* 16(9), 1055–69.
- Bajorath J (1999) *Identification of the Ligand Binding Site in Fas (CD95) and Analysis of Fas-Ligand Interactions*. *PROTEINS Structure, Function, and Genetics* 35, 475–482.
- Bajou K, H Peng, WE Laug, C Maillard, A Noel, JM Foidart, JA Martial, and YA de Clerck (2008) *Plasminogen Activator Inhibitor-1 Protects Endothelial Cells from FasL-Mediated Apoptosis*. *Cancer Cell* 14(4), 324–334.
- Banner DW, A D'Arcy, W Janes, R Gentz, H Schoenfeld, C Broger, H Loetscher, and W Lesslauer (1993) *Crystal Structure of the Soluble Human 55 kd TNF Receptor-Human TNFP Complex: Implications for TNF Receptor Activation*. *Cell* 73, 431–445.
- Barnhart BC, EC Alappat, and ME Peter (2003) *The CD95 Type I/Type II model*. *Seminars in Immunology* 15, 185–193.
- Barnhart BC, P Legembre, E Pietras, C Bubici, G Franzoso, and ME Peter (2004) *CD95 ligand induces motility and invasiveness of apoptosis-resistant tumor cells*. *EMBO J.* 23(15), 3175–3185.
- Barry M, JA Heibin, MJ Pinkoski, SF Lee, RW Moyer, DR Green, and RC Bleackley (2000) *Granzyme B Short-Circuits the Need for Caspase 8 Activity during Granule-Mediated Cytotoxic T-Lymphocyte Killing by Directly Cleaving Bid*. *Mol. Cell. Biol.* 20(11), 3781–3794.
- Bartee E, CA Eyster, K Viswanathan, M Mansouri, JG Donaldson, and K Früh (2010) *Membrane-Associated RING-CH proteins associate with Bap31 and target CD81 and CD44 to lysosomes*. *PLOS ONE* 5(12), e15132.
- Beaudouin J, C Liesche, S Aschenbrenner, M Hörner, and R Eils (2013) *Caspase-8 cleaves its substrates from the plasma membrane upon CD95-induced apoptosis*. *Cell Death Differ.* 20(4), 599–610.
- Beck JS and HJ Goren (1983-1984) *Simulation of association curves and 'scatchard' plots of binding reactions where ligand and receptor are degraded or internalized*. *J. Receptor Res.* 3(6), 745–72.
- Becker V, M Schilling, J Bachmann, U Baumann, A Raue, T Maiwald, J Timmer, and U Klingmüller (2010) *Covering a broad dynamic range: information processing at the erythropoietin receptor*. *Science* 328(5984), 1404–8.
- Berg D, M Lehne, N Müller, D Siegmund, S Münkler, W Sebald, K Pfizenmaier, and H Wajant (2007) *Enforced covalent trimerization increases the activity of the TNF ligand family members TRAIL and CD95L*. *Cell Death Differ.* 14(12), 2021–2034.

- Berndt Johanna (2012) "Mechanisms of CD95-Clustering". PhD thesis. Ruprecht-Karls-Universität, Heidelberg, Germany.
- Bhat R and C Watzl (2007) *Serial Killing of Tumor Cells by Human Natural Killer Cells: Enhancement by Therapeutic Antibodies*. PLOS ONE 2(3), e326.
- Bird CH, VR Sutton, J Sun, CE Hirst, A Novak, S Kumar, JA Trapani, and Bird PI (1998) *Selective regulation of apoptosis: the cytotoxic lymphocyte serpin proteinase inhibitor 9 protects against granzyme B-mediated apoptosis without perturbing the Fas cell death pathway*. Mol Cell Biol. 18(11), 6387–98.
- Bladergroen BA, MC Strik, N Bovenschen, O van Berkum, GL Scheffer, CJ Meijer, CE Hack, and JA Kummer (2001) *The granzyme B inhibitor, protease inhibitor 9, is mainly expressed by dendritic cells and at immune-privileged sites*. J. Immunol. 166(5), 3218–25.
- Bloomfield VA, DM Crothers, and I Tinoco (jun), eds. (2000) *Nucleic Acids: Structures, Properties and Functions*. ISBN 978-0-935702-49-1. University Science Books.
- Boldin MP, EE Varfolomeev, Z Pancer, IL Mett, JH Camonis, and D Wallach (1995) *A Novel Protein That Interacts with the Death Domain of Fas/APO1 Contains a Sequence Motif Related to the Death Domain*. J. Biol. Chem. 270(14), 7795–7798.
- Boschert V, A Krippner-Heidenreich, M Branschädel, J Tepperink, A Aird, and P Scheurich (2010) *Single chain TNF derivatives with individually mutated receptor binding sites reveal differential stoichiometry of ligand receptor complex formation for TNFR1 and TNFR2*. Cell Signal. 22(7), 1088–96.
- Bucan V, K Reimers, CY Choi, MT Eddy, and PM Vogt (2010) *The anti-apoptotic protein lifeguard is expressed in breast cancer cells and tissues*. Cell. Mol. Biol. Lett. 15(2), 296–310.
- Buzza MS, CE Hirst, CH Bird, P Hosking, J McKendrick, and Bird PI (2001) *The granzyme B inhibitor, PI-9, is present in endothelial and mesothelial cells, suggesting that it protects bystander cells during immune responses*. Cell. Immunol. 210, 21–29.
- Carrington PE, C Sandu, Y Wei, JM Hill, G Morisawa, T Huang, E Gavathiotis, Y Wei, and MH Werner (2006) *The Structure of FADD and Its Mode of Interaction with Procaspase-8*. Mol. Cell 22(5), 599–610.
- Chan FK (2007) *Three is better than one: Pre-ligand receptor assembly in the regulation of TNF receptor signaling*. Cytokine 37(2), 101–107.
- Chan FK, HJ Chun, L Zheng, RM Siegel, KL Bui, and MJ Lenardo (2000) *A Domain in TNF Receptors That Mediates Ligand-Independent Receptor Assembly and Signaling*. Science 288(5475), 2351–2354.

- Chan SL, KO Tan, L Zhang, KSY Yee, F Ronca, MY Chan, and VC Yu (1999) *F1Aalpha, a death receptor-binding protein homologous to the Caenorhabditis elegans sex-determining protein, FEM-1, is a caspase substrate that mediates apoptosis*. J. Biol. Chem. 274(45), 32461–32468.
- Chang DW, Z Xing, VL Capacio, ME Peter, and X Yang (2003) *Interdimer processing mechanism of procaspase-8 activation*. EMBO J. 22(16), 4132–4142.
- Chattopadhyay K, UA Ramagopal, A Mukhopadhaya, VN Malashkevich, TP Dilorenzo, M Brenowitz, SG Nathenson, and SC Almo (2007) *Assembly and structural properties of glucocorticoid-induced TNF receptor ligand: Implications for function*. Proc. Natl. Acad. Sci. U.S.A. 104(49), 19452–19457.
- Chen L, SM Park, AV Tumanov, A Hau, K Sawada, C Feig, JR Turner, YX Fu, IL Romero, E Lengyel, and ME Peter (2010) *CD95 promotes tumour growth*. Nature 465(7297), 492–6.
- Chipuk JE, L Bouchier-Hayes, and DR Green (2006) *Mitochondrial outer membrane permeabilization during apoptosis: the innocent bystander scenario*. Cell Death and Differentiation 13, 1396–1402.
- Choi PJ and TJ Mitchison (2013) *Imaging burst kinetics and spatial coordination during serial killing by single natural killer cells*. Proc. Natl. Acad. Sci. U.S.A. 110(16), 6488–6493.
- Cirman T, K Oresić, GD Mazovec, V Turk, JC Reed, RM Myers, GS Salvesen, and B Turk (2003) *Selective Disruption of Lysosomes in HeLa Cells Triggers Apoptosis Mediated by Cleavage of Bid by Multiple Papain-like Lysosomal Cathepsins*. J. Biol. Chem. 179(5), 3578–3587.
- Cormack BP, RH Valdivia, and S Falkow (1996) *FACS-optimized mutants of the green fluorescent protein (GFP)*. Gene 173(1), 33–8.
- Corti A, G Fassina, F Marcucci, E Barbanti, and G Cassani (1992) *Oligomeric tumour necrosis factor alpha slowly converts into inactive forms at bioactive levels*. Biochem. J. 284, 905–10.
- Das SK, M Darshi, S Cheley, MI Wallace, and H Bayley (2007) *Membrane Protein Stoichiometry Determined from the Step-Wise Photobleaching of Dye-Labelled Subunits*. ChemBioChem 8(9), 994–999.
- Dickens LS, RS Boyd, R Jukes-Jones, MA Hughes, GL Robinson, L Fairall, JW Schwabe, K Cain, and M Macfarlane (2012) *A death effector domain chain DISC model reveals a crucial role for caspase-8 chain assembly in mediating apoptotic cell death*. Mol. Cell 47(2), 291–305.
- Digman MA and E Gratton (2011) *Lessons in Fluctuation Correlation Spectroscopy*. Annu Rev Phys Chem. 62, 645–668.

- Doherty GP, K Bailey, and PJ Lewis (2010) *Stage-specific fluorescence intensity of GFP and mCherry during sporulation In Bacillus Subtilis*. BMC 3(303).
- Duricic N, AG Godin, CM Wever, CD Heyes, M Lakadamyali, and JA Dent (2012) *Stoichiometry of the Human Glycine Receptor Revealed by Direct Subunit Counting*. J. Neurosci. 32(37), 12915–12920.
- Edmond V, B Ghali, A Penna, JL Taupin, S Daburon, JF Moreau, and P Legembre (2012) *Precise mapping of the CD95 pre-ligand assembly domain*. PLOS ONE 7(9), e46236.
- Elson EL (2011) *Fluorescence Correlation Spectroscopy: Past, Present, Future*. Biophys J. 101(12), 2855–2870.
- Enari M, H Sakahira, H Yokoyama, K Okawa, A Iwamatsu, and S Nagata (1997) *Cleavage of CAD inhibitor in CAD activation and DNA degradation during apoptosis*. Nature 391, 43–50.
- Eramo A, M Sargiacomo, L Ricci-Vitiani, M Todaro, G Stassi, CG Messina, I Parolini, F Lotti, G Sette, C Peschle, and R De Maria (2004) *CD95 death-inducing signaling complex formation and internalization occur in lipid rafts of type I and type II cells*. Eur. J. Immunol. 34(7), 1930–40.
- Esposito D, A Sankar, N Morgner, CV Robinson, K Rittinger, and PC Driscoll (2010) *Solution NMR investigation of the CD95/FADD homotypic death domain complex suggests lack of engagement of the CD95 C terminus*. Structure 18(10), 1378–90.
- Ewen CL, KP Kane, and RC Bleackley (2012) *A quarter century of granzymes*. Cell Death Differ. 19(1), 28–35.
- Fernandes-Alnemri T, RC Armstrong, J Krebs, SM Srinivasula, L Wang, F Bullrich, LC Fritz, JA Trapani, KJ Tomaselli, G Litwack, and ES Alnemri (1996) *In vitro activation of CPP32 and Mch3 by Mch4, a novel human apoptotic cysteine protease containing two FADD-like domains*. Proc. Natl. Acad. Sci. U. S. A. 93(15), 7464–9.
- Feske S, EY Skolnik, and M Prakriya (2012) *Ion channels and transporters in lymphocyte function and immunity*. Nat. Rev. Immunol. 12(7), 532–47.
- Fischer U, C Stroh, and K Schulze-Osthoff (2006) *Unique and overlapping substrate specificities of caspase-8 and caspase-10*. Oncogene 25(1), 152–159.
- Fricker N, J Beaudouin, P Richter, R Eils, PH Krammer, and N Lavrik (2010) *Model-based dissection of CD95 signaling dynamics reveals both a pro- and antiapoptotic role of c-FLIPL*. J. Cell Biol. 190(3), 377–89.
- Fuchs Y and H Steller (2011) *Programmed Cell Death in Animal Development and Disease*. Cell 147(4), 742–758.

- García-Sáez AJ, J Ries, M Orzáez, E Pérez-Payà, and P Schulle (2009) *Membrane promotes tBID interaction with BCL(XL)*. Nat Struct Mol Biol. 16(11), 1178–85.
- Goehring NW, D Chowdhury, AA Hyman, and SW Grill (2010) *FRAP Analysis of Membrane-Associated Proteins: Lateral Diffusion and Membrane-Cytoplasmic Exchange*. Biophys J. 99(8), 2443–2452.
- Goldstein B and AS Perelson (1984) *Equilibrium theory for the clustering of bivalent cell surface receptors by trivalent ligands. Application to histamine release from basophils*. Biophys J. 45(6), 1109–1123.
- Goldstein P (2000) *FasL Binds Preassembled Fas*. Science 288(5475), 2328–2329.
- Gong JH, G Maki, and HG Klingemann (1994) *Characterization of a human cell line (NK-92) with phenotypical and functional characteristics of activated natural killer cells*. Leukemia 8(4), 652–658.
- Grell M, H Wajant, G Zimmermann, and P Scheurich (1998) *The type 1 receptor (CD120a) is the high-affinity receptor for soluble tumor necrosis factor*. Proc. Natl. Acad. Sci. U. S. A. 95, 570–575.
- Groulx N, H McGuire, R Laprade, JL Schwartz, and R Blunck (2011) *Single Molecule Fluorescence Study of the Bacillus thuringiensis Toxin Cry1Aa Reveals Tetramerization*. J. Biol. Chem. 286(49), 42274–42282.
- Gruenberg J and H Stenmark (2004) *Opinion: The biogenesis of multivesicular endosomes*. Nat. Rev. Mol. Cell Bio. 5, 317–323.
- Grujic M, T Braga, A Lukinius, M Eloranta, SD Knight, G Pejler, and M Åbrink (2005) *Serglycin-deficient Cytotoxic T Lymphocytes Display Defective Secretory Granule Maturation and Granzyme B Storage*. J. Biol. Chem. 280(39), 33411–33418.
- Guigas G and M Weiss (2006) *Size-dependent diffusion of membrane inclusions*. Biophys J. 91(7), 2393–8.
- (2008) *Influence of hydrophobic mismatching on membrane protein diffusion*. Biophys J. 95(3), 25–7.
- Haddad N El, R Moore, D Heathcote, M Mounayar, J Azzi, B Mfarrej, I Batal, C Ting, M Atkinson, MH Sayegh, PG Ashton-Rickardt, and R Abdi (2011) *The novel role of SERPINB9 in cytotoxic protection of human mesenchymal stem cells*. J Immunol. 187(5), 2252–60.
- Han J, CQ Zhong, and DW Zhang (2011) *Programmed necrosis: backup to and competitor with apoptosis in the immune system*. Nature Immunology 12, 1143–1149.

- Han J, LA Goldstein, BR Gastman, CJ Froelich, XM Yin, and H Rabinowich (2004) *Degradation of Mcl-1 by granzyme B: implications for Bim-mediated mitochondrial apoptotic events*. J. Biol. Chem. 279(21), 22020–22029.
- Hanahan D and RA Weinberg (2011) *Hallmarks of Cancer: The Next Generation*. Cell 144(5), 646–674.
- Hastie P, MH Ulbrich, HL Wang, RJ Arant, AG Lau, Z Zhang, EY Isacoff, and L Chen (2013) *AMPA receptor/TARP stoichiometry visualized by single-molecule subunit counting*. Proc. Natl. Acad. Sci. U.S.A. 110(13), 5163–5168.
- Hau A, P Ceppi, and ME Peter (2012) *CD95 Is Part of a Let-7/p53/miR-34 Regulatory Network*. PLOS ONE 7(11), e49636.
- Herrant M, A Jacquél, S Marchetti, N Belhacène, P Colosetti, F Luciano, and P Auburger (2004) *Cleavage of Mcl-1 by caspases impaired its ability to counteract Bim-induced apoptosis*. Oncogene 23, 7863–7873.
- Hinterdorfer P and A Oijen, eds. (2009) *Handbook of Single-Molecule Biophysics*. ISBN 978-0-387-76496-2. Springer.
- Hoffmann JC, A Pappa, PH Krammer, and IN Lavrik (2009) *A new C-terminal cleavage product of procaspase-8, p30, defines an alternative pathway of procaspase-8 activation*. Mol. Cell Biol. 29(16), 4431–4440.
- Hoffmann SC, A Cohnen, T Ludwig, and C Watzl (2010) *2B4 Engagement Mediates Rapid LFA-1 and Actin-Dependent NK Cell Adhesion to Tumor Cells as Measured by Single Cell Force Spectroscopy*. J. Immunol. 186(5), 2757–2764.
- Holler N, A Tardivel, M Kovacsovics-Bankowski, S Hertig, O Gaide, F Martinon, A Tinel, D Deperthes, S Calderara, T Schulthess, J Engel, P Schneider, and J Tschopp (2003) *Two adjacent trimeric Fas ligands are required for Fas signaling and formation of a death-inducing signaling complex*. Mol Cell Biol. 23(4), 1428–40.
- Hughes MA, N Harper, M Butterworth, K Cain, GM Cohen, and M MacFarlane (2009) *Reconstitution of the Death-Inducing Signaling Complex Reveals a Substrate Switch that Determines CD95-Mediated Death or Survival*. Mol. Cell 35(5), 265–279.
- Humphrey W, A Dalke, and K Schulten (1996) *VMD - Visual Molecular Dynamics*. J. Molec. Graphics 14, 33–38.
- Hymowitz SG and VM Dixit (2010) *Unleashing cell death: the Fas-FADD complex*. Nature Structural & Molecular Biology 17(11), 1289–1290.

- Hymowitz SG, HW Christinger, G Fuh, M Ultsch, M O'Connell, RF Kelley, A Ashkenazi, and AM De Vos (1999) *Triggering cell death: the crystal structure of apo2l/trail in a complex with death receptor 5*. *Mol. Cell* 4(4), 563–571.
- Idriss HT and JH Naismith (2000) *TNF α and the TNF Receptor Superfamily: Structure-Function Relationship(s)*. *Microscopy Research and Technique* 50, 184–195.
- Ivanov AI, ed. (2008) *Exocytosis and Endocytosis*. Vol. 440. *Methods in Molecular Biology*. ISBN: 978-1-58829-865-2. Humana Press.
- Joeckel LT and PI Bird (2014) *Are all granzymes cytotoxic in vivo?* *Biol. Chem.* 395(2), 181–202.
- Jung YS, KS Kim, KD Kim, JS Lim, JW Kim, and E Kim (2001) *Apoptosis-linked gene 2 binds to the death domain of Fas and dissociates from Fas during Fas-mediated apoptosis in Jurkat cells*. *Biochem Biophys Res Commun.* 288(2), 420–6.
- Kaiserman D and PI Bird (2010) *Control of granzymes by serpins*. *Cell Death Differ.* 17, 586–595.
- Kallenberger SM, J Beaudouin, J Claus, C Fischer, PK Sorger, S Legewie, and R Eils (2014) *Intra- and Interdimeric Caspase-8 Self-Cleavage Controls Strength and Timing of CD95-Induced Apoptosis*. *Sci Signal.* 7(316).
- Kam CM, D Hudig, and JC Powers (2000) *Granzymes (lymphocyte serine proteases): characterization with natural and synthetic substrates and inhibitors*. *Biochim. Biophys. Acta* 1477, 307–323.
- Kantari C and H Walczak (2011) *Caspase-8 and bid: caught in the act between death receptors and mitochondria*. *Biochim. Biophys. Acta* 1813(4), 558–63.
- Keppler A, M Kindermann, S Gendreizig, H Pick, H Vogel, and K Johnsson (2004) *Labeling of fusion proteins of O6-alkylguanine-DNA alkyltransferase with small molecules in vivo and in vitro*. *Methods* 32(4), 437–44.
- Kerr JFR, AH Wyllie, and AR Currie (1972) *Apoptosis: A Basic Biological Phenomenon with Wide-ranging Implications in Tissue Kinetics*. *Br J Cancer* 26(4), 239–257.
- Kirkin V, N Cahuzac, F Guardiola-Serrano, S Huault, K Lückerrath, E Friedmann, N Novac, WS Wels, B Martoglio, AO Hueber, and M Zörnig (2007) *The Fas ligand intracellular domain is released by ADAM10 and SPPL2a cleavage in T-cells*. *Cell Death Differ.* 14(9), 1009–23.
- Kischkel FC, S Hellbardt, I Behrmann, M Germer, M Pawlita, PH Krammer, and ME Peter (1995) *Cytotoxicity-dependent APO-1 (Fas/CD95)-associated proteins form a death-inducing signaling complex (DISC) with the receptor*. *EMBO J.* 14(22), 5579–5588.

- Kneen M, J Farinas, Y Li, and AS Verkman (1998) *Green fluorescent protein as a noninvasive intracellular pH indicator*. *Biophys J.* 74(3), 1591–9.
- Koch J, A Steinle, C Watzl, and O Mandelboim (2013) *Activating natural cytotoxicity receptors of natural killer cells in cancer and infection*. *Trends Immunol.* 34(4), 182–91.
- Krammer PH (2000) *CD95's deadly mission in the immune system*. *Nature* 407(6805), 789–95.
- Krammer PH, R Arnold, and IN Lavrik (2007) *Life and death in peripheral T cells*. *Nature Reviews Immunology* 7, 532–542.
- Kranz D and M Boutros (2014) *A synthetic lethal screen identifies FAT 1 as an antagonist of caspase- 8 in extrinsic apoptosis*. *EMBO J.* 33(6), 529–664.
- Krippner-Heidenreich A, F Tübing, S Bryde, S Willi, G Zimmermann, and P Scheurich (2002) *Control of Receptor-induced Signaling Complex Formation by the Kinetics of Ligand/Receptor Interaction*. *J. Biol. Chem.* 277(46), 44155–44163.
- Krzewski K and JE Coligan (2012) *Human NK cell lytic granules and regulation of their exocytosis*. *Front. Immunol.* 3(335).
- Kummer JA, AM Kamp, F Citarella, AJG Horrevoets, and CE Hack (1996) *Expression of Human Recombinant Granzyme A Zymogen and Its Activation by the Cysteine Proteinase Cathepsin C*. *J. Biol. Chem.* 271(16), 9281–9286.
- Kummer JA, O Micheau, P Schneider, N Bovenschen, R Broekhuizen, R Quadir, MCM Strik, CE Hack, and J Tschopp (2007) *Ectopic expression of the serine protease inhibitor PI9 modulates death receptor-mediated apoptosis*. *Cell Death Differ.* 14, 1486–1496.
- Lamy T, JH Liu, TH Landowski, WS Dalton, and TP Loughran (1998) *Dysregulation of CD95/CD95 Ligand-Apoptotic Pathway in CD3 Large Granular Lymphocyte Leukemia*. *Blood* 92(12), 4771–4777.
- Lang I, A Fick, V Schäfer, T Giner, D Siegmund, and H Wajant (2012) *Signaling active CD95 receptor molecules trigger co-translocation of inactive CD95 molecules into lipid rafts*. *J. Biol. Chem.* 287(28), 24026–42.
- Lauffenburger DA and JJ Lindermann, eds. (1996) *Receptors: Models for Binding, Trafficking, and Signaling*. ISBN: 978-0-19-510663-3. Oxford University Press, USA.
- Lavrik IN and PH Krammer (2012) *Regulation of CD95/Fas signaling at the DISC*. *Cell Death Differ.* 19, 36–41.

- Lavrik IN, A Golks, D Riess, M Bentele, R Eils, and PH Krammer (2007) *Analysis of CD95 threshold signaling: triggering of CD95 (FAS/APO-1) at low concentrations primarily results in survival signaling*. J. Biol. Chem. 282(18), 13664–71.
- Lavrik IN, T Mock, A Golks, JC Hoffmann, S Baumann, and PH Krammer (2008) *CD95 Stimulation Results in the Formation of a Novel Death Effector Domain Protein-containing Complex*. J. Biol. Chem. 283(39), 26401–26408.
- Law RHP, Q Zhang, S McGowan, AM Buckle, GA Silverman, W Wong, CJ Rosado, CG Langendorf, RN Pike, PI Bird, and JC Whisstock (2006) *An overview of the serpin superfamily*. Genome Biology 7(5), 216.
- Lee KH, C Feig, V Tchikov, R Schickel, S Hallas, S Schütze, ME Peter, and AC Chan (2006) *The role of receptor internalization in CD95 signaling*. EMBO J. 25(5), 1009–23.
- Leverrier S, GS Salvesen, and CM Walsh (2011) *Enzymatically active single chain caspase-8 maintains T-cell survival during clonal expansion*. Cell Death Differ. 18(1), 90–8.
- Li H, H Zhu, C Xu, and J Yuan (1998) *Cleavage of BID by Caspase 8 Mediates the Mitochondrial Damage in the Fas Pathway of Apoptosis*. Cell 94(4), 491–501.
- Li H, X Fan, C Stoicov, JH Liu, S Zubair, E Tsai, Ste R Marie, TC Wang, S Lyle, E Kurt-Jones, and J Houghton (2009) *Human and mouse colon cancer utilizes CD95 signaling for local growth and metastatic spread to liver*. Gastroenterology 137(3), 934–44.
- Lopez JA, O Susanto, MR Jenkins, N Lukoyanova, VR Sutton, RHP Law, A Johnston, CH Bird, PI Bird, JC Whisstock, JA Trapani, HR Saibil, and I Voskoboinik (2013) *Perforin forms transient pores on the target cell plasma membrane to facilitate rapid access of granzymes during killer cell attack*. Blood 121(14), 2659–2668.
- Lucken-Ardjomande S and JC Martinou (2008) *Granzyme A, a Stealth Killer in the Mitochondrion*. Cell 133(4), 568–570.
- Mace EM, P Dongre, HT Hsu, P Sinha, AM James, SS Mann, LR Forbes, LB Watkin, and JS Orange (2014) *Cell biological steps and checkpoints in accessing NK cell cytotoxicity*. Immunology and Cell Biology 92, 245–255.
- Magde D, EL Elson, and WW Webb (1974) *Fluorescence Correlation Spectroscopy. II. An Experimental Realization*. Biopolymers 13, 29–61.
- Mahrus S and CS Craik (2005) *Selective Chemical Functional Probes of Granzymes A and B Reveal Granzyme B Is a Major Effector of Natural Killer Cell-Mediated Lysis of Target Cells*. Chemistry & Biology 12(5), 567–577.

- Mahrus S, W Kisiel, and CS Craik (2004) *Granzyme M Is a Regulatory Protease That Inactivates Proteinase Inhibitor 9, an Endogenous Inhibitor of Granzyme B*. J. Biol. Chem. 279(52), 54275–82.
- Mahrus S, JC Trinidad, DT Barkan, A Sali, AL Burlingame, and JA Wells (2008) *Global Sequencing of Proteolytic Cleavage Sites in Apoptosis by Specific Labeling of Protein N Termini*. Cell 134(5), 866–876.
- Maiwald T and J Timmer (2008) *Dynamical modeling and multi-experiment fitting with PottersWheel*. Bioinformatics 24(18), 2037–2043.
- Martin-Villalba A, E Llorens-Bobadilla, and D Wollny (2013) *CD95 in cancer: tool or target?* Trends in Molecular Medicine 19(6), 329–335.
- Martin-Villalba A, N Schreglmann, E Letellier, S Kleber, and S Klussmann (2008) “The death receptor cd95 controls neurogenesis of adult neural stem cells in vivo and in vitro”. Pat. WO2008034608 A1.
- Martinvalet D, DM Dykxhoorn, R Ferrini, and J Lieberman (2008) *Granzyme A cleaves a mitochondrial complex I protein to initiate caspase-independent cell death*. Cell 133(4), 681–692.
- Martinvalet D, M Walch, DK Jensen, J Thiery, and J Lieberman (2009) *Response: Granzyme A: cell death-inducing protease, proinflammatory agent, or both?* Blood 114(18), 3969–3970.
- Masson D and J Tschopp (1987) *A family of serine esterases in lytic granules of cytolytic T lymphocytes*. Cell 49(5), 679–85.
- Mattson MP (2000) *Apoptosis in neurodegenerative disorders*. Nat. Rev. Mol. Cell Bio. 1, 120–130.
- Mayor S and RE Pagano (2007) *Pathways of clathrin-independent endocytosis*. Nat. Rev. Mol. Cell Bio. 8, 603–612.
- McGuire H, MRP Arousseau, D Bowie, and R Blunck (2012) *Automating Single Subunit Counting of Membrane Proteins in Mammalian Cells*. J. Biol. Chem. 287(43), 35912–35921.
- Medema JP, J deJong, LT Peltenburg, EM Verdegaal, A Gorter, SA Bres, KL Franken, M Hahne, JP Albar, CJ Melief, and R Offringa (2001) *Blockade of the granzymeB / perforin pathway through overexpression of the serine protease inhibitor PI-9 / SPI-6 constitutes a mechanism for immune escape by tumors*. Proc. Natl. Acad. Sci. U.S.A. 98, 11515–11520.
- Micheau O and J Tschopp (2003) *Induction of TNF receptor I-mediated apoptosis via two sequential signaling complexes*. Cell 114(2), 181–90.

- Micheau O, M Thome, P Schneider, N Holler, J Tschopp, DW Nicholson, C Briand, and MG Grütter (2002) *The Long Form of FLIP Is an Activator of Caspase-8 at the Fas Death-inducing Signaling Complex*. J. Biol. Chem. 277(47), 45162–45171.
- Mollenhauer HH, DJ Morre, and LD Rowe (1990) *Alteration of intracellular traffic by monensin; mechanism, specificity and relationship to toxicity*. Biochim. Biophys. Acta. 1031(2), 225–246.
- Momburg F, C Watzl, and A Cerwenka (2013) *NK cells-versatile tools for viral defense and cancer treatment*. Eur. J. Immunol. 43(4), 860–3.
- Montecucco A and G Biamonti (2007) *Cellular response to etoposide treatment*. Cancer Lett. 252(1), 9–18.
- Moubarak RS, L Planells-Ferrer, J Urresti, S Reix, MF Segura, P Carriba, F Marqués-Fernàndez, C Sole, N Llecha-Cano, J Lopez-Soriano, D Sanchis, VJ Yuste, and JX Comella (2013) *FAIM-L is an IAP-binding protein that inhibits XIAP ubiquitinylation and protects from Fas-induced apoptosis*. J Neurosci. 33(49), 19262–75.
- Mukai Y, T Nakamura, M Yoshikawa, Y Yoshioka, S Tsunoda, S Nakagawa, Y Yamagata, and Y Tsutsumi (2010) *Solution of the structure of the TNF-TNFR2 complex*. Sci Signal. 3(148), ra83.
- Muppidi JR, AA Lobito, M Ramaswamy, JK Yang, L Wang, H Wu, and RM Siegel (2006) *Homotypic FADD interactions through a conserved RXDLL motif are required for death receptor-induced apoptosis*. Cell Death Differ. 13(10), 1641–50.
- Muzio M, RB Stockwell, RH Stennicke, GS Salvesen, and VM Dixit (1998) *An Induced Proximity Model for Caspase-8 Activation*. J. Biol. Chem. 273(5), 2926–2930.
- Nagata S (1997) *Apoptosis by Death Factor*. Cell 88, 355–365.
- Naismith JH, TQ Devine, BJ Brandhuber, and SR Sprang (1995) *Crystallographic evidence for dimerization of unliganded tumor necrosis factor receptor*. J. Biol. Chem. 270(22), 13303–7.
- Neumann S, T Bidon, M Branschädel, A Krippner-Heidenreich, and P Scheurich (2012) *The Transmembrane Domains of TNF-Related Apoptosis-Inducing Ligand (TRAIL) Receptors 1 and 2 Co-Regulate Apoptotic Signaling Capacity*. PLOS ONE 7(8), 42526.
- Oberst A, CP Dillon, R Weinlich, LL McCormick, P Fitzgerald, C Pop, R Hakem, GS Salvesen, and DR Green (2011) *Catalytic activity of the caspase-8-FLIP(L) complex inhibits RIPK3-dependent necrosis*. Nature 471(7338), 363–7.
- Orange JS, MS Fassett, LA Koopman, JE Boyson, and JL Strominger (2002) *Viral evasion of natural killer cells*. Nat. Immunol. 3(11), 1006–1012.

- O'Reilly LA, L Tai, L Lee, EA Kruse, S Grabow, WD Fairlie, NM Haynes, DM Tarlinton, JG Zhang, GT Belz, MJ Smyth, P Bouillet, L Robb, and A Strasser (2009) *Membrane-bound Fas ligand only is essential for Fas-induced apoptosis*. *Nature* 461(7264), 659–63.
- Packard BZ, WG Telford, A Komoriya, and PA Henkart (2007) *Granzyme B Activity in Target Cells Detects Attack by Cytotoxic Lymphocytes*. *J. Immunol.* 179(6), 3812–3820.
- Papoff G, P Hausler, A Eramo, MG Pagano, G Leve Di, A Signore, and G Ruberti (1999) *Identification and Characterization of a Ligand-independent Oligomerization Domain in the Extracellular Region of the CD95 Death Receptor*. *J. Biol. Chem.* 274(53), 38241–38250.
- Patron JP, A Fendler, M Bild, U Jung, H Müller, MØ Arntzen, C Piso, C Stephan, B Thiede, H Mollenkopf, K Jung, SHE Kaufmann, and J Schreiber (2012) *microRNA MiR-133b reduces FAIM expression and sensitized HeLa cells to CD95-induced apoptosis*. *PLOS ONE* 7(4), e35345.
- Paulsen M and O Janssen (2011) *Pro- and anti-apoptotic CD95 signaling in T cells*. *Cell Communication and Signaling* 9(7).
- Perez-Hernandez D, C Gutierrez-Vazquez, I Jorge, S Lopez-Martin, A Ursa, F Sanchez-Madrid, J Vazquez, and M Yanez-Mo (2013) *The Intracellular Interactome of Tetraspanin-enriched Microdomains Reveals Their Function as Sorting Machineries toward Exosomes*. *J. Biol. Chem.* 288(17), 11649–11661.
- Peter ME, P Legembre, and BC Barnhart (2005) *Does CD95 have tumor promoting activities?* *Biochim Biophys Acta.* 1755(1), 25–36.
- Pinkoski MJ, M Hobman, JA Heibei, K Tomaselli, F Li, P Seth, CJ Froelich, and RC Bleackley (1998) *Entry and Trafficking of Granzyme B in Target Cells During Granzyme B-Perforin Mediated Apoptosis*. *Blood* 92(3), 1044–1054.
- Pitti RM, SA Marsters, DA Lawrence, M Roy, FC Kischkel, P Dowd, A Huang, CJ Donahue, SW Sherwood, DT Baldwin, PJ Godowski, WI Wood, AL Gurney, KJ Hillan, RL Cohen, AD Goddard, D Botstein, and A Ashkenazi (1998) *Genomic amplification of a decoy receptor for Fas ligand in lung and colon cancer*. *Nature* 396(6712), 699–703.
- Politz JC, RA Tuft, T Pederson, and RH Singer (1999) *Movement of nuclear poly(A) RNA throughout the interchromatin space in living cells*. *Current Biology* 9(6), 285–291.
- Pop C and GS Salvesen (2009) *Human Caspases: Activation, Specificity, and Regulation*. *J. Biol. Chem.* 284(33), 21777–21781.
- Pop C, P Fitzgerald, DR Green, and GS Salvesen (2007) *Role of proteolysis in caspase-8 activation and stabilization*. *Biochemistry.* 46(14), 4398–407.

- Prior IA, C Muncke, RG Parton, and JF Hancock (2003) *Direct visualization of Ras proteins in spatially distinct cell surface microdomains*. J. Cell Biol. 160(2), 165–170.
- Raiborg C, TE Rusten, and H Stenmark (2003) *Protein sorting into multivesicular endosomes*. Current Opinion in Cell Biology 15, 446–455.
- Ramsdell F, MS Seaman, RE Miller, TW Tough, MR Alderson, and DH Lynch (1994) *gld/gld mice are unable to express a functional ligand for Fas*. Eur J Immunol. 24(4), 928–33.
- Rasband WS (1997-2014) *ImageJ*. U. S. National Institutes of Health, Bethesda, Maryland, USA. <http://imagej.nih.gov/ij/>.
- Ravichandran KS (2011) *Beginnings of a Good Apoptotic Meal: The Find-Me and Eat-Me Signaling Pathways*. Immunity 35(4), 445–455.
- Rayan G, JE Guet, N Taulier, F Pincet, and W Urbach (2010) *Recent Applications of Fluorescence Recovery after Photobleaching (FRAP) to Membrane Bio-Macromolecules*. Sensors (Basel) 10(6), 5927–5948.
- Rehm M, H Düßmann, RU Jänicke, JM Tavaré, D Kögel, and JHM Prehn (2002) *Single-cell Fluorescence Resonance Energy Transfer Analysis Demonstrates That Caspase Activation during Apoptosis Is a Rapid Process* ROLE OF CASPASE-3. J. Biol. Chem. 277(27), 24506–24514.
- Reis CR, AHG van Assen, WJ Quax, and RH Cool (2011) *Unraveling the Binding Mechanism of Trivalent Tumor Necrosis Factor Ligands and Their Receptors*. Molecular & Cellular Proteomics 10(1).
- Ren J, L Wen, X Gao, C Jin, Y Xue, and X Yao (2008) *CSS-Palm 2.0: an updated software for palmitoylation sites prediction*. Protein Engineering, Design and Selection 21(11), 639–644.
- Roberts RL, MA Barbieri, KM Pryse, M Chua, JH Morisaki, and PD Stahl (1999) *Endosome fusion in living cells overexpressing GFP-rab5*. J. Cell Sci. 112(12), 3667–3675.
- Roger H, AB Cubitt, and RY Tsien (1995) *Improved green fluorescence*. Nature 373(6516), 663–664.
- Roy C and JL Wrana (2005) *Clathrin- and non-clathrin-mediated endocytic regulation of cell signalling*. Nat. Rev. Mol. Cell Bio. 6, 112–126.
- Saffman PG and M Delbrück (1975) *Brownian motion in biological membranes*. Proc. Natl. Acad. Sci. U.S.A. 72(8), 3111–3113.
- Sandu C, G Morisawa, I Wegorzewska, T Huang, AF Arechiga, JM Hill, T Kim, CM Walsh, and MH Werner (2006) *FADD self-association is required for stable interaction with an activated death receptor*. Cell Death Differ. 13(12), 2052–61.

- Scaffidi C, JP Medema, PH Krammer, and ME Peter (1997) *FLICE is predominantly expressed as two functionally active isoforms, caspase-8/a and caspase-8/b*. J. Biol. Chem. 272(43), 26953–8.
- Scaffidi C, S Fulda, A Srinivasan, C Friesen, F Li, KJ Tomaselli, K Debatin, PH Krammer, and ME Peter (1998) *Two CD95 (APO-1/Fas) signaling pathways*. EMBO J. 17(6), 1675–1687.
- Scaffidi C, I Schmitz, PH Krammer, and ME Peter (1999) *The role of c-FLIP in modulation of CD95-induced apoptosis*. J. Biol. Chem. 274(3), 1541–8.
- Scaffidi C, J Volkland, I Blomberg, I Hoffmann, PH Krammer, and ME Peter (2000) *Phosphorylation of FADD/ MORT at serine 194 and association with a 70-kDa cell cycle-regulated protein kinase*. J. Immunol. 164(3), 1236–1242.
- Schleich Kolja, U Warnken, N Fricker, S Öztürk, P Richter, K Kammerer, M Schnölzer, PH Krammer, and IN Lavrik (2012) *Stoichiometry of the CD95 Death-Inducing Signaling Complex: Experimental and Modeling Evidence for a Death Effector Domain Chain Model*. Mol. Cell 47(2), 306–319.
- Schmidt H, C Gelhaus, M Nebendahl, M Lettau, R Lucius, M Leippe, D Kabelitz, and O Janssen (2011) *Effector granules in human T lymphocytes: proteomic evidence for two distinct species of cytotoxic effector vesicles*. J Proteome Res. 10(4), 1603–20.
- Schneider P, JL Bodmer, N Holler, C Mattmann, P Scuderi, A Terskikh, MC Peitsch, and J Tschopp (1997) *Characterization of Fas (Apo-1, CD95)-Fas Ligand Interaction*. J. Biol. Chem. 272(30), 18827–18833.
- Schneider P, N Holler, J Bodmer, M Hahne, K Frei, A Fontana, and Jürg Tschopp (1998) *Conversion of Membrane-bound Fas(CD95) Ligand to Its Soluble Form Is Associated with Downregulation of Its Proapoptotic Activity and Loss of Liver Toxicity*. J. Exp. Med. 187(8), 1205–1213.
- Schneider TJ, GM Fischer, TJ Donohoe, TP Colarusso, and TL Rothstein (1999) *A novel gene coding for a Fas apoptosis inhibitory molecule (FAIM) isolated from inducibly Fas-resistant B lymphocytes*. J Exp Med. 189(6), 949–56.
- Schoenborn JR and CB Wilson (2007) *Regulation of Interferon- γ During Innate and Adaptive Immune Responses*. Adv. Immunol. 96, 41–101.
- Schütze S, V Tchikov, and W Schneider-Brachert (2008) *Opinion: Regulation of TNFR1 and CD95 signalling by receptor compartmentalization*. Nat. Rev. Mol. Cell Bio. 9, 655–662.
- Schulte M, K Reiss, M Lettau, T Maretzky, A Ludwig, D Hartmann, B de Strooper, O Janssen, and P Saftig (2007) *ADAM10 regulates FasL cell surface expression and modulates FasL-induced cytotoxicity and activation-induced cell death*. Cell Death Differ. 14, 1040–1049.

- Schwering Michael (2012) "Die Entwicklung neuer Methoden in der Fluoreszenzmikroskopie auf Basis reversibler chemischer Reaktionen". PhD thesis. Ruprecht-Karls-Universität, Heidelberg, Germany.
- Scott FL, B Stec, C Pop, MK Dobaczewska, JJ Lee, V Monosov, H Robinson, GS Salvesen, R Schwarzenbacher, and SJ Riedl (2009) *The Fas-FADD death domain complex structure unravels signalling by receptor clustering*. *Nature* 457(7232), 1019–22.
- Segura MF, C Sole, M Pascual, RS Moubarak, MJ Perez-Garcia, R Gozzelino V Iglesias, N Badiola, JR Bayasas, N Llecha, J Rodriguez-Alvarez, E Soriano, VJ Yuste, and JX Comella (2007) *The long form of Fas apoptotic inhibitory molecule is expressed specifically in neurons and protects them against death receptor-triggered apoptosis*. *J. Neurosci.* 27(42), 11228–41.
- Shaner NC, PA Steinbach, and RY Tsien (2005) *A guide to choosing fluorescent proteins*. *Nat. Methods* 2, 905–909.
- Shaner NC, RE Campbell, PA Steinbach, BN Giepmans, AE Palmer, and RY Tsien (2004) *Improved monomeric red, orange and yellow fluorescent proteins derived from *Discosoma* sp. red fluorescent protein*. *Nat. Biotechnol.* 22(12), 1567–1572.
- Shankaran H, H Resat, and HS Wiley (2007) *Cell Surface Receptors for Signal Transduction and Ligand Transport: A Design Principles Study*. *PLoS Comput. Biol.* 3(6), e101.
- Shiraishi T, K Suzuyama, H Okamoto, T Mineta, K Tabuchi, K Nakayama, T Shimizu, J Tohma, T Ogihara, H Naba, H Mochizuki, and S Nagata (2004) *Increased cytotoxicity of soluble Fas ligand by fusing isoleucine zipper motif*. *Biochem Biophys Res Commun.* 322(1), 197–202.
- Siegel RM, DA Martin, L Zheng, SY Ng, J Bertin, J Cohen, and MJ Lenardo (1998) *Death-effector filaments: novel cytoplasmic structures that recruit caspases and trigger apoptosis*. *J. Cell Biol.* 141(5), 1243–53.
- Siegel RM, JK Frederiksen, DA Zacharias, FK Chan, M Johnson, and D Lynch (2000) *Fas preassociation required for apoptosis signaling and dominant inhibition by pathogenic mutations*. *Science* 288(5475), 2354–2357.
- Snapp EL, RS Hegde, M Francolini, F Lombardo, S Colombo, E Pedrazzini, N Borgese, and J Lippincott-Schwartz (2003) *Formation of stacked ER cisternae by low affinity protein interactions*. *J. Cell Biol.* 163(2), 257–69.
- Somia NV, MJ Schmitt, DE Vetter, D Van Antwerp, SF Heinemann, and IM Verma (1999) *LFG: an anti-apoptotic gene that provides protection from Fas-mediated cell death*. *Proc. Natl. Acad. Sci. U. S. A.* 96(22), 12667–72.

- Srikanth RC and KJ Rakesh (1989) *Direct measurement of interstitial convection and diffusion of albumin in normal and neoplastic tissues by fluorescence photobleaching*. Proc. Natl. Acad. Sci. U.S.A. 86, 5385–5389.
- Stenmark H (2009) *Rab GTPases as coordinators of vesicle traffic*. Nat. Rev. Mol. Cell Bio. 10, 513–525.
- Stout-Delgado HW, Y Getachew, TE Rogers, BC Miller, and DL Thiele (2007) *The role of serpinb9/serine protease inhibitor 6 in preventing granzyme B-dependent hepatotoxicity*. Hepatology 46(5), 1530–40.
- Strand S, P Vollmer, L van den Abeelen, D Gottfried, V Alla, H Heid, J Kuball, M Theobald, PR Galle, and D Strand (2004) *Cleavage of CD95 by matrix metalloproteinase-7 induces apoptosis resistance in tumour cells*. Oncogene 23(20), 3732–6.
- Strasser A, PJ Jost, and S Nagata (2009) *The many roles of FAS receptor signaling in the immune system*. Immunity 30(2), 180–92.
- Susanto O, JA Trapani, and D Brasacchio (2012) *Controversies in granzyme biology*. Tissue Antigens 80(6), 477–87.
- Susanto O, K Sedelies, J Trapani, and N Waterhouse (2009) *Granule-mediated death by cytotoxic lymphocytes does not require mitochondrial polarization toward the immunologic synapse in target cells*. Blood 113(7), 1609–1611.
- Suzanne M and H Steller (2013) *Shaping organisms with apoptosis*. Cell Death Differ. 20, 669–675.
- Tait SWG and DR Green (2010) *Mitochondria and cell death: outer membrane permeabilization and beyond*. Nat. Rev. Mol. Cell Bio. 11, 621–632.
- Talanian RV, X Yang, J Turbov, P Seth, T Ghayur, CA Casiano, K Orth, and CJ Froelich (1997) *Granule-mediated killing: pathways for granzyme B-initiated apoptosis*. J. Exp. Med. 186(8), 1323–1331.
- Tanaka M, T Suda, T Takahashi, and S Nagata (1995) *Expression of the functional soluble form of human fas ligand in activated lymphocytes*. EMBO J. 14(6), 1129–35.
- Tanaka M, T Suda, T Yatomi, N Nakamura, and S Nagata (1997) *Lethal Effect of Recombinant Human Fas Ligand in Mice Pretreated with Propionibacterium acnes*. J. Immunol. 158(5), 2303–9.
- Tchikov V, U Bertsch, J Fritsch, B Edelmann, and S Schutze (2011) *Subcellular compartmentalization of TNF receptor-1 and CD95 signaling pathways*. Eur. J. Cell Biol. 90(6-7), 467–75.

- Tewari M, WG Telford, RA Miller, and VM Dixit (1995) *CrmA, a Poxvirus-encoded Serpin, Inhibits Cytotoxic T-lymphocyte-mediated Apoptosis*. J. Biol. Chem. 270(39), 22705–22708.
- Thiery J, D Keefe S Boulant, E Boucrot, M Walch, D Martinvalet, IS Goping, RC Bleackley, T Kirchhausen, and J Lieberman (2011) *Perforin pores in the endosomal membrane trigger the release of endocytosed granzyme B into the cytosol of target cells*. Nat Immunol. 12(8), 770–7.
- Thomas DA, L Scorrano, GV Putcha, SJ Korsmeyer, and TJ Ley (2001) *Granzyme B can cause mitochondrial depolarization and cell death in the absence of BID, BAX, and BAK*. Proc. Natl. Acad. Sci. U.S.A. 98, 14985–14990.
- Thomas LR, DJ Stillman, and A Thorburn (2002) *Regulation of FADD death domain interactions by the death effector domain identified by a modified reverse two-hybrid screen*. J. Biol. Chem. 277(37), 34343–34348.
- Thomas LR, A Henson, JC Reed, FR Salsbury, and A Thorburn (2004) *Direct binding of Fas-associated death domain (FADD) to the tumor necrosis factor-related apoptosis-inducing ligand receptor DR5 is regulated by the death effector domain of FADD*. J. Biol. Chem. 279(31), 32780–32785.
- Ulbrich MH and EY Isacoff (2007) *Subunit counting in membrane-bound proteins*. Nat. Methods. 4(4), 319–321.
- Valley CC, AK Lewis, DJ Mudaliar, JD Perlmutter, AR Braun, CB Karim, DD Thomas, JR Brody, and JN Sachs (2012) *Tumor necrosis factor-related apoptosis-inducing ligand (TRAIL) induces death receptor 5 networks that are highly organized*. J. Biol. Chem. 287(25), 21265–78.
- Veugelers K, B Motyka, IS Goping, I Shostak, T Sawchuk, and BC Bleackley (2006) *Granule-mediated killing by granzyme B and perforin requires a mannose 6-phosphate receptor and is augmented by cell surface heparan sulfate*. Mol Biol Cell. 17(2), 623–33.
- Volkman M, J Schiff, Y Hajjar, G Otto, F Stilgenbauer, W Fiehn, PR Galle, and WJ Hofmann (2001) *Loss of CD95 expression is linked to most but not all p53 mutants in European hepatocellular carcinoma*. J. Mol. Med. 79, 594–600.
- Wang L, JK Yang, V Kabaleeswaran, AJ Rice, AC Cruz, AY Park, Q Yin, E Damko, SB Jang, S Raunser, CV Robinson, RM Siegel, T Walz, and H Wu (2010) *The Fas-FADD death domain complex structure reveals the basis of DISC assembly and disease mutations*. Nature Structural & Molecular Biology 17(11), 1324–1329.
- Waterhouse NJ, KA Sedelies, VR Sutton, MJ Pinkoski, KY Thia, R Johnstone, PI Bird, DR Green, and JA Trapani (2006) *Functional dissociation of $\Delta\Psi_m$ and cytochrome c release*

- defines the contribution of mitochondria upstream of caspase activation during granzyme B-induced apoptosis. *Cell Death Differ.* 13, 607–618.
- Weiß K, A Neef, Q Van, S Kramer, I Gregor, and J Enderlein (2013) *Quantifying the Diffusion of Membrane Proteins and Peptides in Black Lipid Membranes with 2-Focus Fluorescence Correlation Spectroscopy.* *Biophys J.* 105(2), 455–462.
- Wickman GR, L Julian, K Mardilovich, S Schumacher, J Munro, N Rath, SAL Zander, A Mleczak, D Sumpton, N Morrice, WV Bienvenut, and MF Olson (2013) *Blebs produced by actin–myosin contraction during apoptosis release damage-associated molecular pattern proteins before secondary necrosis occurs.* *Cell Death Differ.* 20, 1293–1305.
- Worth A, AJ Thrasher, and HB Gaspar (2006) *Autoimmune lymphoproliferative syndrome: molecular basis of disease and clinical phenotype.* *Br. J. Hematol.* 133, 124–140.
- Wörz S, P Sander, M Pfannmüller, RJ Rieker, S Joos, G Mechtersheimer, P Boukamp, P Lichter, and K Rohr (2010) *3D Geometry-Based Quantification of Colocalizations in Multi-Channel 3D Microscopy Images of Human Soft Tissue Tumors.* *IEEE Trans. on Medical Imaging* 29(8), 1474–1484.
- Yang TT, L Cheng, and SR Kain (1996) *Optimized Codon Usage and Chromophore Mutations Provide Enhanced Sensitivity with the Green Fluorescent Protein.* *Nucl. Acids Res.* 24(22), 4592–4593.
- Yu JW, PD Jeffrey, and Y Shi (2009) *Mechanism of procaspase-8 activation by c-FLIPL.* *Proc. Natl. Acad. Sci. U.S.A.* 106(20), 8169–74.
- Zhang D, PJ Beresford, AH Greenberg, and J Lieberman (2001) *Granzymes A and B directly cleave lamins and disrupt the nuclear lamina during granule-mediated cytotoxicity.* *Proc. Natl. Acad. Sci. U.S.A.* 98(10), 5746–51.
- Zhou Q, S Snipas, K Orth, M Muzio, VM Dixit, and GS Salvesen (1997) *Target Protease Specificity of the Viral Serpin CrmA—Analysis of five Caspases.* *J. Biol. Chem.* 272(12), 7797–7800.
- Zhou Z, X Song, A Berezov, G Zhang, Y Li, H Zhang, R Murali, B Li, and MI Greene (2008) *Human glucocorticoid-induced TNF receptor ligand regulates its signaling activity through multiple oligomerization states.* *Proc. Natl. Acad. Sci. U.S.A.* 105(14), 5465–70.
- Ziegler U and P Groscurth (2004) *Morphological Features of Cell Death.* *News Physiol. Sci.* 19, 124–128.
- Zong WX and CB Thompson (2006) *Necrotic death as a cell fate.* *Genes & Dev.* 20, 1–15.

Zwietering MH, Jongenburger I, Rombouts FM, and van't Riet K (1990) *Modeling of the bacterial growth curve*. Appl. Environ. Microbiol. 56(6), 1875–81.